Development of zebrafish and computational models of neurovascular coupling in health and disease

By:

Karishma Chhabria

A thesis submitted in partial fulfilment of the requirements for the degree of Doctor of Philosophy

The University of Sheffield
Faculty of Medicine Dentistry and Health
Department of Infection, Immunity and Cardiovascular Disease

Submission Date: 21/12/18

Acknowledgments

I would like to thank my supervisors Tim and Clare for their support and guidance throughout my PhD. Their never ending enthusiasm and drive for research kept me ticking. Especially their unique sense of humour helped me go through the hard times, effortlessly. Not many PhD students get to understand the importance of marmite in our life and research! I could have never imagined finishing the accolade of work within the time constraint without their (Tim and Clare's) timely help and feedback. In particular, I would like to thank Tim for prioritising me above all his clinic work and head of the department responsibilities (I am still amazed and inspired by how beautifully he manages several of his lives!). I am especially immensely indebted to Clare for all the brainstorming sessions-they truly strengthen my interests and understanding of the field of neurovascular coupling.

I would like to acknowledge Dr. Rob Wilkinson, Prof. Oliver Bandmann, Dr. Ryan MacDonald, Dr. Vincent Cunliffe, Dr. Freek van Eeden, Dr Emily Noël for their guidance and provision of transgenic lines, experimental materials and protocols used for my PhD research.

To my other two *musketeers*, August and Marialena, I have very fond memories all the times we spent together including our crazy propositions of our future research (I am looking forward to our future collaborations!).

Special mention goes to my *lab-mom* K-Cat (Karen) for all the personal and professional help and encouragement throughout my PhD life. Learning new skills (be it bench work or crocheting) wouldn't be as enjoyable experience as without her.

Cheers to my *buddy*, Hannah for being as weird as me that truly sparked our conversations and of course our scientific collaboration. To my other collaborators + fellow labmates, Yan and Aaron, thanks for all the bubble tea visits and for all the warmth that they have shown at all

times (and not just in time of need). I would also take this opportunity to thank all the other people in the lab or associated groups, Chris, Eric, Emily, Jane, Elisabeth, Rosemary, Davide, Julia, Matt, Lisa, Marcus, Rings, Ryan and Eleanor for all their help and support throughout my PhD.

I express my profound gratitude to my dear friends and housemates Haroula, Sherry and Helen for their unwavering loyalty and friendship. Special thanks to Haroula for making those late sleepless nights back home fun filled.

To my *Sheffield limers*, Loren, Carol, Andrea, Serena and Rodney for sharing and discussing the PhD fun and blues. Some of my best PhD times were spent procrastinating together with them.

My in-depth gratitude to all the Bateson center aquarium staff, especially Claire, Vicky, Susie, Mat and Mike for all the guidance and help with the zebrafish work throughout my PhD.

I would also like to thank all the Firth court porters, Paul1, Paul2, Alan, Stuart and Steve for making those weekends and late nights' fun and chatty. My special gratitude to Paul1 for his support and friendship and for being my Firth Court family.

Cheers to the developers of Spotify.com for developing the most amazing application that made my thesis writing significantly more fun ($p<0.001$) compared to youtube.

My deepest gratitude to mum, dad and brother, for their constant faith in me and being with me in thick and thin. They are the most important people in my life and I dedicate my research and thesis to them. Finally, to my Murph-being able to see him was like my reward in my rat-maze. It kept me going through my PhD.

Contents

List of Abbreviations

+/+	Wild type sibling
+/-	Heterozygous sibling
-/-	Homozygous sibling
1°	Primary
2°	Secondary
Ab	Antibody
Aβ	Amyloid beta
AD	Alzheimer's disease
AJs	Adherens junctions
ANOVA	Analysis of Variance
AP	Action Potential
AQP	Aquaporin
ARRIVE	Animal Research: Reporting of In Vivo Experiments
ASPA	Animals Scientific Procedures Act
ATP	Adenosine Triphosphate
BBB	Blood Brain Barrier
B-Buffer	Blocking Buffer
BDNF	Brain Derived Neutrotrophic Factor
BOLD	Blood Oxygenation Level Dependence
bp	Base-pair
bpm	beats per minute
BSA	Bovine Serum Albumin
Ca^{2+}	Calcium ion
CBF	Cerebral blood flow
COX	Cyclo-oxygenase
CNS	Central Nervous system
d	Days
DA	Dorsal Aorta
DAF-FM	4-Amino-5- Methylamino-2',7'-Difluorofluorescein Diacetate
DEPC	Diethylpyrocarbonate

dH_2O	Distilled water
DMSO	Dimethylsulfoxide
DNA	Deoxyribonucleic Acid
dpf	Days Post Fertilization
EC	Endothelial cell
EDA	Experimental Design Analysis
EEG	Electroencephalogram
EET	Epoxyeicosatrienoids
eNOS	endothelial Nitric oxide synthase
ER	Endoplasmic Reticulum
fli1	Friend Leukaemia integration 1 transcription factor
***f*MRI**	Functional Magnetic Resonance Imaging
fps	Frames Per Second
GCaMP	Fusion protein of GFP, calmodulin and M13
gch1	GTP (guanine triphosphate) cyclohydrolase 1
GDM	Gestational diabetes mellitus
gDNA	Genomic DNA
GECI	Genetically encoded calcium indicator
GFAP	Glial Fibrilliary Acidic Protein
GFP	Green Fluorescent Protein
GluR	Glutamate receptors
GLUT	Glucose transporter
h	Hours
HCl	Hydrocholoric Acid
HCO_3^-	Bicarbonate ions
HH	Hodgkin Huxley
HIF	Hypoxia inducible factor
hpf	Hours Post Fertilization
HRF	Hemodynamic response function
I-Buffer	Incubation Buffer
iGluSnFR	Intensity Based Glutamate Sensing Fluorescent Reporter
IHC	Immunohistochemistry

iNOS	inducible Nitric oxide synthase
IP_3	Inositol Triphosphate
IR	Infrared
JAM	Junctional adhesion molecules
K^+	Potassium ions
kdr	Kinase-insert Domain Receptor
kdrl	Kinase-insert Domain Receptor-like
K_{ir}	Inward rectifying Potassium channel
klf2a	Kruppel like factor 2a
LC	Locus coerulus
LDL	Low density lipoprotein
LED	Light Emitting Diode
LFP	Local Field Potential
LIF	Leukaemia inhibiting factor
L-NAME	N(ω)-nitro-L-arginine methyl ester
LSFM	Lightsheet Fluorescent Microscopy
LTP	Long term plasticity
M13	Peptide sequence from myosin light chain kinase
MAPK	Mitogen activated protein kinase
MeOH	Methanol
µF	MicroFarads
ml	Millilitres
mM	Millimolar
µM	Micromolar
MO	Morpholino
MRI	Magnetic Resonance Imaging
ms	milliseconds
mS	milliSiemen
MS222	Tricaine
Na^+	Sodium ions
NaOH	Sodium Hydroxide
NAWCO	Named Animal Welfare and Care Officer

nbt	n-beta tubulin
nm	nanometers
NMDAR	N-Methyl D-Aspartate Receptor
NSS	Non stimulus specific
NVC	Neurovascular coupling
NVU	Neurovascular unit
NO	Nitric oxide
NOR	Novel Object Recognition
NRP-1	Neuropilin-1
ns	non-significant
PBS	Phosphate Buffer Saline
PBST	PBS with Tween
PBS-TS	PBS with Triton X100 and Sheep Serum
PCR	Polymerase Chain Reaction
PD	Parkinson's Disease
PET	Positron Emission Tomography
pF	picofarads
PDGF	Platelet Derived Growth Factor
PDGFRβ	Platelet Derived Growth Factor Receptor Beta
PGE2	Prostaglandin E2
PKC	Protein kinase C
pS	picoSiemens
pH	power of Hydrogen ions
QIF	Quadratic Integrate and Fire
RBC	Red Blood Cell
RFP	Red fluorescent protein
RGC	Retinal ganglion cells
ROI	Region of Interest
ROS	Reactive Oxygen Species
RNS	Reactive Nitrogen Species
RT	Room Temperature
SAB	Spontaneous Alternation Behavior

s.e.m.	standard error of mean
Sem3A	Semaphorin 3A
SHP1	Src-homology 2 domain containing phosphatase 1
SNP	Sodium Nitroprusside
SNR	Signal to Noise ratio
SPIM	Selective Plane Illumination Microscopy
STDP	Spike time dependent plasticity
STP	Short term plasticity
$\mathbf{t_{1/2}}$	Time to half peak
TeO	Optic tectum
Tg	Transgenic
TJs	Tight junctions
TRP	Transient Receptor Potential (channel)
TRPM	Melanostatin Transient Receptor Potential subfamily
TRPV4	Vallinoid Transient Receptor Potential subfamily
TS	Triton with Sheep serum
Vd	Ventral telencephalic area
Ve-Cad	Vascular endothelium cadherin
VEGF	Vascular endothelial growth factor
VNC	Vasculoneuronal coupling
VSMC	Vascular Smooth muscle cell
v/v	volume by volume
WT	Wildtype
ZO	zona occudens

List of Tables

List of Figures

Abstract

In this thesis, I have developed a novel zebrafish model of neurovascular coupling. Combining lightsheet imaging, compound transgenic zebrafish models and custom MATLAB based analysis pipelines, I characterised the neurovascular responses (neuronal calcium increases and change in red blood cell speed) in the optic tectum in response to visual stimulation. I determined the development stage at which neurovascular coupling in zebrafish larvae develops, followed by testing the requirement for nitric oxide or astrocyte cyclo-oxygenase in my model. I then used this model to investigate factors influencing neurovascular function. I first characterized the effect of glucose exposure and the role of nitric oxide in modulating neurovascular coupling. I then examined the effect of genetic mutation of Guanosine Triphosphate cyclohydrolase (an enzyme involved in nitric oxide and dopamine production in the brain) on neurovascular coupling. Finally, I have developed a minimal mathematical model of the neurovascular unit. To demonstrate the potential of this model I have simulated the effect of high blood glucose and low nitric oxide on neurovascular coupling and show this conforms with experimental data obtained in zebrafish.

1 Introduction

The brain accounts for 2% of body weight but consumes 20% of cardiac output. Active neurons depend on increases in local cerebral blood flow (CBF) through neurovascular coupling (NVC) as first described by Roy and Sherrington (1).

Many human diseases are associated with neurovascular dysfunction (2-5). Several studies have shown neurodegenerative disorders such as Alzheimer's and Parkinson's disease are associated with reduced cerebral blood flow and neurovascular deficits (6-8). Although there is an increase in the number of drugs being discovered to treat various symptoms of such diseases, the fundamental mechanisms of these pathologies are not well understood, hindering the progress to find a cure for neurodegenerative diseases.

Micro and macrovascular diseases such as hypertension, diabetes and stroke are major risk factors of neurodegenerative disorders (9-11). Recent studies have also demonstrated cerebral blood flow deficits in such vascular diseases suggesting the possibility of common pathological mechanisms between cardiovascular and neurological diseases.

1.1 Neurovascular coupling

Neurons, unlike other cells, possess limited energy reserves (12). Hence, it is essential that increased neuronal energy demands are rapidly met (spatially and temporally) by an increase in blood flow to supply the requisite oxygen and glucose to the neuron. This process, termed NVC, results from crosstalk between the cellular elements of the neurovascular unit (NVU) (13). These neuronal activity-evoked changes in blood flow and oxygenation underlie functional neuroimaging techniques such as BOLD-fMRI (blood oxygen level dependent-functional magnetic resonance imaging) (14, 15).

The NVU comprises neurons, astrocytes, pericytes, vascular smooth muscle cells (VSMCs)

and endothelial cells (ECs) (**Figure 1-1** and **Figure 1-2**). Neurons depolarize in response to a stimulus and consume energy to restore their electrochemical gradients. Depolarization leads to release of synaptic neurotransmitters, which can act on post-synaptic neurons and surrounding astrocytes (16). Astrocytes in turn respond to neurotransmitters by increasing intracellular calcium, leading to release of vasodilators (16). Surrounding blood vessels dilate due to hyperpolarization of VSMCs and calcium increases in ECs (16), leading to increased local blood flow. Vasodilation can also be induced by mechanisms such as increased extracellular potassium or neuronal nitric oxide (NO) release (17). These mechanisms contribute to NVC, communicating the cerebral energy demands to the vasculature. While Angelo Mosso was the first to measure the relationship between neuronal firing and cerebral hemodynamics (18, 19), their functional association was first proposed by Roy and Sherrington (1). Although this view of neuronal activity-induced local increases in blood flow is widely accepted, recent studies have challenged the conventional picture of NVC. For example, Huo et al. (20) suggest that neuronal activity and blood flow are uncoupled in the frontal cortex during locomotion in rodent models.

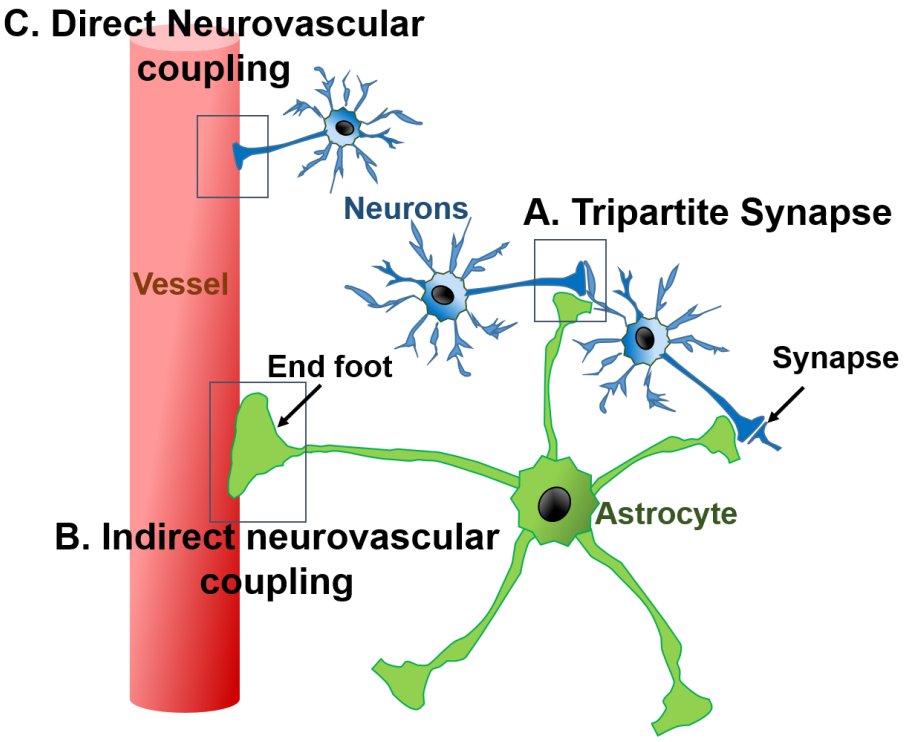

Figure 1-1: A schematic representation of neurovascular coupling with its main elements. A: Tripartite synapse consisting of a neuronal synapse ensheathed by an astrocyte process. Two commonly known mechanisms of neurovascular coupling **B:** Direct neurovascular coupling occurs through direct contact between axon terminals of neurons and the blood vessel and **C:** Indirect neurovascular coupling occurs through the interface of astrocytes and blood vessels.

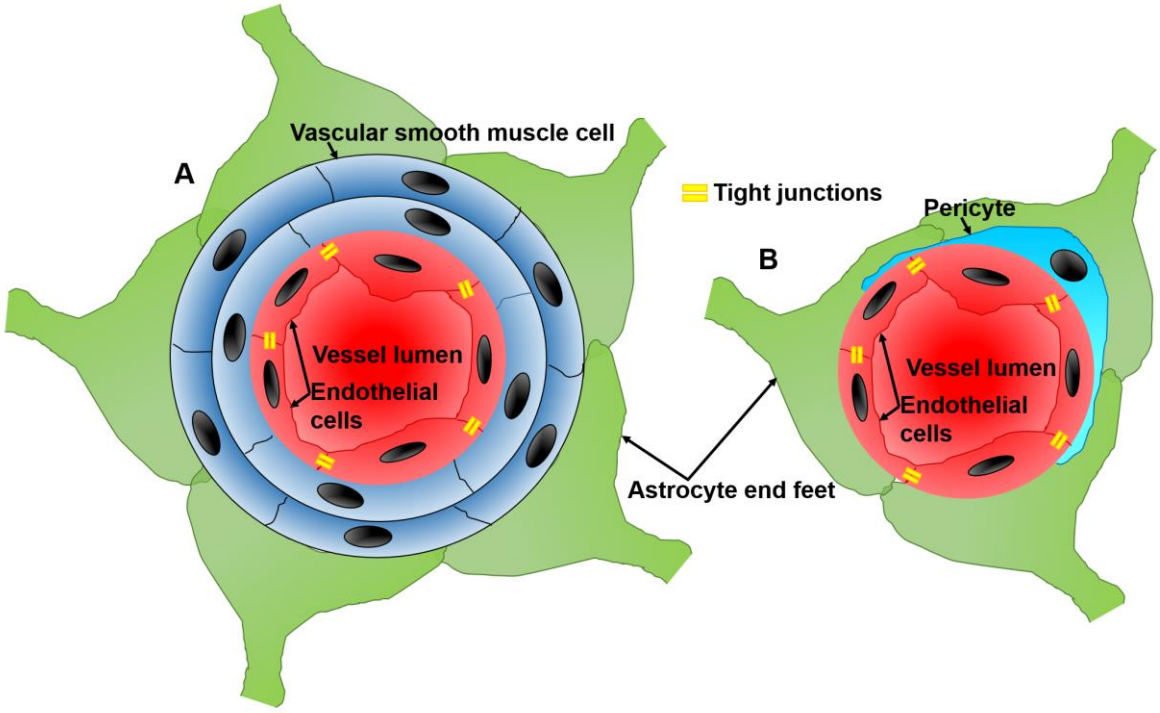

Figure 1-2: Cross section of blood brain barrier. **A:** illustrates cross section at the arteriolar level where astrocytic endfeet interact with the smooth muscle layer. **B:** illustrates the cross section at the capillary level where the smooth muscle cell layer is absent and contractility is controlled by pericytes.

The neurons interact with the vascular endothelium, the anatomical substrate of blood brain barrier (BBB) via the interface of astrocytes, pericytes and VSMCs, forming a functional NVU. Each element of the NVU is described below.

1.2 Neurovascular unit: functional components

1.2.1 Neurons

Neurons form the fundamental functional elements of the brain. They interact with each other through the synapse that forms the contact unit.

The input to a neuron comprises signals coming from different nearby neurons. These are processed in the soma of the receiving neuron (through the dendritic end) and an output response is produced. The effect of input signals from other neurons is to inject currents, positive and negative, into the receiving neuron. The currents change the membrane voltage of the receiving neuron, where positive (negative) currents increase (decrease) membrane voltage.

Such change in the membrane voltage is caused by influx and/or efflux of potassium/sodium/calcium ions ($K^+/Na^+/Ca^{2+}$). Unstimulated neurons have a negative resting membrane potential (21, 22). When stimulated, the membrane potential rises until it reaches a set threshold followed by a steep rise in membrane potential. The ion gradients are restored back to the resting potential within 1ms and this is propagated as an action potential (AP) in the axon. Restoration of the ionic gradient is energetically expensive, as it requires Adenosine triphosphate (ATP)-dependent pumps (23, 24). Originally, the energy deficit (due to the activity of these pumps) was considered to be the signal communicated to the blood vessels (1). However, it is now known that it is neurotransmitters which act as the signal conveyed to the vasculature (25). Neurons are known to directly mediate NVC through neuronal nitric oxide

synthetase (nNOS) activations, followed by release of NO (26) or release of prostaglandins through cyclooxygenase (COX) 2 mediated pathways (27).

1.2.2 Astrocytes

Glial cells play many functions in the brain such as modulating synaptic activity through uptake of neurotransmitters and release of gliotransmitters (28, 29). Astrocytes are glial cells, which account for the another important cell type within the brain (than the neurons) (30) that are now known to occupy 15- 50% of brain volume (31). These star shaped cells have extremely large processes which contact approximately 10,000-100,000 synapses per astrocyte (32). Astrocytes perform a variety of functions. Some astrocyte processes contact neurons while others contact capillaries and arterioles (33, 34). Synaptic glutamate binds to the metabotropic and ionotropic receptors on astrocytes (35) via the tripartite synapse (36) leading to intracellular calcium signalling (37). This leads to activation of pathways releasing gliotransmitters (29) or vasoactive elements such as prostaglandins (16, 38). The vasoactive agents lead to calcium signalling in the ECs and hyperpolarization of VSMCs, causing vasodilation/vasoconstriction. On the other hand, gliotransmitters such as ATP and D-Serine are involved in modulating synaptic plasticity (39-41). Astrocytes are also involved in spatial buffering of extracellular potassium (post neuronal depolarization) to maintain ionic homeostasis in extracellular matrix (42). Furthermore, they contact other types of glia, sensing their activations constantly. For example, myelination can be induced by astrocytic leukaemia inhibiting factor (LIF), released in response to ATP released by neurons (43).

As a bridge between neurons and vessels, astrocytes are central to NVC (44). Glutamate released by active neurons has been shown to activate metabotropic glutamate receptor

(mGluR) 5 dependent astrocyte calcium activations (27). This is followed by COX1 mediated release of prostaglandins and cytochrome P450 mediated epoxyeicosatrienoids (EETs) release by astrocytes, leading to vasodilation (27, 45). Although various studies have established the importance of astrocytes, there are studies contradicting their role in NVC. Sun et al., (46) have shown adults mouse to lack mGluR5 thus contracting the astrocyte based modulation of NVC. Recent studies have questioned the contribution of astrocytes as the astrocyte calcium signals are very slow compared to neuronal activity (47) and that arterial vasodilation can occur in the absence of calcium (48). Recent studies have now shown role of astrocytes at capillary (pericyte) control of NVC rather than arteriole (49).

1.2.3 Vascular smooth muscle cells

VSMCs regulate vessel tone. All types of vasoregulation (mechanical, chemical and humoral) of CBF involves VSMCs (50-54). Vasoactive agents/neuromodulators/neurotransmitters released by neurons and/or astrocytes act on messenger specific receptors on VSMCs causing arteriole dilation/constriction. For example, neurons release NO leading to hyperpolarization of the VSMCs and vasodilation (26, 55-57). End feet of stimulated astrocytes can alter the diameter of their enveloped vessels by signalling to VSMCs (58). Modest increases in extracellular [K^+], (above physiological 10-15 mM) have been shown to increase the conductance of inward rectifier potassium channels causing VSMC hyperpolarization (59). Prostaglandins, specifically prostaglandin E2 (PGE_2), relax VSMCs by binding to EP_4 receptors, decreasing the phosphorylation of myosin light chain by the activation of protein kinase A (58, 60). In addition to vasodilation, studies in brain slices and isolated retina have demonstrated vessel constriction mediated by the enzyme, cytochrome P450 4A in VSMCs (31). Hypoxia-associated vasoconstriction is mediated by the activation of A_{2A} receptors on

VSMCs by extracellular adenosine (61). All of these effects modulate the tone of VSMCs causing significant changes in blood flow. Interestingly, studies have shown that VSMCs can indirectly affect NVC by setting the basal tone of arterioles thereby determining the magnitude and polarity of the vascular response to neural activity (vasoconstriction or vasodilation) (62, 63).

1.2.4 Pericytes

Pericytes are contractile components of the NVU that wrap around the abluminal surface of blood vessels (in particular, capillaries). Pericytes share their precursors with VSMC (64). Mature pericytes and ECs share a common basement membrane which acts as a substrate for exchanging signals (65). Pericytes are known to aid EC development (66-68). Pericytes have multiple processes and cover several ECs (69, 70). The central nervous system (CNS) vasculature has the greatest pericyte coverage of any organ (71). The ratio of ECs to pericytes in the CNS is 1:1-3:1 (65, 70). Pericyte coverage is associated with the barrier properties of the ECs, EC turnover and blood pressure (72) and is affected in various pathologies (70, 73-75). Pericyte-deficient mice show higher BBB permeability (76) and recent work has suggested this promotes neurodegeneration (73). Pericyte dysfunction has also been observed in retinal diabetic neuropathy (77-79).

Until recently it was thought that NVC was solely modulated by changes in VSMC tone (50, 80) but studies have demonstrated the ability of pericytes to regulate blood flow at the capillary level (81, 82), although their role *in vivo* remains unresolved (83). Despite convincing evidence, there are a number of issues hindering the determination of pericyte function in NVC, in particular the lack of an agreed definition of pericytes and their detailed role in the NVU (84, 85).

1.2.5 Endothelium

Since the identification of vasoactive substances such as NO (86, 87), ECs have been shown to play a role in vasculogenesis, regulation of vascular tone and inflammation (88, 89).

In addition, brain ECs are the main cellular elements responsible for maintaining homeostasis of the NVU by secreting various trophic factors (90). Unlike peripheral ECs, cerebral endothelium forms tight junctions (TJs) (91, 92) to contribute to the BBB. Together with the adherens junctions (AJs) TJs form a selective barrier establishing a regulated communication between blood and brain tissue (93, 94). TJs seal the inter-endothelial cleft forming a continuous vessel structure (94). On the other hand, AJs initiate and maintain endothelial cell-to-cell contact (95-97). TJs and AJ proteins provide cells with a mode to physically communicate with their neighbours and also play a role in intercellular signalling (93). These can be either transmembrane proteins (claudins, occludins, junctional adhesion molecules (JAM) and vascular endothelium cadherin; (Ve-Cad)) or cytoplasmic plaque proteins (cingulin, 7H6, Rab13, ZONAB, AP-1, protein kinase C (PKC) ζ, PKCλ, heterotrimeric G protein and catenin family (α, β, γ, p120)) (93, 94).

Numerous studies point to dysfunction of the endothelium in various pathologies (98-100). BBB disruption leads to increased paracellular permeability, entry of both inflammatory leukocytes and inflammatory macromolecules (101-103). Studies have shown this increases BBB permeability and thus various neuropathologies such as CNS inflammation, Alzheimer's disease (AD), Parkinson's disease (PD) and epilepsy (104, 105). Pathological studies indicate that there are specific sets of mediators causing BBB disruption such as vascular endothelial growth factor (VEGF), histamines, interferons, cytokines, chemokines, free radicals, amyloid-β, and thrombins (105-111). Microorganisms and other infective agents also breach the barrier

leading to “opening” of the BBB in conditions such as meningitis and encephalitis (112, 113). Another common mechanism of BBB disruption is by abnormal signalling pathways through junctional complexes (110).

ECs have a neuroprotective role as they secrete matrix-trophic factors such as brain derived neurotrophic factor (BDNF) (114). They also release vasoactive substances that modulate vascular tone (115). These substances can be dilatory, such as NO, or constrictive, such as endothelin and thromboxane (116, 117). Some studies suggest ECs play a role in long range propagation of vasodilation during NVC (118).

1.3 Neurovascular development

1.3.1 Neurovascular congruence

Vertebrate nervous and vascular systems are anatomically complex and follow a branched hierarchical morphology (119, 120). Earlier studies suggested that both systems rely heavily on each other for their development. Factors provided by each of the systems are necessary for the development of the other (121, 122). Recent research emphasizes the independency of these systems (123-126). It is now known that these two systems can develop independently however with a level of congruency due to the shared developmental mechanisms, hence termed neurovascular congruency (124).

Proponents of neurovascular congruency have shown that nerves and vessels tend to follow the same route of development and at the same time avoid similar areas such as muscles (124). *In vivo* and *in vitro* studies have shown similar effects of various trophic factors on both systems, for example VEGF increases angiogenesis as well as axonal growth (126, 127) while semphorin-3A (Sem3A) inhibits capillary growth and neuronal proliferation (124, 128). Detailed mechanistic studies have demonstrated that nerve proliferation during development is

not dependent on VSMC development (124, 129). However, expression of a similar profile of receptors such as Neuropilin1 (NRP1) on both neurons and ECs provides evidence for shared mechanisms of neuronal and endothelial development (130, 131). A recent study in rodent whisker barrel development, demonstrates the independent development of the neuronal and the vascular ring with common development factors such as Sem3E and Plexin-D1 (123). The intimate association between the two systems is important given that the functional relation formed between the two becomes important for NVC. Moreover, recent evidences demonstrating the link between vascular anomalies and cognitive impairments further corroborate the importance of the association of the two systems (132, 133). It is thus a more generally accepted view that both systems develop independently with a similar set of trophic factors contributing to intricate remodelling.

1.3.2 Development of functional neurovascular coupling

Recent developmental studies have explored the nature of the hemodynamic response function (HRF) in postnatal, adolescents and adults in humans and rodent models (134). Various differences in the neurovascular responses between adults and new-borns have been suggested, however the characteristic pattern is not thoroughly established in rodents (135, 136).

Functional imaging studies in rodents demonstrated a negative (inverted) BOLD response which was speculated to switch to a positive response with age (134, 137, 138). A recent study confirmed this switch in the BOLD response while also showing a local vasoconstriction in postnatal rats (P21) (137). Various reasons were suggested to cause the differences in HRF between new-borns and adults. The NVU has been shown to be incompletely developed at P7 which could result in local or global irregular tone leading to vasoconstriction 1(134, 139, 140). Premature cerebral tissue is more sensitive to hypoxia due to the high metabolic demand of the

developing tissue which, coupled to developing cerebral autoregulation, could result in negative BOLD responses (141). Vessel architecture becomes more hierarchically complex with age which might cause a premature smaller or reverse stimulus-evoked hemodynamic response (142, 143). Astrocytes and pericytes have also been shown to develop during the early postnatal period (139, 144, 145). Other studies demonstrate spontaneous neural firing early in development, a possible result of developing inhibitory neuronal networks (146, 147). This is also supported by studies showing differences in the maturation time of the inhibitory and excitatory circuitries (148, 149). However, the exact age for complete maturation of the neurovascular response in rodents remains unclear.

1.4 Hemoneural hypothesis of vascular feedback

NVC suggests a unidirectional communication between neurons and vessels via the interface of astrocytes (described above). In 2008, Moore and Cao (150) proposed the 'hemoneural hypothesis', which suggests the vasculature can modulate neuronal activity and that NVC is thus not unidirectional.

The mechanisms by which the vasculature can influence neural activity have been proposed to be either direct or indirect (via astrocytes). Direct vasculo-to-neural regulation could be mediated via diffusible vascular derived NO through the BBB (151), hyperemia-induced activation of neuronal mechanosensitive ion channels, or temperature-dependent activation/inactivation of neuronal activity. Indirect or astrocyte-mediated hemo-to-neuronal signalling could occur on a second-to-tens of seconds time scale compared to millisecond-to-second time scale for the direct pathway. Astrocyte mediated neuronal activity modulation has been well studied through the effect of astrocyte-released gliotransmitters such as glutamate, ATP and D-serine (152-154). Furthermore, it is known that vascular derived NO can lead to

calcium oscillations in astrocytes followed by release of glutamate and ATP (155). These observations suggest astrocytes are plausible players in 'hemoneural coupling.' Another potential mechanism suggested in the hemoneural hypothesis was through transduction of mechanical changes in the vasculature via mechanosensitive channels (156-158). The proximity of astrocyte processes to the vasculature make them ideal for sensing mechanical changes in the vasculature (159, 160). The role of astrocyte vallinoid transient receptor potential (TRPV4) channels in mediating vasodilation has been previously described (161). A recent *in vitro* study emphasized the role of cerebral vasculature in adjusting neuronal resting activity through the activation of TRPV4 channels on the astrocytes (160).

1.5 Neurovascular dysfunction in various neurological and vascular disorders

Neurovascular dysfunction broadly encompasses anomalies in both NVC and improper functioning of the NVU. fMRI-BOLD studies show that impaired brain vascularization is a predictor of dementia (162).

Various pathological states are associated with impaired NVC known as neurovascular 'uncoupling' (163). Clinical studies have shown that astrocytoma induced neurovascular uncoupling causes speech arrest in patients (164). Hypoxia studies in rodent models demonstrate impaired CBF during forepaw stimulation (165).

The conventional hypothesis of AD pathogenesis emphasizes on amyloid-β accumulation as the initiation various pathways leading to tau pathology and neuronal dysfunction. Various experimental studies over more than a decade have shown cerebral blood flow is impaired in AD which may be due to impaired NVC (166, 167). Thus, an alternative hypothesis was suggested (two-hit vascular hypothesis of AD) proposing damaged brain microcirculation initiating a non-amyloidogenic pathway of vascular mediated neuronal dysfunction (hit one)

caused by dysfunctional BBB (168). Impaired amyloid-β clearance and increased amyloid-β production have been shown to be an effect of BBB disruption thus causing an accumulation of amyloid-β (hit two) in the brain (133, 168-171). Thus, the alternative hypothesis suggests tau pathology in AD to be an outcome of vascular dysfunction which could be associated of impaired NVC (168). Disruption of NVC in mice is associated with impaired spatial and recognition memory alongside motor incoordination (172). Amongst the various reasons attributed to these impairments, inflammation and infiltration of leukocytes are major factors (169). Recent studies have shown that amyloid deposition in AD affects VSMC contractility (173), Astrocyte degeneration has also been suggested to be involved in the pathogenesis of AD (174). While there are various studies discussing neurovascular dysfunction in AD, few studies have shown NVC deficits in PD. Using simultaneous Electroencephalogram (EEG)-Doppler technique, a recent clinical study has shown neurovascular uncoupling in PD patients (175). Gait dysfunctions as seen in PD are also observed in mouse models with cerebrovascular dysfunctions (176, 177). Genetic studies have shown various genes to be mutated in familial PD such as phosphatase and tensin homolog (*PTEN)* induced putative kinase 1(*PINK1, (178)),* various domains of α-synuclein *(SCNA, (179)),* leucine-rich repeat kinase 2*(LRRK1, (180)), parkin (181),* protein deglycase *(DJ-1, (182)),* lysosomal membrane protein, *(ATP13A2, (183))* and guanine triphosphate (GTP)-hydrolase *(GCH1, (184)).* Recent clinical studies have shown *GCH1* to be one of the major risk factors for Dopa-responsive dystonia (DRD) and PD (185). This gene will be a focus of some of my data in subsequent chapters.

Demographic studies suggest vascular disorders are one of the central risk factors in neurological conditions such as stroke and dementia. Conversely, AD and PD lead to a cholinergic deficit which impairs NVC (186). Recent findings also demonstrate a link between cerebral small vessel disease and cognitive impairment (187).

Hyperglycemia is a major component of type II diabetes mellitus (T2DM), and various studies elucidate the effect of hyperglycemia on components of the NVU morphologically and anatomically in either cerebral or retinal models such as streptozotocin induction of diabetes in mammalian (188, 189) and other approaches in non-mammalian systems (190, 191). The retina has been the most used system since retinopathy is a prominent complication of T2DM (192, 193).

1.6 Effect of hyperglycaemia on components of NVU

1.6.1 The effect of hyperglycaemia on the endothelium

EC dysfunction occurs in diabetes prior to macro and microvascular complications such as nephropathy, retinopathy, atherosclerosis and coronary heart disease (194). EC possess remarkable phenotypic plasticity in response to physiological variations (195). Normal blood glucose ranges from 3.6-5.8 mmol/l which is tightly regulated by metabolic homeostasis (196). In this range ECs are in a 'quiescent' state (196, 197). Under hyperglycemic condition (>10 mmol/l) ECs lose their quiescence and acquire new phenotypes also termed 'endothelial cell dysfunction' (196). Impaired endothelial function is characterized by features such as a deficit in the bioavailability of NO, reduced endothelial-mediated vasorelaxation, increased expression of adhesion molecules and inflammatory genes, overproduction of reactive oxygen and nitric species (ROS and RNS) and increased BBB permeability (198, 199). These events are speculated to be followed by 'endothelial senescence' leading to microvascular complications (200). Retinal studies in mouse have shown upregulation of FOXO1 transcription factor which is known to promote inducible NOS (iNOS) dependent peroxynitrite generation leading to low density lipoprotein (LDL) oxidation and endothelial NOS (eNOS) dysfunction (201). Corroborating this, other studies have confirmed a link between FOXO1 upregulation and EC loss in the retina of diabetic rats (201, 202). Recent data have additionally

shown activation of JAK2/STAT3 pathway and of VEGF and of NADP(H) oxidase followed by ROS generation under hyperglycemia (202).

1.6.2 The effect of hyperglycemia on neurons

Various studies have associated hyperglycemia with cognitive impairments (203). The effects of hyperglycemia on the components of the NVU as described above results in neuroinflammation (204, 205). Psychophysical studies involving tests such as contrast sensitivity, color vision and focal electroretinography (ERG) have shown significant differences in diabetic individuals (206). It is unclear if these neurosensory deficits occur prior to identifiable vascular complications.

At the neuronal level, cell viability studies with PC12 cell cultures have shown increased neurotoxicity with high glucose conditions similar to Parkinson's studies with PC12 cell lines (207). Glutamate is one of the most important excitatory neurotransmitters in the brain and increased levels of extracellular glutamate are observed in diabetic retina (208). Adenosine, another important molecule with respect to neurotransmission and gliotransmission has the capability to inhibit the extracellular accumulation of the excitatory amino acids. Studies have shown that adenosine signalling is affected under high glucose conditions with downregulation of A1 adenosine receptor and upregulation of A2 adenosine receptor (209). Thus ameliorating the adenosine system could be a possible way to prevent neuropathy associated with diabetes.

In addition to the excitotoxic effects and abnormalities in the neurotransmission system, high glucose is also shown to induce changes in the conduction velocity of neurons (210).

1.6.3 The effect of hyperglycemia on astrocytes

Astrocytes or astroglial cells are critically placed between the neurons and blood vessels. Given their role in the NVU and NVC (as described earlier), understanding this role may help our understanding of diabetic neuro and vasculopathy. Retinal studies with streptozotocin-induced hyperglycemia in rodents have shown that within 4 weeks, there is a significant vascular leakage and the number of astrocytes reduces alongside macroglial abnormalities (211, 212). Studies have speculated that these multiple insults to the glial system lead to hyperplasia of the Muller cells (retinal analog of astrocytes) followed by an increase in glial fibrilliary acidic protein (GFAP) (211).

Recent studies have shown changes in the morphology of astrocytes in the forebrain of induced ischemic rats (213). These studies show astrocyte endfoot retraction from the cerebral blood vessel walls, providing evidence for astrocyte-related detrimental effects of ischemia observed during hyperglycemia (213). Another feature of hyperglycemia is astroglial acidosis wherein the role of astrocytes in maintaining an alkaline pH is compromised due to inhibition of transport of bicarbonate (*HCO3-)* ions (214, 215). While acidosis is a prominent feature of the ischaemic brain, it has been recently attributed to astrocyte malfunction of spatial buffering (214, 215). Apart from maintaining pH balance, another important role of astrocytes is to maintain ionic balance by regulating extracellular ionic concentrations. Firing neurons release potassium ions in the extracellular space which are taken up by astrocytes via inward rectifying potassium (K_{ir}) receptors, (216). Failing this uptake, the membrane potential of the surrounding neurons would stay in the depolarized condition changing the ions homeostasis in the neurons. In vitro studies with cultured astrocytes demonstrate that high glucose reduces expression of *Kir4.1* by 50% (216, 217). In addition, astrocytic glutamate clearance is also impaired under high glucose conditions making neurons extremely susceptible to depolarization, a possible cause of neurotoxicity (217, 218).

1.6.4 The effect of hyperglycemia on microglial cells

Microglia are resident immune cells of the CNS and are derived from myeloid progenitors that migrate to the periphery during late embryonic life (219). They use phagocytic and cytotoxic mechanisms against pathogens and other substances, similar to macrophages (219, 220). They can be either neuroprotective or toxic depending on the brain state (220). Several studies have characterized the resting state morphology of microglial cells (221). They are shown to have long and diffused processes under basal state which are transformed during inflammation to a hypertrophic and proliferative state with less ramified morphology (221). Under inflammatory conditions, microglial activation is followed by activation of the macroglia such as astrocytes as well (222). However, few studies have shown the direct relation between microglial and macroglial activation. On the contrary retinal studies in rodent have speculated the nature of activation of microglial cells to be either from the damaged/injured neural parenchyma and/or activated macroglial cells (223). Studies have also suggested that during early diabetes microglial cells closely approach the axons and ganglion cells making them more vulnerable to activated state (223).

Studies with postnatal P2-6-day old rat pups have shown hyperglycemia to be characterized by significant CCL2 chemokine activation at P6 alongside increases in the total number of macrophages/microglial cells in the inner nuclear layers of the retina (224, 225).

1.6.5 The effect of hyperglycemia on pericytes

Pericytes are the contractile machinery of the microvasculature and form a crucial unit of the NVU (as described earlier). Various pathological studies have implicated anomalies in the pericytes to accompany microvasculopathies (75) related to cardiovascular disorders (226).

Clinical studies have shown fewer pericytes (possibly due to increased migration), termed 'pericyte dropout', in patients with diabetic retinopathy (77, 79). Research in platelet derived growth factor receptor β (PDGFRβ) null (-/-) mice have shown a reduction (50%) in pericytes similar to that in diabetic mice (40%) (73, 227). This reduction correlates with more acellular capillaries that could induce angiogenic defects and increased vessel permeability (228, 229). Interestingly, a few studies have suggested that these pericyte alterations occur prior to the endothelial dysfunction observed under various microangiopathies (74).

Various cell signalling pathways in pericytes are affected by hyperglycemia. Human retina studies have shown increases in methylglyoxal and α-oxalodehyde in pericytes exposed to hyperglycemia (230). These increases have been attributed to defective glyoxylase-I function in the pericytes which has a protective role (230). In addition, studies with mouse retina have shown loss of platelet derived growth factor (PDGF) mediated survival mechanisms in pericytes attributed to activation of PKC-α and p38 alpha mitogen activated protein kinase (MAPK) which overexpresses a protein tyrosine phosphatase called Src-homology 2 domain containing phosphatase (SHP-1) (231). This leads to downstream phosphorylation of the PDGF receptor, possibly leading to apoptosis underlying the vascular complications of hyperglycemia.

1.7 The effect of hyperglycemia on neurovascular coupling

Our brain consumes around 20% of the cardiac output and thus consumes a relatively higher amount of glucose and oxygen compared to any other organ in the body. This is mainly attributed to the neurons not having their own energy storage system in form of glycogen reserves. The BBB and its components maintain the requisite resistance for particles and/or substances entering the bloodstream. Glucose is the main energy molecule in the brain although

there are controversial studies suggesting lactate can also act as an energy source for neurons (232, 233). Although the extracellular matrix surrounding the neurons maintains a glucose concentration of 2-4 µmol/g (234), glucose can pass through the selectively permeable BBB formed by astrocytes and ECs (235). Glucose transport from the bloodstream is mainly aided by glucose transporters (GLUT)1-5 (236, 237). Dysfunction of glucose transport may lead to hypo or hyperglycemia in the brain; hyperglycemia being the fundamental phenotype of diabetes (238).

Diabetes mellitus and its related vascular complications are one of the leading causes of death in the western world. Diabetes leads to a range of effects, one of the most crucial being cognitive impairment (239, 240). This could be due to defects in the NVU such as endothelial senescence, astrocyte disruption and neuroinflammation leading to impairment of NVC. Other studies have shown association of diabetic retinopathy with microvascular dysfunction and NVC (241, 242). Acute streptozotocin injection causes a reduction in hyperaemia in rodent models (243). Furthermore, mechanistic studies have described the role of protein kinase C (PKC) and modulation of BK_{Ca} (calcium dependent potassium channels) and K_{ir} channels in diabetes (244). However, it is unclear whether impaired NVC observed as a result of diabetes makes the brain more prone to dementia and related cognitive defects.

1.8 The pathological consequence of hyperglycemia as gestational diabetes

Gestational diabetes mellitus (GDM) is a common phenomenon associated with 2-9% pregnancies. Women with GDM have an increased risk of adverse perinatal outcomes including macrosomia, early induction of labour and caesarean section (245). GDM increases the risk of the offspring to develop cardiovascular disease in later life (246, 247). GDM is thus associated with ill health outcomes in both the mother and the offspring (248). Given that

hyperglycemia affects neurovascular function and possibly cognition (as discussed earlier), GDM might cause cognitive defects in the later life of offspring.

1.9 Possible role of vascular feedback in hyperglycemia (role of TRPV4)

The transient receptor potential (TRP) family of genes comprises canonical TRPC, melastatin (TRPM), polycystin (TRPP) and vallinoid (TRPV) (249, 250). The TRPV subfamily is composed of various homologues which play a role in nociception, mechano-sensing, osmolarity-sensing and thermosensing (251, 252). All are Ca^{2+} selective channels gated by capsaicin, acidosis and endogenous ligands such as anandamide (252).

Emerging evidence suggests that TRP channels play a role in neuronal Ca^{2+} signalling (253). TRPV4 channels are known to be expressed on astrocytes, neurons and ECs (253-255). Interestingly studies have shown that TRPV4 in ECs can regulate eNOS (256) and that there exists a feedback loop from endothelial NOS to TRPV4 to modulate TRPV4 based Ca^{2+} signalling (257). Recent studies have shown the presence of TRPV4 on the endfeet of cortical astrocytes causing changes in the intracellular astrocyte calcium and therefore modulating the vascular tone and contributing to NVC (157, 258).

Clinical and experimental studies have shown TRPV4 dysfunction to be associated with hyperglycemia and diabetes (31). Studies on rodent retinal microvasculature have described retinopathy induced by streptozotocin injection to be associated with downregulation of TRPV4 in the ECs and thereby reduction in retinal endothelial Ca^{2+} signalling (259). TRPV4 mutations are linked to neuropathies and play a role in inflammation via its interaction with eNOS (260). TRPV4 is also associated with axonal degeneration (261) attributed to TRPV4 associated neuroglial swelling and inflammatory signalling (262). However, as the link

between neurodegeneration and dysfunctional NVC is unclear, the contribution of TRPV4 dysfunction to NVC and neurodegenerative diseases is not precisely known.

1.10 Imaging paradigms for investigating functional neurovascular coupling

There are several methods for studying NVC in mammalian models with a range of spatial and temporal resolutions. Frequently used techniques include minimally invasive modalities such as fMRI-BOLD (263), laser speckle contrast imaging (264), photoacoustic microscopy, near infrared spectroscopy (265), 2D optical intrinsic spectroscopy (266) and invasive modalities such as voltage sensitive dye imaging using multi-photon imaging (267). Although requiring chronic surgery, there is now an increasing use of invasive methodologies for investigating NVC. This is due to several reasons such as: better spatio-temporal resolution compared with non-invasive methodologies, and blood flow measures (such as BOLD) being surrogate measures of the neuronal activity rather than directly reflecting neuronal activity (268). Furthermore, lightsheet microscopy is also being used to image GCaMP dynamics, and NVU in awake mouse preparations (269). Lightsheet microscopy, due to its high spatial and temporal dynamics, has been proposed to be better than multiphoton imaging due to less photo bleaching (270, 271).

1.11 The use of zebrafish as a model for studying disease and neuroscience

There are various animal models used in neuroscience; primate models such as monkeys, rodent models such as mice, rats, other non-mammalian models include zebrafish, *Drosophila* and *C. elegans.* While primate models are important for cognitive studies, rodent models dominate experimental neurophysiology. However, non-mammalian models such as zebrafish are increasingly being used (272, 273). The first use of zebrafish models dates to the 1950s and

since then they have become a common model for developmental biology and genetics. A range of genetic and imaging technologies have been developed allowing application of the model to neurophysiology, biomedical research and ethology (274). With the advent of genome sequencing their use in biology and medicine has increased (275), including in the study of various disorders such as PD, AD, Huntington's disease and psychiatric diseases (276-278). Their tractable genome gives the advantage of various mutagenesis and functional genomic studies (279). In addition, their physical properties such as transparency and short life span makes them amenable to many research questions.

1.11.1 Zebrafish nervous system

With development in imaging technologies, the use of zebrafish in neuroscience has increased (280). Zebrafish provide an intermediate level of complexity between mammals and invertebrates. Current studies employ both adult and larval zebrafish to understand brain physiology (280). Due to ease of genetic manipulation and novel microscopy techniques, a range of transgenic models have been generated to study various aspects of neuronal activity and function such as a quadruple transgenic line labelling four different retinal cell types (281, 282). With the advent of genetically encoded calcium reporters, any neuronal cell type responses can be characterized and studied in response to stimulus (283). In addition, studies characterizing various other neuronal subtypes have shown similar brain stratification in zebrafish as in mammals. While it is well known that the zebrafish have distinct forebrain (284)have also shown the dorsal telencephalic region (Dm) to be the anatomical homologue of the mammalian amygdala (285, 286). Decision making in zebrafish involves the dorsal nucleus of the ventral telencephalic area (Vd), the zebrafish homolog of the mammalian striatum (285). The zebrafish visual circuitry is composed of retinal ganglion cells, amacrine cells, bipolar cells similar to other vertebrates (287, 288). The main system of the visual processing circuitry is the seven layered optic tectum (teO) which is analogous to the visual cortex in

rodents/humans. Furthermore, the architecture of zebrafish brain systems such as retina, olfactory bulb, cerebellum and spinal cord is similar to other vertebrates (288). Retinal inputs are carried by the retinal ganglion cells (RGCs) to ten different anatomical areas known as arborisation fields (AF1-10) (289). These are homologous to parts of the human visual circuitry (290). For example, AF1 is homologous to the suprachiasmatic nuclei and AF9 to the pretectal nucleus of the optic tract. AF10, the teO, is a homologue of the mammalian superior colliculus (SC) (290). However, the architecture of teO is much more complex than that of the SC and comprises seven layers with unique cell types (290, 291). It is speculated that one of the main reasons for such complexity is that teO performs the visual processing performed by the neocortex in mammals (289). TeO is accessible to electrophysiology, optical imaging, laser ablation and control of neuronal activity by optogenetic effectors due to its position on the surface of the brain. Studies suggest that the teO is primarily involved in tasks requiring a map of the visual space such as phototaxis, the approach of prey, or avoiding obstacles (292). A functional teO is necessary for assessing illumination, reflexes to moving stimuli such as optomotor or optokinetic responses, visual background adaptation, dorsal light reflexes or adjustment to the circadian rhythm (292). Anatomically the teO comprises two regions, a deep cell body layer, the stratum ventriculare (SPV), and a superficial neuropil area consisting of dendrites and axons from tectal neurons, some tectal interneurons, and afferent axons arriving at the tectum from the retina (293, 294). At the cellular level, responses in the tectum itself are variable and heterogeneous. Calcium imaging studies show that some neurons respond to looming stimuli, some to moving edges, others to objects within a certain size range (293). Different object positions are mapped onto different regions in the tectum. Objects in the forward visual field are mapped onto anterior tectum and those behind the fish to posterior tectum (294, 295). Similarly, objects in the upper and lower visual field activate dorsal and ventral tectum, respectively (294, 295). Furthermore, there is hard wired direction sensitivity

in the zebrafish teO (295, 296). The information from the tectum is received by premotor areas in the midbrain/hindbrain (reticular formation) and passed on by hindbrain target areas to spinal cord to elicit coordinated motor responses (290, 291).

Neuronal circuit mapping studies have established that the afferents from the teO to Vd and Dm (290, 291). Recent studies have established zebrafish necessitate light/dark choice selection by sending information about the ambient light conditions (297). Hence the conventional light/dark test used for testing anxiety in zebrafish (297) could be considered as a cognitive test of amygdala/striatum function or connectivity between TeO and Vd/Dm. Larval zebrafish prefer light to dark while the adult form prefers dark to light (298, 299).

Using high speed cameras along with high resolution microscopy, various studies have established the existence of behaviours such as escape, hunting, shoaling, association, sleep and learning in larval zebrafish (300-302). Another well characterized behaviour in zebrafish is optokinetic reflex established in 5 dpf old zebrafish larva (303). Zebrafish are also known to have complex swimming patterns and tail movements, all of which are developed from 4-5 dpf alongside the development of the visual system (304). These swimming bouts have been compared to motion trajectories observed and computationally characterized in mammalian models such as rodents (305). However, attempts to model and characterize behaviours using machine learning approaches have only started to be pursued recently. An interesting object familiarity recognition based on saccadic movement has also been recently described using 10 dpf zebrafish (306). Functionally, zebrafish exhibit complex conditioning such as reward and fear based learning (307). The larval zebrafish is also capable of responding to aversive stimuli such as electric shock (307). Imaging studies demonstrate the presence of a core network area such as in locus coerulus (LC) which responds to multiple stimuli (308). The same study also found a well-organized activity map during complex behaviours such as prey hunting (308,

309). Given this repertoire of behaviours, larval zebrafish have gained popularity in functional neural circuit research.

1.11.2 Zebrafish glial system

Both adult and larval zebrafish brains contain radial glial cells, microglia, niched ependymal cells and oligodendrocytes (310-312). The presence of typical stellate astrocytes in zebrafish brain is unclear. There are tandem arrays of stellate cells (astrocytes) in the spinal cord contacting the spinal veins with their end feet (313). However, no studies have shown the presence of stellate astrocyte-like cells in the central nervous system of zebrafish. Recent studies have shown radial glial cells in zebrafish brain to possess astrocyte-like physiology in terms of expression of various astrocyte specific receptors (314, 315). Immunostaining has established the presence of tight junction proteins; zona occludins- 1 (ZO-1), glutamine synthase (GS), claudin-5a and GFAP in radial glial cells of adult zebrafish (316, 317). Larval zebrafish radial glial cells express the above proteins from 3 dpf, suggesting the BBB to be formed from this stage (318, 319). Zebrafish glial cells have been shown to express aquaporin channel 4, a characteristic of mammalian astrocytes (315), thus getting the name 'astroglial cells.' Radial glial cell ablation studies have now established their importance in venous vascular sprouting in the trunk (319). This study also suggested a differential influence of radial glial cell on cerebral and trunk vascular development. On similar lines, recent research has demonstrated the presence of glutamate transporter, *Glt1*, on radial glial cells suggesting their role in synaptic modulation and recycling similar to astrocytes (320). While a typical regenerative function of radial glial cell is well established in both larval and adult forms, their role in NVC and synaptic plasticity is not known to date.

1.11.3 Zebrafish vascular system

Zebrafish are an established model to study vascular development due to advantages such as optical clarity and rapid development. Due to their size, zebrafish embryos obtain enough oxygen by diffusion for survival and development for several dpf in the absence of blood flow (321).

The basic layout of the circulatory system is conserved between fish and other vertebrates such as mammals (321), and blood vessel patterning in developing teleosts is also similar (321). Formation of vasculature involves *vasculogenesis* and *angiogenesis* (321, 322). Vasculogenesis starts ~12 hours post fertilization (hpf) and is the process of formation of new blood vessels without pre-existing vessels. This establishes the major axial vessels and is followed by angiogenesis such as vessel sprouting from the dorsal aorta (DA) at ~22 hpf (322). Each angiogenic sprout comprises several ECs that migrate dorsally anastomosing to form a vascular network (322, 323). This is remodelled following onset of circulation at ~1-1.5 dpf (321). In the midbrain, the vasculature undergoes stereotypic pruning events driven by blood flow between 3-8 dpf (321, 324). This is also marked by formation of the blood brain barrier by interactions between ECs, pericytes, astrocytes and neurons (325, 326).

1.12 Computational approaches to modelling brain function

1.12.1 Computational models of the neurovascular unit

NVC is often examined by functional imaging studies which measure the hemodynamic responses to neural activity. Although fMRI signals are informative, it is not straightforward to precisely predict the underlying neural activations from the BOLD response. The main challenge involved in accurate interpretation of fMRI signals is the incomplete understanding of NVC mechanisms. There is need for computational models to improve our understanding

of NVC. There have been various modelling efforts but these are restricted to modelling neuron-vessel (327, 328) and neuron-glia interactions (327, 329, 330). Only a small number of studies model neuron-glia-vessel interactions (331-334).

Neuron-glia models have been recently emerging in keeping with the growing importance of glial cells in modulating neuronal function. Kaeger et al. (335) modelled the buffering role of glial cells using Hodgkin Huxley (HH) conductance models (336) for neurons and first order kinetic system for glial potassium buffering.

Neuron-vessel models have mostly aimed to understand functional imaging signals (BOLD) and their dependence on neuronal metabolism. The Aubert and Costalat model was amongst the first to describe a mathematical relation between stimulation evoked neuronal activity and hemodynamic response (327). A detailed vascular network model was later proposed that successfully reproduced the BOLD response using a simple stimulus induced neuronal response (328). This model also predicted baseline blood pressure and haemoglobin oxygen saturation close to that observed in rodents. Although elegant, this model did not account for complex features such as surround negativity of the BOLD response.

Neuron-glia-vessel models have recently been proposed with both the aim of understanding BOLD responses (328, 337) and investigating NVC mechanisms (331, 334). Although most of these models have been very detailed with several differential equations, recent simple low dimensional models recapitulate the findings of these more detailed models (333). Such simple computational models incorporate essential aspects of neuron, glial and vessel compartments and are extremely convenient to model neurovascular networks, predicting the effect of various pathologies on local field potential (LFP) and vascular network activity.

There is a need to develop such models to understand the basis of neurovascular uncoupling observed in various neurodegenerative and cardiovascular disorders. The feature of scalability

to networks is important to investigate disease phenotypes (such as those measurable by EEG and BOLD) which are a result of network interactions between neurons or glia or blood vessels. Another interesting application of developing computational models of the NVU is to investigate the role of the vascular system in modulating neuronal and glial activity. At a systems level, the neuronal system is coupled to the vascular system which makes it difficult to study either in isolation with current experimental technologies. Hence, having a plausible computational model of NVC grounded in experimental reality would help understand the impact of the vascular system on neuronal excitability.

Vascular tone is suggested to influence astrocyte and neuronal activation as suggested by the hemoneural hypothesis. Recent studies (338), have attempted to model the influence of vascular feedback on astrocytes through TRPV4 channels. However, the effect of such blood vessel-astrocyte interaction on neuronal excitability (339) has not been examined.

1.12.2 Modelling of synaptic plasticity

A fascinating feature of the brain is its ability to modify neuronal circuitry depending on activity known as *brain plasticity*. This governs learning in neuronal networks and is necessary to form memory representations.

Several studies have proposed various mechanisms of synaptic plasticity. There are mainly two forms of induction of synaptic plasticity; short term plasticity (STP) and long term plasticity (LTP).

STP is the first form of synaptic plasticity discovered in Aplysia (340). It is in the order of shorter time scales such as from milliseconds to several minutes. It is generally associated with short term adaptation of sensory stimulations and could be also generated by short bursts of

neuronal activity. Studies have shown that STP causes a change in the probability of neurotransmitter release (341). There are various mechanisms proposed for STP such as paired pulse facilitation and depression of synapses (342), modulation of neurotransmission by changing occupancy of presynaptic receptors (343) and glia driven clearance and release of modulators such as glutamate and ATP (344).

LTP is on the order of hours and is responsible for long term modulation of synaptic strength (345). LTP is a common mechanism adopted by all types of synapses in the brain (346) and has been comprehensively studied in the hippocampus in form of N-methyl D-aspartate receptor (NMDAR) based facilitation/depression of synapses. Pioneers of the field such as Ramon y Cajal and Donald Hebbs proposed the association between memories formed in the brain and synaptic modification based strengthening of neuronal connections (347). In this framework, synaptic strength (also called synaptic weight) is governed by temporal correlations between pre- and post-synaptic neuronal activity (348). Various studies have proposed the importance of this temporal correlation within a defined 'critical window' for spike timing which are on the order of tens of milliseconds (349). This is commonly referred to as spike time dependent plasticity (STDP) and experimental data have established the time scale of the *critical window* by correlating the change in the evoked potentials (synaptic strength) after repetitive retinal stimulation (**Figure 2-4**). STDP is now widely implemented in computational modelling of neuronal networks to show learning and memory in spiking neuronal networks (350). In this thesis, I have proposed a computational model demonstrating a vascular NO based modulation of STDP (**chapter 6**).

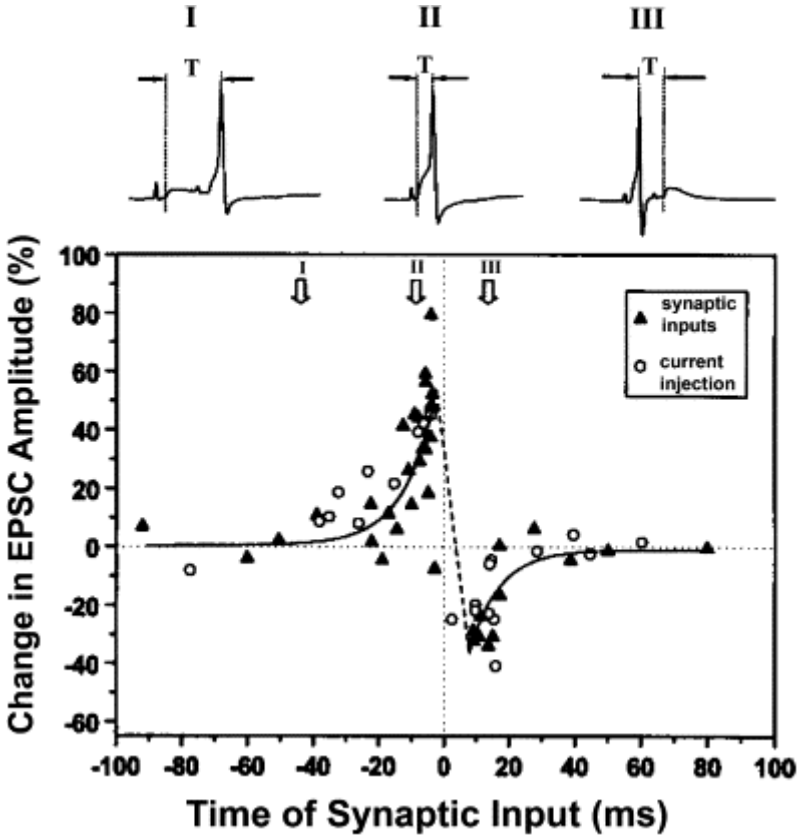

Figure 2-3: The Critical window for STDP established from experiments by Zhang et al. (345) [Figure adapted from (350)]

1.13 Aims and hypotheses

In this thesis, I aimed to develop a zebrafish model of NVC using novel compound transgenics, lightsheet microscopy and custom made analytical computational tools in MATLAB. Using this, I tested the following hypotheses:

1. NVC in zebrafish is similar to mammals in spatiotemporal scale and is mediated by NO and COX (**Chapter 3**).
2. Hyperglycemia impairs NVC through its impact on various cells forming the functional NVU (**Chapter 4**).
3. Since NO availability is affected in hyperglycemia and is important for NVC, augmenting NO will ameliorate hyperglycemic neurovascular deficits (Chapter 4).
4. *gch1* mutant zebrafish will display alterations in NVC similar to that observed under hyperglycemia (**Chapter 5**).
5. It is possible to generate a computational model of neuron-astrocyte-vessel interactions with NO dynamics and vessel-to-neuron feedback to explain the observation of hyperglycemia induced neurovascular impairment and predict possible effects on synaptic plasticity (**Chapter 6**).

2 Materials and methods

2.1 Zebrafish maintenance and manipulation

All zebrafish maintenance and manipulation were carried out in accordance with the Animals (Scientific Procedures) Act (ASPA), 1986, United Kingdom and were performed under Home office project licence 70/8588 held by Prof. Tim Chico. All experiments are reported in compliance with ARRIVE (Animal Research: Reporting *in vivo* experiments) guidelines (351).

2.1.1 Zebrafish husbandry

Adult zebrafish were housed in monitored aquariums with 14 hour (h) light/10 h dark cycle, at 28 °C with regular feeding with protein rich mix of Artemia and flake food. The tanks of each strain were maintained at 0.25l/water per fish tank.

2.1.2 Zebrafish embryo collection and maintenance

Zebrafish embryos were obtained by in-crossing adults unless specified. Eggs were kept in E3 medium (5 mM NaCl, 0.17 mM KCl, 0.33 mM $CaCl_2$, 0.33 mM $MgSO_4$, 10^{-5}% Methylene Blue) at 28 °C in an incubator up until 5.2 dpf. Post 5.2 dpf, embryos require external feeding and are therefore protected (Animal scientific procedures act, ASPA), and maintained by the Named Animal Care and Welfare officer (NAWCO) with proper feeding (Gemma Micro 75 Fry powder) and regular changing of E3 media (without Methylene blue). Embryos were kept in a 50 ml petridish in numbers not exceeding 60 per plate from 1-10 dpf.

2.1.3 Zebrafish transgenic lines for visualizing neurovascular unit

I have combined various transgenics (Tg) including neuronal, erythrocyte, endothelial, glial and VSMC transgenics to investigate NVC and anatomy (shown in ***Table 2-1***).

2.1.4 Zebrafish euthanasia and confirmation of death

Post 5.2 dpf, embryos undergo Schedule I procedures involving treatment with 4.2% (v/v) tricaine mesylate (MS222) in for 20 minutes, followed by confirmation of death. Standard methods used for confirmation of death include permanent cessation of blood flow or destruction of the brain. Culled zebrafish are subsequently stored in a freezer prior to disposal.

Zebrafish strain	Cell type Specificity	Description	Fluorescent moiety and excitation wavelength	Origin
nbt:GCaMP3	Pan- neuronal	Improved form of GCaMP with higher signal to noise (SNR) ratio (352) (353, 354), specific to neurons in zebrafish expressing n-beta tubulin (nbt) (355)	GFP (488 nm)	Dr. Vincent Cunliffe and Dr. Paola Meza Santoscoy, University of Sheffield
kdrl:HRAS-mcherry	Membrane EC reporter	Promoter is specific for kinase inset domain receptor like (*kdrl*)(356) to visualize developing vascular morphology	mcherry (561 nm)	Siekmann group, Max Planck Institute for Molecular Biomedicine Laboratory of Cardiovascular patterning
klf2: GFP	Endothelial transcription factor reporter	Kruppel like factor 2a (*klf2a*) is a zinc finger transcription factor that transduces physical forces of blood flow into various biological responses including endothelial calcium signalling (unpublished)	GFP (488 nm)	Dr. Caroline Gray University of Sheffield
claudin5: GFP	Endothelial junctional reporter	*Claudin5a* determines the paracellular permeability of tight junctions the BBB and neuroepithelial-ventricular barrier (326)	GFP (488 nm)	Dr. Simon Andrew Johnston, University of Sheffield
fli1: GFF: UAS: GCaMP6f	Endothelial calcium reporter	Endothelial specific calcium reporter driven by friend leukaemia integration transcription factor 1(*fli1*) promoter	GFP (488 nm)	Dr. Aylin Metzner, Dr. Aaron Savage and Dr. Rob Wilkinson, University of Sheffield
gata1: DsRed	Erythrocyte reporter	*gata1* (encoding for GATA binding protein) promoter drives the expression of DsRed in erythropoetic cells, thus marking all mature erythrocytes (357)	DsRed (561 nm)	ZIRC (Zebrafish International Resource Centre, Oregon, USA) Dr Leonard Zon (Howard Hughes Medical Institute, Maryland, USA)
GFAP: iGluSnFr	Glial cell membrane reporter	Expressed on the surface of the glial cells in the central nervous system and marks the glutamate uptake by the glial cells (358)	modified GFP (488 nm)	Dr. Ryan MacDonald, University of Sheffield
sm22ab: mcherrys^{441} (nuclear)	Mural cell reporter	Expressed in all mural cells (VSMC, pericytes) with smooth muscle actin (unpublished)	mcherry (561 nm)	Dr. Rob Wilkinson, University of Sheffield

Table 2-1: Table of various transgenic reporter lines used to investigate neurovascular function.

2.2 Lightsheet microscopy of live zebrafish embryos

Lightsheet fluorescent microscopy (LSFM) was used for acquiring two dimensional time series *(2D+t)* with simultaneous visual stimulation, or for acquiring 3D z stacks for analysis of cerebrovascular anatomy. For single z plane imaging, a region of 800 x 600 pixels was chosen, and for 3D imaging the same X-Y dimensions were used with a depth of 90 planes in Z dimension. Each pixel in X-Y had a scaling factor of 0.6 µm and each of the z plane thickness was 1 µm.

A compound transgenic, *Tg(nbt:GCaMP3;kdrl:HRAS-mcherry;gata1:Dsred)* was generated using the transgenics detailed in **Table 2-1** for quantifying NVC and for analysing cerebrovascular patterning.

LSFM was performed on 4-9 dpf embryos on a Zeiss Lightsheet Z.1 microscope (Carl Zeiss ®). The embryo was embedded in 1% or 3.5% low melting agarose (*Sigma* ®), and loaded in a glass capillary (with inner diameter ~ 1mm). 1% agarose was used for embryos minimally anaesthetised with MS222 before imaging, whereas 3.5% agarose was used for un-anaesthetised embryos to restrict movement of the embryo while imaging. Embryos were suspended vertically in a chamber filled with E3. Physiological conditions were maintained using a Peltier based heating and cooling block to maintain temperature at 28 °C.

2.3 Simultaneous visual stimulation and imaging of neurovascular function

An external red light emitting diode (LED) was attached to the top of microscope chamber and connected to a circuit board with 220 Ω resistors in series connection to the *Arduino*® board (5V). *Arduino* board was controlled through custom MATLAB® 2017b scripts such that the LED turned ON and OFF automatically alongside imaging (set up shown in **Figure 2-1A**). Total duration of each trial was 72 seconds, with 32 seconds of pre-stimulus imaging (12 seconds of

laser adaptation followed by 20 seconds of actual baseline imaging) followed by 8 seconds of light stimulation, and eventually 32 seconds of post-stimulus or recovery imaging.

Data was acquired at 33 frames per second (*fps*) with separate tracks for the red (561 nm) and green channel (488 nm). Each embryo underwent two trials for neurovascular function with an intermediate dark adaptation for 3-4 minutes. For acquiring images for vascular segmentation of teO, an average depth of 90-95 um was imaged for all embryos with *x, y* dimensions as 800 x 600 pixels (scale: 1 pixel = 0.6 µm) (**Figure 2-1B**). I imaged single z plane (*2D+t*) of the same *x, y* dimensions as for the *z* stack from the superficial teO layers having visibly dense axonal projections (**Figure 2-1C**).

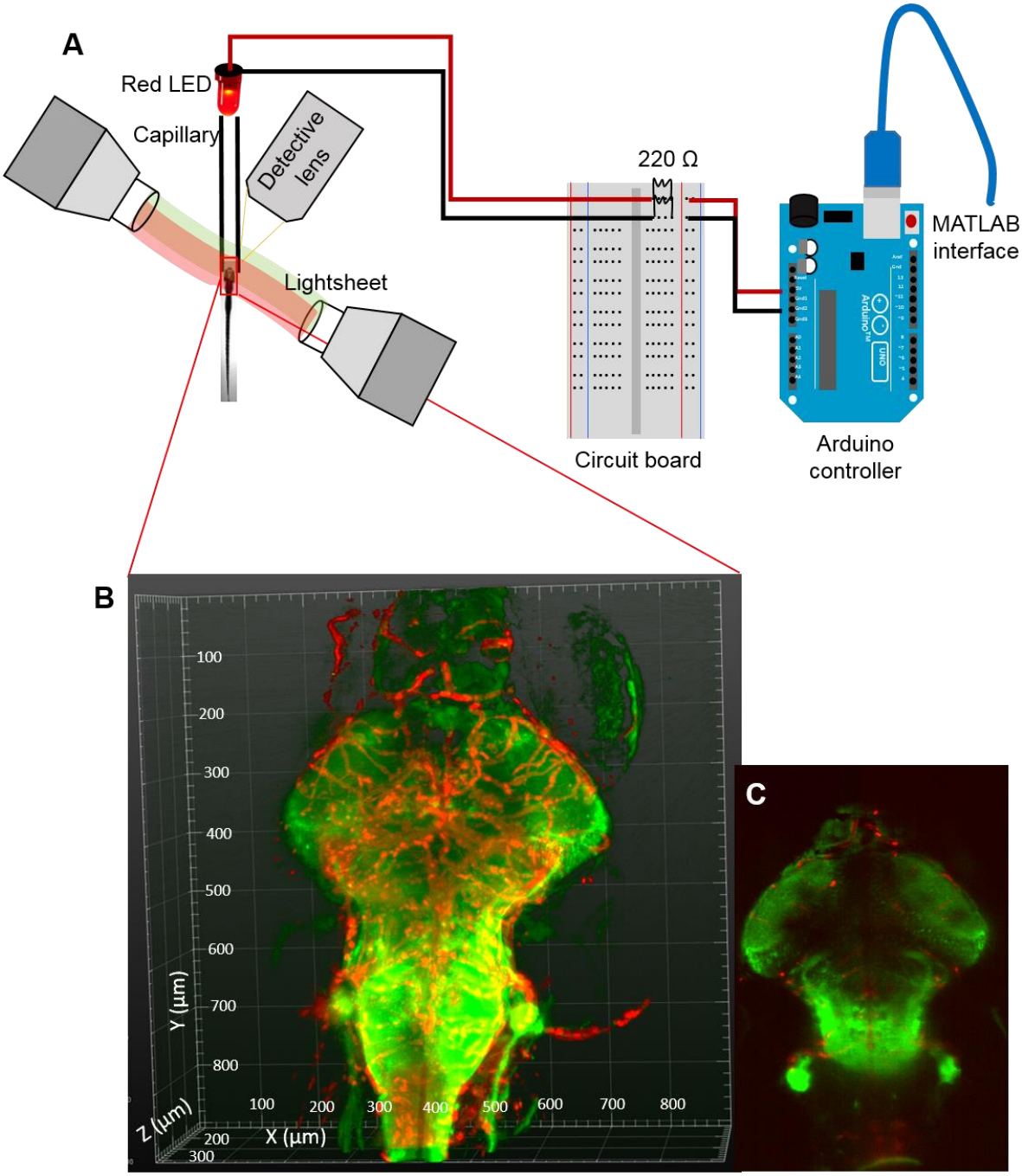

Figure 2-1: Imaging neurovascular function in 8dpf zebrafish: A: Set up with red LED for simultaneous imaging and visual stimulation in LSFM. A red LED is wired to the circuit board and controlled through MATLAB codes via an Arduino controller board. **B:** 3D rendered volume of 8dpf old zebrafish brain showing the neuronal *GCaMP3* reported labelling the neurons, *mcherry* labelling the red blood cells (RBCs) and the vascular endothelial cells. **C:** Single 'z' slice through the 3D volume indicating the plane of imaging used for NVC.

2.4 Computational tool development for neurovascular data analysis

2.4.1 Quantification of neuronal calcium fluorescence

Neuronal calcium was quantified in the teO using Zen Black ® software to measure GCaMP3 intensities for tectum and background. Relative change in fluorescence was calculated using the following equation:

$$\frac{\triangle F}{F_o} = \frac{(F - B) - (F_o - B_o)}{F_o - B_o} \quad (1)$$

where, F is GCaMP3 intensity in the teO, B is intensity of background area, F_o and B_o are baseline fluorescence (average of 10 seconds before stimulus onset) for the teO (F_o) and background (B_o) given by the general equation:

$$X_o = \frac{1}{10} \sum_{t_{stim-10}}^{t_{stim}} X \quad (2)$$

where $X \rightarrow F$ for teO and $X \rightarrow B$ for background area, and t_{stim} represents the time at which the LED is turned ON.

I further developed an automatic analysis pipeline for characterizing the neuronal responses in terms of quantified measures such as:

1. *Peak frequency,*

2. *Peak amplitude,* and

3. *Time to peak with respect to stimulus onset or offset*

Peak frequency calculation comprised of multiple processing steps. The change in fluorescence $dF = {}^{\triangle F}\!/_{F_o}$ was first normalized between 0 and 1 for all trials per fish, and then for all fish using the following:

$$F_{norm} = \frac{dF - \min(dF)}{\max(dF) - \min(dF)} \tag{3}$$

F_{norm} was further de-noised using a one dimensional (1-D) wavelet based heuristic method (359) of smoothing (predefined function in MATLAB®2017b) where the signal (here F_{norm}) was considered to be represented by:

$$F_{norm}(t) = F_{norm}^{denoised}(t) + \sigma e(t) \tag{4}$$

where, time *t* is equally spaced, and *e(t)* is a Gaussian white noise with noise level $\sigma = 1$. The objective of the de-noising algorithm was to suppress the noise part of the signal (F_{norm}), and retrieve the de-noised part ($F_{norm}^{denoised}$). De-noising comprised of three parts: decomposition, detailed coefficient thresholding, and reconstruction (359), details of which are beyond the scope of the current section.

Peaks are detected from the smoothened signal using a slope prominence threshold of 0.3, and a binary signal was created for calculating the peak frequency. The signal before calculation of the peaks is segregated into three time epochs: *Baseline*, *Respons*e and *Recovery*, to calculate the relative change in the number of peaks in response to stimulus.

Peak amplitude was calculated using an inbuilt function in MATLAB which calculates the perpendicular length of the baseline to the prominence of the peak.

Time to peak with respect to the stimulus was calculated as a measure to compare the response time of the teO. It was defined as the time during the stimulus window at which the stimulus response peak was observed. Peaks were observed at various times during the visual stimulus, but was most reliably seen in association with onset (9% of all animals), offset (78% of all animals) and both onset and offset (13% of all the animals) of the visual stimulus. Thus, I calculated the time to peak as time at which peak is observed (black arrowhead in **Figure 2-2**) with respect to both stimulus onset and stimulus offset (red arrowhead in **Figure 2-2**).

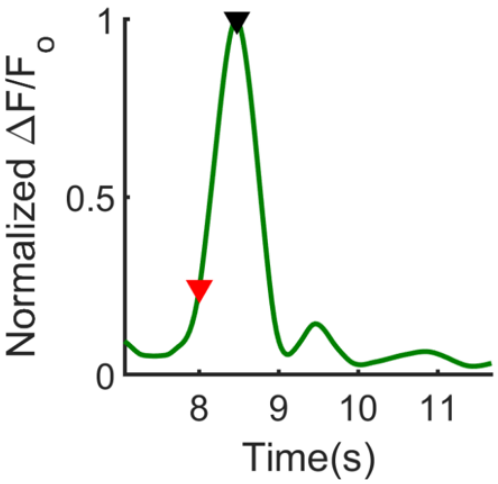

Figure 2-2: Example trace showing the detection of time to peak (black arrowhead) with respect to stimulus offset (red arrowhead).

2.4.2 Quantification of Red blood cell speed

I developed various analysis pipelines to analyse blood flow in different blood vessels of zebrafish based on pre-existing velocimetry/object tracking algorithms (360). Depending on the density of the red blood cells (RBC) (which depends on the size of the vessel), I used either centroid based object tracking algorithm (similar to digital motion analysis) (361), or pixel correlation based velocimetry algorithm (similar to axial line scanning) (362, 363).

2.4.2.1 Centroid based particle tracing for velocimetry

To analyse RBC speed, I developed MATLAB scripts based on the algorithm for velocity or displacement quantification within single vessels (local blood flow velocity) (361), which could be further extrapolated to automatically calculate blood flow velocity of larger brain regions (or the whole brain). Prior to the red blood cell (RBC) segmentation, vessels were chosen in the tectal and non tectal region of the zebrafish brain. A total of four vessels were chosen semi-manually from the tectum, and a further four from forebrain and hind brain combined. Once selected, the analysis ran automatically to segment the RBCs and eventually calculate the velocity profiles for each of the vessels. I designed the method by adapting the parameters of various pre-existing functions for image processing in MATLAB® 2017b (364) which had the following steps:

1. Segmentation of RBCs across time using the following pipeline:

   1a.) *Channel Isolation*

   Red blood cells were labelled by *gata1:DsRed*, thus the red channel was first isolated from the RGB *unit8* image format (default read image format in MATLAB) (**Figure 2-3 A**).

   1b.) *Median filtering*

Non-linear median filter (365) was designed based on assigning the median value of a neighbourhood *(W(i,j))* of a $(x,y)^{th}$ pixel and assigning it to the pixel (x,y) using:

$$g(x,y) = med\{f(x-i, y-j), i, j \in W\} \quad (5)$$

where, *W(i,j)* is the single channel isolated red image with *x* and *y* number of pixels, and *g(i,j)* is the output image post median filtering (**Figure 2-3 B**).

1c.) *Local Contrast Enhancement using 'CLAHE' method*

Image histogram, *h(x,y)* was then calculated for each of the k^{th} luminance values using:

$$h_k(x,y) = \frac{n_k}{N} \quad (6)$$

where, n_k is the number of pixels for k^{th} luminance and *N* is the total number of pixels. The histogram was then clipped at contrast limit, *cl*, and redistributed to generate a flat histogram, *G(x,y)*. Histogram equalization (364) was then performed within permissible luminance values (*Lmn, Lmx*) which is (0,1).

$$G_k(x,y) = \sum_{s=cl}^{s=K} h_k(x,y) \quad (7)$$

$$L_{out}(x,y) = L_{mn} + (L_{mn} - L_{mx})G_k(x,y) \quad (8)$$

where *cl* is the contrast limit luminance value (defining the lower limit of the clipped histogram), *K* is the upper limit of the clipped histogram and $L_{out}(x,y)$ is the output contrasted image (**Figure 2-3 C**).

1d.) *Background subtraction*

Using a threshold, t_e, background image, *Bg*, was calculated which was then subtracted from contrasted image ($L_{out}(x,y)$) to get subtracted image ($I_{sub}(x,y)$)

$$Bg(x,y) = L_{out}(x,y), (x \cup y) \leq t_e \quad (9)$$

$$I_{sub}(x,y) = L_{out}(x,y) - Bg(x,y) \quad (10)$$

where, $I_{sub}(x,y)$ is the background subtracted image (**Figure 2-3 D**).

1e.) *Thresholded image binarization*

Using fixed threshold, *T*, images were assigned 0's and 1's for all pixels (*x,y*) in image $I_{sub}(x,y)$.

$$I_{bin}(x,y) = \begin{Bmatrix} 1, I_{sub}(x,y) > T \\ 0 \end{Bmatrix} \quad (12)$$

where, I_{bin}(x,y) is the binarized image (**Figure 2-3 E**).

1f.) *Centroid detection*

To detect position of segmented RBC, centroid (*Cent*) was computed by mean of pixel positions (366).

$$Cent = \left\{ \frac{1}{n_x} \sum_x I_{bin}(x,y), \frac{1}{n_y} \sum_y I_{bin}(x,y) \right\} \quad (13)$$

$$D = Cent(t) - Cent(t-1) \quad (14)$$

where, *D* is the displacement vector of the RBC centroids and (n_x, n_y) is the coordinate vector of the total number of RBC centroids detected per time frame (**Figure 2-3 F-G**).

2. Single pixel centroids were tracked for each of the 2100 time frames of the experiment, with simultaneous calculation of the displacement (*D*) in *x* and *y* directions. The relative RBC speed was calculated as Euclidean norm of the displacements in *x* and *y* directions as follows:

$$RBC_{speed}(\mu m/\mathrm{s}) = fps \times scale \times \sqrt{D_x^{\,2} + D_y^{\,2}} \quad (15)$$

where, *fps* is the image acquisition rate (in *frames/s*), *scale* is the pixel to μm conversion, and D_x and D_y are the calculated displacements in *x* and *y* directions.

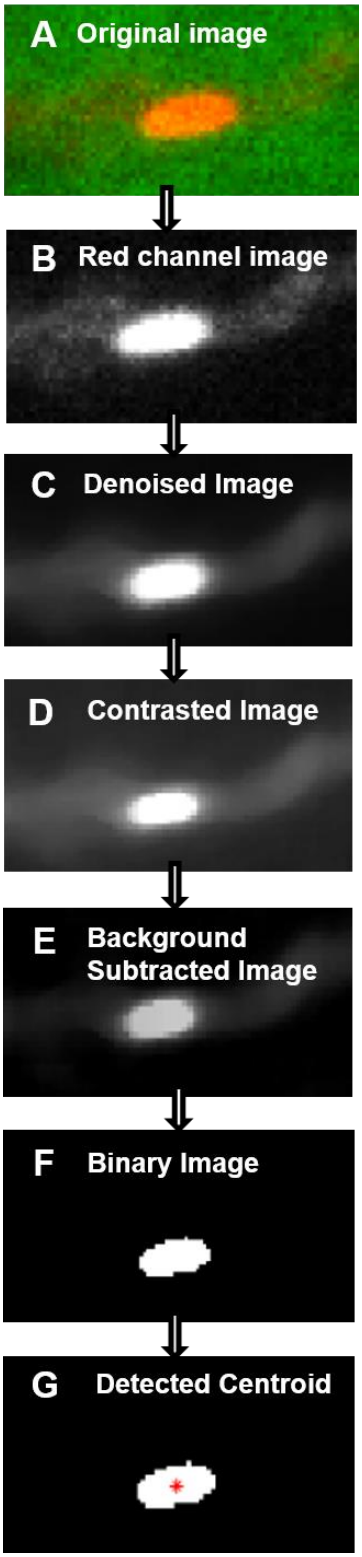

Figure 2-3: RBC tracking pipeline for velocimetry: **A:** Original cropped image with focus on RBC passing through tectal vessel. **B:** Red channel image of the same tectal vessel as **A. C:** Median filtering of image in **B** using the de-noising algorithm. **D:** Contrast enhancement of image **C** using CLAHE. **E:** Background subtraction of image **D** using threshold based background selected as described. **F:** Threshold based binarization of image **E. G:** Red star indicates detected centroid of segmented RBC using the corresponding described equations.

The RBC speed profiles observed had a discontinuous nature since the velocity can only be measured when the RBCs are detected and segmented. If an RBC was not labelled with *gata1:DsRed* (which is possible, given the variability of the transgenic) it was not detected. Hence, the speed profile comprises of the epochs in which RBC/s were detected, segmented and had their speed quantified. The time epochs in which RBCs were not detected have a zero-valued speed. In order to avoid a bias due to the zero-valued speed time epochs, I designed a custom interpolation method to get a non-zero continuous speed curve. The rate of interpolation was governed by the length of zero-valued speed epochs. Thus, the slope of increase/decrease of speed during those zero-valued velocity epochs depends on the difference between the absolute speed values surrounding the zero-speed epochs and the length of the zero-velocity epochs.

Obtaining continuous RBC speed curves in this manner, I segregated speed (in $\mu m/s$) into three timeframes (baseline, response and recovery). The mean values for each timeframe were calculated as a metric for comparison of response to baseline and recovery.

The RBC speed for each vessel, each trial, and each fish was further characterized using metrics such as absolute change in speed during response compared to baseline, and time to peak response with respect to stimulus onset/offset wherever applicable.

Absolute change in the velocity during response compared to the baseline time period was used as a direct metric for assessing the increase in RBC speed in response to visual stimulation:

$$\Delta Vel_{abs} = \frac{1}{t_{resp}} \sum_{t_{resp}} Vel - \frac{1}{t_{base}} \sum_{t_{base}} Vel \tag{16}$$

Time to peak for RBC speed was calculated with respect to the stimulus onset, as for the calculation of time to peak for the neuronal calcium peak.

2.4.2.2 Correlation based RBC speed quantification

While the digital motion based centroid detection method (as described in **section 2.4.2.1** was suitable for assessing RBC speed in the cerebral vessels where vessel thickness is equivalent to the diameter of RBCs, a correlation based RBC speed quantification is more appropriate for assessing RBC speed in vessels with high RBC density. Therefore, for analysis of RBC speed in larger blood vessels such as the dorsal aorta, I developed a correlation based velocimetry method similar to that used in conventional axial line scanning method. Using self-written scripts in MATLAB 2017b ®, RBCs were segmented using the method described earlier (**Figure 2-3**A-F). Thresholded 2D images for each time frame were converted into 1D signal by summation in 'y' direction (all column pixels). The 1D signal obtained was then low pass filtered to remove spurious and highly correlated pixels (low correlation implies the displacement of 1D wave signal). Cross correlation across time was calculated on filtered images for each time frame using an inbuilt MATLAB 2017b ® *xcorr()* function. Thus, the obtained correlation (in pixels/frames) could then be converted to mm/sec using the following equation:

$$Velocity(mm/s) = \frac{Correlation(pixels/\ frame) \times fps \times 10^{-3}}{Scale(pixels/\mu m)} \quad (17)$$

2.4.3 Quantification of vascular anatomy

3D stacks acquired were converted to 2D maximum intensity projections, followed by an automated pipeline (MATLAB) similar to RBC segmentation involving red channel isolation, median filtering and contrast enhancement. The remaining steps were customized for vasculature and comprised of the following.

2.4.3.1 Otsu's method for thresholded vascular segmentation

Contrasted images were converted to binary images using *Otsu's method of thresholding* with parameters such as cluster size and inter-cluster threshold adjusted for the zebrafish vasculature datasets **(Figure 2-4)**. Binary vasculature was then subjected to morphological thinning as described in the next sections.

2.4.3.2 Two dimensional centreline extraction and vascular feature characterization

Morphological thinning was applied to obtain the centerlines from the vasculature, followed by branch points, vessel lengths, density and diameter quantification.

Branchpoint number, $B_p(x,p)$, was calculated from the centreline map by automatic iterative search for overlapping 6 x 6 pixel regions for Y shaped 3-pixel connected structures [*(i,j), (i-1,j), (i,j-1)*] (**Figure 2-5A**) as described by the following:

$$Bp(x,p) = 1; \{C_{i-1,j}, C_{i,j-1}, C_{i,j}\} = 1 \quad (18)$$

where, *p* is the iteration number for 6 x 6 pixel regions in the centreline map, *C*.

Vascular length (VL) was calculated as a simple summation of total white (=1) pixels of the C matrix, multiplied by scale bar (**Figure 2-5B**) as described by the following:

$$VL = \sum_{i,j} C_{i,j} = 1 \quad (19)$$

For *radius* measurements, edge information was obtained from the binary segmented vasculature (**Figure 2-5C**). Radius, *R*, is then calculated as twice the Euclidean distance between the centerlines, *C*, and vasculature edges, *E*, for all the vessels using the following:

$$R = \sqrt{(C-E)^2} \quad (20)$$

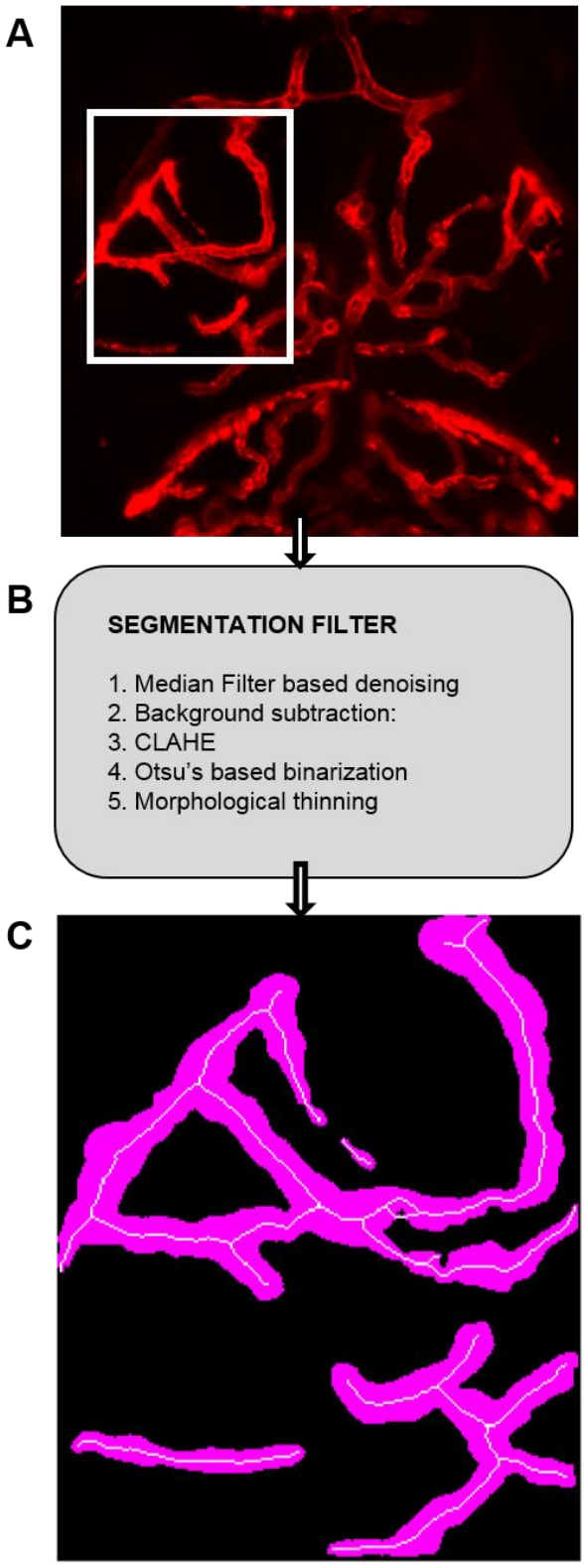

Figure 2-4: Vascular segmentation pipeline. **A:** Red channel micrograph of *Tg(kdrl:HRAS-mcherry)* with the white box (marking the left optic tectum) analysed for vascular features. **B:** Processing steps in the vascular segmentation pipeline. **C:** Segmented binary vasculature (in magenta) overlapped with extracted centerlines (in white).

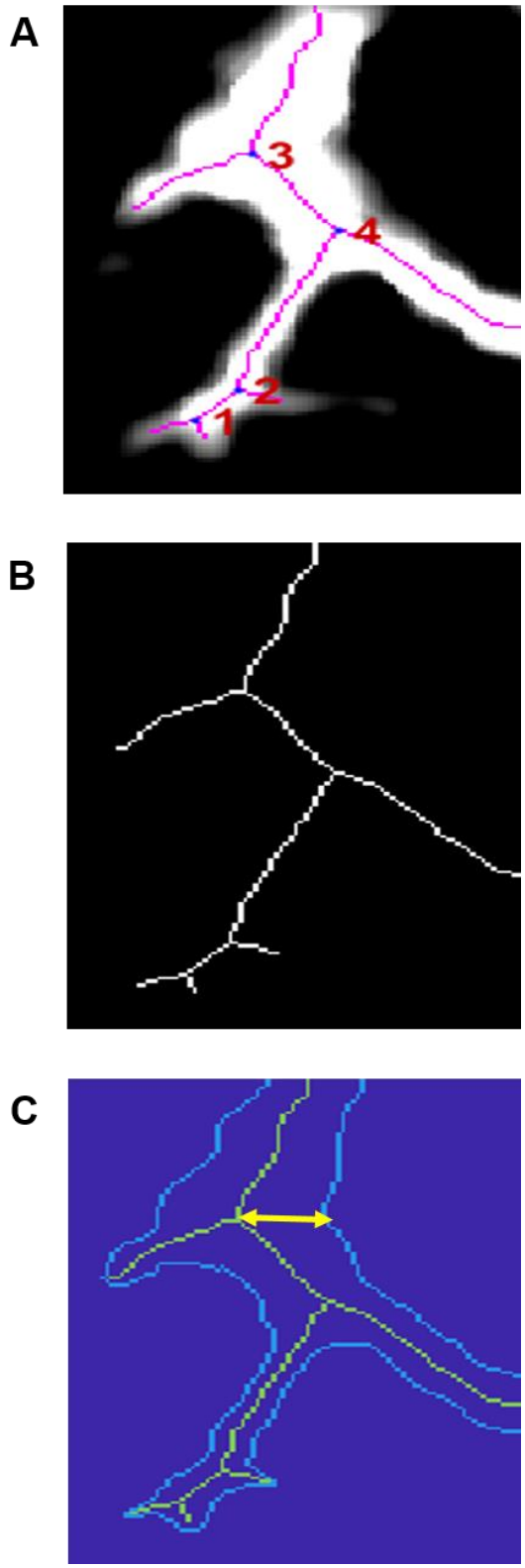

Figure 2-5: Vasculature feature extraction from centreline matrix. A: Detected branch points (in magenta) with their corresponding numbers marked by the algorithm in a region in the vasculature overlapped onto the segmented binary vasculature (in white). **B:** Centerlines for the same region as A used for quantifying the vascular length. **C:** Edges of the vasculature in the same region as A overlapped onto the centerlines to illustrate the calculated radius.

2.4.4 Quantification of vasculature specific *klf2a* and *claudin5a* expression

3D image stacks acquired were first converted to 2D maximum intensity projections. I then segmented out the tectal vasculature from the red channel (*kdrl:HRAS-mcherry*), followed by calculation of the tectal vascular length using the method described in **section 2.4.3**. This segmented vasculature was then used as a binary mask for the green channel, followed by normalizing the mean intensity of the green channel (*klf2a:GFP or claudin5a:GFP*) to the tectal vascular length. This was done to remove any biases in quantification of reporters due to changes in the vasculature (if any).

2.4.5 Quantification of tectal *iGluSnFr* intensity (glial cell marker)

3D image stacks acquired were first converted to 2D maximum intensity projections. I then segmented out the teO followed by calculation of average intensity of the region in the green channel, representing expression of intensity based glutamate sensing fluorescent reporter (*iGluSnFr).* Tectal segmentation was done using MATLAB® 2017b image free hand tool, considering midbrain-forebrain and midbrain-hindbrain boundaries as the markers for segmentation.

2.4.6 Intensity based quantification of heart rate

As described earlier, each stimulation trial comprised of 32 seconds of baseline, followed by 8 seconds of light stimulation, and then 32 seconds of post stimulus imaging. I performed the same paradigm imaging the heart instead of the teO to observe any changes due to systemic effects of the light stimulation protocol. With single plane imaging, structural changes in a beating heart can be assessed by quantification of the average changes in the red fluorescence (from the labelled RBCs). This caused changes in the intensity of ventricle selected on the

surface of the heart plane of imaging. Thus using the average changes in intensity of the red channel on the specific area, a waveform of heart rate as a measure of heart beat was obtained. For my measurements, I selected the in plane ventricular region as the region for quantification of average intensity. I measured the frequency of peaks to get a peaks/min equivalent to beats/min as an estimate of heart rate. Subsequently, I segregated the complete heart rate signal into the three time periods (baseline, response and recovery) as described for the neuronal and RBC speed quantification.

2.5 Drug treatment

All the drugs were acquired from SIGMA ® and administered through bath application. Bath application was of overnight duration (14-16 h), unless otherwise specified.

2.5.1 Nitric oxide synthase inhibition

For NOS inhibition experiments 0.5mM N(ω)-nitro-L-arginine methyl ester (L-NAME) was prepared in E3 media and administered at 7dpf, with larvae imaged using LSFM at 8dpf.

2.5.2 Cyclooxygenase inhibition

10μM of Indomethacin was used for non-specific COX (1 and 2) inhibition. Indomethacin was made up using 0.1% dimethyl sulfoxide (DMSO), and applied to the bath from 7dpf, followed by imaging using LSFM at 8dpf.

2.5.3 Glucose/Mannitol administration for hyperglycemia experiments

Glucose and mannitol (Sigma®) were prepared at 20mM concentration in E3 media. Larvae were exposed to glucose or mannitol solution from 4 dpf-9 dpf (chronic administration), with solution replaced every day after 5.2 dpf until 9 dpf.

For testing the effect of acute glucose administration, larvae were fed with Gemma Micro ® from 4-8 dpf, followed by addition of glucose from 8-9 dpf. The same procedure was repeated for acute mannitol treatment.

2.5.4 Sodium nitroprusside treatment

For hyperglycemia experiments, 100mM stock solution of sodium nitroprusside (SNP) (Sigma®) was diluted to 0.1mM in either 20mM glucose and mannitol solutions comprising 8 dpf larvae, followed by imaging on LSFM at 9 dpf (24 h treatment).

2.5.5 TRPV4 antagonist treatment

For blocking TRPV4 activity, 100mM stock solution of TRPV4 antagonist III (Sigma®) was diluted to 0.2mM in E3 and applied to the bath from 7 dpf, followed by imaging using LSFM at 8dpf.

2.5.6 Assessment of NO reactivity in the brain vessels

For quantification of NO levels in the vascular and/or brain tissue, 9 dpf zebrafish larvae with mannitol/glucose with/without SNP were treated with 2.5 µM Diaminofluorescein-FM (DAF-FM). For preparing stock solutions, lysophilized DAF-FM was solubilized in DMSO to a stock concentration of 0.1mM and stored at -20°C. On the day of experiments, DAF-FM stocks were diluted to a concentration of 2.5µM in either glucose or mannitol solution. Zebrafish larvae

were then incubated in the solutions at 28°C in the incubator, in the dark, for 3 hours. Larvae were then visualized under a fluorescent microscope (Zeiss Axiocam 503) to check staining in the green channel, and staining was continued for another half hour with constant checking of stain intensity. Larvae were washed with glucose/mannitol solution to wash off excess DAF-FM, and then imaged on the LSFM.

2.6 Genotyping protocol for *gch1* mutants

NVC measurements were performed post 6 dpf for all experiments, including when evaluating NVC in *gch1* mutants (generated by Dr. Marcus Keating and Prof. Oliver Bandmann). Heterozygous *gch1* mutants with 94 base pair (bp) deletion (**Figure 2-6**) were crossed into the triple transgenic neurovascular line *Tg(nbt:GCaMP3;kdrl:HRAS-mcherry;gata1:DsRed)*. Embryos from this cross were selected for green neuronal calcium, red RBCs, and red ECs at 2 dpf prior to *gch1* genotyping at 3 dpf using a tail fin-clipping protocol (367).

DELETION

TAAAACCCACCGGCTTCCCCTCAGAGAGCGCTGAGTTTGACAGGAGTATAAC
AACATTCGAACTTCACTCAAAAGTTTGTTCTCGACACGGATAGAAGCGAAAT
AGTGACTTACAGCACACGTCTAGGCAATTATGGAGCGCTCCAAACAGAAACC
GGTGAATCAAAGCGAAAAAGAAACTGACGGAGCGATCAACGGACACTTTGA
TGGCCGGGTGAAGATGCCCGGATGGAAAGCTGGAAGTGCCTCCGGGGACCC
GGGCAGTGTGCCGACCTCCAGCGTGATGGAGAGCTGGCGAGAAGAGCGCAC
CCGGAGCCTGGAGGACAACGAGATGAGCCTGCCGAGCATCGCCGCGGCTTAC
ACCACTATTCTTCGGGGTCTCGGGGAGGATCCGCAGCGCCAGGGGCTCCTCA
AAACTCCCTGGAGAGCCGCGACAGCCATGCAGTTCTTCACCAAGGGATACCA
GGAGAAAATCATCG

Figure 2-6: Nucleotide sequence of *gch1* gene with deletion site highlighted in red in reference to the mutants.

For genomic DNA (*gDNA)* extraction, a small amount of tail tissue was dissected from anesthetized 3 dpf embryos using a sterilized scalpel blade, followed by suspension in 15mM NaOH in a 96 well PCR plate. This was then incubated at 95°C for 10 minutes for tissue lysis, followed by inactivation with 1/10 volume of 1M Tris-HCl (pH 8.0) neutralisation buffer.

Extracted gDNA was used for per tube for a 10 µl PCR reaction with the composition described in **Table 2-2**.

PCR mix content	**Volume (in µl)**
Biomix Red (*Invitrogen*)	5
Forward primer	1
Reverse primer	1
Diethylypyrocarbonate (DEPC) water	2
Extracted *gDNA*	1
	10 (total)

Table 2-2: Table describing the composition of the PCR mix with the corresponding volumes.

The specific primers (IDT) for *gch1* were prepared using Diethyly Pyrocarbonate (DEPC) water and diluted at 1:10 with DEPC water for working concentrations. The primer sequences are as follows:

Forward Primer 5'- AAACTGACGGAGCGATCAAC

Reverse Primer 5'- TCTCCTGGTATCCCTTGGTG

PCR reaction was mixed with gentle pipetting up and down, followed by amplification on a PCR machine (Multigene Optimax) using the PCR60 (with annealing temperature 60°C)

Wild types, heterozygous and homozygous mutants were selected based on singe/double band obtained on gel electrophoresis of the PCR products run against 100 base pair (bp) ladder (Bioline) (**Figure 2-7*).***

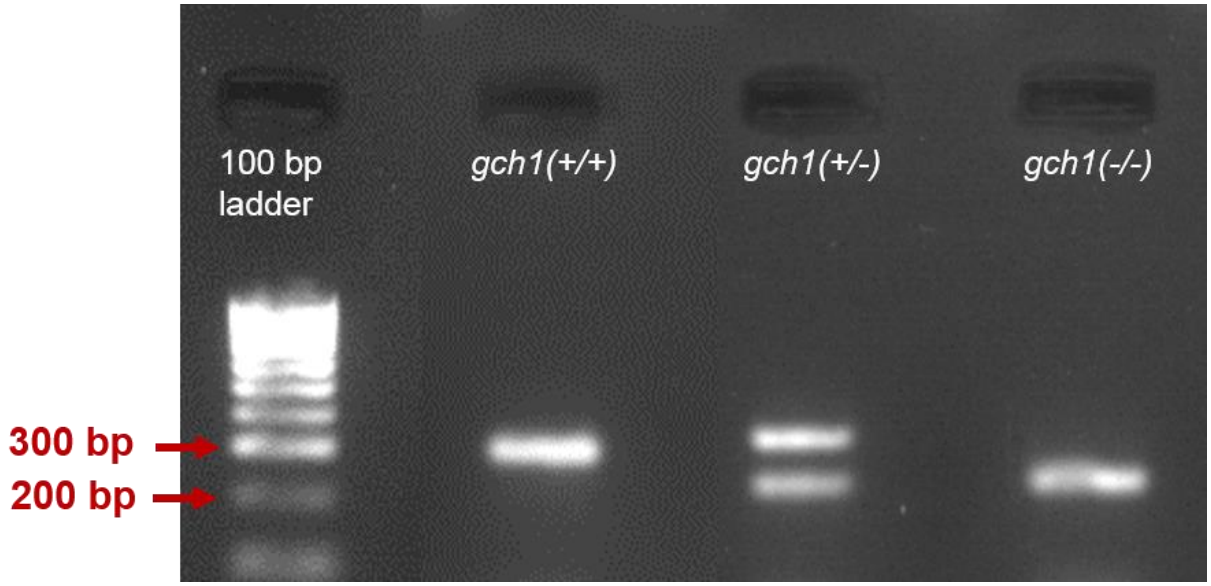

Figure 2-7: PCR amplicons for wildtype (*gch1(+/+)*) of size of 300 bp, heterozygous (*gch1(+/-)*) with band sizes 300 bp and 206 bp, respectively and homozygous (*gch1(-/-)*) siblings with band size 206 bp compared against 100 base-pair (bp) ladder.

2.7 Behavioural analysis

2.7.1 General locomotion analysis with Viewpoint-Zebrabox system

All locomotion was analysed using the Viewpoint-Zebrabox system. For general locomotion analysis one larva was placed per well in a 96 well plate, each well filled with a volume of 800 µl E3. The plate was placed inside the Zebrabox, with light settings at 1% intensity, and left for 10mins prior to actual experimental recording to allow the larvae to acclimatize While the larvae were acclimatizing the tracking protocol was built using the viewpoint tracking software, wherein a region of interest (ROI) was manually drawn on the wells positioned top left, top right and bottom right for the software to build automatically for all ROIs corresponding to each well in the 96 well plate. Total length for the complete plate was selected as 107 mm, followed by setting zebrafish detection intensity threshold to 115 intensity units which was then calibrated for the complete plate. Speed thresholds were set for large movement at 64mm/s, small movement at 33-64 mm/s, and anything less than 33mm/s to be classed as inactivity to analyse various types of locomotion. Sampling time was set to one minute and the movie was acquired for 30 minutes once the 10 min acclimatization was complete. Data was generated in the form of excel files, and was then analysed for parameters such as distance moved with high and low speed using MATLAB.

2.7.2 Light/Dark preference test with Viewpoint-Zebrabox system

Analysis of Light/Dark preference of the larval zebrafish was designed on a similar principle to that of the adult light/dark preference test (299). A 12-welled plate was modified by adhering three cellophane films (blue, green and yellow) to half of each well to create a 'dark' side but keep enough visibility for the camera to track the larvae movement through infrared (IR) camera. Alternate sides of the wells were darkened (also using cellophane) in order to avoid bias due to left-right preference in zebrafish (if any) (schematic shown in **Figure 2-8**).

Each well of the 12 welled plate was labelled as an arena for an individual animal. Parameters for the imaging were as described in 2.8.1 above for locomotion analysis. Larvae were imaged for a one-hour duration, inclusive of the acclimatization (recording was started immediately post adding larvae to individual well).

Post imaging, basic features such as time spent in light vs dark, distance travelled in dark vs light, with inter-group comparisons, were computed from the excel spreadsheets imported from the viewpoint tracking system. Quantitative data for each of the animal was obtained by processing these data in MATLAB, followed by input into Graph Pad for statistical comparisons.

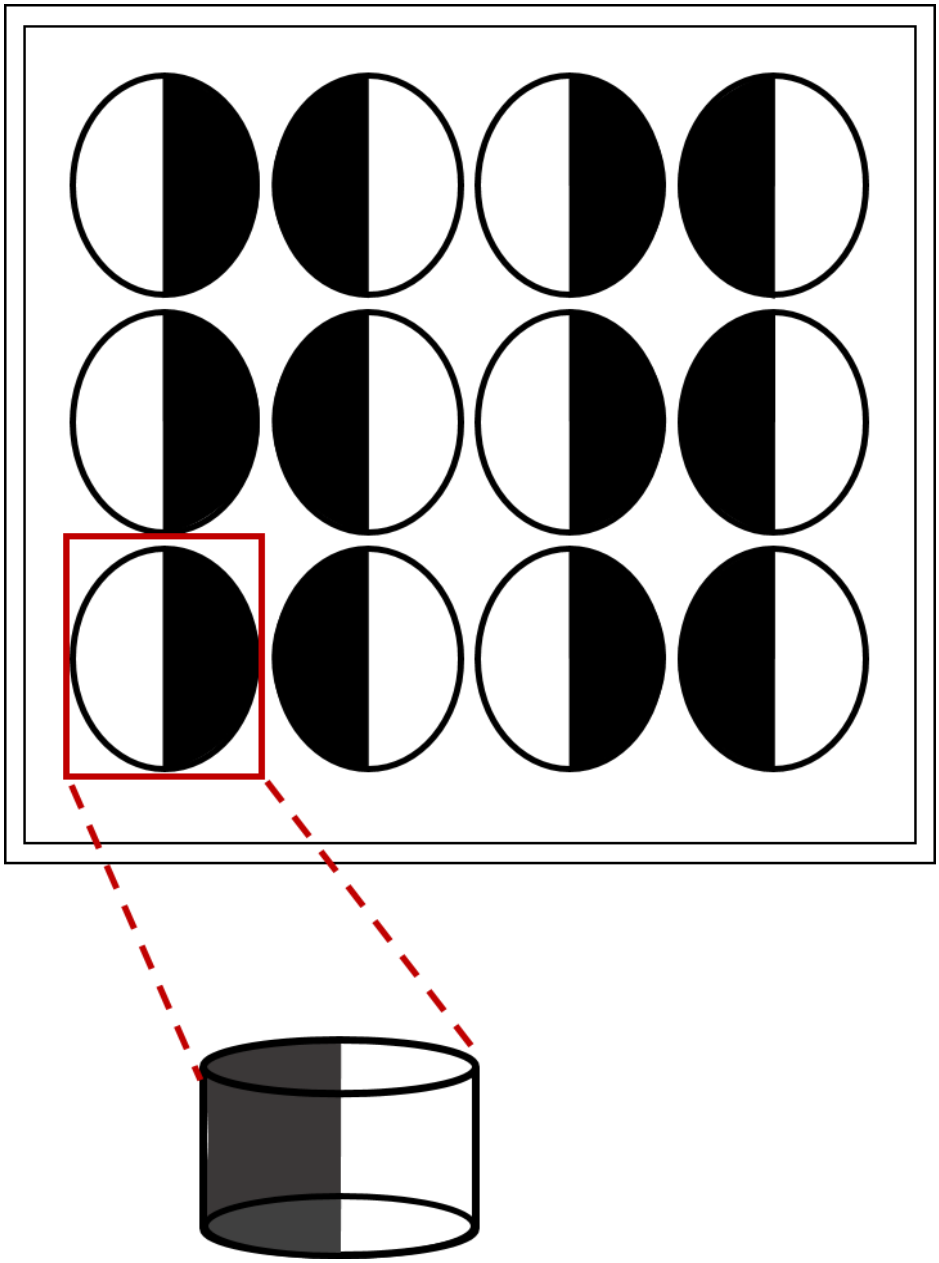

Figure 2-8: Schematic representation of the half darkened wells of a 12 well plate used for light/dark preference test for larval zebrafish. Dark side of each of the wells represent cellophane adhered to the bottom of the wells with walls darkened (as shown in the inset).

2.8 Immunohistochemistry

Immunohistochemistry (IHC) was used to observe and quantify changes in glial specific markers such as glutamine synthetase (GS), GFAP, and TRPV4. The protocol was adapted from (368). The various steps in the protocol are described as follows including reagent preparation (**Table 2-3**). All the steps were carried out for 30-50 larvae per 1.5 ml Eppendorf tube with 1 ml of reagents (or lesser volume enough to cover all the larvae in the tube).

2.8.1 Reagent preparation

Reagent	Composition	Description	Storage
Phosphate Buffer Saline (PBS) – Tween (PBST)	1x PBS (1 PBS tablet in 100 ml MilliQ) with 0.1% Tween	Working PBS-Tween is made in 50 ml aliquots with dilution of tween at 0.1% Tween (from 20% stock)	Room Temperature (RT)
Tris- HCl	150mM Tris Buffer with HCl	5M HCl/ NaOH pellets were used to equillibrate to pH=9	RT
Blocking Buffer (B-Buffer)	10% sheep serum, 0.8% Triton-X100, 1% Bovine Serum Albumin (BSA) in PBST		4°C
Incubation Buffer (I-Buffer)	1% sheep serum, 0.8% Triton-X100, 1% BSA in PBST	All primary (1°) and secondary (2°) antibodies were suspended in I-buffer.	4°C
PBS with Triton and Sheep Serum (PBS-TS)	10% sheep serum, 1% Triton-X100 in PBS		4°C

Table 2-3: Table describing the various reagents for IHC protocol with their corresponding composition and storage conditions

2.8.2 Larval fixation

Larvae for each different treatment (mannitol or glucose, with or without co-treatment with SNP) were fixed in 4% Paraformaldehyde (PFA) for overnight at 4°C followed by a 5min wash with 1x PBS before re-suspending in 100% Methanol (MeOH) for long term storage at -20°C.

2.8.3 Sample rehydration and equilibration

Larvae were rehydrated from MeOH with three 10min washes with PBST, with gentle agitation on a rocker (with tubes aligned along their side).

2.8.4 Heating procedure

Larvae were then suspended in 150 mM Tris-HCl (pH 9) for 5 minutes, followed by heating at 70°C for 15 minutes. Larvae then underwent two 10min washes with PBST, followed by two 5min washes with distilled water (dH2O).

2.8.5 Permeabilization

Larvae were permeabilised using ice cold acetone at -20°C for 20 minutes, followed by two 5min washes with dH2O, then equilibrated twice with 5min washes in PBST.

2.8.6 Blocking and 1° Ab incubation

For the initial blocking stage, larvae were incubated in blocking buffer (B-buffer) for 3 hours at 4°C. B-buffer was removed and the larvae were then incubated in I-buffer containing the 1° Abs listed in **Table 2-4**, for 3 days at 4°C with gentle agitation on a rocker.

Residual primary antibody residue was removed by three 1 hour washes in PBST (at room temperature (RT)). Larvae then underwent two 10min washes with PBS-Triton, followed by two equilibration washes in PBS-TS, for 1 hour each.

Primary Antibody	Host Organism	Dilution
Glutamine Synthetase (GS)	Mouse	1:250
GFAP	Mouse	1:100
TRPV4	Rabbit	1:300
DAPI	-	1:1000

Table 2-4: Table listing the primary antibodies used, with their corresponding host organisms and dilutions.

2.8.7 Equilibration and 2° Ab incubation

Larvae were incubated in I-buffer containing secondary antibodies listed in **Table 2-5**, at 1:500 dilutions for 2.5 days, in the dark on a rocker at 4°C.

Prior to imaging on the Lightsheet microscope, larvae were washed three times in PBS-TS (at RT), followed by two 1 hour washes with PBST, each at RT. Larvae were mounted in 1% LMP (Sigma) and imaged for the glial patterning in the brain for different markers.

Secondary Antibody	Wavelength (nm)	Dilution
Anti- mouse	647 (Far red)	1:500
Anti-rabbit	488 (Green)	1:500
Anti-rabbit	561 (Red)	1:500

Table 2-5: Table listing the secondary antibodies used, with the corresponding wavelengths of the conjugated fluorophores and dilutions, respectively.

2.9 Experimental design and statistical analysis

All experiments were designed using the NC3Rs experimental design analysis (EDA) tool. GraphPad Prism (La Jolla, CA®) was used for all statistical comparisons. Shapiro-Wilk test for normality was performed prior to statistical analysis. Neuronal calcium peaks and RBC

speed in different time periods were compared either using parametric one-way repeated measure analysis of variance (RM-ANOVA) for normally distributed data or Friedman's test, otherwise. All the intergroup comparisons of neuronal activations and RBC speed between different time periods (baseline, response and recovery) for various treatments (drugs/mannitol/glucose) were performed using two-way ANOVA. Post-hoc multiple comparison tests (Sidak's test) were used for all the ANOVA tests. Comparison of tectal and non tectal RBC speed changes in response to visual stimulation were done using paired t-tests or one-way ANOVA in case of more than two groups. *P* values <0.05 were considered to be statistically significant. All the data are mean ± standard error of mean (s.e.m.), unless otherwise specified. Imaging was performed unblinded to the treatment allocation. Most of the data analysis was automated hence not subjected to operator bias. Wherever the data was semi-automated, blinded analysis was performed.

2.10 Development of computational model of neurovascular coupling

In this section, I have described the equations used to simulate NVC in a minimal model of NVU. Neuron, astrocyte and vessel model equations are adapted from pre-existing models with modifications to simulate eight second stimulation, as used for the experimental zebrafish model. Each of the component in the NVU modelled in the present thesis is described with its corresponding equations in the following sections (schematic model diagram shown in **Figure 2-9**).

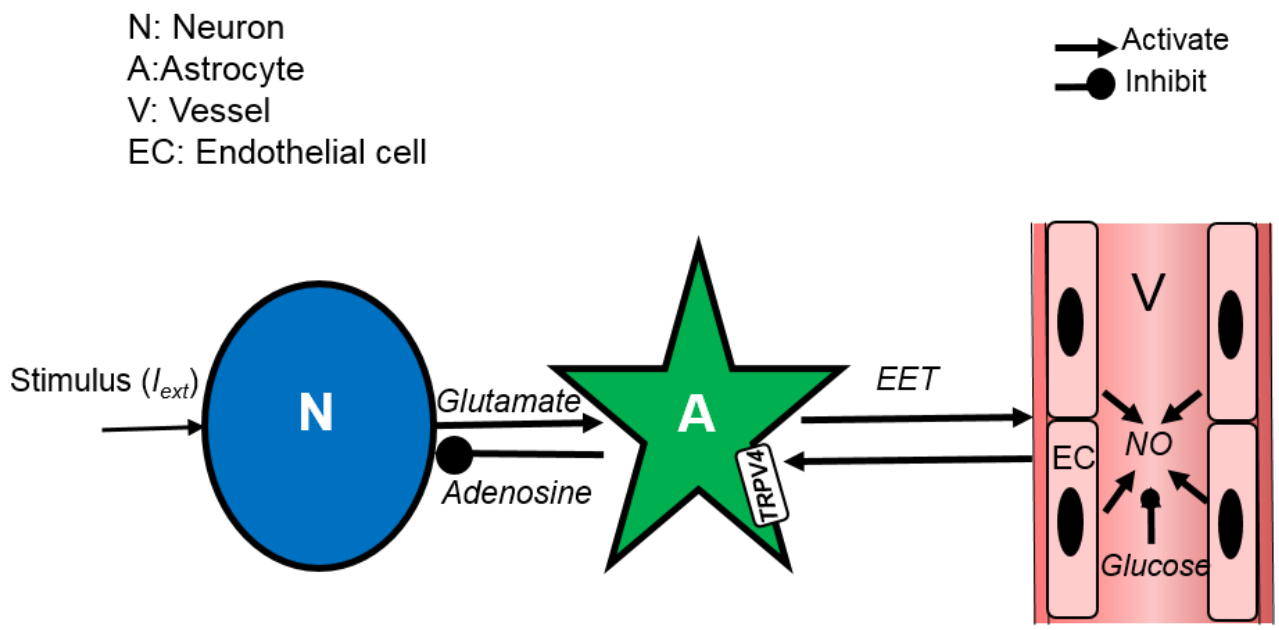

Figure 2-9: Schematic representation of the neurovascular unit showing the connections between each of the compartments (Neuron: N, astrocyte: A and blood vessel: V). Each of the compartments is an input/output system with output of each of the compartment acting as the input to the next. Input to the neuron is the external current, I_{ext} and the output is glutamate released. Input to the astrocyte is the glutamate released from the neuron and output is vasodilator EET released that acts as the input to the vessel compartment. Blood vessel dilation (diameter changes) is the output of the vessel compartment and a feedback input to the astrocyte compartment (activating the TRPV4 current). Activation of TRPV4 current on the astrocyte causes a change in the astrocyte $[Ca^{2+}]_i$ causing release of adenosine that increases the neuronal firing threshold.

2.10.1 Neuron Model

Neuronal spike dynamics are described using standard quadratic integrate and fire (QIF) (369) using the following equations:

$$\frac{dV}{dt} = a(V - V_{th})(V - V_{rest}) + I_{ext} - threshold(a) \quad (21)$$

where V represents the neuronal membrane potential, V_{th} being the spiking threshold, V_{rest} as the resting membrane potential, a representing the QIF parameter, I_{ext} representing the external stimulus current and *threshold* is the negative control reducing the threshold of neuronal firing as a function of adenosine released by the astrocyte compartment.

Neuronal firing leads to release in glutamate (*Glut*) in the synaptic cleft and is modelled as a slow integral function of V:

$$\frac{dGlut}{dt} = -\alpha Glut + H(V - \theta) \quad (22)$$

where $H(V-\theta)$ represents the step function (H: heaviside) of V with a threshold (θ) and α is the glutamate decay parameter.

Synaptic glutamate acts on the membrane glutamate receptors (*mGluR*) on the astrocyte compartment.

Neuronal model parameters	Values
G^{K}_{max}	80 mS/cm^2
G^{Na}_{max}	100 mS/cm^2
V_{Na}	50 mV
G_L	*0.1 mS/cm^2*
V_L	*-67 mS/cm^2*
C_M	*1 µF*
M	*0.0530*
H	*0.5960*
N	*0.3177*
$G_{K_{ATP}}$	*0.15 mS/cm^2*
I_{max}	*1.3 mµA/cm^2*
V_K	*-100 mV*
Surface area (sa)	*1586 mµm^2*
Volume	*2160 mµm^3*
Faraday's constant (F)	*96500 C/mol*
dt (time constant for simulations)	*0.01*

Table 2-6: Table listing all the neuronal model parameters with their corresponding values used for simulations

2.10.2 Astrocyte Model

The astrocyte model is adapted from (334) modelling the binding of glutamate to the *mgluR* depending on the active g-protein receptor binding sites given by:

$$G = \frac{\rho + \delta}{K_G + \rho + \delta} \tag{23}$$

where δ is the ratio of activities of bound to unbound receptors and ρ is the ratio of bound to unbound receptors and is given by:

$$\rho = \frac{Glut}{K_{Glut} + Glut} \tag{24}$$

The binding of synaptic glutamate to the astrocyte mGluR leads to the production of inositol phosphate 3, IP_3 as described by (370), given by:

$$\frac{d[IP_3]}{dt} = r_h G - k_{\deg}[IP3] \tag{25}$$

where, r_h is the $[IP_3]$ production rate and k_{deg} is the destruction rate.

$[IP_3]$ production leads to the activation of IP_3 receptors on the endoplasmic reticulum leading to an influx of calcium, J_{IP3} into the intracellular space, given by:

$$J_{IP_3} = J_{\max}\left[\left(\frac{IP_3}{IP_3 + K_l}\right)\left(\frac{[Ca^{2+}]_i}{[Ca^{2+}]_i + K_{act}}\right)h\right]^3\left(1 - \frac{[Ca^{2+}]_i}{[Ca_{ER}]}\right) \tag{26}$$

where, J_{max} is the maximum rate, K_l is the dissociation constant for calcium binding to n activation site on the IP_3 receptors and Ca_{ER} is the calcium concentration in the endoplasmic reticulum (ER). The gating variable h is modelled as in (334) and is given by:

$$\frac{dh}{dt} = k_{on}\left[K_{inh} - ([Ca^{2+}]_i - K_{inh})h\right] \tag{27}$$

where k_{on} and K_{inh} are the Ca^{2+} binding and dissociation constants, respectively at the inhibitory IP_3 receptor binding site.

Astrocyte intracellular calcium, $[Ca^{2+}]$ (eq.28) is modelled to be minimally dependent on IP_3 current based influx and TRPV4 current from the perivascular space.

$$\frac{d[Ca^{2+}]_i}{dt} = \beta(J_{IP_3} - J_{pump} + J_{leak} + J_{TRPV4}) \tag{28}$$

where, $[Ca^{2+}]$is the cytosolic calcium concentration in astrocyte, J_{pump} represents the Ca^{2+} flux from the cytosol to endoplasmic reticulum (eq.29), J_{leak} is the Ca^{2+} leak flux from the endoplasmic reticulum to the cytosol (eq.30).

$$J_{pump} = V_{\max}\left(\frac{[Ca^{2+}]_i^2}{[Ca^{2+}]_i^2 + K_p^2}\right) \tag{29}$$

and,

$$J_{leak} = P_L\left(1 - \frac{[Ca^{2+}]_i}{[Ca_{ER}]}\right) \tag{30}$$

where V_{max} is the maximum pump rate, K_p is the pump constant and P_L is determined by steady state flux balance.

Calcium influx from the extracellular flux, J_{TRPV4} depends on the arteriolar tone (considered to be a continuous sinusoidal pulse for the current study) and is given by:

$$J_{TRPV4} = -\frac{I_{TRPV4}}{C_{astr}\gamma} \tag{31}$$

where C_{astr} is the astrocyte capacitance, γ is the scaling factor described by (334), and I_{TRPV4} is the current through the channel given by:

$$I_{TRPV4} = g_{TRPV4}s(V_k - v_{TRPV4}) \tag{32}$$

where g_{TRPV4} is the maximal channel conductance, v_k is the channel reversal potential, V_k is the membrane potential (eq.35) and s is the gating variable whose dynamics are given by:

$$\frac{ds}{dt} = \frac{Ca_P}{\tau_{TRVP4}}(s_\infty - s) \tag{33}$$

where Ca_P is the perivascular calcium concentration (μM) and is assumed to change slowly and hence static. τ_{TRPV4} is the time constant for TRPV4 channel. s_∞ is the strain and Ca dependent steady state channel open probability and is given by the Boltzmann equation as described by (334):

$$s_{\infty} = \left(\frac{1}{1+e^{-(\varepsilon_1-\varepsilon_2)/\kappa}}\right)\left[\frac{1}{H_{Ca}}\left(H_{Ca}+\tanh\left(\frac{V_k - v_{1,TRPV4}}{v_{2,TRPV4}}\right)\right)\right] \quad (34)$$

where ε is the strain parameter and depends on changes in cerebral vascular tone (modelled as slow sinusoid in the present model4), $v_{1,TRPV4}$ and $v_{2,TRPV}$ are the channel constants adapted from Withoft et al. V_k is the astrocyte membrane potential and H_{Ca} is the inhibitory term given by the following equations:

$$V_k = \frac{1}{C_{astr}}\left(-I_{leak} - I_{TRPV4}\right) \quad (35)$$

and,

$$H_{Ca} = \frac{[Ca^{2+}]_i}{\gamma_{Ca_i}} + \frac{[Ca]_P}{\gamma_{Ca_e}} \quad (36)$$

where γ_{Cai} and γ_{Cae} are constants for calcium influx and efflux.

$[Ca^{2+}]_i$ changes as described in eq.33 influence the *EET* production, their relation given by the following:

$$\frac{d[EET]}{dt} = V_{EET}\left([Ca^{2+}]_i - [Ca]_{\min}\right) - k_{EET}[EET] \quad (37)$$

where V_{EET} is the *EET* production rate, Ca_{min} is the minimum calcium required for *EET* production and k_{EET} is the *EET* decay rate, all adapted (334). *EET* being a vasodilator impacts the blood flow through changes in vascular *NO* described in eq.38. Various constants used in the eq.23-37 are adapted from (370) and given in **Table 2-7**.

Astrocyte model parameters	**Value**
K_G	8.82
Δ	0.001235
K_{Glut}	10
Rh	4.8
K_{deg}	1.25 /s
B	0.0244
K_L	0.03 µM
K_{act}	0.17 µM
k_{on}	2 µM/s
K_{inh}	0.1 µM
Ca_{ER}	400 µM
V_{max}	20 µM/s
K_P	0.24 µM
P_L	5.2 µM/s
v_{TRPV4}	6 mV
g_{TRPV4}	200 pS
C_{ast}	40 pF
Γ	1970 mV/ µM
J_{max}	2880 µm/s
K	0.04
γ_{Ca_i}	0.2 µM
γ_{Ca_e}	0.2 µM
$v_{1,TRPV4}$	120 mV
$v_{2,TRPV4}$	12 mV
τ_{Ca}	0.9 /s
V_{EET}	72 /s
Ca_{min}	0.1 µM
K_{EET}	7.1 /s
G_{Leak}	78.54 pS
V_{Leak}	-70 mV

Ca_{decay}	0.5 /s
Ca_{P0}	2000 µM
α	1
$V_{4,BK}$	14.5 mV
$V_{5,BK}$	8 mV
$V_{6,BK}$	-15 mV
$Ca_{3,BK}$	400 nM
$Ca_{4,BK}$	150 nM
ψ_{BK}	2.665 /s
EET_{shift}	2 mV
g_{BK}	225.6 pS
V_{BK}	-95 mV

Table 2-7: Table listing all the astrocyte model parameters used for simulations

2.10.3 Blood vessel model

To keep the model simple and minimal, I have developed a lumped two-variable (*NO* and diameter, *D*) model of the blood vessel wherein vessel diameter changes are dependent on the *NO* levels in the blood vessel. *EET* released from the astrocytes increase vascular *NO* (given by the *f(EET)* in eq. 38).

$$\frac{dNO}{dt} = f(NO) - \alpha A + \frac{\beta_v \theta (G_{\max} - G)}{1 + e^{-a(NO-b)}} + \delta NO f(EET) \quad (38)$$

where, α represents the *NO* diffusion constant in the vessel for a given area, G_{max} is set maximum glucose level (=20mM) to represent the upper hyperglycemic threshold and *G* is the model glucose parameter used to switch from normoglycemic (*G* = 5mM) to hyperglycemic (*G* = 25mM). *f(NO)* represents a non-linear production of *NO* by the ECs and is given by eq. 39.

$$f(NO) = -NO(NO - p)(NO - q) \tag{39}$$

f(EET) is a heaviside function of EET released by astrocyte and is given by eq. 40.

$$f(EET) = H(EET - e) \tag{40}$$

and *A* is the area of the vessel given by eq. 41.

$$A = \pi\left(\frac{D}{2}\right)^2 \tag{41}$$

where, *D* is the vessel diameter and is described by eq. 42.

$$\frac{dD}{dt} = \rho NO - \omega D + \frac{1}{\lambda\left(1 + e^{-k(NO-l)}\right)} \tag{42}$$

where, ω and ρ are model parameters fixed for the simulations. Various other constants used in the eq.38-40 are given in **Table 2-8**.

Blood vessel parameters	
A	0.054 μm^{-2}
β_v	1.8
A	0.2
B	0.2
P	2
Q	1.4
Ω	0.05 μm^{-1}
P	0.05
K	0.1
L	0.1
Λ	0.5
E	1
Π	3.14

Table 2-8: Table listing all the blood vessel parameters used for simulations.

3 Developing a model of neurovascular coupling in zebrafish

3.1 Aims

This chapter describes the development and characterization of a novel non-invasive zebrafish model of NVC. My aim was to determine whether visual stimulus led to a specific increase in neuronal calcium in the teO and a corresponding increase in the RBC speed in the optic tectal blood vessels. I quantified and compared this response at different stages of zebrafish development. I also explore the mechanisms of NVC in zebrafish such as direct (NO dependent) or indirect (glial/COX dependent) pathways known to contribute to NVC in mammals.

3.2 Visual stimulus induces specific increases in fluorescence in the optic tectum of 8 dpf *Tg(nbt:GCaMP3;kdrl:HRAS-mcherry;gata1:DsRed)* larvae

To investigate the presence of NVC, I first sought to induce and quantify visual stimulus-evoked neuronal activation in *Tg(nbt:GCaMP3;kdrl:HRAS-mcherry;gata1:DsRed)*. Individual animals were embedded in agarose within the lightsheet microscope chamber as described in **section 2.2**. The plane of imaging focused on the dendritic fibre-like structure in the superficial layers of the teO. After 32 seconds of baseline imaging, the animal was exposed to a red light square pulse of 8 seconds duration followed by 32 seconds of recovery imaging. I quantified tectal fluorescence as $\Delta F/F_o$ as described in **section 2.4.1**. **Figure 3-1A** shows representative images of the left teO during these experiments. Increases in the fluorescent intensity of neuronal GCaMP3 (shown in green) were observed in response to visual stimulus before returning to baseline 14 s after stimulus. This increase in fluorescence represents an increase in neuronal calcium levels indicating increased neuronal activity. On quantification of the

neuronal responses (expressed as $\Delta F/F_o$) I observed peaks at various times during the visual stimulus but peaks were most reliably seen in association with onset (9% of animals), offset (78% of animals) and both onset and offset (13% of animals) of the visual stimulus. Representative examples are shown in **Figure 3-1B-C.**

Since most neuronal calcium peaks were observed in response to stimulus offset (78%), averaging the responses of five larvae reveals a robust peak in neuronal calcium at stimulus offset (**Figure 3-2A**). To quantify the response, I divided the time series shown in **Figure 3-2A** into three time periods (as described in **section 2.6.1**), *baseline, response* and *recovery*. I observed significant increases in the average frequency of neuronal calcium peaks during the response compared to baseline and recovery time periods as shown in **Figure 3-2B**.

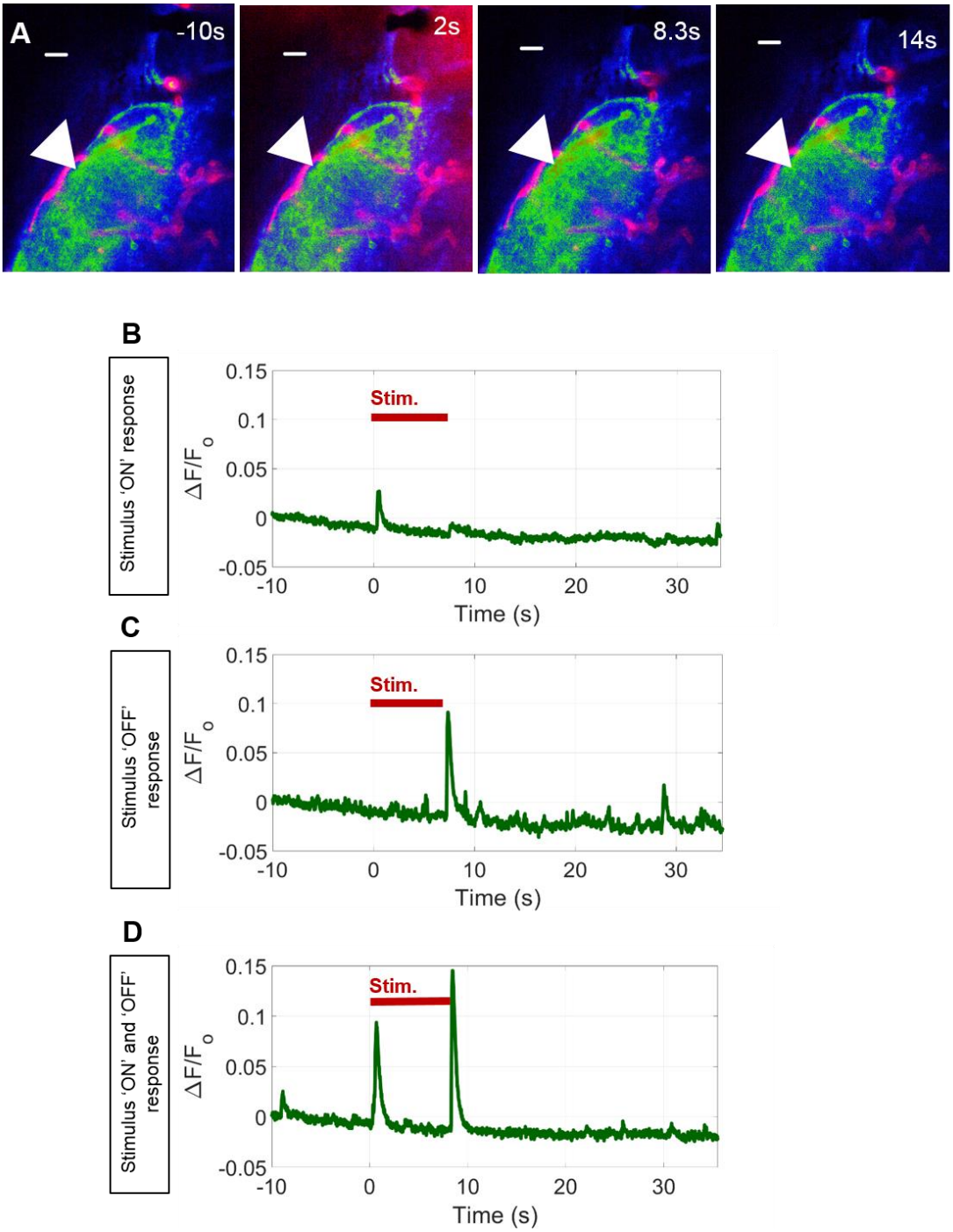

Figure 3-1: Visual stimulus induces optic tectal calcium responses to 8 s visual stimulation in 8 dpf zebrafish. A: The left optic tectum of an 8 dpf *Tg(nbt:GCaMP3; kdrl:mCherry;gata1:DsRED)* embryo before (-10s), during (2s and 8.3s) and after (14s) visual stimulus by red light. Arrow indicates area of increased tectal calcium levels in response to the stimulus. **B-D:** Quantification of neuronal activation ($\Delta F/F_o$) in the optic tectum in three individual larvae, showing neuronal calcium peaks at stimulus ON, stimulus OFF and both stimulus ON and OFF. Visual stimulus was administered 0-8s (indicated on the graphs by red bar). Scale bar in A is 20 µm.

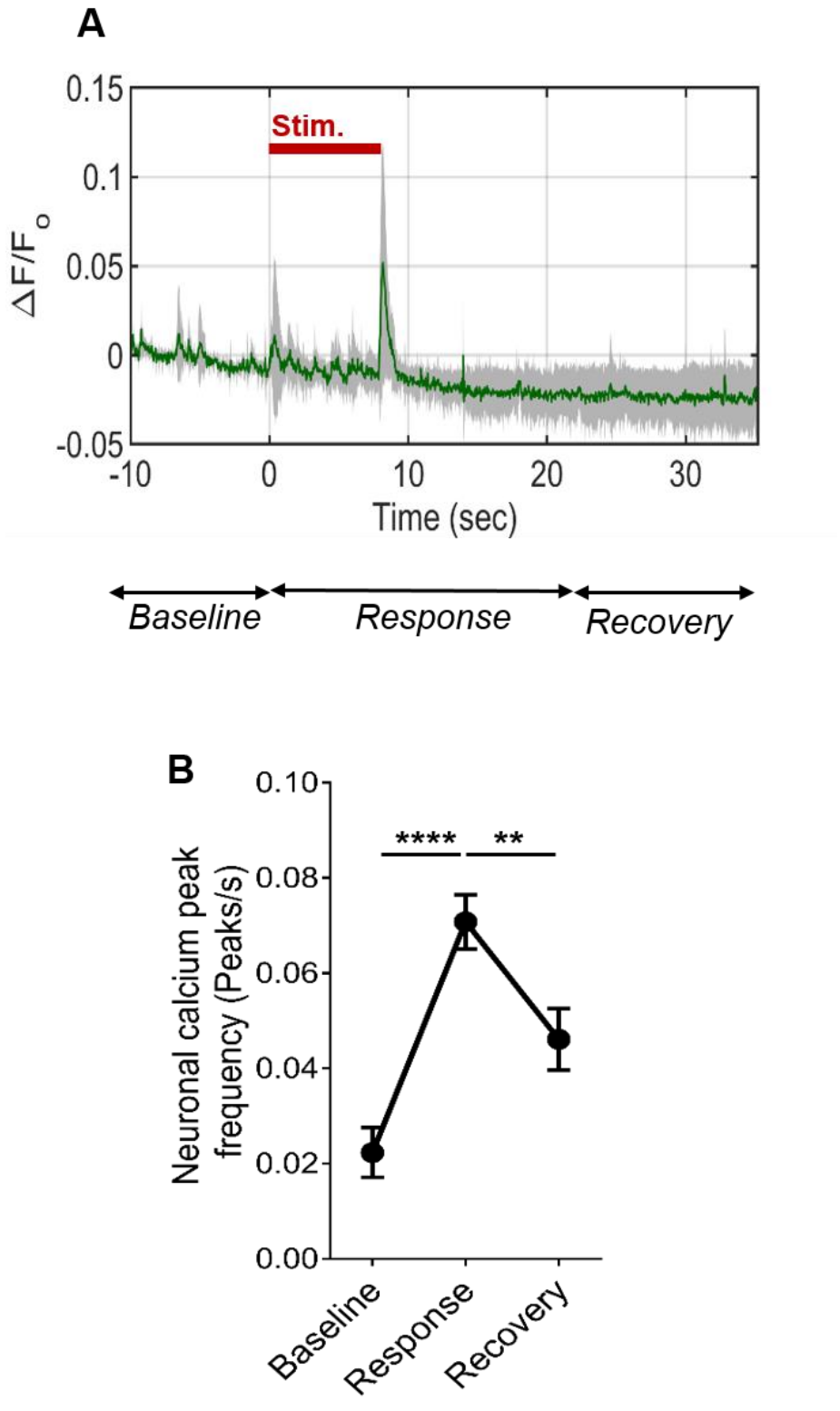

Figure 3-2:Average neuronal calcium response in the optic tectum to visual stimulus in 8 dpf larvae. A: Quantification of neuronal activation ($\Delta F/F_o$) in optic tectum over time (n=5 larvae). Visual stimulus was administered 0-8s (indicated on graph by red bar). Time-series was divided into baseline (-10-0s), response (0-20s), and recovery (20-30s) periods. **B:** Quantification of frequency of peaks in ($\Delta F/F_o$) as a measure of neuronal activation during baseline, response and recovery time periods (n=40 larvae). Data in **A** is mean ± s.d. and **B** is mean ± s.e.m. **p<0.01, ****p<0.0001 (Friedman's test)

3.3 Tectal neuronal calcium peak onsets demonstrate a decreasing trend with increasing the stimulus duration

To examine the relationship between stimulus duration and neuronal calcium response, and to optimise my protocol to find the stimulus that induced the greatest neuronal activation, I quantified neuronal peak frequency in response to different durations of stimulus (4, 8 and 12 seconds). The response was not significantly different between these stimulus durations (**Figure 3-3A-D**). I quantified the speed of peak onset (quantified as time to half peak, $t_{1/2}$) but found only a non-significant trend to a faster onset with increasing stimulus duration between 4-8sec (**Figure 3-3E**).

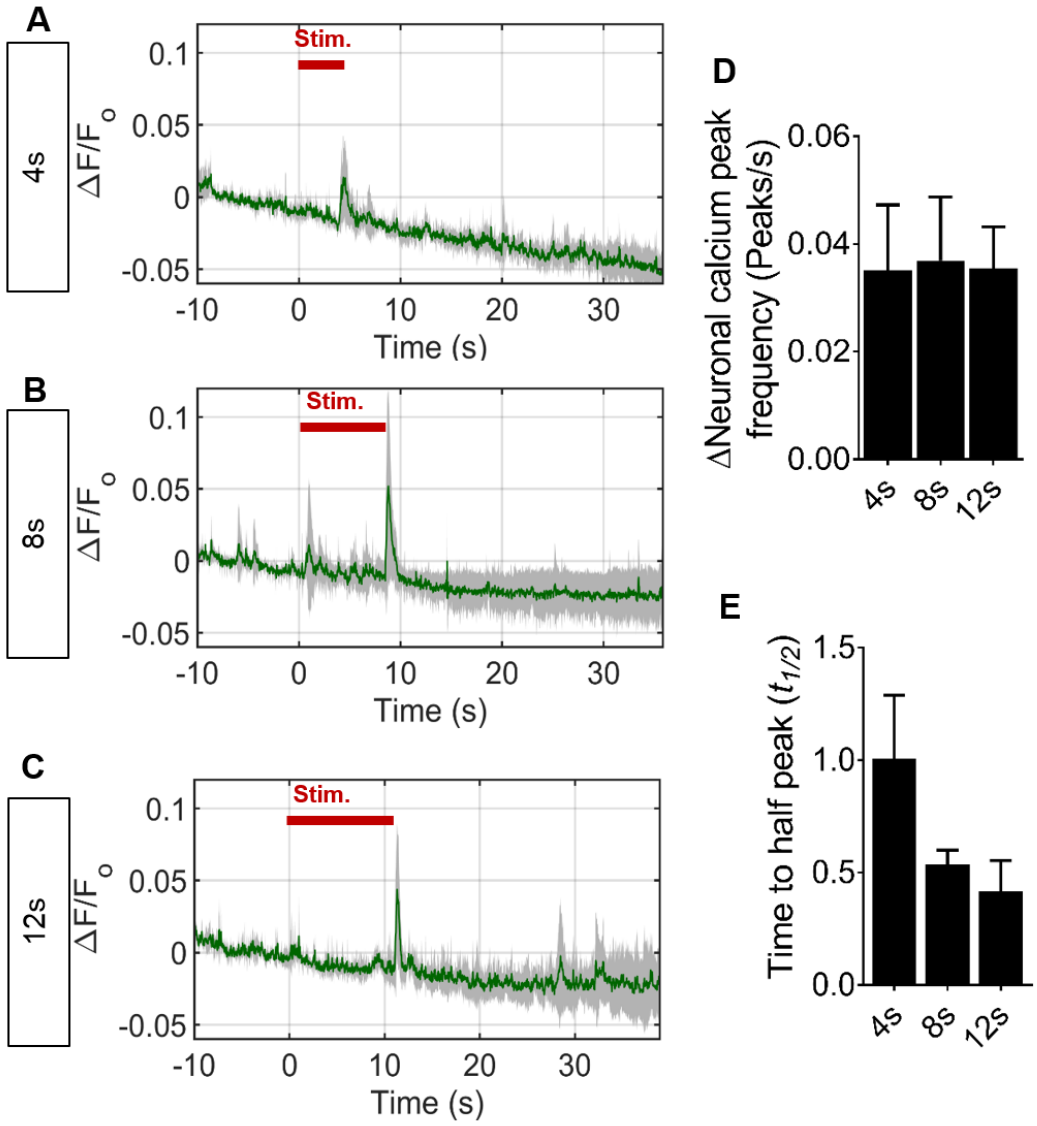

Figure 3-3: Neuronal calcium peak activation in the optic tectum of 8 dpf zebrafish in response to different stimulus durations. A-C: Quantification of neuronal calcium peak responses to 4, 8 and 12 s visual stimulation (n=5 larvae/group). Visual stimulus was administered 0-8s (indicated on the graphs by red bar). **D:** Change in the neuronal calcium peak frequency during response compared to baseline for 4,8 and 12 seconds of light stimulus (n=14, 15 and 12 larvae for 4, 8 and 12s, respectively, at 8 dpf). **E:** Peak onset time expressed as time to half peak ($t_{1/2}$) for 4,8 and 12s stimulus duration for same animals as in A. Data in **A-C** are mean ± s.d. and **D-E** are mean ± s.e.m (Friedman's test used for statistical comparisons).

3.4 Visual stimulus induces specific increases in the RBC speed in *Tg(nbt:GCaMP3;kdrl:HRAS-mcherry;gata1:DsRed)* larvae

Having observed prominent neuronal calcium peaks in response to visual stimulus, I next quantified RBC speed in blood vessels in the teO of 8 dpf larvae. Using the method described in **section 2.4.2.1**, I quantified RBC speed changes in the tectal vessels in the imaging plane. Representative example of RBC tracking during different time periods of the experiments is shown in **Figure 3-4A**. As I observed neuronal calcium peaks at both onset and offset of the visual stimulus (as described in **section 3.2**), I then quantified the corresponding RBC changes in the same animals shown in **Figure 3-1B-D**. **Figure 3-4B-D** shows the RBC speed increases for onset and/or offset of the stimulus.

I then quantified a mean RBC speed for a group of five larvae (same animals as in **Figure 3-2A**) and observed a prominent peak in RBC speed at ~13.5 s with respect to stimulus onset (**Figure 3-6A**). For further quantification, I segregated the time series for all the animals into three time periods (as described in **section 2.4.1**), *baseline*, *response* and *recovery*. I observed statistically significant increases in mean RBC speed during the response time period compared to baseline and recovery time periods as shown in **Figure 3-6B**.

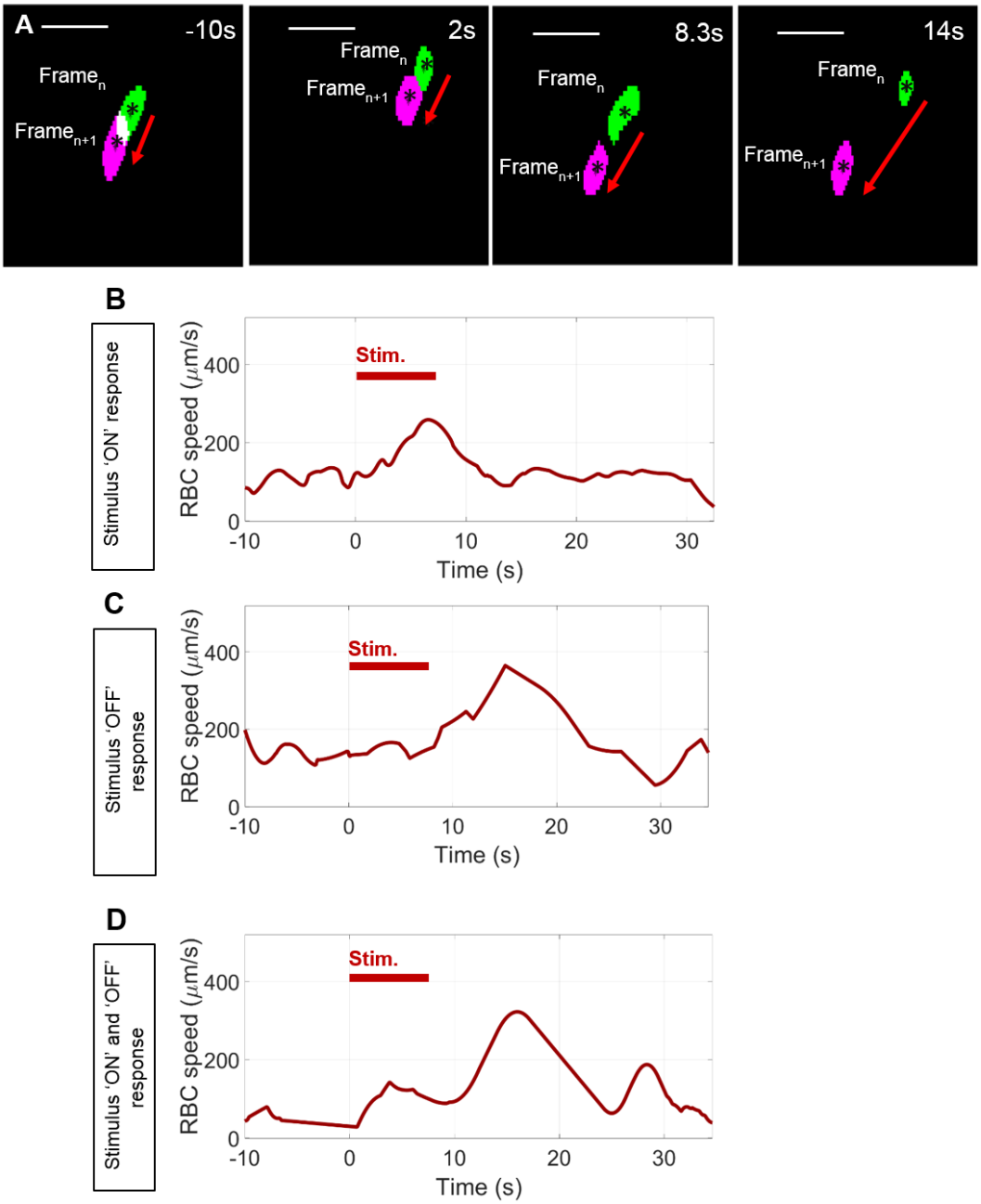

Figure 3-4: RBC speed changes in the optic tectum of 8 dpf zebrafish in response to 8s visual stimulation. A: Segmented RBCs shown for two consecutive frames ($Frame_n$ and $Frame_{n+1}$) for corresponding time point of the neuronal responses shown in **Figure 3-1A**. Individual RBCs are labelled in green to represent $Frame_n$ and magenta to represent $Frame_{n+1}$. **B:** Quantification of RBC speed in the blood vessels in the optic tectum over time, showing examples where neuronal calcium peaks occurred at stimulus ON, stimulus OFF and both stimulus ON and OFF. Visual stimulus is administered 0-8s (indicated on the graphs by red bar).

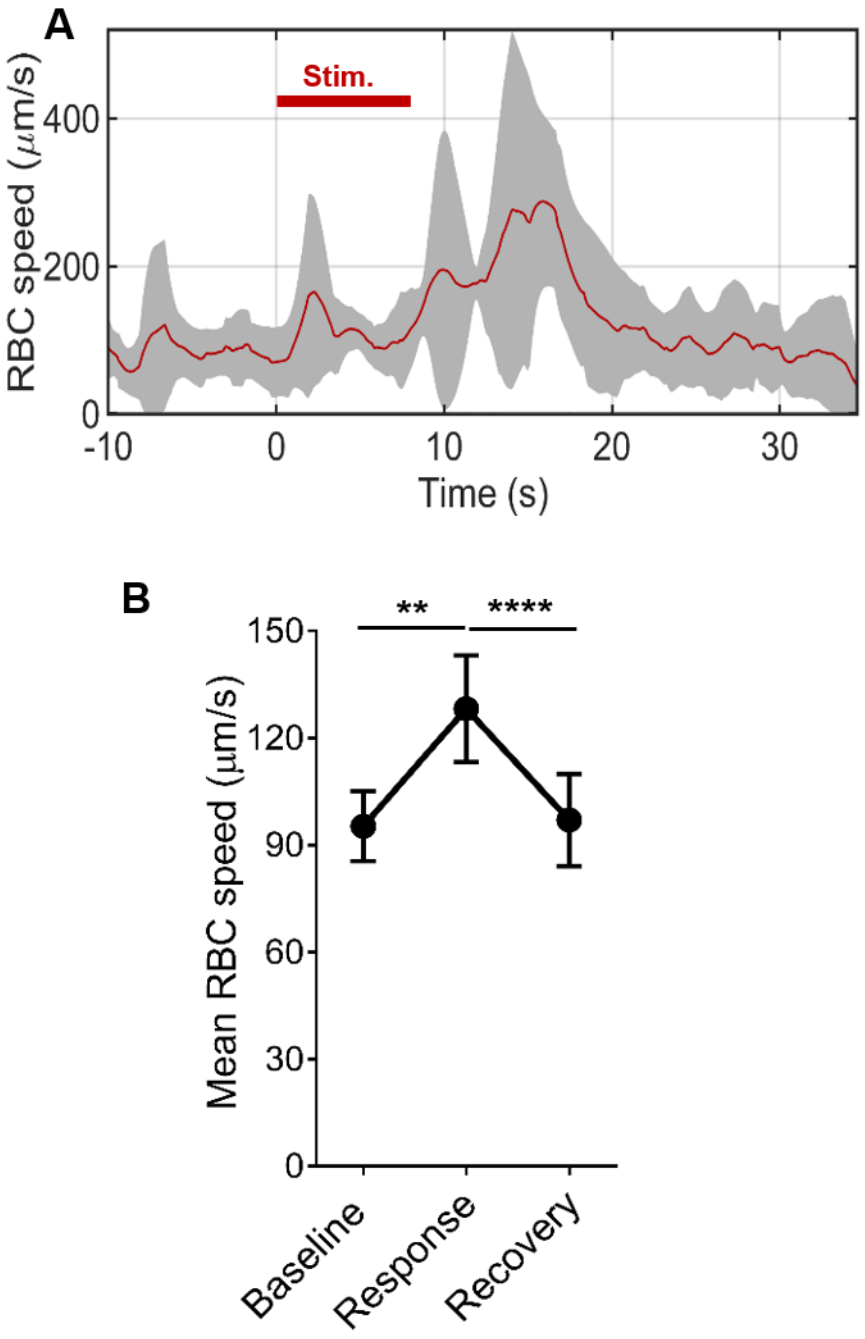

Figure 3-5: RBC speed changes in response to visual stimulation. A: Erythrocyte (RBC) speed in tectal vessels in the same animals as **Figure 3-1. B:** Mean RBC speed in the tectal vessels during baseline, response and recovery time periods in the same animals as **Figure 3-1**. Data in **A** is mean ± s.d. and **B** is mean ± s.e.m. **p<0.01, ****p<0.0001 (RM-ANOVA).

3.5 Red blood cell speed is not statistically different in groups with different duration of light stimulation

As described in **section 3.3**, onset times to neuronal calcium peaks showed a decreasing trend with increasing stimulus duration. I then quantified the differences in the RBC speed in response to different duration of stimulus (4, 6 and 12 seconds). No significant differences were observed in change in RBC speed with different durations of stimulus (**Figure 3-6**).

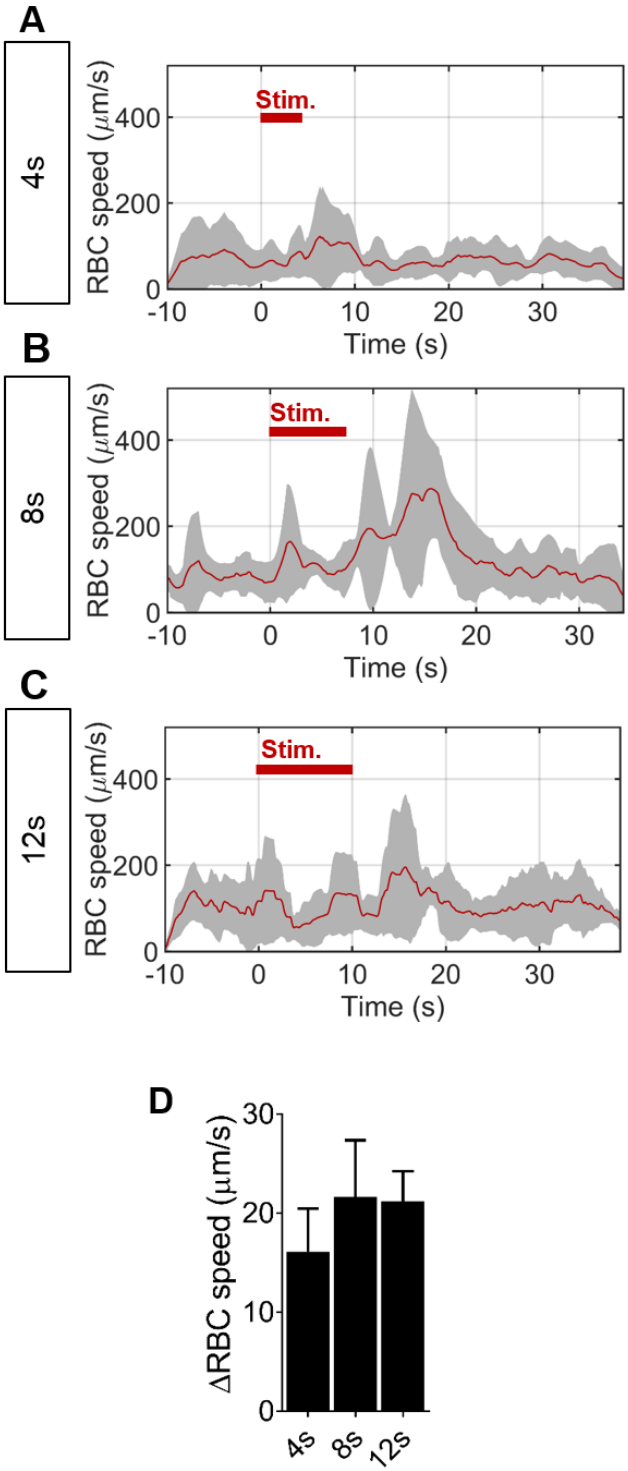

Figure 3-6: RBC speed changes in response to different stimulus duration. A-C: Quantification of RBC speed in response to 4, 8 and 12s visual stimulation (n= 5 larvae/group). Visual stimulus is delivered for 0-8s shown by red bar on the graphs**. D:** Change in RBC speed during response time period compared to baseline for 4,8 and 12s stimulus duration for same animals (n=14, 15 and 12 larvae for 4, 8 and 12s, respectively) as in **Figure 3-3**. Data in **A-C** is mean ± s.d. and **D** is mean ± s.e.m (one-way ANOVA).

3.6 Light stimulus associated neuronal calcium peak and blood velocity peak are temporally coupled

On comparing the mean time to peak of neuronal activation and RBC speed, I found the RBC speed peak to be delayed by 6.33±3.19 s from the neuronal calcium activations (**Figure 3-7**), suggesting a delayed coupling of the vascular responses, similar to the response in mammalian models (371).

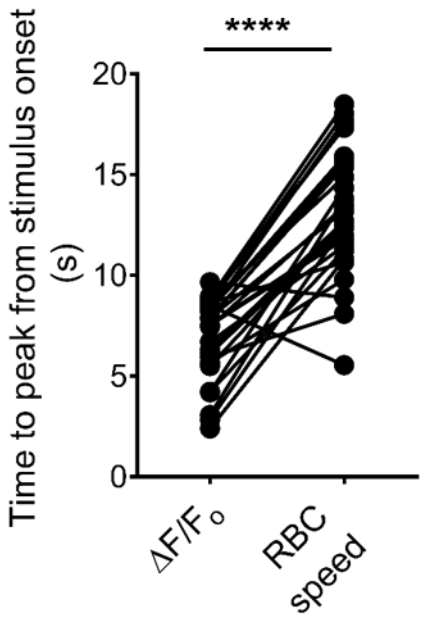

Figure 3-7: Temporal relationships between stimulus onset, change in neuronal activations and RBC speed. Quantification of mean time to peak for neuronal calcium responses ($\Delta F/F_o$) and RBC speed with respect to stimulus onset (n= 30 larvae). ****p<0.0001 (unpaired t-test).

3.7 Neurovascular responses in response to light stimulation are spatially restricted to the optic tectum

To determine the spatial specificity of the RBC response, I measured RBC speed in the blood vessels in forebrain and hindbrain (i.e. non tectal vessels) and dorsal aorta. Representative images are shown in **Figure 3-8A**. Quantification of mean RBC speed in response to visual stimulus showed no significant difference in the response period compared to baseline unlike in the tectal vessels (See **section 3.4 and 3.5**) **Figure 3-8B**. Comparing the absolute change in RBC speed, I found stimulus associated increases in the RBC speed in the tectal vessels to be significantly higher than non tectal vessels **Figure 3-8C**. This suggests a local blood flow response constrained to the area of neuronal activation.

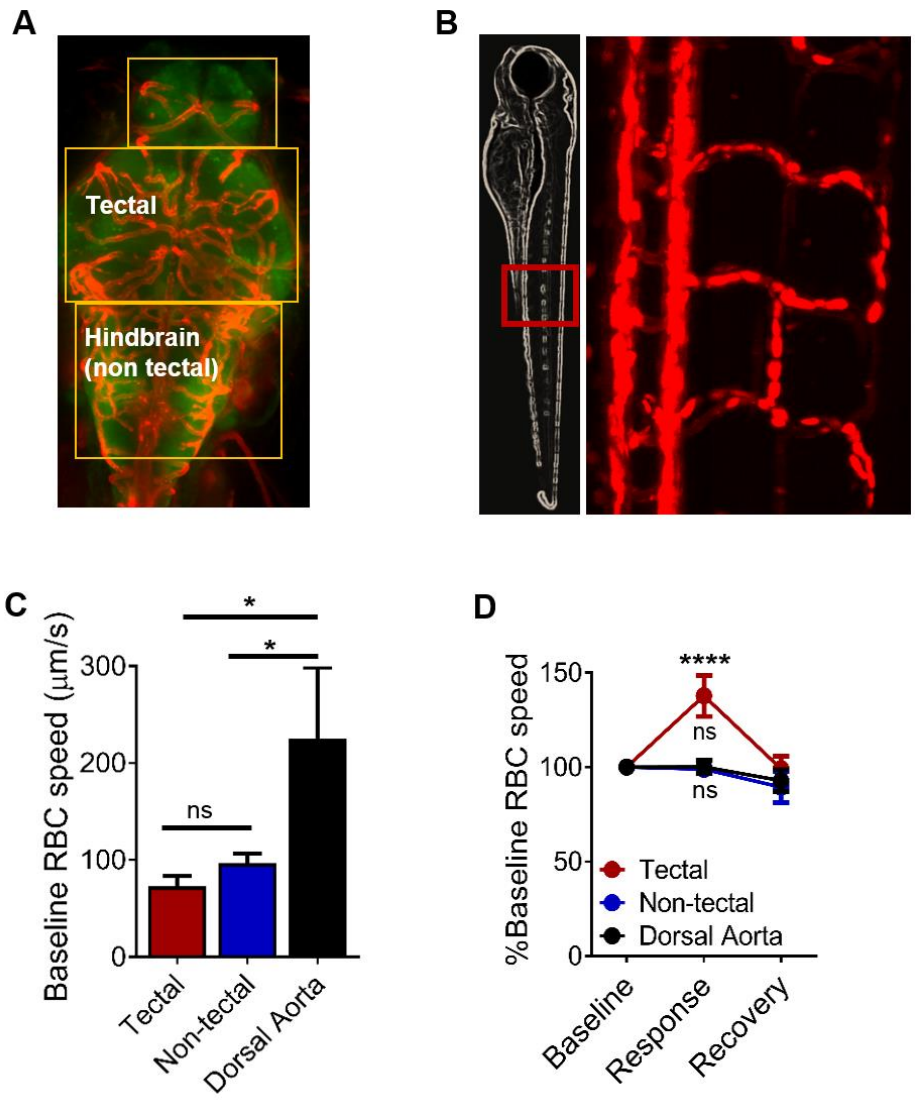

Figure 3-8: Spatial specificity of increase in RBC speed in response to visual stimulus in tectal compared to non tectal blood vessels. A: Representative micrograph of *Tg(nbt:GCaMP3;kdrl:mcherry)* showing tectal and non-tectal vessels in the brain of 8 dpf old zebrafish. **B:** Representative micrograph showing the location of dorsal aorta for quantification of RBC speed comparisons in **C** and **D. C:** Baseline RBC speed in tectal vessels, non-tectal (hindbrain and forebrain) vessels and dorsal aorta. **D:** RBC speed expressed as percentage from the baseline for baseline, response and recovery for tectal vessels, non-tectal vessels and dorsal aorta (n=17 larvae/group). Data in **C**-**D** are mean ± s.e.m. *p<0.05, ****p<0.0001 (one-way ANOVA).

3.8 Light stimulation does not affect heart rate

To examine the possibility that systemic effects were responsible for changes in RBC speed in the teO, I measured the heart rate in response to visual stimulus (as described in **section 2.4.6**). Since the compound transgenic (*Tg(nbt:GCaMP3;kdrl:HRAS-mcherry;gata1:DsRed)*) labels the red blood cells I quantified the change in the red channel intensity averaged over the ventricular area for the three time periods (baseline, response and recovery). The change in intensity for a typical quantification is shown in **Figure 3-9**. I then calculated the number of peaks from the signal obtained. I found that visual stimulation had no effect on the heart rate when comparing peak frequency of the heart rate signal during the response time period compared to baseline **Figure 3-9**. This confirms that the changes in RBC speed in the teO are not mediated by changes in cardiac output.

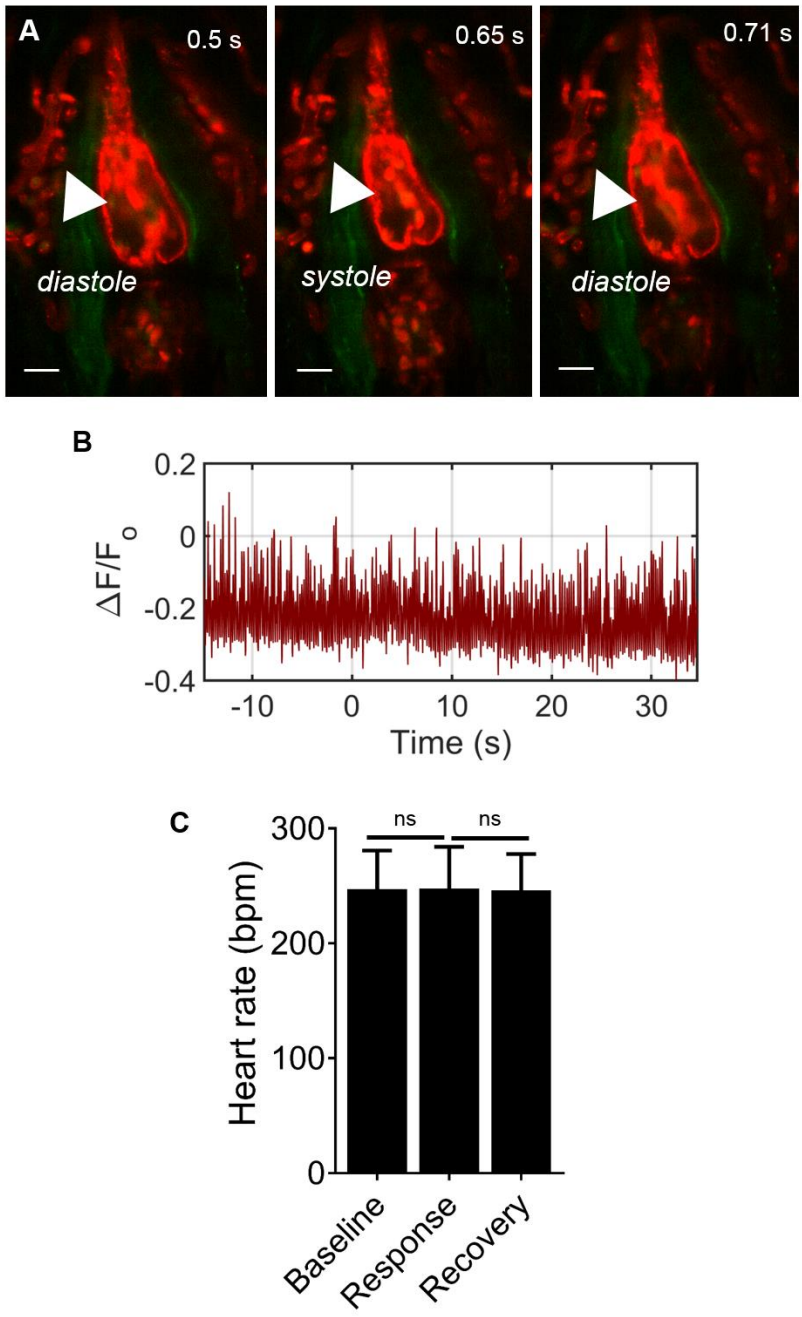

Figure 3-9: Effect of visual stimulation on heart rate. A: Representative micrographs showing a systole and a diastole (white arrowhead) corresponding to one peak on the time series graph on **B. C.** Quantification of heart rate as beats per minute (bpm) during all baseline, response and recovery time periods (n = 12 larvae). Scale bar is 20 µm (RM-ANOVA).

3.9 Neurovascular coupling in zebrafish is not evident until 6 dpf

Studies have shown rodents develop NVC only after a certain period in development (134, 137, 372). I therefore examined the neurovascular responses to light stimulation at 4, 6 and 8 dpf to detect whether zebrafish display a similar developmental threshold. Quantification of the neuronal response to visual stimulation for baseline, response and recovery found no stimulus evoked neuronal calcium peaks at 4 dpf but these were present at 6 dpf (**Figure 3-10**). Comparing the mean RBC speeds for the same animals, I found no significant changes in RBC speed either at 4 or 6 dpf (**Figure 3-10**). This suggests in spite of having stimulus evoked neuronal activation, NVC is not present at 6 dpf.

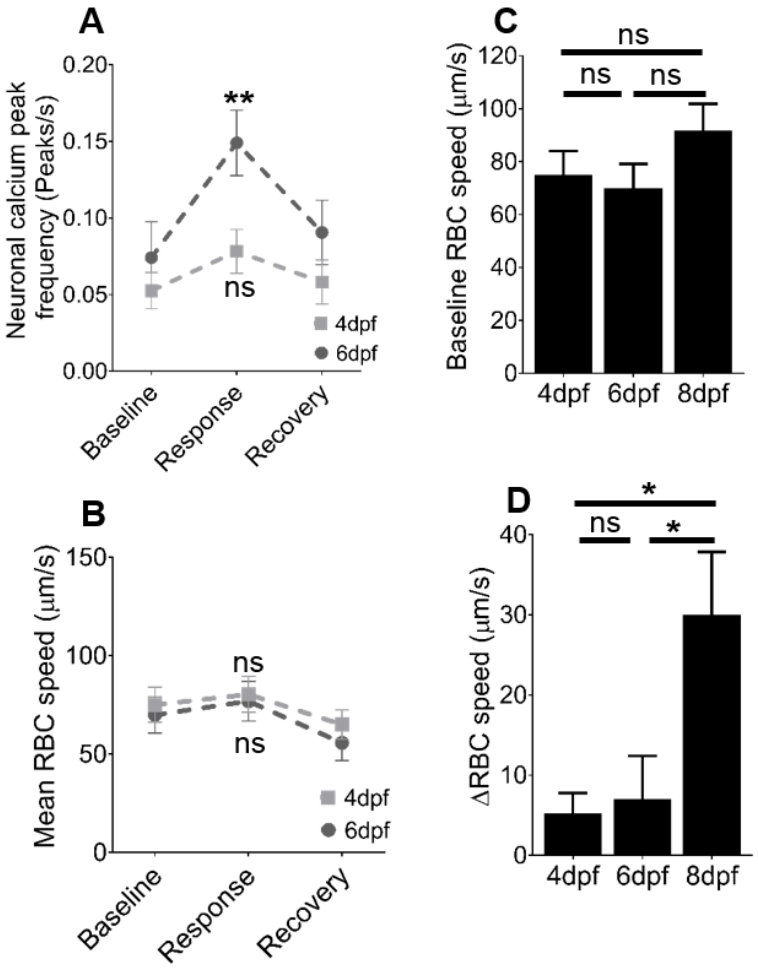

Figure 3-10**: Neurovascular coupling in zebrafish develops after 6 dpf. A:** Quantification of frequency of peaks in ($\Delta F/F_o$) as a measure of neuronal activation during the baseline, response and recovery time periods for 4d and 6d post fertilization (n=17 larvae/group). **B:** Mean RBC speed during baseline, response and recovery time periods in the same animals as **A** (n=17 larvae/group). **C:** Mean baseline RBC speed in tectal vessels in 4, 6 and 8 dpf zebrafish. **D:** Change in RBC speed (ΔRBC) in response to stimulus in 4, 6, and 8 dpf (n=17 larvae/group). *p<0.05, **p<0.01. Data in **A-D** are mean ± s.e.m. *p<0.05, **p<0.01 (one-way ANOVA).

3.10 Nitric oxide synthase inhibition prevents the increase in RBC speed in tectal vessels in response to visual stimulation

I next tested the effect of the NOS inhibitor L-NAME on NVC. I incubated 7 dpf zebrafish with 0.5mM L-NAME in E3 or E3 alone and imaged them at 8 dpf (16-18 h treatment). Following imaging, I quantified change in neuronal calcium fluorescence (quantified as $\Delta F/F_o$) and corresponding RBC speed in both groups (time series shown in **Figure 3-11A-B**). I observed both E3 and L-NAME groups responded to visual stimulation by increasing neuronal calcium peak frequency during the response time period compared to baseline and recovery (**Figure 3-12A**). However, in the L-NAME treated larvae, RBC speed did not increase during the response time period compared to baseline and recovery (**Figure 3-12B**). L-NAME significantly reduced the change in the RBC speed during the response time period compared to baseline (described as *ΔRBC)* compared to E3 controls (**Figure 3-12C**).

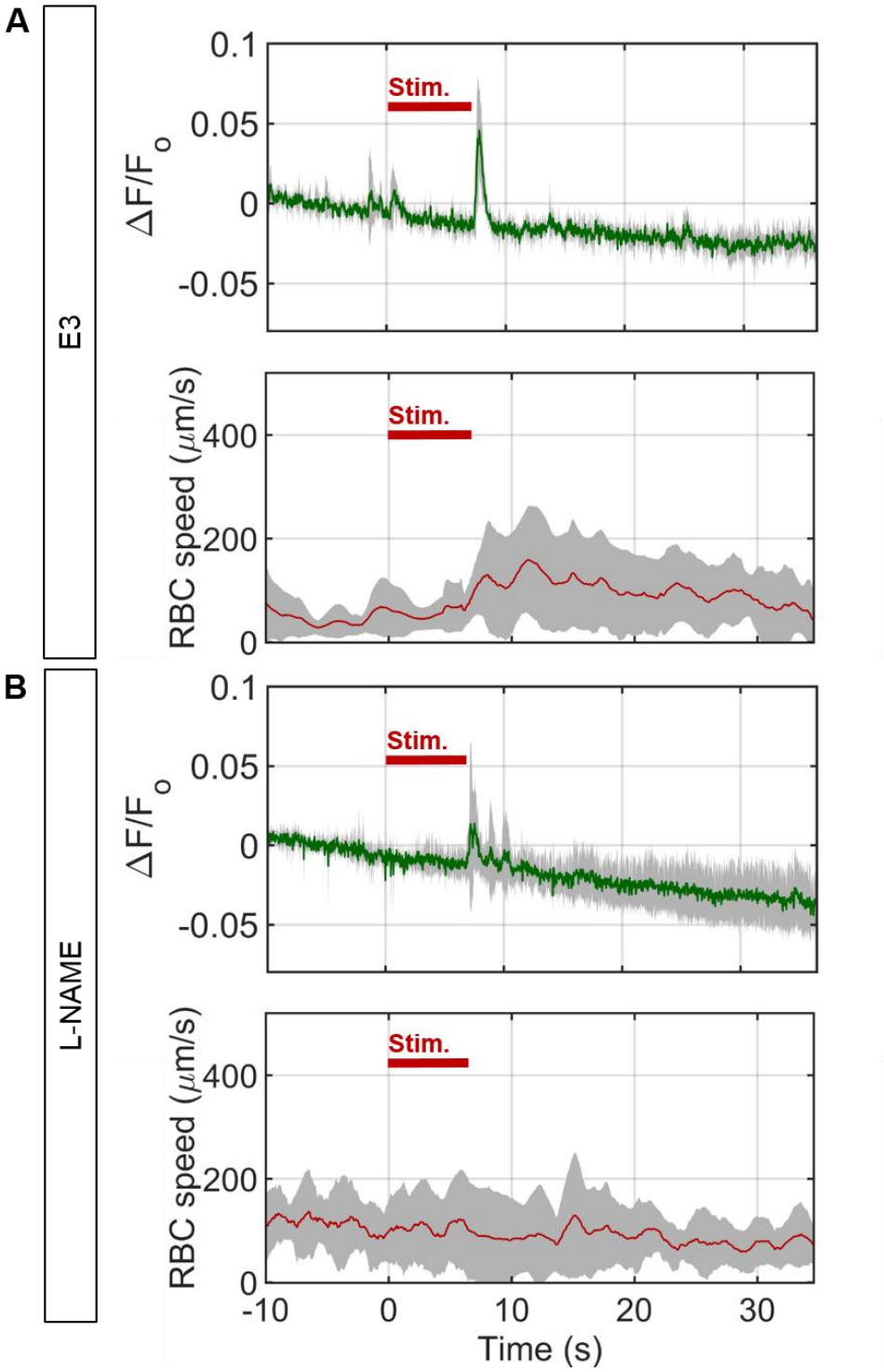

Figure 3-11: Nitric oxide inhibition causes neurovascular uncoupling. Quantification of neuronal activation ($\Delta F/F_o$) in the optic tectum and RBC speed for 8 s visual stimulus for **A:** controls (E3) and **B:** L-NAME treated 8 dpf *Tg(nbt:GCaMP3;kdrl:HRAS-mcherry;gata1:DsRed)* larvae (n=5 larvae/group). Visual stimulus is delivered for 0-8s shown by red bar on the graphs**.** Data in **A-B** is mean ± s.d.

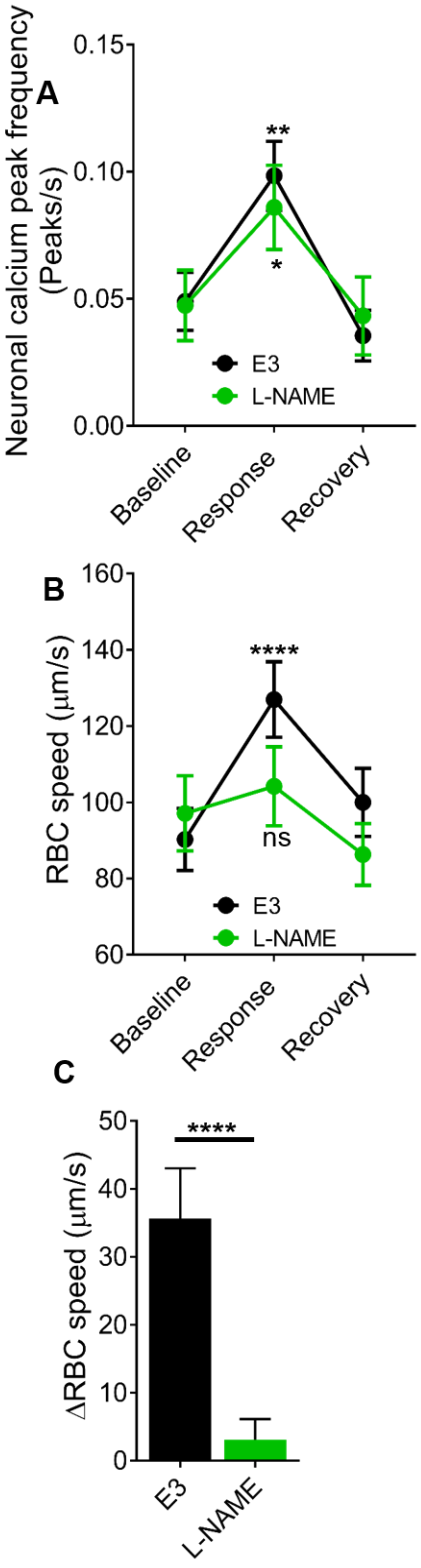

Figure 3-12: Nitric oxide inhibition prevents neurovascular coupling in 8 dpf zebrafish. A: Quantification of frequency of peaks in ($\Delta F/F_o$) as a measure of neuronal activation during the baseline, response and recovery time periods for E3 (n=36 larvae) and L-NAME treated groups (n=32 larvae). **B:** Mean RBC speed during baseline, response and recovery time periods in the same animals as **A**. **C:** Change in RBC speed (ΔRBC) in response to stimulus. Data in **A-C** are mean ± s.e.m. *p<0.05, **p<0.01, ****p<0.0001 (two-way ANOVA and unpaired t-test for **A-B** and **C**, respectively).

3.11 Cyclooxygenase inhibition reduced neurovascular coupling in zebrafish

I next tested the presence of an indirect pathway of NVC mediated by cyclo-oxygenase as shown in mammalian models. Using a non-specific COX inhibitor, indomethacin (10 µM) for overnight incubation (16-18 h), I quantified the changes in the neuronal calcium fluorescence in the teO ($\Delta F/F_o$) and RBC speed in response to 8 s visual stimulation (**Figure 3-13A-B**) for 0.1% DMSO (control) and indomethacin treated groups. Both DMSO and indomethacin treated larvae showed significantly increased neuronal calcium peak frequency during the response time period compared to baseline and recovery (**Figure 3-14A**). However, indomethacin significantly attenuated the stimulus-evoked change in RBC speed (**Figure 3-14B and C**).

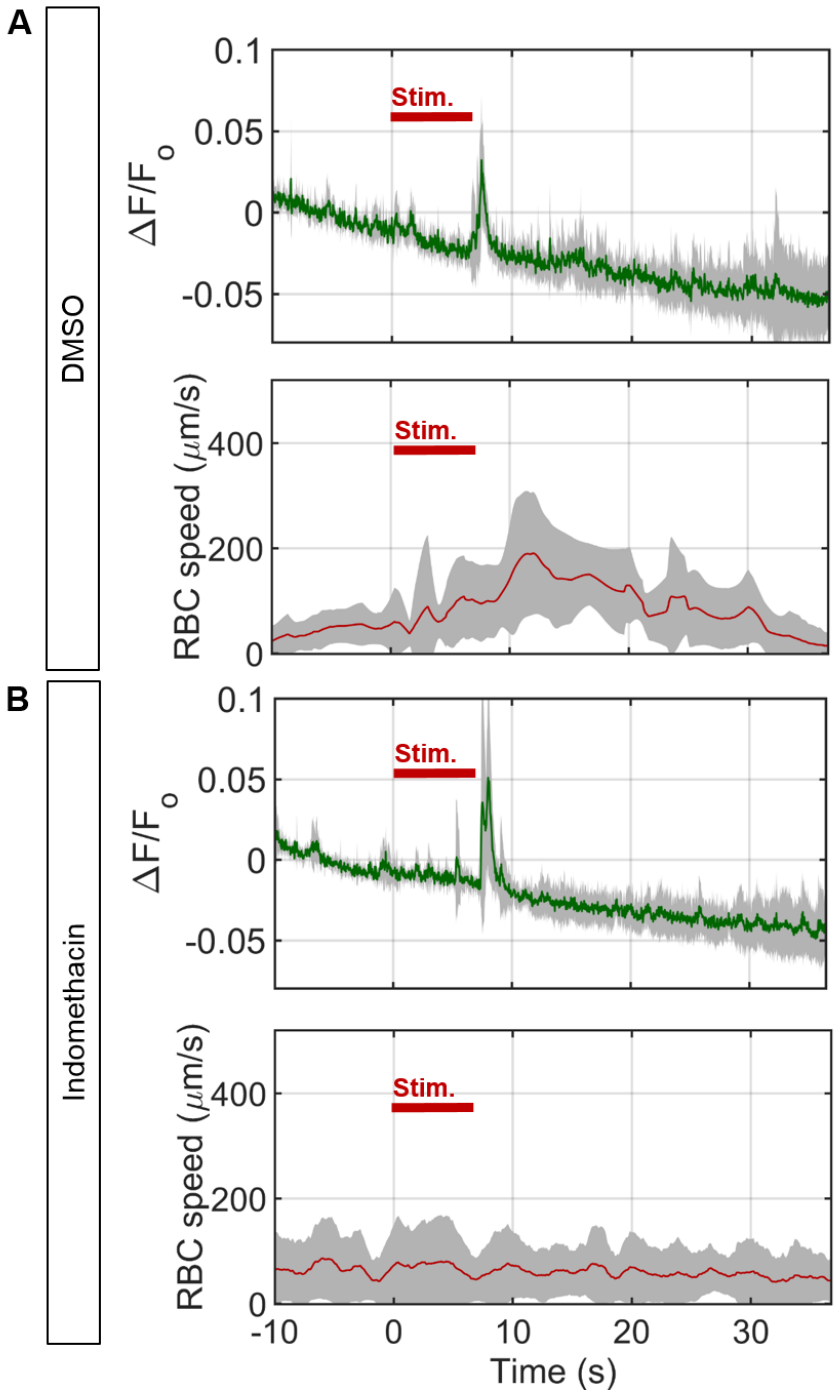

Figure 3-13**: COX inhibition causes neurovascular uncoupling.** Quantification of neuronal activation ($\Delta F/F_o$) in the optic tectum and RBC speed for 8 s visual stimulus for **A:** controls (DMSO) and **B:** Indomethacin treated 8 dpf *Tg(nbt:GCaMP3;kdrl:HRAS-mcherry;gata1:DsRed)* larvae (n=5 larvae/group). Visual stimulus is delivered for 0-8s shown by red bar on the graphs**.** Data in **A-B** is mean ± s.d.

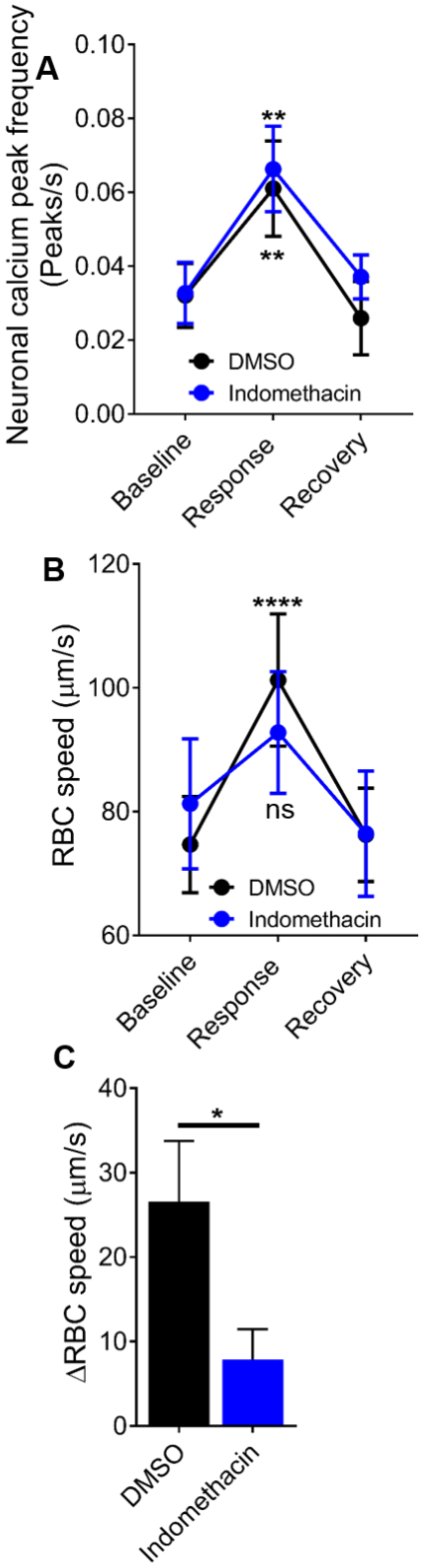

Figure 3-14: COX inhibition causes neurovascular uncoupling. A: Quantification of frequency of peaks in ($\Delta F/F_o$) as a measure of neuronal activation during the baseline, response and recovery time periods for E3 (n=28 larvae) and Indomethacin treated groups (n=26 larvae). **B:** Mean RBC speed during baseline, response and recovery time periods in the same animals as **A**. **C:** Change in RBC speed (ΔRBC) in response to stimulus. Data in **A** and **B** are mean ± s.e.m. *p<0.05, **p<0.01, ****p<0.0001(two-way ANOVA and unpaired t-test for A-B and C, respectively).

3.12 Discussion

I here describe a novel larval zebrafish model of NVC. On stimulation with 8 seconds of red light I found increases in neuronal calcium and RBC speed in the teO. I have then shown that the teO neurons can respond phasically at ON or OFF or both depending on the layer of SPV being imaged (294). Zebrafish tectal neuropil is densely populated with periventricular layer (PVL) interneurons which could explain majority of the responses being in response to turning off the light stimulus (373). I demonstrated the local specificity of the neurovascular responses by showing increases in RBC speed were confined to the teO and not detected in blood vessels in the hindbrain and/or the forebrain. I found no evidence of a systemic effect of the stimulation as the stimulus induced no change in dorsal aorta RBC speed or heart rate. I therefore conclude that zebrafish do indeed display NVC analogous to the response that has previously only been described in mammals. I found that zebrafish demonstrate a developmental threshold for NVC as they do not display NVC until after 6 dpf. Furthermore, neuronal calcium responses are spontaneous till 6 dpf, a marker of development of neuronal circuitry similar to shown in neonatal mammalian reports (134, 137).

Mammalian studies have shown NVC can be modulated by multiple redundant mechanisms. In mammals, local regulation of blood flow is known to occur via neuronally derived signals such as glutamate and NO (374). Further work also suggested mechanisms involving astrocytes (38), interneurons (26) and pericytes (82). However, the exact role of various cellular candidates is under debate, for example COX-mediated astrocyte regulation of blood flow has been suggested to be involved in indirect, rather than direct regulation of blood flow (26, 48). I have tested the presence of NO and COX based mechanisms in the zebrafish model of NVC by using L-NAME (non-specific NOS inhibitor) and Indomethacin (non-specific COX inhibitor). I found that inhibition of either the NOS or COX-mediated pathways resulted in inhibition of the RBC speed increase associated with visual stimulation in 8 dpf zebrafish

larvae. This suggests that both NO and COX based mechanisms of neurovascular coupling exist in zebrafish. There is an ongoing debate on specific contribution of neuronal COX (COX2 in pyramidal neurons) and astrocyte COX (COX1 in cortical neurons) in mammalian models of NVC (27, 375). Furthermore, neuronal NO based NVC regulation is known to be a characteristic of cerebellar neurons (376). This points to brain region specific mechanisms of NVC regulation. Hence, further research is needed to investigate specificity of NO and COX based mechanisms of NVC in zebrafish.

3.13 Conclusions

Here I have demonstrated a non-invasive zebrafish model which can be used to further investigate the detailed mechanisms which underlie NVC. Similar to the mammalian system, I have demonstrated the existence in zebrafish of several pathways which can result in NVC, in particular I have demonstrated the involvement of both NOS and COX-mediated pathways. By avoiding the need for invasive surgery and anaesthetics (commonly used in mammalian models), this zebrafish model provides an opportunity to study NVC under more physiological conditions than mammalian. Furthermore, the ease of performing genetic manipulation makes zebrafish an appealing model allowing us to investigate genetic regulators of NVC. The ease of genetic manipulation in zebrafish would facilitate the study of the association between disease-related mutants and neurovascular dysfunction.

4 The effect of hyperglycemia on neurovascular coupling and function

4.1 Aims

In this chapter, I describe application of the NVC zebrafish model to understand the effect of hyperglycemia (a key component of diabetes) on NVC. I first examined the effect of physiologically high levels of glucose on NVC and cerebrovascular patterning. I next sought to determine if sodium nitroprusside, an NO donor, could rescue the effect of glucose on neurovascular anatomy and function. Using DAF-FM staining, I confirmed NO deficiency in glucose treated larvae and that this is ameliorated by SNP treatment. I next examined the effect of glucose with or without SNP co-treatment on different functional markers of the cells in the NVU, including *klf2a:GFP* intensity in the ECs as a marker of shear stress sensing function, *claudin5a:GFP* and *sm22ab:mcherry*^{s441} nuclei (pericytes) on the tectal vessels as a marker of blood brain barrier integrity.

4.2 24h treatment with 20mM glucose does not affect cerebrovascular patterning and neurovascular coupling in 9 dpf old zebrafish

I evaluated the effect of a glucose concentration comparable to that found in poorly controlled diabetes (20mM). 8 dpf larvae were immersed in 20mM glucose or mannitol for 24h followed by imaging of cerebrovascular anatomy and neurovascular function at 9 dpf. Representative micrographs comparing cerebral anatomy of mannitol and glucose treated larvae are shown in **Figure 4-1A**. Quantification of vascular anatomy (see methods **section 2.4.3**) showed no significant difference in tectal branch points, vascular length and vessel radius between larvae exposed to glucose or mannitol (as an osmotic control) (**Figure 4-1B-E**).

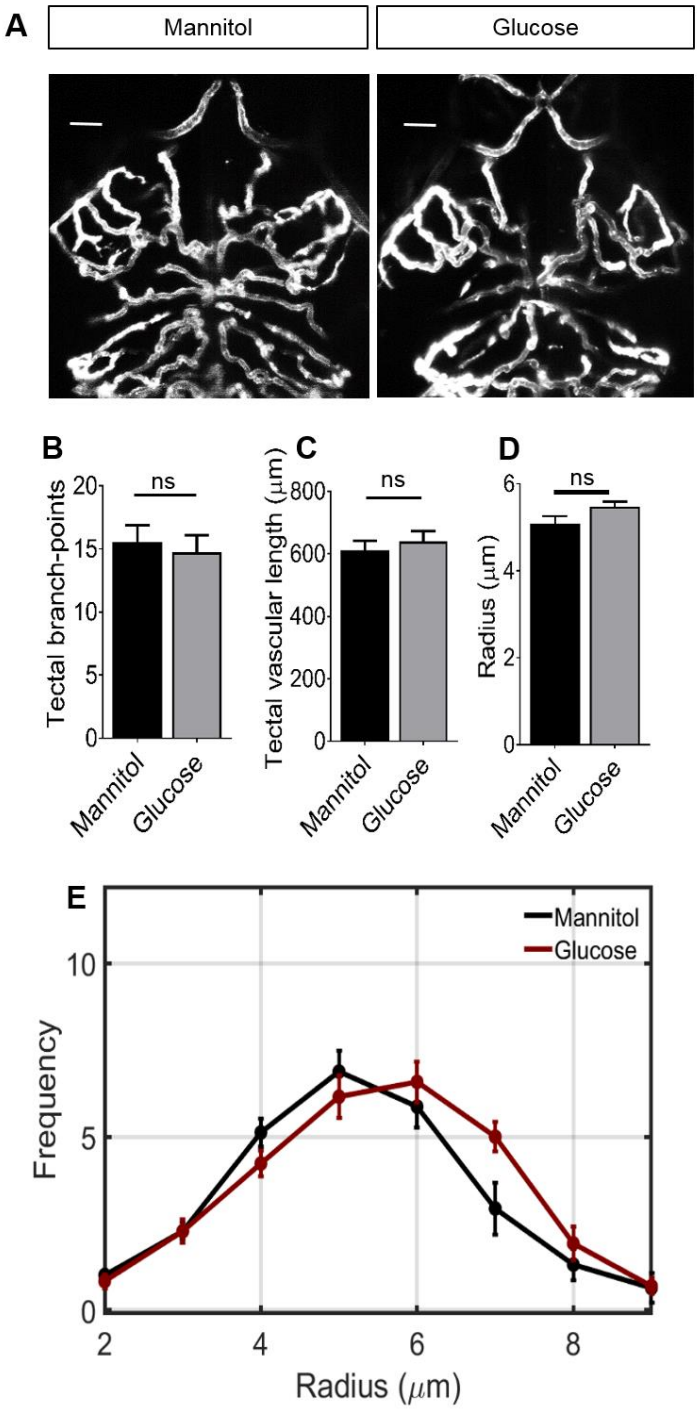

Figure 4-1: Effect of 24h glucose exposure from 8-9 dpf on cerebrovascular patterning in zebrafish A: Representative micrographs of cerebral vessels exposed to 20mM mannitol or glucose for 24h (8-9 dpf). **B:** Square indicates region of the left optic tectum quantified in **B-E. B:** Number of tectal vessel branchpoints (n=11 larvae/group). **C:** Total tectal vessel length in same animals as **B. D:** Mean tectal vessel radius in same animals as in **B. E:** Histograms of tectal vessel radii of tectal vessels in same animals as in **B.** Scale bar represents 20 µm. Data in **A-E** are mean ± s.e.m (unpaired t-test used for statistical comparisons).

I next examined the effect of 24h exposure to 20mM glucose from 8-9 dpf in my model of NVC. Neuronal calcium and RBC speed from five larvae for both glucose and mannitol treated groups are shown in **Figure 4-2A** and **B**, respectively. I found no significant differences between the glucose and mannitol treated groups, suggesting 24h glucose treatment between 8-9 dpf does not affect neurovascular function or anatomy (**Figure 4-3A-C**)

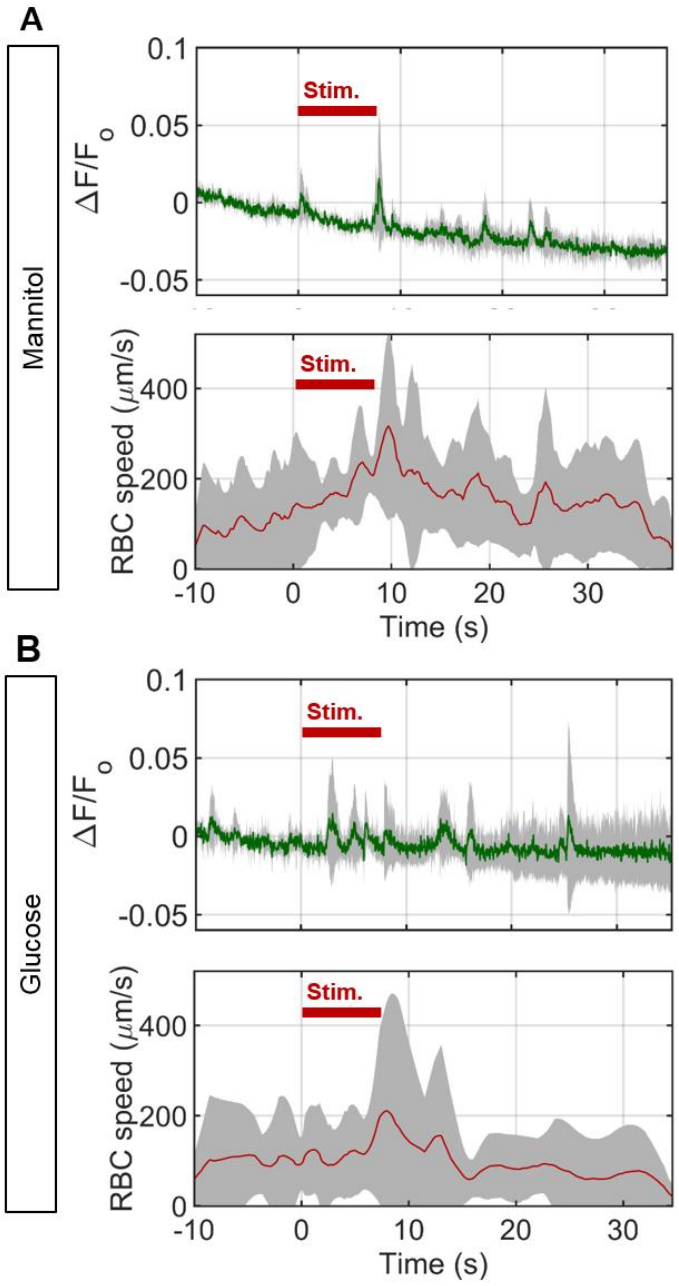

Figure 4-2: Effect of 24h glucose exposure on neurovascular function. Time series of neuronal activation ($\Delta F/F_o$) and tectal vessel RBC speed in zebrafish exposed to **A:** 20mM mannitol and **B:** 20mM glucose from 8-9 dpf (24 h) (n = 5 larvae/group). Visual stimulus is delivered for 0-8s shown by red bar on the graphs**.** Data in **A-B** is mean ± s.d.

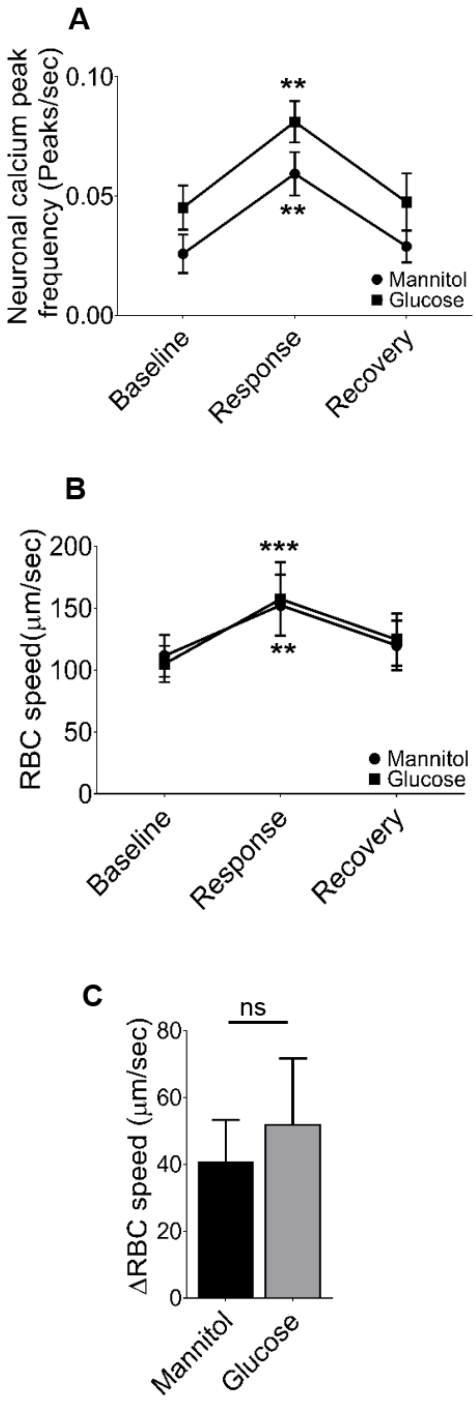

Figure 4-3: Effect of 24h glucose exposure on neurovascular coupling. A: Frequency of peaks of neuronal activation during baseline, response and recovery time periods in mannitol or glucose exposed larvae (n=11 larvae/group). **B:** RBC speed for baseline, response and recovery for same animals in **A. C:** Change in RBC speed (ΔRBC) between baseline and response time periods for the same animals as **B.** Data in **A-C** are mean ± s.e.m. **p<0.01, ***p<0.001(two-way ANOVA and unpaired t-test for A-B and C, respectively).

4.3 120h treatment of 20mM glucose impairs cerebrovascular patterning and neurovascular coupling in response to light stimulation in the optic tectum of 9 dpf old zebrafish

I next examined the effect of 20mM glucose for a longer duration (from 4-9 dpf). 4 dpf larvae were exposed to 20mM glucose and mannitol by immersion followed by imaging for neurovascular anatomy and function at 4.5 dpf (12h exposure), 6.5 dpf (60h exposure), 8 dpf (96h exposure) and 9 dpf (120h exposure). Representative micrographs are shown in **Figure 4-4**. Quantification of vascular features showed significantly lesser number of branch points, reduced vascular length and reduced vessel radius in glucose treated group compared to mannitol group from 8 dpf (96h exposure) (**Figure 4-5A-C**). A leftward shift in the radius frequency histogram was observed in the glucose compared to mannitol group from 8 dpf implying fewer vessels and reduced mean radius (**Figure 4-6A-D**).

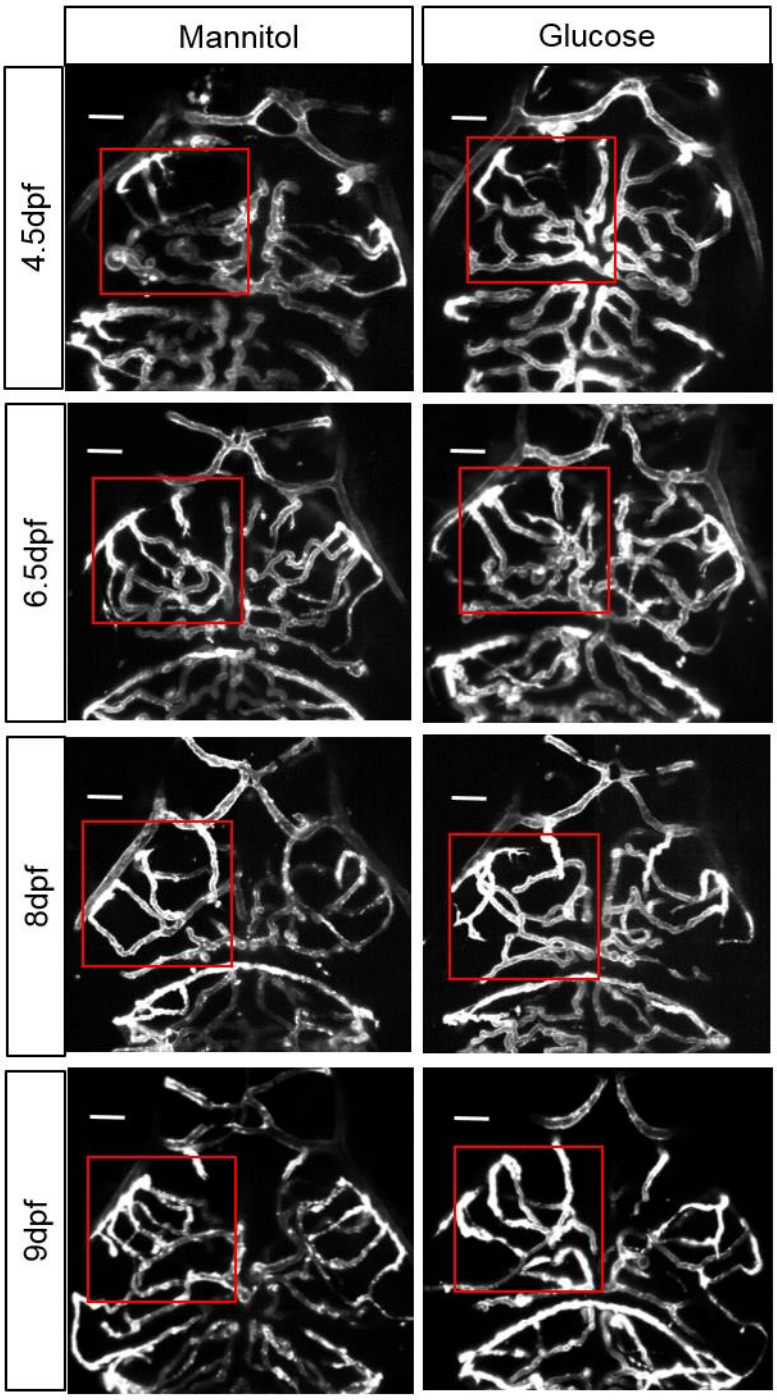

Figure 4-4: Representative micrographs comparing mannitol and glucose treated larvae during the course of 120h (4-9 dpf) of treatment (4.5 dpf, 6.5 dpf, 8 dpf and 9 dpf). Red box indicates the region of the optic tectum quantified for the various anatomical vascular features. Scale bar represents 20 µm.

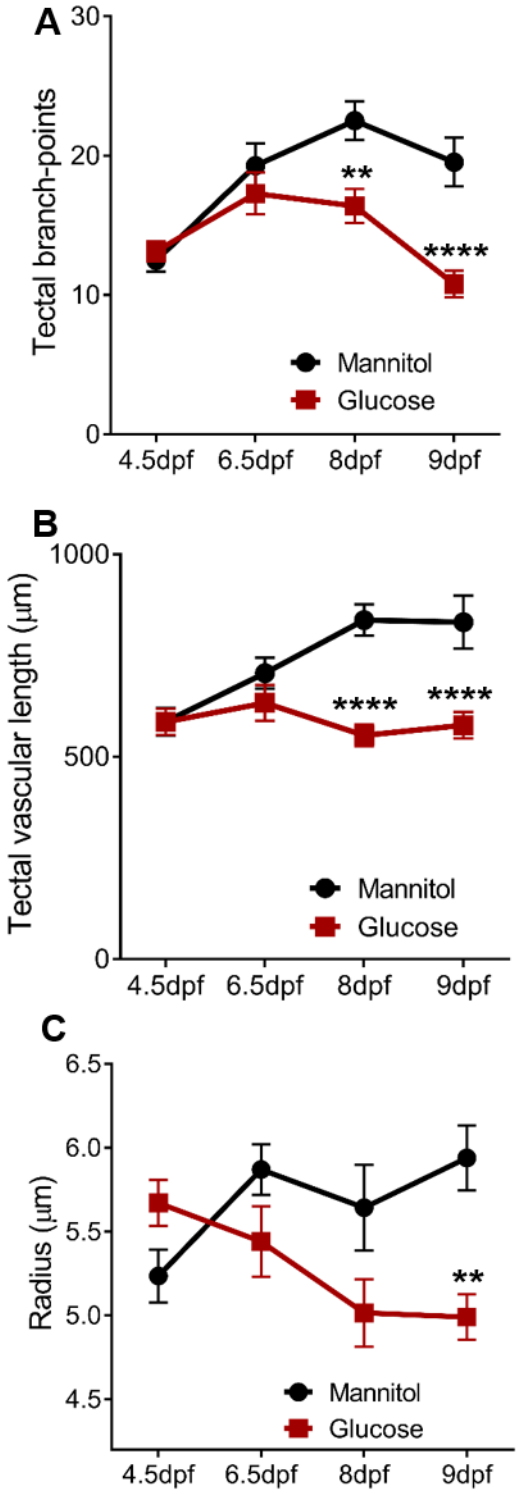

Figure 4-5: Effect of 120h of glucose exposure on cerebrovascular patterning during the course of treatment (4.5 dpf, 6.5 dpf, 8 dpf and 9 dpf). A: Number of tectal vessel branchpoints (n=17, 16, 15 and 20 larvae for 12h, 60h, 96h and 120h exposure, respectively). **B:** Total tectal vessel length in same animals as **A. C:** Mean tectal vessel radius in same animals as in **A.** Data in **A-C** are mean ± s.e.m. **p<0.01, ****p<0.0001 (one-way ANOVA).

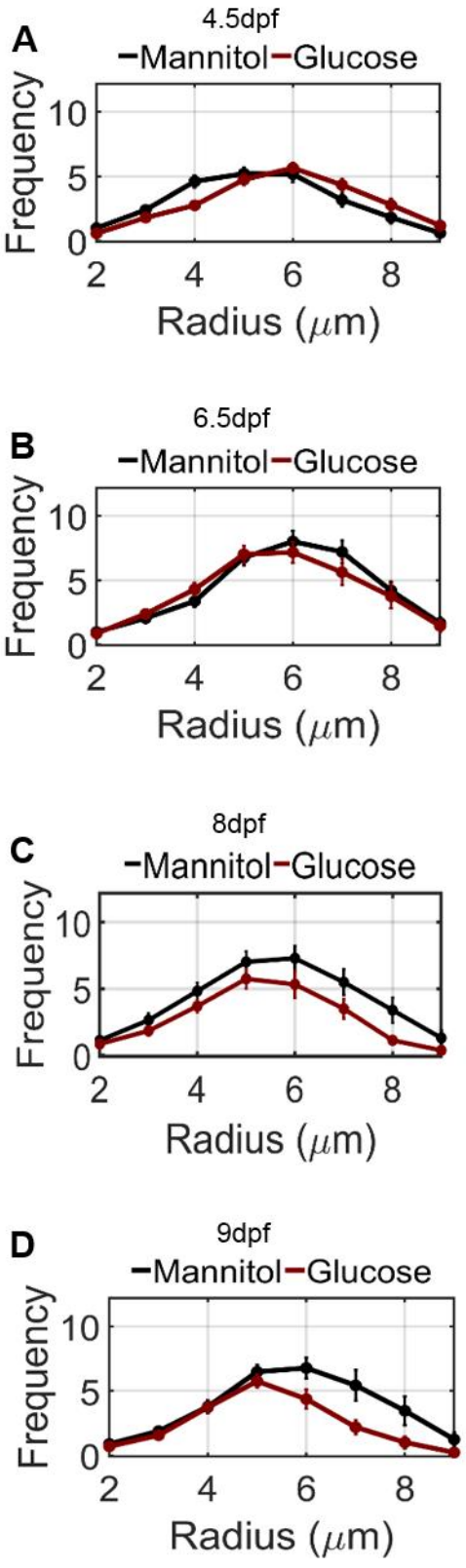

Figure 4-6: A-D: Histograms of tectal vessel radii of tectal vessels in same animals as in Figure 4-5 (n=17, 16, 15 and 20 larvae for 12h, 60h, 96h and 120h exposure, respectively)**.** Data in **A-D** are mean ± s.e.m.

I next examined the neuronal calcium and RBC speed changes in response to visual stimulation at 4.5 dpf, 6.5 dpf, 8 dpf and 9 dpf (**Figure 4-7**). There were no significant differences in calcium peak frequencies between glucose and mannitol treated groups at any time point (**Figure 4-8)**. However, quantification of mean RBC speeds showed a lower value at each of the time periods (baseline, response and recovery) in the glucose compared to the mannitol treated group at 9 dpf (**Figure 4-8**). This suggests 120h of glucose treatment results in neurovascular uncoupling in 9 dpf larvae.

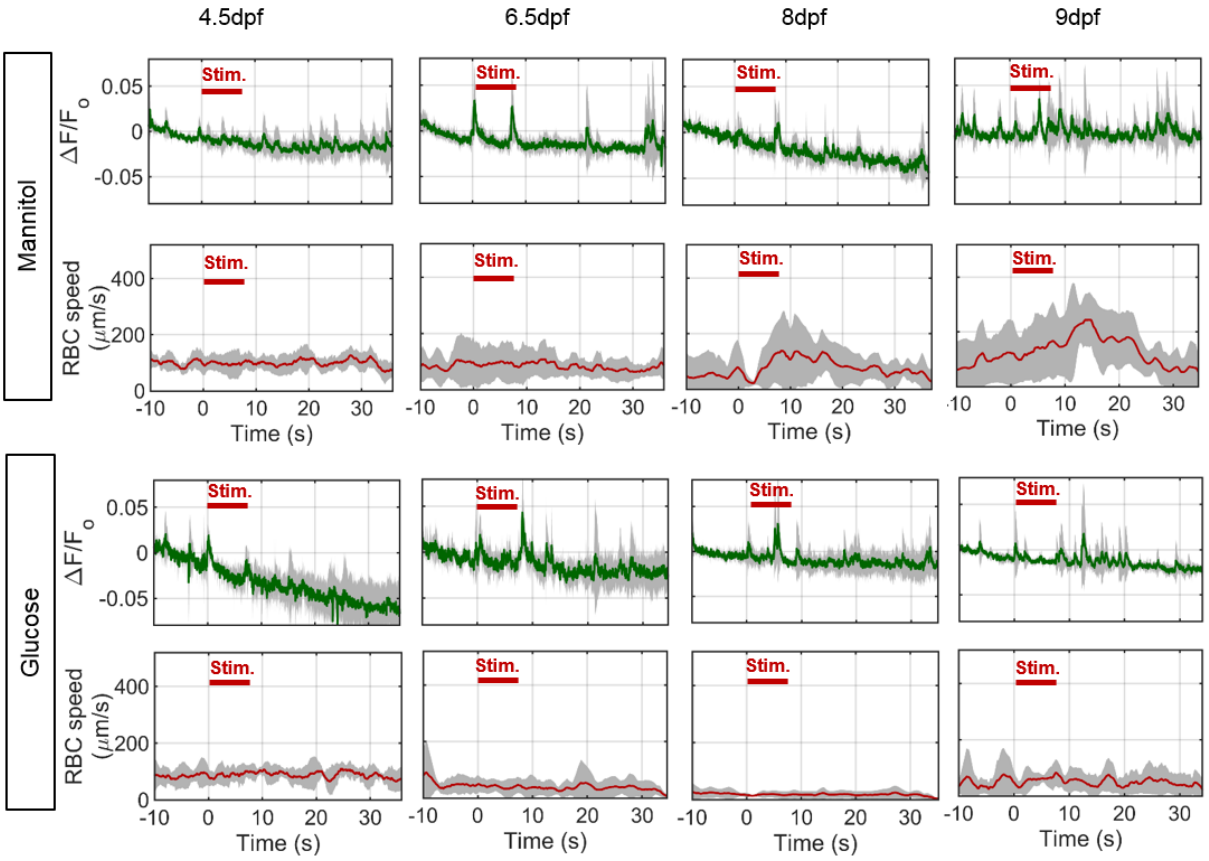

Figure 4-7**: Time series of neuronal activation (*ΔF/F*$_o$) and tectal vessel RBC speed in zebrafish exposed to 20mM mannitol or glucose from 4 dpf for 12h, 60h, 96h and 120h (n=5 larvae/group).** Visual stimulus is delivered for 0-8s shown by red bar on the graphs**.** Data are mean ± s.d.

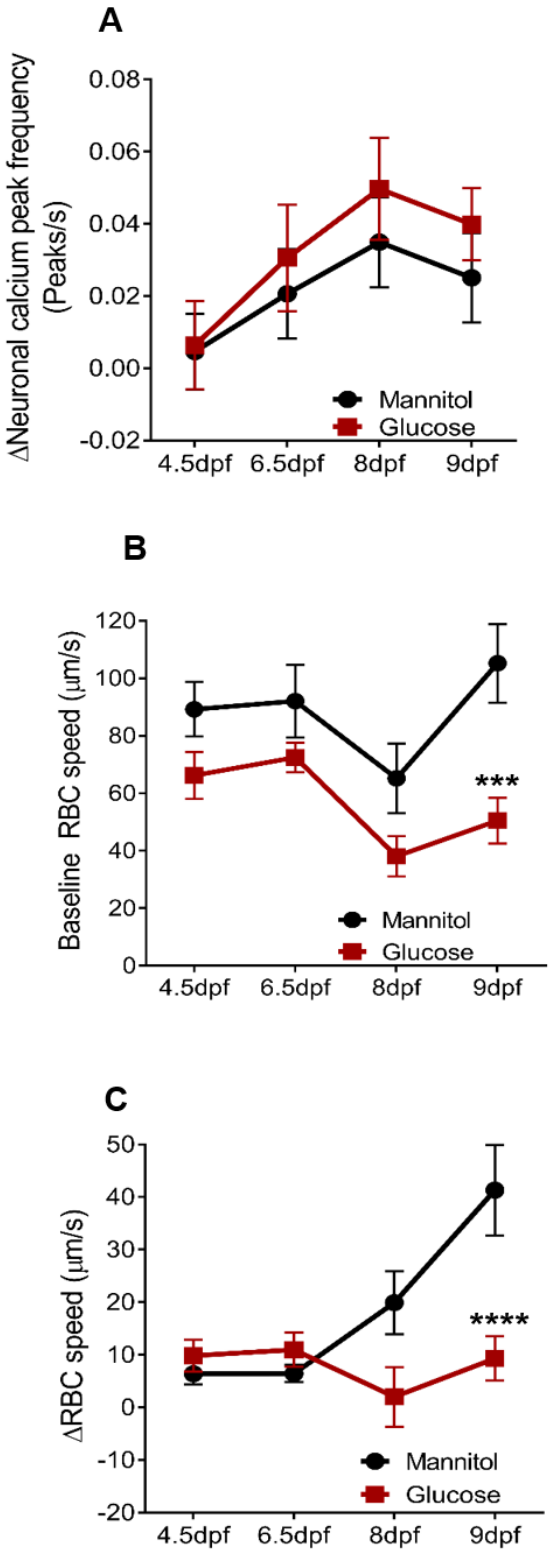

Figure 4-8**: Effect of glucose treatment on neurovascular coupling. A:** Change in neuronal calcium peak frequency in the left optic tectum during response compared to baseline periods (n=17, 17, 15 and 20 for 12h, 60h, 96h and 120h exposure, respectively). **B:** Baseline RBC speed at the same time points in **A & B. C:** Change in RBC speed (ΔRBC) between baseline and response time periods for the same animals as **A.** Data in **A-C** are mean ± s.e.m. ***p<0.001, ****p<0.0001 (two-way ANOVA).

4.4 The nitric oxide donor (0.1mM SNP) ameliorates 20mM glucose induced impairment in neurovascular coupling and cerebrovascular patterning

Various studies have shown reduced bioavailability of NO in ECs to be associated with diabetes. I therefore examined the effect of the NO donor SNP on NVC and cerebrovascular patterning. For this, I co-treated larvae with 0.1 mM SNP and glucose/mannitol from 8-9 dpf (24 h) (**Figure 4-9A**). Representative micrographs are shown in **Figure 4-9B**.

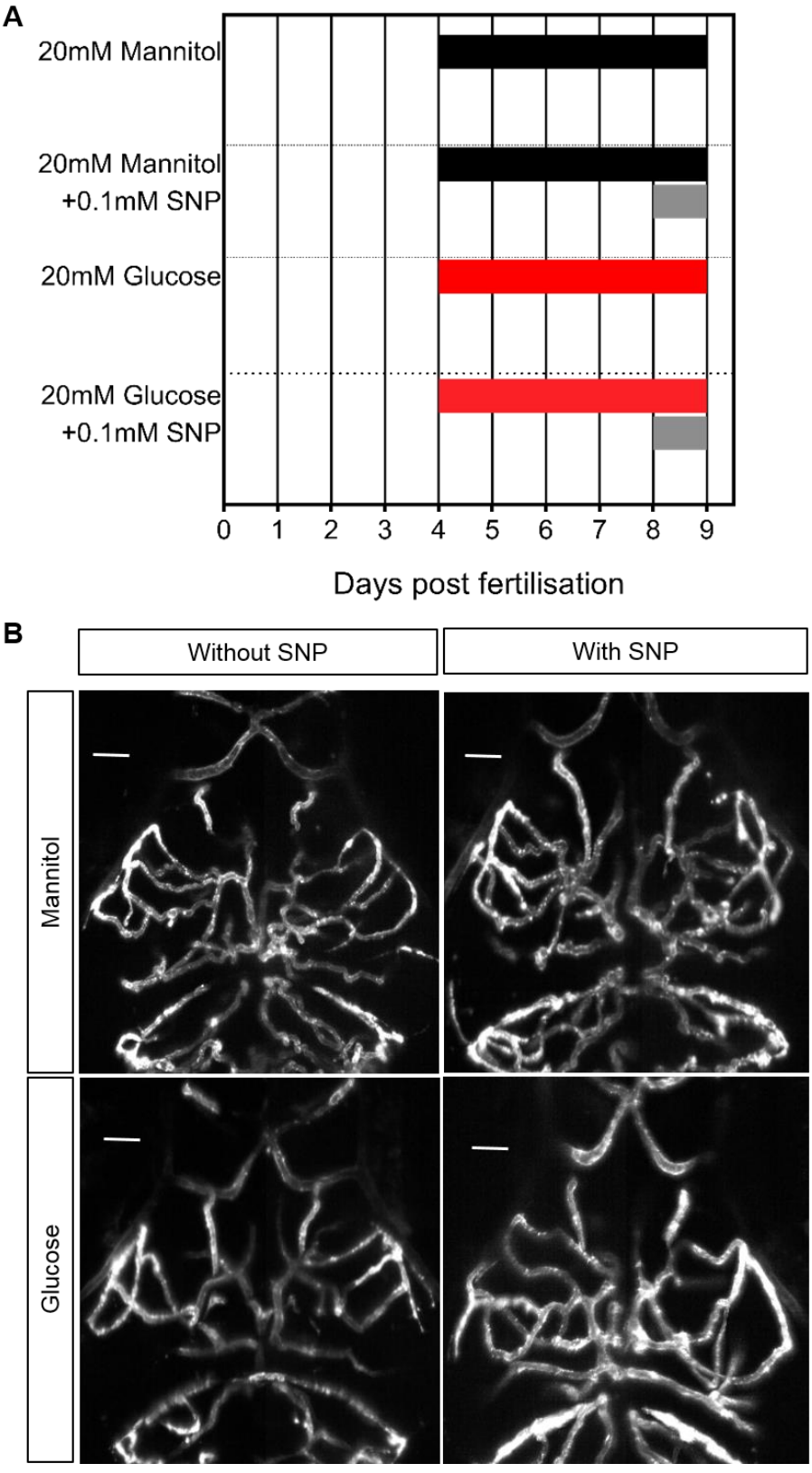

Figure 4-9: Mannitol/Glucose treatment with/without SNP treatment. A: Gantt chart showing the duration of mannitol, glucose and SNP treatment**. B:** Representative micrographs of cerebral vessels in larvae exposed to mannitol/glucose co-treated with/without SNP. Scale bar represents 20 µm.

SNP (plus mannitol) does not affect cerebrovascular patterning as shown by no statistically significant differences between tectal branch points, vascular length and vessel radii (**Figure 4-10A-C**). However, co treatment of SNP with glucose prevented the deleterious effects on cerebrovascular patterning as can be seen in **Figure 4-10D**.

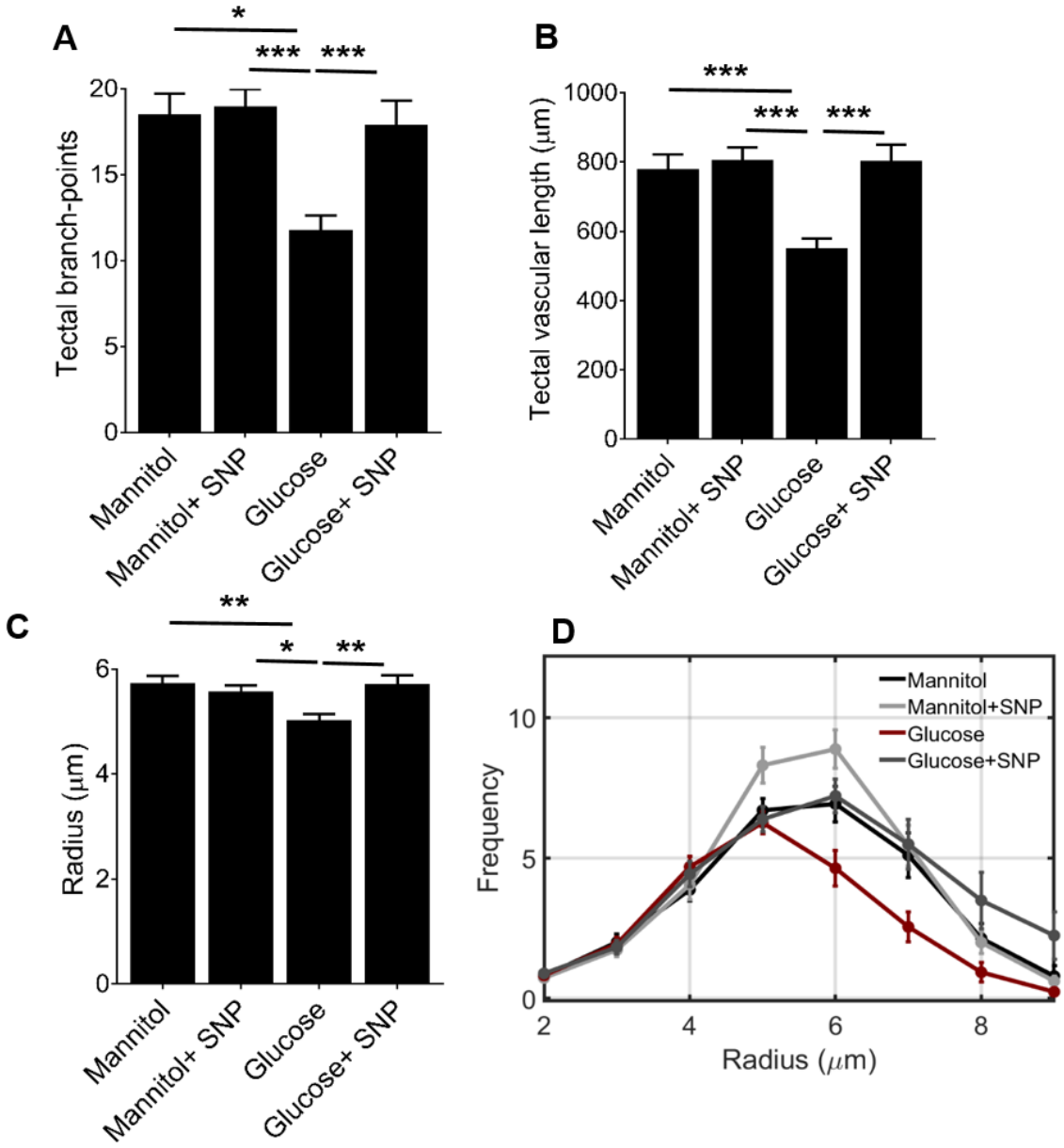

Figure 4-10: Sodium Nitroprusside reverses the effect of glucose exposure on cerebrovascular patterning. A: Quantification of number of tectal vascular branch points in all groups (n=23 larvae/group). **B:** Quantification of total tectal vessel length in same animals as in **A. C:** Mean tectal vessel radius for the same animals as in A (n=23 larvae/group). **D:** Histogram of radii of vessels in the left optic tectum in the same animals as in **A.** Data in **A-D** are mean ± s.e.m. *p<0.05, **p<0.01 and ***p<0.001 (one-way ANOVA).

I further quantified the effect of SNP on NVC (**Figure 4-11A-D**) and observed no significant differences in neuronal calcium between any of the groups (**Figure 4-12A-B**). However, decrease in baseline RBC speed and neurovascular uncoupling observed in glucose exposed larvae was reversed by co treatment with SNP (**Figure 4-12A-B**), thus restoring NVC.

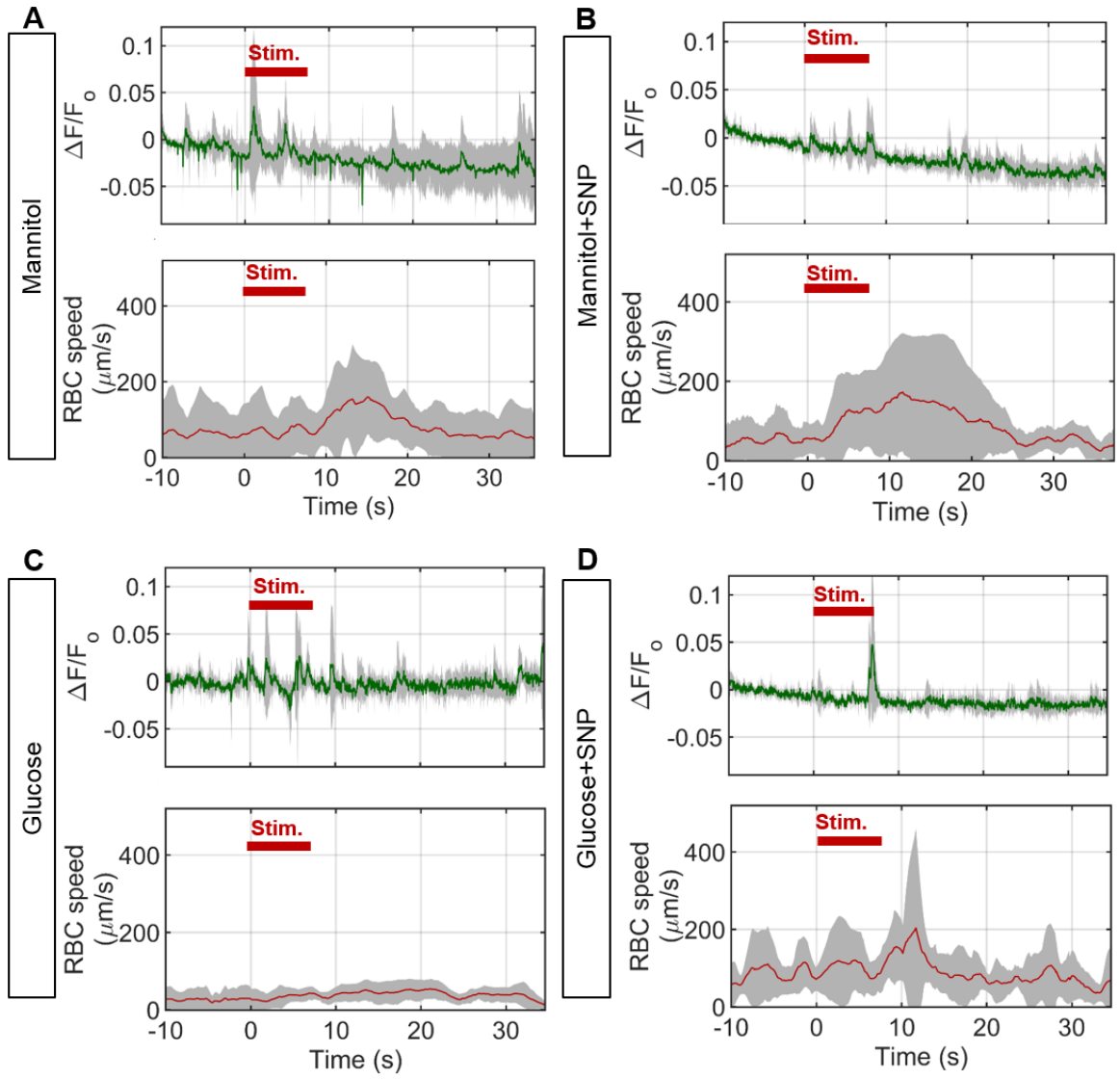

Figure 4-11: Time series of neuronal activation ($\Delta F/F_0$) and tectal vessel RBC speed in zebrafish (5 larvae/group) exposed to; **A:** 20mM mannitol for 120h from 4-9 dpf **B:** 20mM mannitol for 120h from 4-9 dpf and 0.1mM SNP for 24h from 8-9 dpf. **C:** 20mM Glucose for 120h from 4-9 dpf. **D:** 20mM glucose for 120h from 4-9 dpf and 0.1mM SNP for 24h from 8-9 dpf. Visual stimulus is delivered for 0-8s shown by red bar on the graphs**.** Data in **A-D** is mean ± s.d.

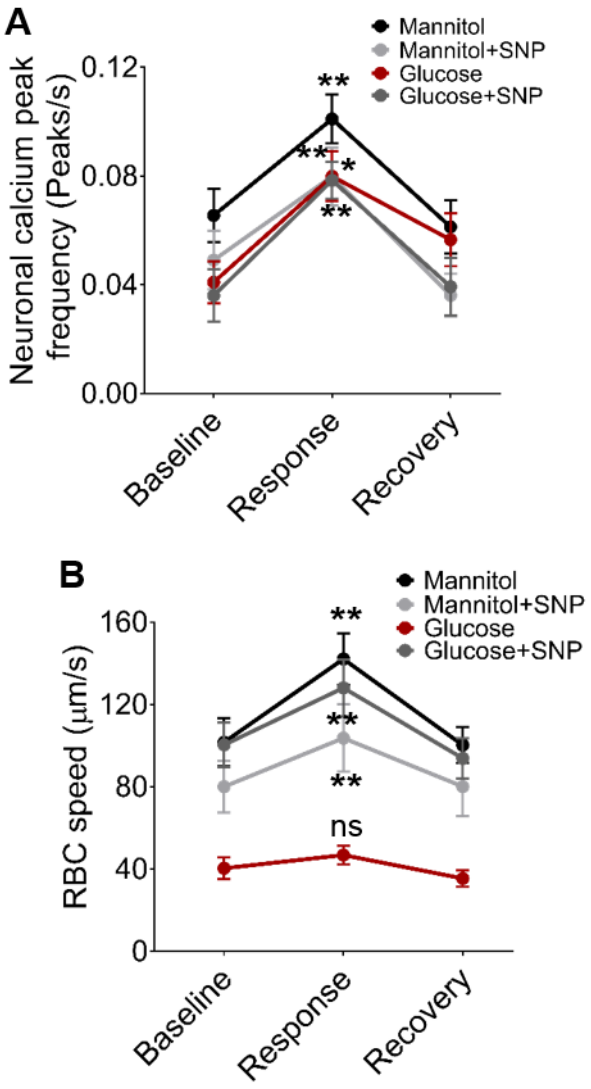

Figure 4-12: Sodium Nitroprusside reverses the effect of glucose on neurovascular coupling. **A:** Frequency of peaks of neuronal activation during baseline, response and recovery time periods in mannitol or glucose exposed larvae with or without co-treatment with 0.1mM SNP (n=20 larvae/group). **B:** RBC speed for baseline, response and recovery for same animals in **A.** Data in **A** and **B** are mean ± s.e.m. *p<0.05, **p<0.001, ****p<0.0001 (two-way ANOVA).

4.5 20mM mannitol/glucose with or without 0.1mM SNP does not affect heart rate

To assess the systemic cardiovascular effects of the treatments used I measured heart rate using the method described earlier (**Figure 4-13**). I found no statistically significant differences between groups treated with mannitol or glucose with/without SNP (**Figure 4-13**). This suggests the preventative effect of SNP was not mediated by systemic effects on cardiac function.

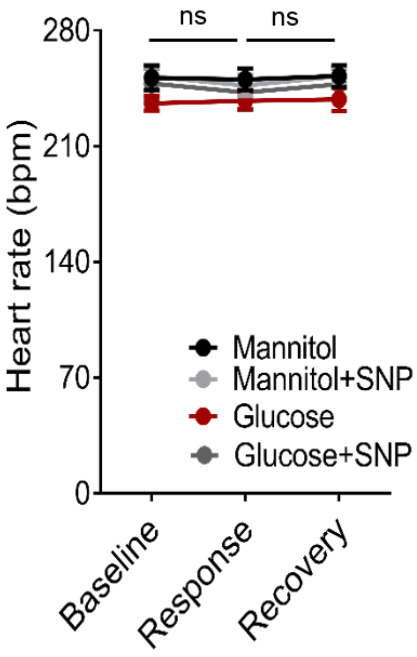

Figure 4-13: Beating heart rate quantified as beats per minute (bpm) for baseline, response and recovery time periods for larvae exposed to 20mM mannitol, 20mM glucose with or without SNP treatment. Data is mean ± s.e.m (RM-ANOVA).

4.6 The effect of glucose with and without SNP on vascular nitric oxide reactivity

Various studies have shown diabetes to be associated to reduced bioavailability of NO (377). Due to the transient nature of NO, dyes such as DAF-FM are used to detect NO reactivity in live zebrafish and cell culture (378). I thus used DAF-FM staining to examine whether glucose exposure reduces NO in the tectal vessels and the effect of SNP co-treatment. DAF-FM showed a marked reduced fluorescence intensity in the vessels in glucose-exposed compared to mannitol treated larvae (**Figure 4-14**). SNP co-treatment with mannitol has no effect compared to mannitol alone whereas co-treatment with glucose increases the vascular green channel intensity compared to glucose alone treated larvae (**Figure 4-14**). This confirms a reduction in NO reactivity by exposure to glucose which SNP is able to rescue by raising vascular NO levels.

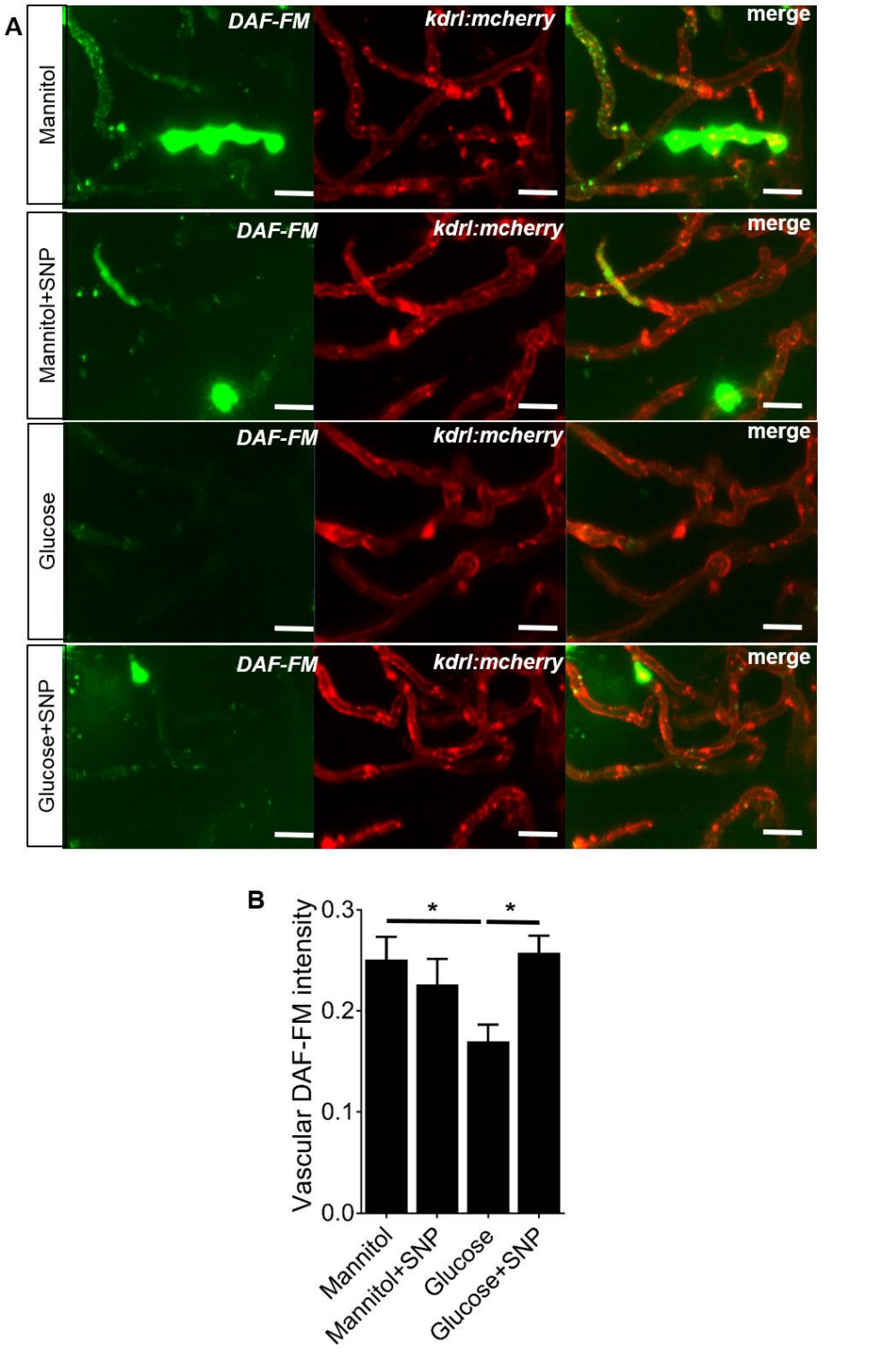

Figure 4-14: Effect of mannitol/glucose treatment on NO reactivity, quantified by intensity of DAF-FM staining. A: Representative micrograph of tectal vessels showing separate and merged channels (green channel: DAF-FM staining, red channel: *kdrl:mcherry*) for 20mM mannitol or glucose exposed larvae co-treated with or without SNP. **B:** Quantification of the DAF-FM intensity in the tectal vessels for 20mM mannitol or glucose exposed larvae co-treated with or without SNP (n=25, 24, 27 and 24 larvae for mannitol, mannitol + SNP, glucose and glucose + SNP, respectively). Scale bar represents 20 µm. Data in **B** is mean ± s.e.m. *$p<0.05$ (one-way ANOVA).

4.7 The effect of glucose with or without SNP treatment on *klf2a: GFP* reporter expression

Studies have shown upregulation of endothelial *klf2a* by shear stress (379). Shear stress sensing is an important function of the ECs and is abnormal in pathologies such as atherosclerosis (380). However, it is not well understood if it is affected in hyperglycemia. Using *Tg(klf2a:GFP)* larvae, I repeated the same protocol of mannitol or glucose exposure with or without SNP co-treatment. Glucose exposure reduced *klf2a:GFP* intensity compared to mannitol (**Figure 4-15**). Co-treatment with SNP and glucose restored *klf2a:GFP* intensity (**Figure 4-15**). Since it is not known if NO could modulate expression of *klf2a*, this suggests the effect of SNP in recovering the expression could be secondary to its effect on RBC speed. However, this needs further investigation if NO could directly target *klf2a* expression.

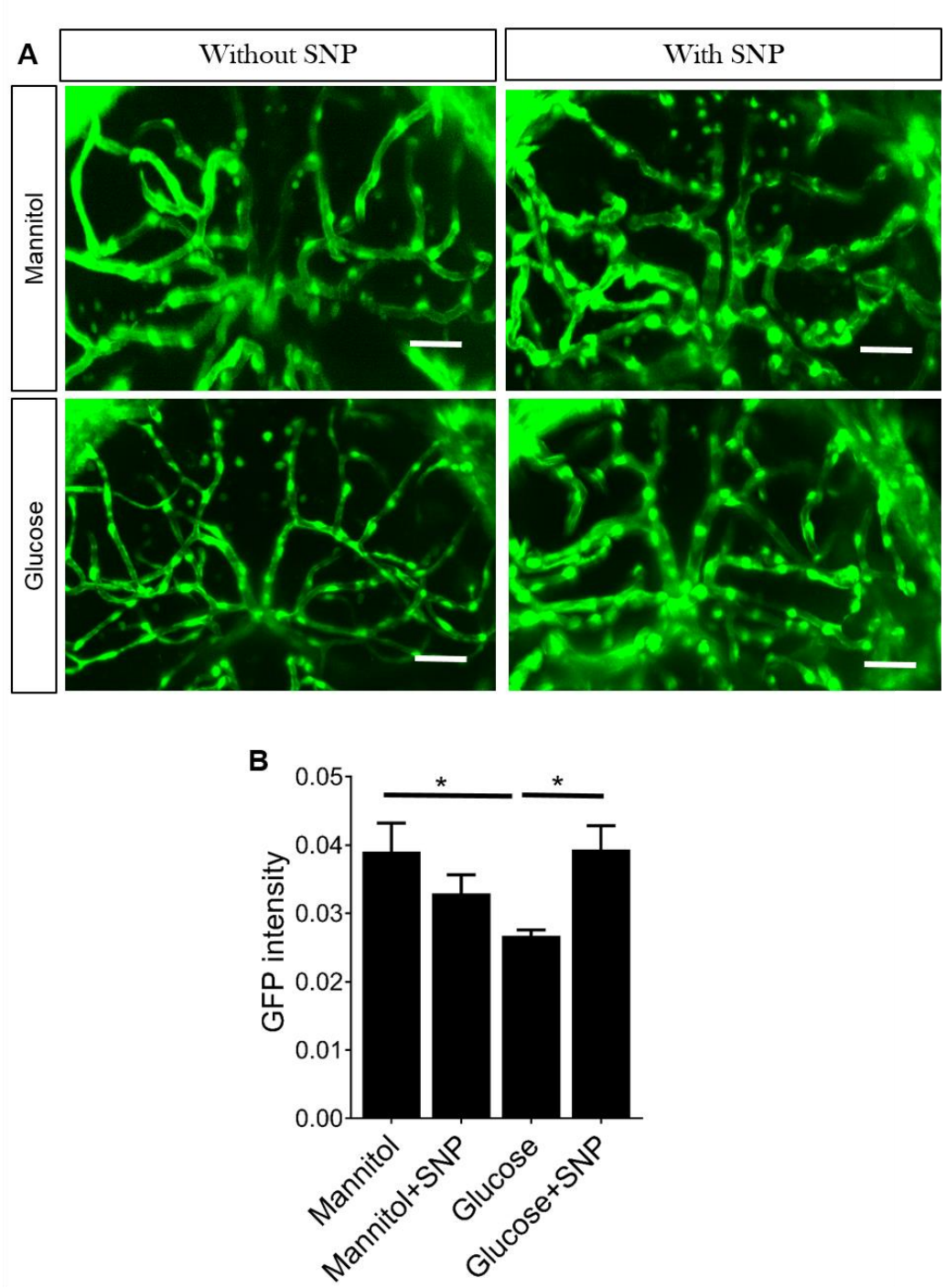

Figure 4-15: Effect of mannitol/glucose treatment with/without SNP on expression of *klf2a:GFP* expression. A: Representative micrograph of tectal vessels in *Tg(klf2a:GFP)* exposed to 20mM mannitol or glucose co-treated with or without SNP. **B:** Quantification of the *klf2a:GFP* intensity in the tectal vessels for 20mM mannitol or glucose exposed larvae co-treated with or without SNP (n=26 larvae/group). Scale bar represents 20 µm. Data in **B** is mean ± s.e.m. *p<0.05 (one-way ANOVA).

4.8 The effect of glucose with or without SNP treatment on *claudin5a: GFP* reporter expression

Multiple reports have shown BBB to be affected in ageing and dementia (381, 382). Few studies have also shown BBB pathologies in diabetes (383). I therefore tested the effect of glucose exposure on BBB permeability using a novel transgenic zebrafish model expressing *claudin5a* as a marker of BBB development (326). Representative micrographs of *Tg(claudin5a:GFP;kdrl:HRAS-mcherry)* are shown in **Figure 4-16**. Similarly to the *klf2a* reporter, glucose exposure reduced vascular *claudin5a:GFP* expression which was restored by co-treatment with SNP (**Figure 4-16B**).

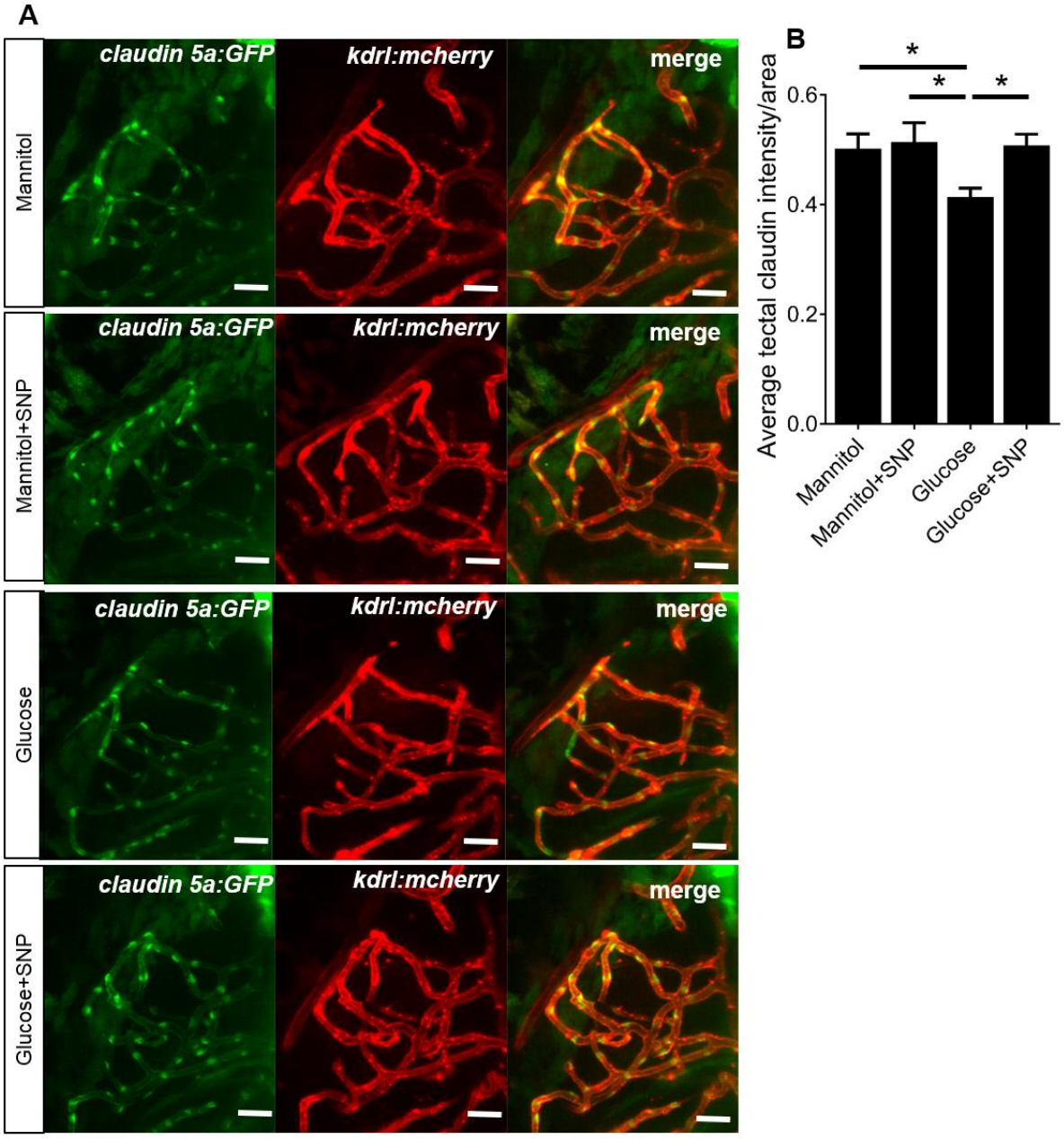

Figure 4-16: Effect of mannitol/glucose treatment with/without SNP treatment on *claudin5a:GFP* expression. A: Representative micrograph of tectal vessels showing separate and merged channels (green channel: *claudin5a:GFP*, red channel: *kdrl:mcherry*) for 20mM mannitol or glucose exposed larvae co-treated with or without SNP. **B:** Quantification of the *claudin5a:GFP* intensity in the tectal vessels for 20mM mannitol or glucose exposed larvae co-treated with or without SNP (n=21,20,18 and 23 larvae for mannitol, mannitol + SNP, glucose and glucose + SNP, respectively). Scale bar represents 20 µm. Data in **B** are mean ± s.e.m. *p<0.05 (one-way ANOVA).

4.9 Glucose exposure reduced the number of *sm22ab:mcherry^{s441}* labelled nuclei on the tectal vessels which was restored by SNP co-treatment

Smooth muscle cell protein 22 (*sm22*) is known to be expressed in contractile mural cells (384). Pericytes have been shown to be contractile and to express smooth muscle cell actin and desmin (385). As discussed in **chapter 1,** few studies have demonstrated increased pericyte migration in diabetes (79) and recent advances have shown pericytes to be involved in NVC (82). Since I observed neurovascular uncoupling in glucose exposed larvae, I therefore examines pericyte function in zebrafish with mannitol/glucose with or without SNP co-treatment. Pericytes are not well characterised in zebrafish. Using a novel transgenic line developed by Dr. Rob Wilkinson, *Tg(sm22ab:mcherry^{s441})* I quantified the number of mural cells (pericytes/VSMCs) on the tectal vessels (480 x 360 x 54 μm^3) in embryos exposed to glucose or mannitol with or without co-treatment with SNP. Glucose exposure induced a statistically significant reduction in the *sm22ab:mcherry ^{s441}* labelled nuclei on the tectal vessels suggesting a reduction in the mural cells (pericytes/VSMCs) which was rescued by SNP co-treatment (**Figure 4-17B**).

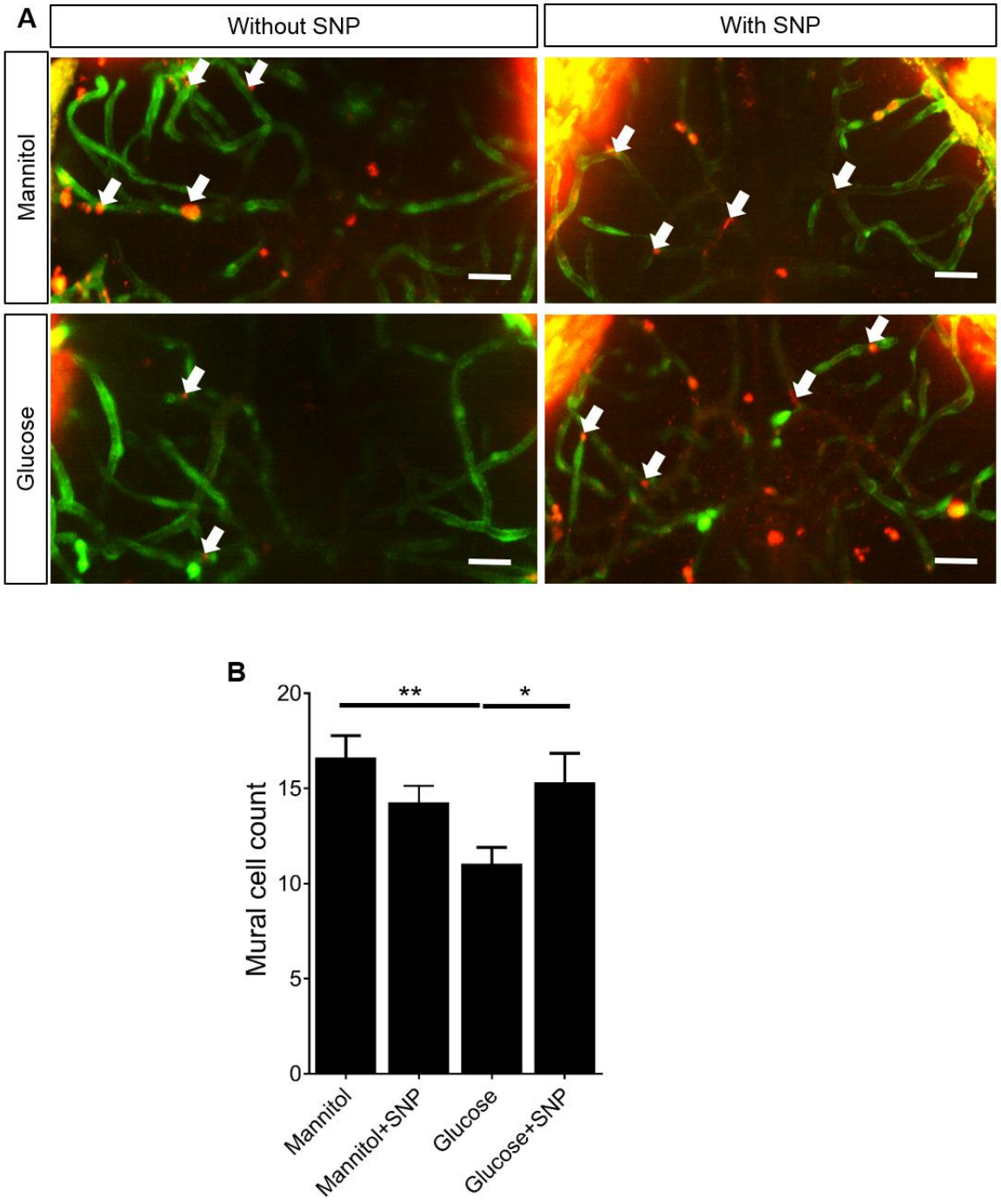

Figure 4-17: Effect of mannitol/glucose treatment ± SNP on mural cell count on the tectal vessels. **A:** Representative micrograph of tectal vessels showing separate and merged channels (green channel: *fli1:GFF:UAS:GCaMP6f*, red channel: *sm222ab:mcherry*^{s441}) for 20mM mannitol or glucose exposed larvae co-treated with or without SNP. **B:** Quantification of the number of *sm22ab:mcherry*^{s441} nuclei on the tectal vessels for 20mM mannitol or glucose exposed larvae co-treated with or without SNP (n=28 larvae/group). Scale bar represents 20 µm. Data in **B** is mean ± s.e.m. *p<0.05, **p<0.01 (one-way ANOVA).

4.10 The effect of glucose with or without SNP treatment on *iGluSnFr* reporter intensity

Multiple reports have suggested zebrafish possess radial glial cells with astrocyte-like characteristics such as presence of glutamate transporters and aquaporin channels (314, 386) as described earlier (**section 1.13.2**). The role of glial cells in NVC is still under debate however there are studies suggesting in mammalian models suggesting glial dysfunction in diabetes (as discussed in **section 1.6.3**). I therefore sought to examine the effect of glucose exposure on astroglial structures in 9 dpf old zebrafish. Using a novel transgenic line that indicates glial glutamate signalling by expressing *iGluSnFR* driven by GFAP, I quantified intensity of *iGluSnFR* in the teO of zebrafish larvae exposed to mannitol or glucose with or without SNP treatment (**Figure 4-18A**). Glucose exposure induced a statistically significant reduction of *iGluSnFR* intensity in the teO compared to mannitol (**Figure 4-18B**). Co-treatment with SNP resulted in recovery of *iGluSnFR* intensity compared to glucose alone (**Figure 4-18B**).

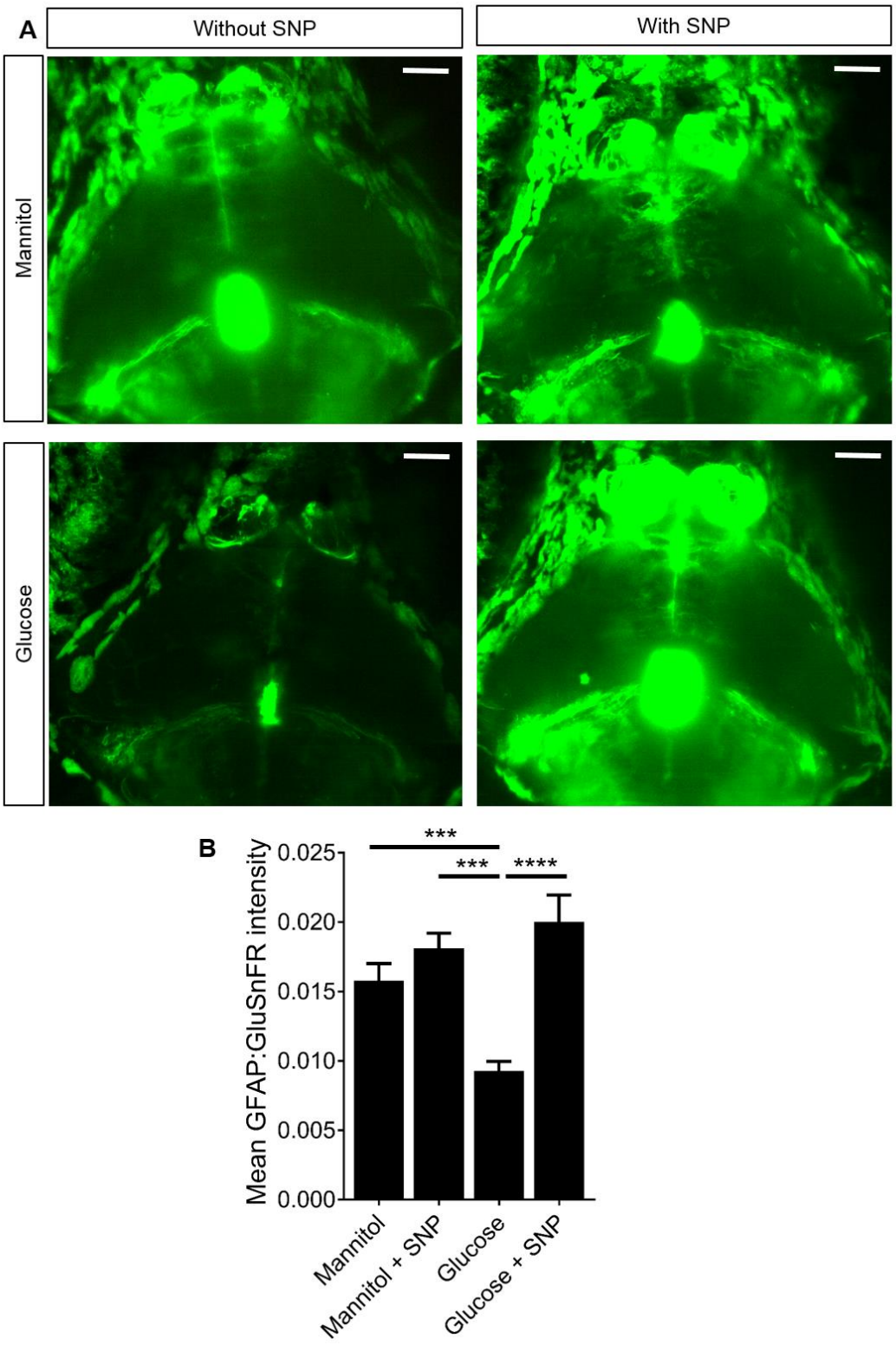

Figure 4-18: Effect of mannitol/glucose treatment on *GFAP:iGluSnFR* intensity in the tectum. A: Representative micrograph of optic tectum in *Tg(GFAP:iGluSnFR)* for 20mM mannitol or glucose exposed larvae co-treated with or without SNP. **B:** Quantification of *iGluSnFR* intensity in the optic tectum for 20mM mannitol or glucose exposed larvae co-treated with or without SNP (n=32,30,28 and 29 larvae for mannitol, mannitol + SNP, glucose and glucose + SNP, respectively). Scale bar 20µm. Data in **B** is mean ± s.e.m. ***p<0.001, ****p<0.0001 (one-way ANOVA).

Glutamine synthetase (GS) is an astroglial-specific enzyme which converts glutamate released by neurons to glutamine (386, 387). Using IHC, I examined the effect of glucose exposure with or without SNP on expression of GS in the teO of 9 dpf old zebrafish. Glucose exposure reduced expression of GS compared to mannitol (**Figure 4-19** and **Figure 4-20**). Co-treatment of SNP with mannitol had no effect however co-treatment of glucose with SNP increases the tectal expression of GS compared to glucose alone (**Figure 4-20** and **Figure 4-21B**). The mechanisms by which increasing NO could improve glial function are not known.

4.11 The effect of glucose with or without SNP treatment on TRPV4 and glutamine synthetase expression

Since hyperglycemia has been shown to downregulate TRPV4 in the ECs of the retinal microvasculature (259). I investigated TRPV4 expression by immunohistochemistry in 9 dpf old zebrafish larvae exposed to glucose or mannitol with or without SNP treatment. I performed immunohistochemistry with combined antibodies for glutamine synthetase (as described in the previous section) to first compare expression patterns in the teO. Glucose exposure decreased overall TRPV4 expression in the tectum (which could include radial glial, endothelial and neuronal expression of TRPV4) compared to mannitol exposed larvae (**Figure 4-20A**). A similar reduction was observed in the glutamine synthetase expression (**Figure 4-20B**). Further, co-treatment of glucose exposed larvae with SNP lead to an increase in the TRPV4 and glutamine synthetase expression in the teO compared to glucose only treated larvae (**Figure 4-19** and **Figure 4-20**).

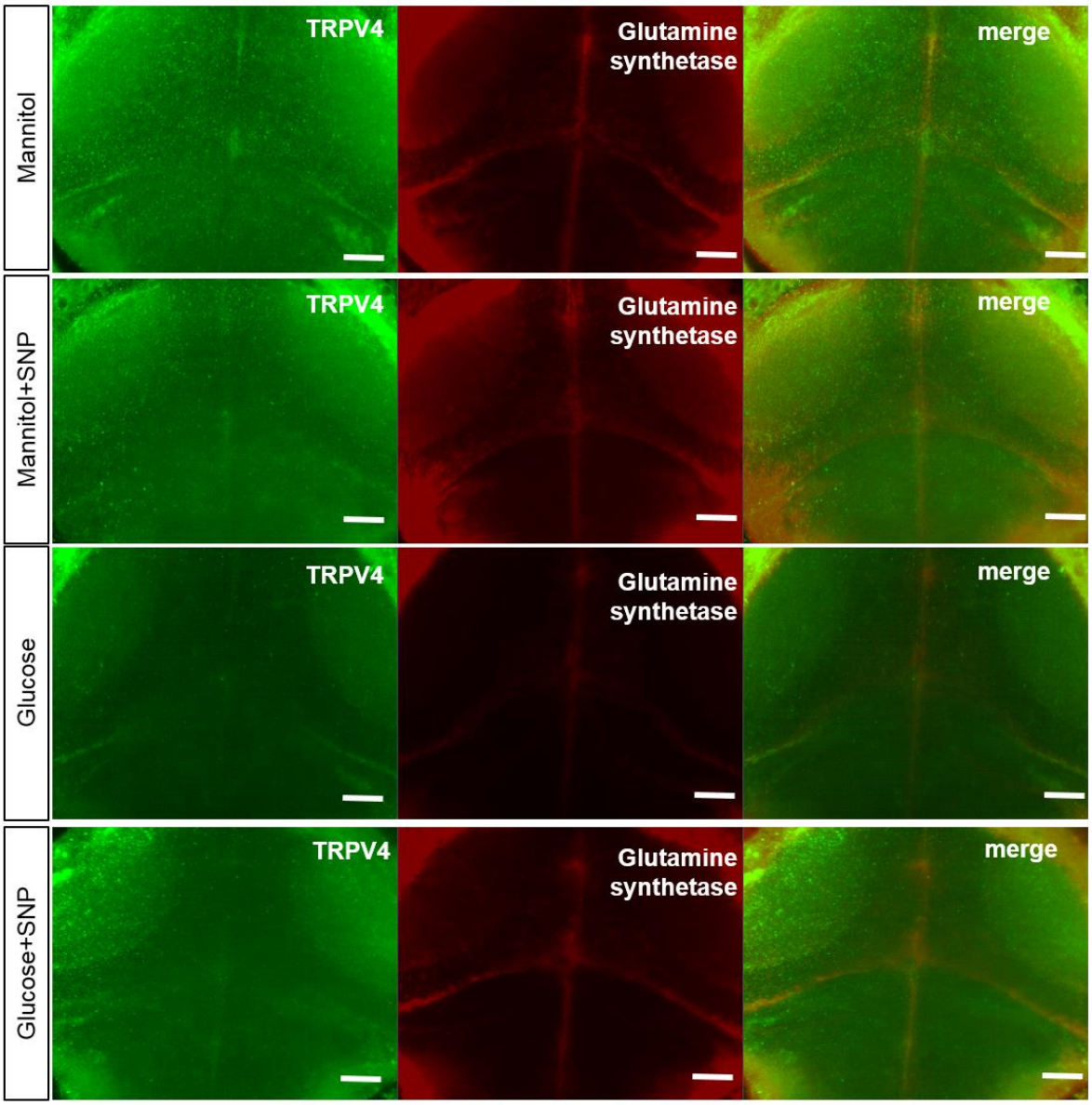

Figure 4-19: Representative micrographs of optic tectum showing the effect of mannitol/glucose treatment with/without SNP treatment on the expression of glutamine synthetase (red channel) and TRPV4 (green channel). Scale bar represents 20 µm.

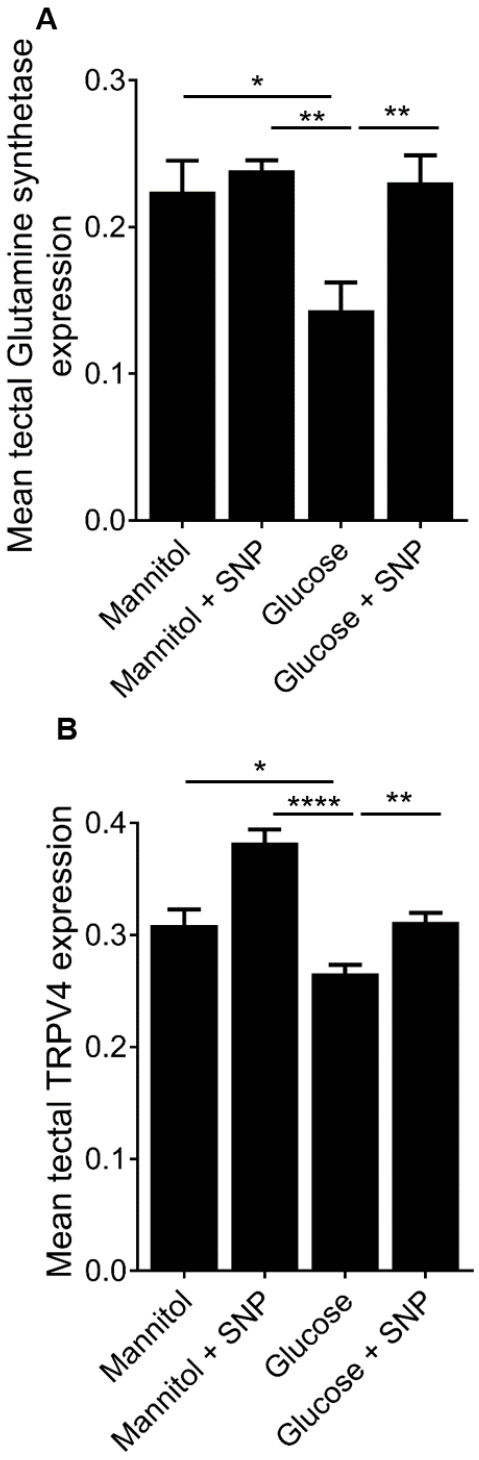

Figure 4-20: Effect of mannitol/glucose exposure on the glutamine synthetase and TRPV4 expression in tectum. Quantification of **A:** TRPV4 and **B:** glutamine synthetase expression in the optic tectum in mannitol/glucose exposed larvae co-treated with/without SNP (n=24, 25, 21 and 27 larvae for larvae for mannitol, mannitol + SNP, glucose and glucose + SNP, respectively). Data in **A** and **B** are mean ± s.e.m. *p<0.05, **p<0.01, ****p<0.0001 (one-way ANOVA).

4.12 The effect of glucose with or without SNP treatment on GFAP expression

Experimental studies have shown reduction in glial function with hyperglycemia and type 1 diabetes, particularly astrogliosis (indicated by over-expression of GFAP) (388). I therefore examined GFAP expression by immunohistochemistry in mannitol or glucose treated animals with or without SNP treatment. Representative micrographs of whole mount 9 dpf old zebrafish stained for GFAP and DAPI are shown in **Figure 4-21**. Glucose exposure increased GFAP expression compared to mannitol, quantified by mean intensity of red fluorescence in the teO (**Figure 4-22**). This was significantly reduced by co-treatment with SNP (**Figure 4-22**).

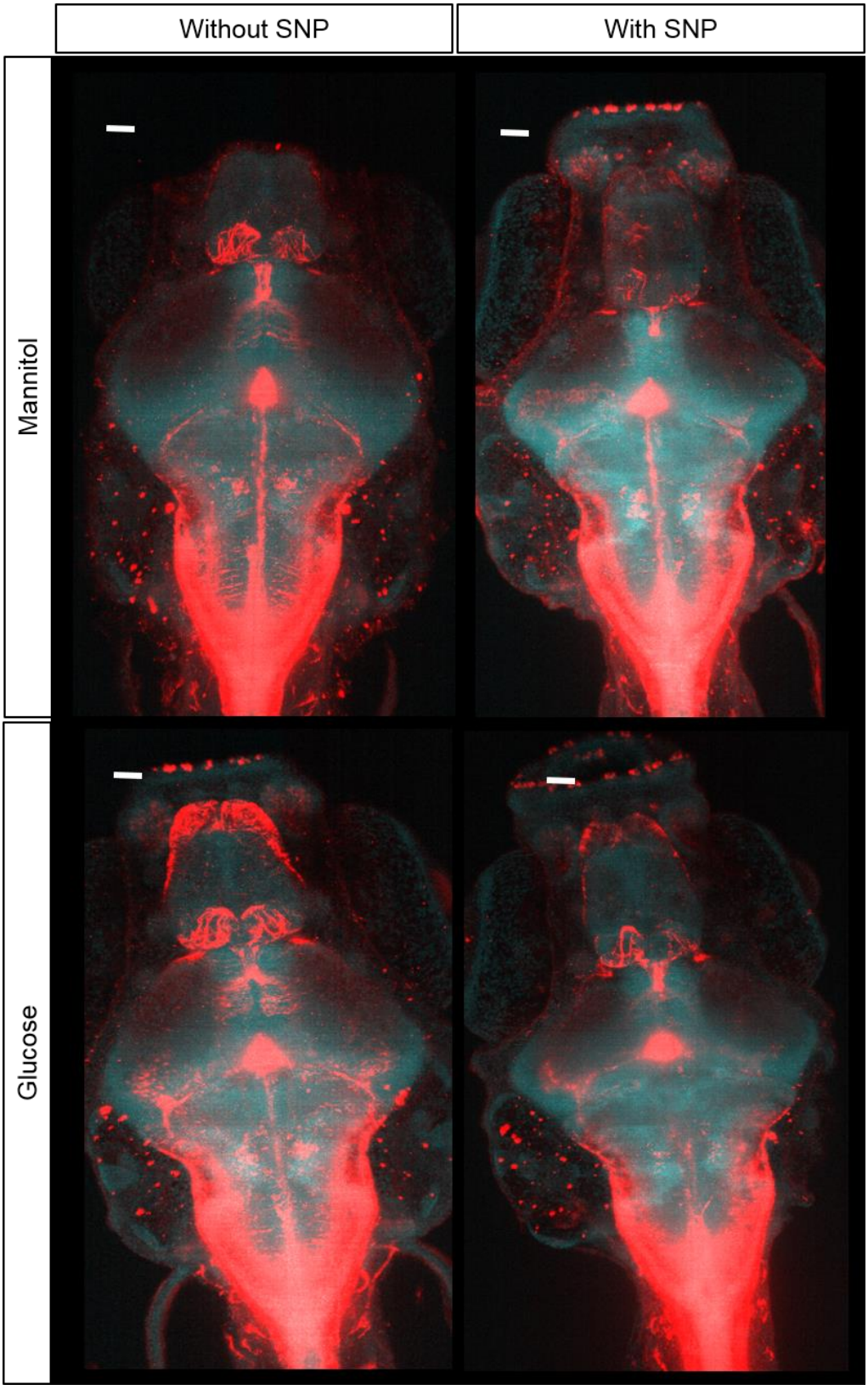

Figure 4-21: Representative micrographs showing the effect of mannitol/glucose exposure with/without SNP treatment on GFAP expression (red channel: GFAP and blue channel: DAPI). Scale bar 20 µm.

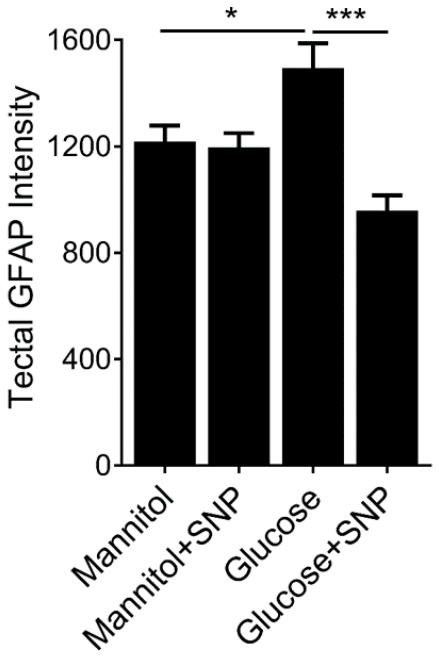

Figure 4-22: Quantification of GFAP expression in the optic tectum in mannitol/glucose exposed group with/without SNP treatment (n=16, 12, 18 and 20 larvae for larvae for mannitol, mannitol + SNP, glucose and glucose + SNP, respectively). Data is mean ± s.e.m. *p<0.05, ***p<0.001 (one-way ANOVA).

4.13 The effect of glucose with or without SNP treatment on locomotion and light/dark preference

In the previous sections, I described various functional and anatomical defects in the NVU induced by glucose exposure and show that SNP is largely able to rescue these. I next examined the effect of glucose exposure on locomotion and behaviour in 9 dpf old zebrafish larvae. Using viewpoint system for larval tracking (as described in **section 2.8**), I first tested for light-dark preference in mannitol or glucose exposed larvae with or without co-treatment with SNP. **Figure 4-23** shows the trajectories of four representative zebrafish larvae for a period of 1 h in each treatment group. Red and green colours mark the high and low speed locomotion, respectively (as described in **section 2.8**). I tested the light dark preference using two measures; percentage of time spent in light and dark side of the well and the ratio of time spent in light vs dark (L/D ratio). Mannitol exposed larvae at 9 dpf showed a preference for light, spending ~80% time in the light and ~20% time in dark (**Figure 4-24A**). Glucose exposure reduced this light-dark preference (**Figure 4-24**) which was rescued by co-treatment with SNP (**Figure 4-24**).

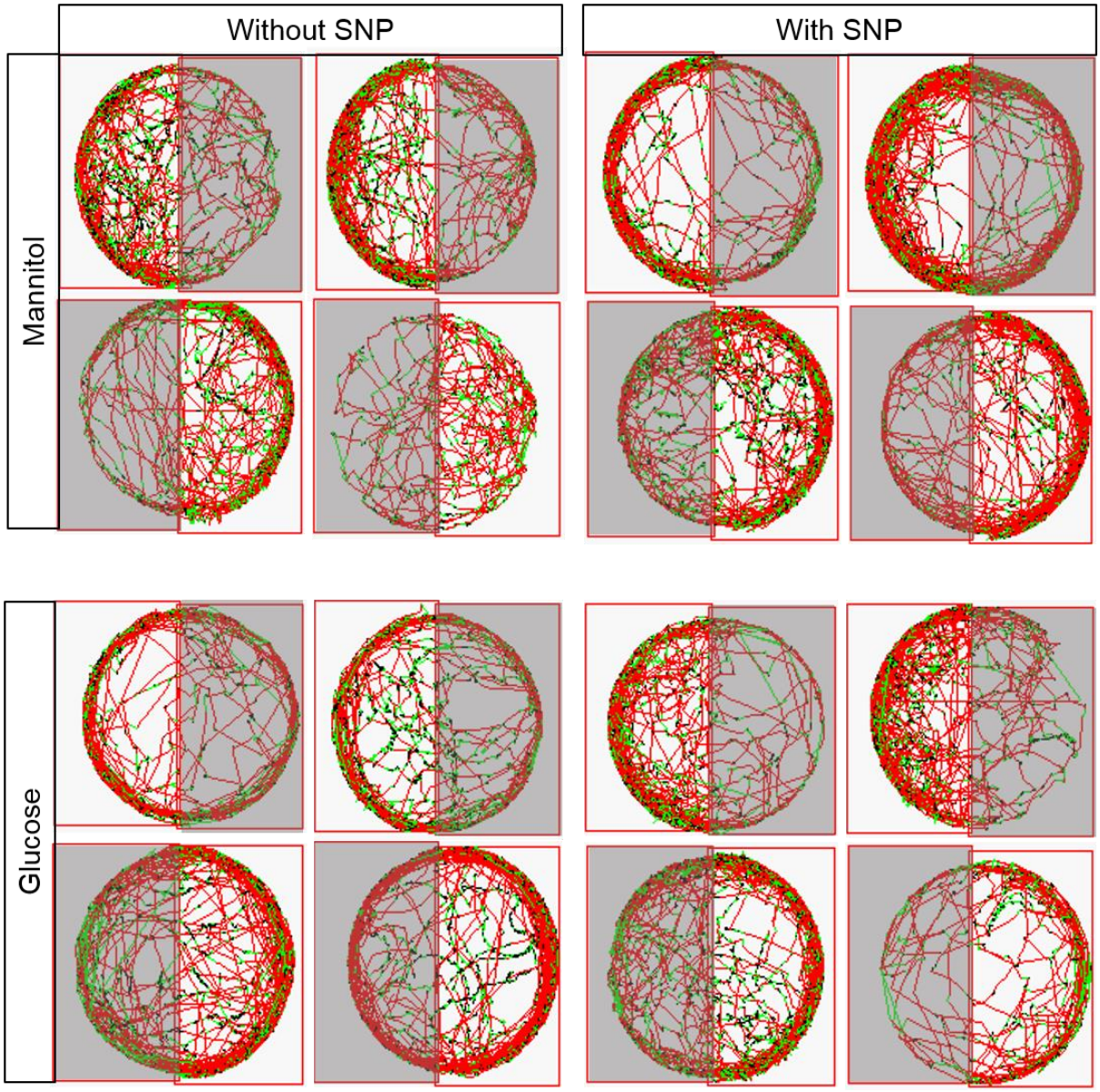

Figure 4-23: Representative trajectories of 9 dpf old zebrafish moving in half darkened wells (of a 12 well plate) as tracked by Viewpoint software for mannitol or glucose with or without SNP treatment. Red trajectories represent high speed locomotion (> 64 mm/s), green represents low speed locomotion (30-64 mm/s) and black marks inactivity (<30 mm/s).

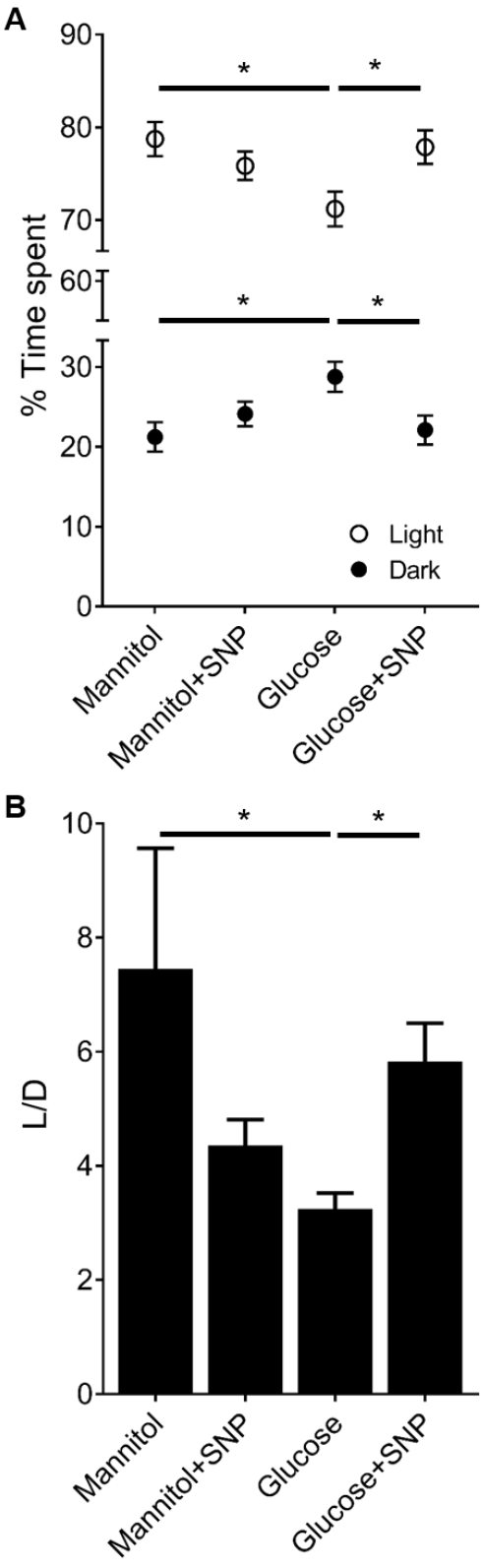

Figure 4-24: Quantification of time spent by zebrafish larvae in light and dark sides of the wells. **A**: Percentage of time spent in light and dark regions of the well by larvae exposed to mannitol or glucose with or without SNP (n = 50, 45, 44 and 56 larvae for mannitol, mannitol+SNP, glucose and glucose+SNP, respectively). **B**: Light/Dark (L/D) ratios for the same animals as in **A.** Data in **A** and **B** are mean ± s.e.m. *$p<0.05$ (one-way ANOVA).

I further investigated the effect on glucose with/without SNP exposure on the time spent in inactivity, low speed and high speed locomotion, in both light and dark regions of the well. I found a significant increase in the time spent in both the low and high speed locomotion in the glucose exposed larvae in the light region of the well with an associated reduction in the time spent inactive (**Figure 4-25**). SNP co-treatment reversed this effect (**Figure 4-25**). Quantifying the time spent in inactivity, I found the glucose exposed larvae show reduced inactivity compared to mannitol exposed larvae (**Figure 4-25**) and that co-treatment with SNP increased the inactivity similar to that observed in the mannitol exposed larvae (**Figure 4-25**). Quantifying the same measures for the dark region of the well, I found similar trends to that seen in light area but these were non-significant (**Figure 4-26**).

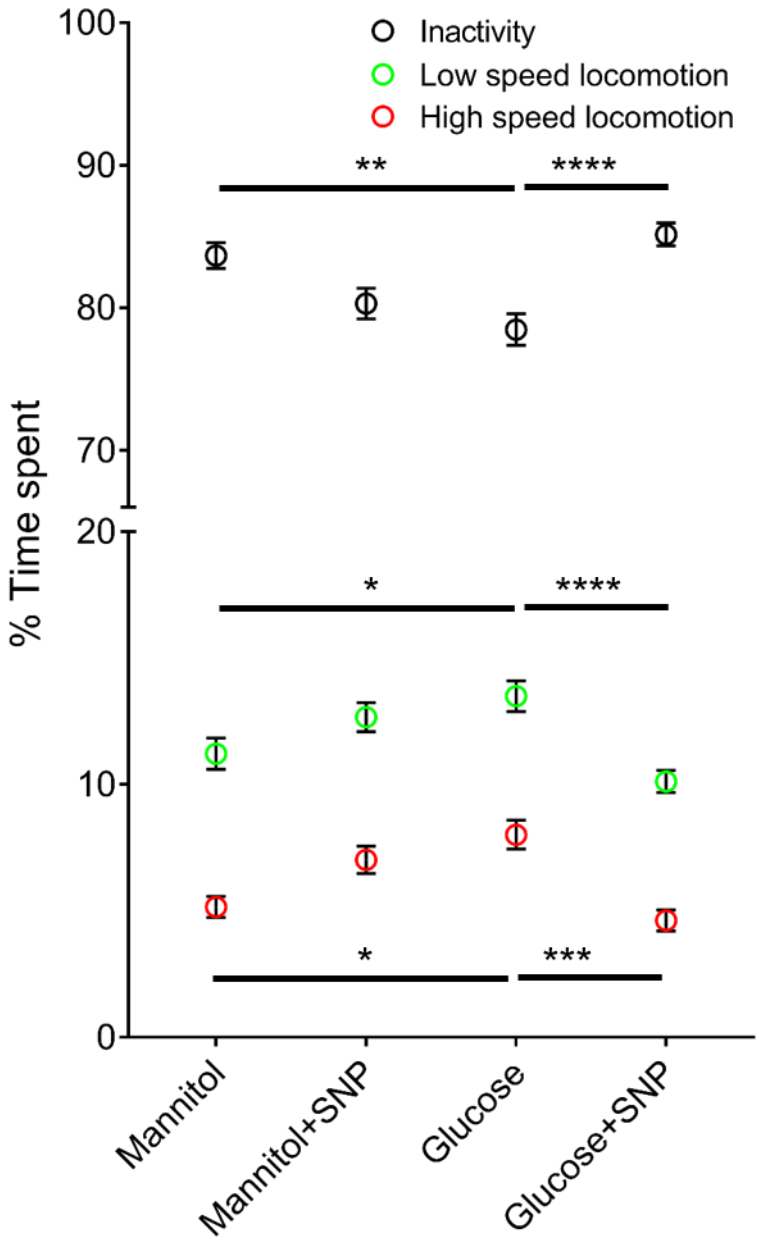

Figure 4-25: Quantification of percentage time spent in inactivity, low and high speed locomotion in the light region by the same animals as in Figure 4-24 (n = 50, 45, 44 and 56 larvae for mannitol, mannitol+SNP, glucose and glucose+SNP, respectively). Data is mean ± s.e.m. *p<0.05, **p<0.01, ***p<0.001 and ****p<0.0001 (one-way ANOVA for different speed groups).

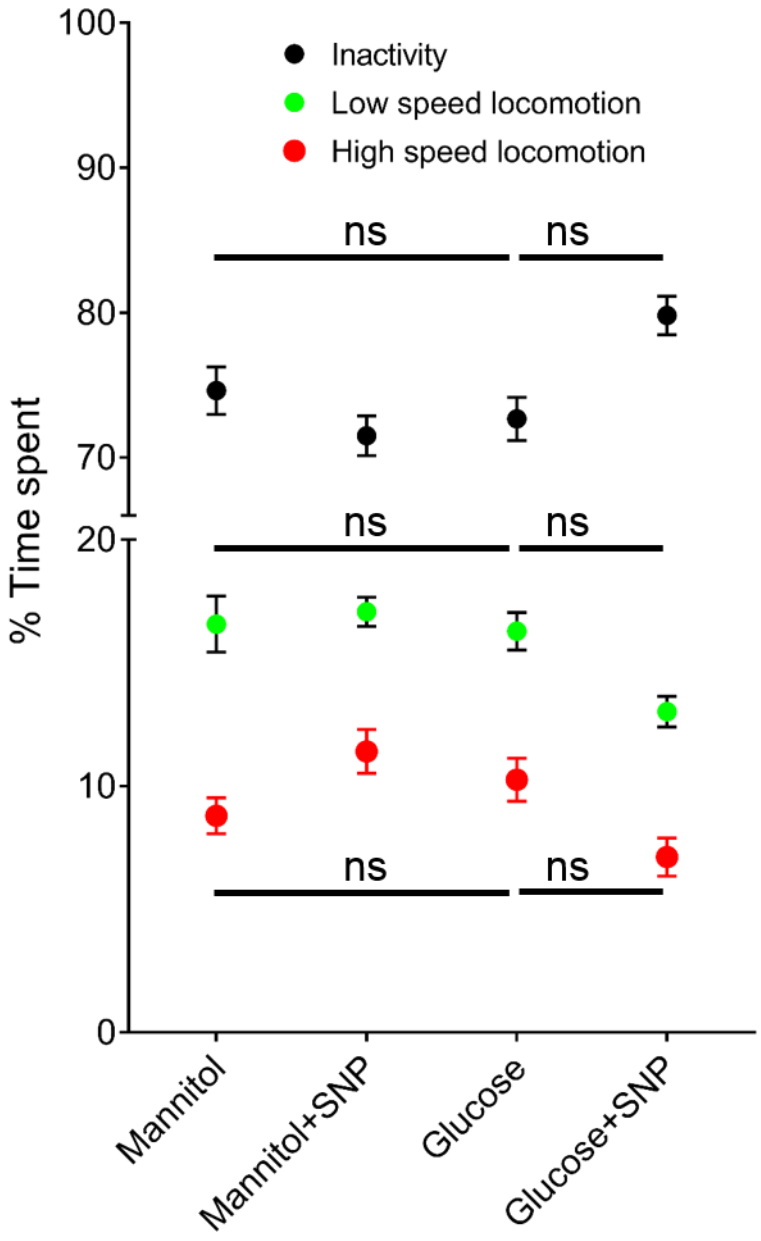

Figure 4-26: Quantification of percentage time spent in inactivity, low and high speed locomotion in the dark region by the same animals as in Figure 4-25 (n = 50, 45, 44 and 56 larvae for mannitol, mannitol+SNP, glucose and glucose+SNP, respectively). Data is mean ± s.e.m. *p<0.05, **p<0.01, ***p<0.001 and ****p<0.0001 (one-way ANOVA for different speed groups).

4.14 Increase in the baseline neuronal calcium activity with glucose treatment is normalized by co-treatment with SNP

Various clinical and experimental studies have shown associations between hyperglycemia and seizures (389). There are no precise mechanisms described as to how hyperglycemia or any diabetes pathology could result in neuronal hyperexcitability. I therefore tested the occurrence neuronal calcium peaks without any light stimulation to observe baseline neuronal firing activity. Representative time series of baseline neuronal firing in larvae exposed to mannitol or glucose with or without SNP quantified as $\Delta F/F_o$ are shown in **Figure 4-27A**. I found glucose exposure increased baseline firing activity compared to mannitol (**Figure 4-27B**). Co-treatment with SNP and glucose reduced neuronal calcium peak frequency compared to glucose alone (**Figure 4-27B**). This suggests NO could be also a key factor in modulating the excitability of neurons.

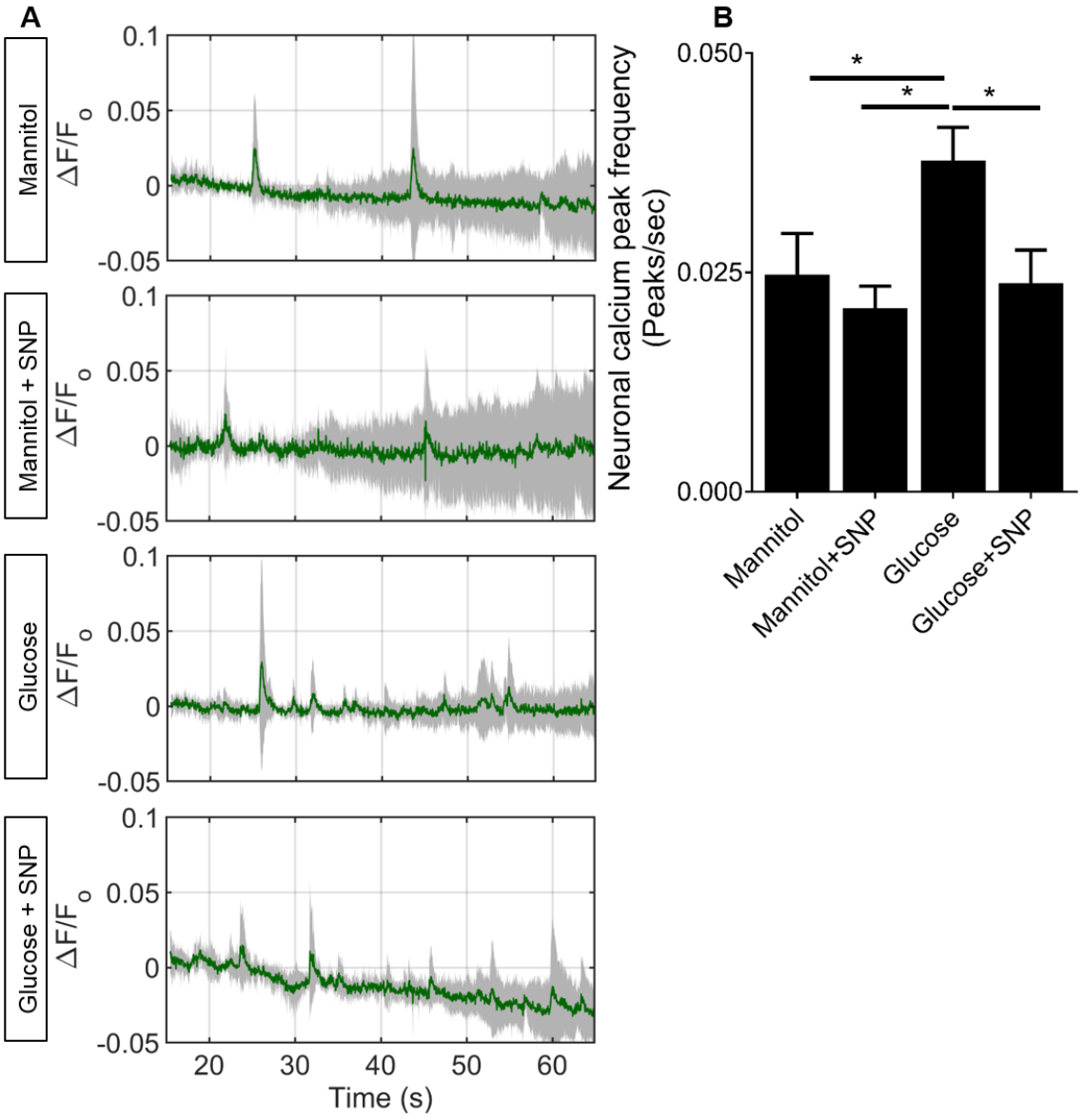

Figure 4-27: Effect of mannitol/glucose treatment with/without SNP on baseline neuronal calcium peak frequency. A: Time series of neuronal activation ($\Delta F/F_o$ in zebrafish (5 larvae/group) exposed to (left: top to bottom); 20mM mannitol for 120h from 4-9 dpf, 20mM mannitol for 120h from 4-9 dpf and 0.1mM SNP for 24h from 8-9 dpf, 20mM Glucose for 120h from 4-9 dpf and 20mM glucose for 120h from 4-9 dpf and 0.1mM SNP for 24h from 8-9 dpf. **B:** Quantification of neuronal calcium peak frequency for each of the groups (n=28 larvae/group). Data is mean ± s.d. in **A** and mean ± s.e.m. *p<0.05 (one-way ANOVA)

Kim et al., (160) proposed that vascular tone can decrease neuronal firing through astrocyte TRPV4 activation, thereby suggesting a way of vascular control of neuronal activity. I have described earlier the glucose exposure decreases the vessel thickness (**section 4.3**), RBC speed (**section 4.3**) and TRPV4 expression (**section 4.12**). This suggests that the increase in neuronal calcium peak frequency induced by glucose exposure could also be associated with a decrease in TRPV4 expression, on the lines of vasculoneuronal coupling (160). To investigate if increases in neuronal firing could be mediated by TRPV4, I quantified neuronal calcium peak frequency with and without treatment with a TRPV4 antagonist III (24 h treatment). Representative time series of neuronal firing in controls (E3) and TRPV4 antagonist treated larvae are shown in **Figure 4-28A.** I found larvae exposed to the TRPV4 antagonist had statistically significant higher neuronal calcium peak frequency (**Figure 4-28**) similar to glucose exposed larvae (**Figure 4-28**).

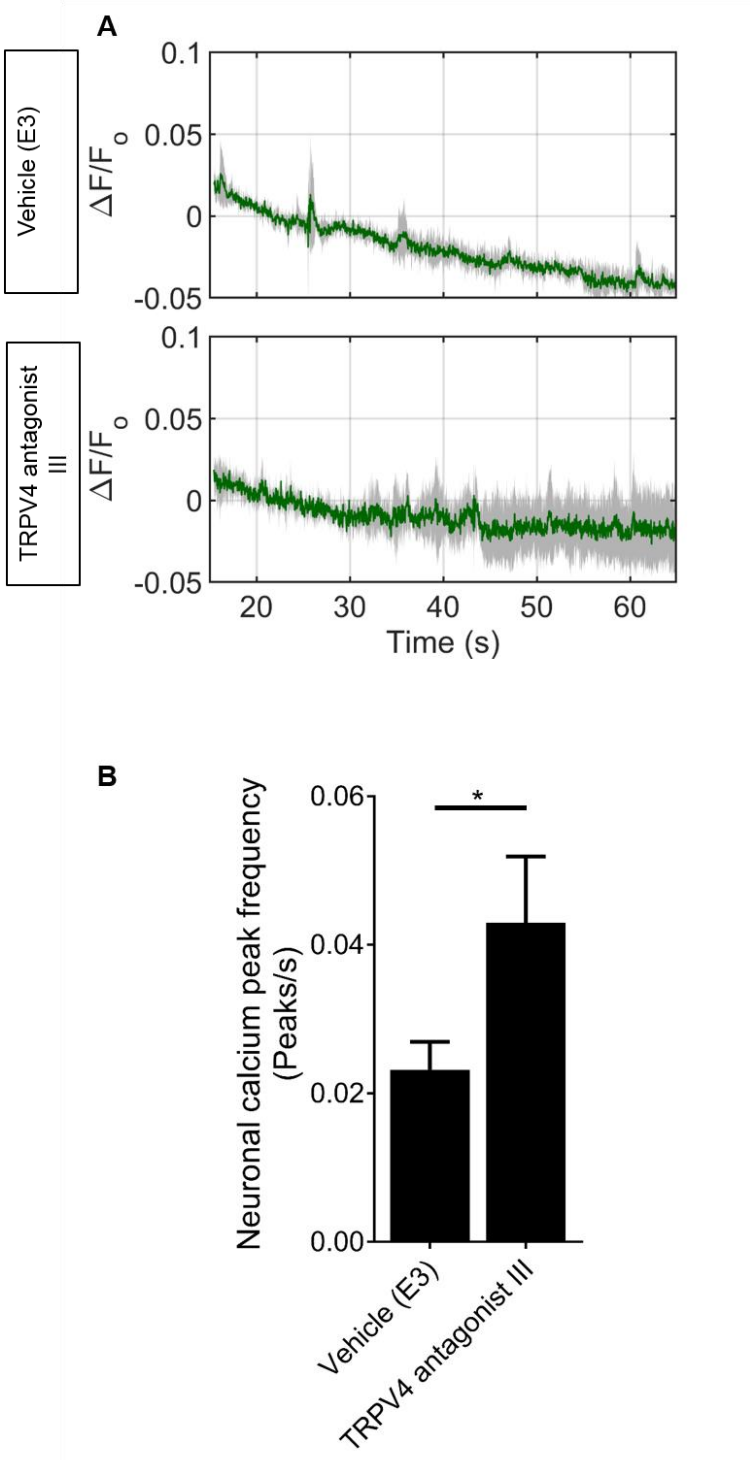

Figure 4-28: Effect of 24h treatment of TRPV4 antagonist on baseline neuronal calcium peak frequency. A: Time series of neuronal activation ($\Delta F/F_o$) in zebrafish (5 larvae/group) in vehicle (E3) and exposed to TRPV4 antagonist III for 24h from 8-9 dpf. **B:** Quantification of neuronal calcium peak frequency for each of the groups (n=22 larvae/group).*$p<0.05$ (unpaired t-test).

4.15 Discussion

In this chapter I described application of the model of NVC developed in **Chapter 3** to hyperglycemia (an important pathology of diabetes). Exposing zebrafish larvae to 20 mM glucose (levels seen in poorly controlled diabetes) from 8-9 dpf did not affect either NVC or cerebrovascular patterning. However, with glucose exposure from 4-9 dpf, I found a reduction in baseline RBC speed, neurovascular uncoupling and cerebrovascular patterning defects. I performed DAF-FM staining on groups exposed to mannitol or glucose and found a decrease in the staining with glucose treatment compared to mannitol exposed group. All these effects were ameliorated by 24 h treatment with the NO donor, SNP (that increased NO reactivity by DAF-FM staining), suggesting the potential for NO as a therapeutic strategy for diabetes and/or hyperglycemia related neurovascular dysfunction. To further understand the mechanism of action of SNP in restoring NVC, I investigated the effect of glucose exposure with or without SNP on different cell types within the NVU such as ECs, pericytes and radial glial cells. Overall I observed decreases in *klf2a:GFP* expression (EC marker), *claudin5a:GFP* expression (EC marker and representative of blood brain barrier permeability), reduction in the number of *sm22ab:mcherry*^{s441} nuclei (pericytes on the tectal vessels), reduction in glutamine synthetase (marker of glutamate uptake by the radial glial cells), increase in GFAP expression (marker of reactive astroglial cells) and overall decrease in TRPV4 expression in the teO. This suggests the neurovascular uncoupling observed with glucose exposure is accompanied by defects in various cells in the NVU suggesting involvement of these cells in mediating the NVC. Further, co-treatment of glucose exposed animals with SNP corrected all these defects confirming the importance and multiple downstream targets of NO in the NVU. Some of these observations are supported by the literature (**section 1.6**), however I here present a comprehensive description of the defects induced by glucose exposure. I have further described reduced dark-light preference and increased locomotion in 9 dpf old zebrafish larvae exposed to glucose.

Light/Dark preference is generally used as a measure for unconditioned anxiety and related disorders in rodents and zebrafish (390, 391). Unconditioned anxiety is influenced by environmental, emotional and cognitive factors (391, 392). It is based on an approach/avoidance conflict between the drive to explore novel area and an aversion to brightly lit/completely dark open spaces (393). The approach/avoidance conflict is a well-studied behaviour in mammals and is known to have various neural substrates in the brain such as the limbic system, anterior cingulate cortex, ventral striatum and prefrontal cortex (393). Although zebrafish do not possess a cortex, they have Vd/Dm as the homologous structures to mammalian amygdala and striatum (described in **section 1.11.1**). Thus impaired light/dark preference could imply an abnormal circuitry in the zebrafish Vd/Dm. Anatomical studies with zebrafish have shown that Vd/Dm project to the teO and hence any defects in the Vd/Dm circuitry could also affect the teO. Hyperglycemia induced changes in the light/dark preference shown in this thesis could suggest that impaired NVC in teO possibly leading to circuitry defects between teO and other brain areas such as Vd/Dm involved in choice preference. Furthermore, increased baseline neuronal calcium peak frequency observed in glucose exposed larvae could support the finding of increased locomotion in response to hyperglycemia.

Radial glial cells are speculated to be an early form of stellate astrocytes found in mammalian species and hence could share few to several functionality of the mammalian astrocytes (320). Furthermore, there are studies showing their role in glutamate recycling from the extra synaptic space (394). Hence any abnormal calcium signalling following glucose exposure could also affect other functions of these cells, including uptake of glutamate as what I have shown with immunostaining with glutamine synthetase antibodies post glucose exposure. Further this speculated abnormal glutamate uptake could result in accumulation of glutamate in the extrasynaptic space leading to possible recurrent neuronal depolarization, i.e., increase in baseline neuronal firing. This fits with the observation of increased number of calcium peaks

observed post glucose treatment. Neuronal hyperexcitability and increased firing is known to be associated to the seizures, commonly observed in diabetic patients. Hence the various cellular markers shown here to be affected by the glucose exposure could explain this observation of higher predisposition of the diabetic patients to epileptic episodes or seizures. Further increased neuronal firing could also lead to abnormal and non – precise pre and post synaptic neuronal firing causing possible defects in the synaptic plasticity mechanisms necessary to bring about cognition and memory. Further exploration of this could help us understand the relation between diabetic pathology and underlying reasons for the observation of cognitive defects observed in the patients. Further this theory qualitatively fits the notion suggesting diabetes to be a risk factor for dementia and neurodegenerative disorders.

4.16 Conclusions

Previous studies have linked hyperglycemia and pharmacologically induced diabetes to reduction in cerebral blood flow. However, this is the first such study in zebrafish and the first in any model demonstrating that SNP reverses these negative consequences.

The rescuing effect of NO on the all the NVC and anatomical cellular parameters studies suggests a possible way to treat diabetes associated neurovascular dysfunction. With emerging evidences about increased importance of NO in NVC, this seems pragmatic as NO is not only important signalling molecule to mediate NVC but also important in mediating endothelial function and vascular tone (395). Hence, the rescuing effect of NO further impinges on the importance on maintaining endothelial and therefore vascular health for normal brain function. Future studies are needed to corroborate if these effects of glucose exposure and NO donors are seen even in mammalian models and also possibly explaining the trigger effect of the drug SNP. With the multifaceted data presented here demonstrating the importance of NO in

maintaining neurovascular function and vascular health, it seems imperative to further explore the precise mechanisms of actions of SNP and possibly other NO donors. All these are necessary to push forward the idea of the use of NO based therapeutics for the treatment of diabetes and even for targeting disorders associated with neurovascular uncoupling and low cerebral perfusion.

5 Effect of *gch1* mutation on neurovascular coupling and cerebrovascular patterning

5.1 Aims

In this chapter I study NVC in a novel *gch1* mutant line generated by Dr. Marcus Keatinge. *GCH1* is an enzyme called GTP cyclohydrolase 1, required in the first three steps in production of tetrahydrobiopterin (BH4). BH4 is involved in physiological processes including production of neurotransmitters such as dopamine and serotonin (396). Lack of dopamine is a hallmark of prominent neurodegenerative diseases such as Parkinson's disease. In humans, *gch1* mutations are associated with Dopa-responsive dystonia and parkinsonism (397, 398).

5.2 Cerebrovascular patterning is affected in homozygous mutants (*gch1*(-/-)) compared to wild type (*gch1*(+/+)) and heterozygous mutants (*gch1(+/-)*)

I first assessed the effect of the homozygous *gch1* mutation on cerebrovascular anatomy. Representative micrographs for the anatomy from *gch1*(+/+), *gch1*(+/-) and *gch1*(-/-) are shown in **Figure 5-1**. I observed reduced branchpoint number and vascular length in *gch1*(-/-) compared to *gch1*(+/+) and *gch1*(+/-) (**Figure 5-2A-B**). Mean vessel radius in the *gch1*(-/-) was lower compared to *gch1*(+/-) while it was not statistically different from the *gch1*(+/+) (**Figure 5-2C**). Radius frequency histograms for all the three groups are shown in **Figure 5-2D**. All these results demonstrate a deleterious effect of the homozygous *gch1* mutation on the cerebrovascular patterning although the effect on vessel radius appears modest.

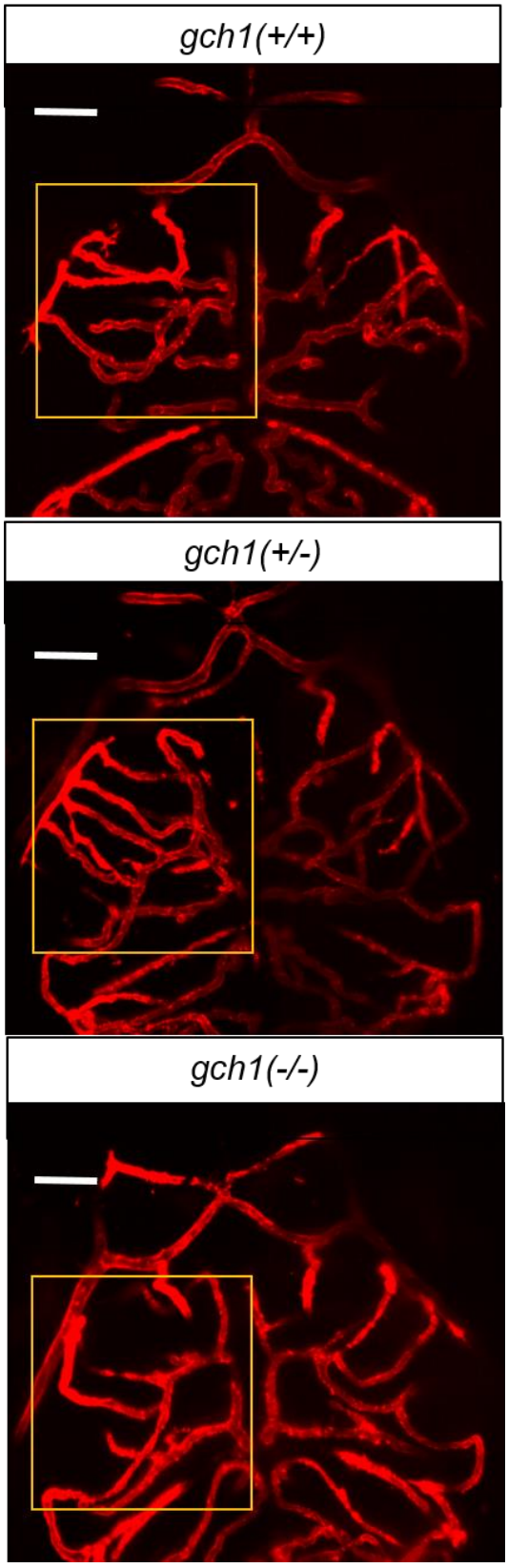

Figure 5-1: Representative micrographs of tectal vessels in wildtype (*gch1*(+/+)), heterozygous (*gch1*(+/-)) and homozygous *gch1* mutants (*gch1*(-/-)). Box indicates the region of the left optic tectum quantified for vascular features (branchpoints, tectal vascular length and vessel radius). Scale bar represents 20 µm.

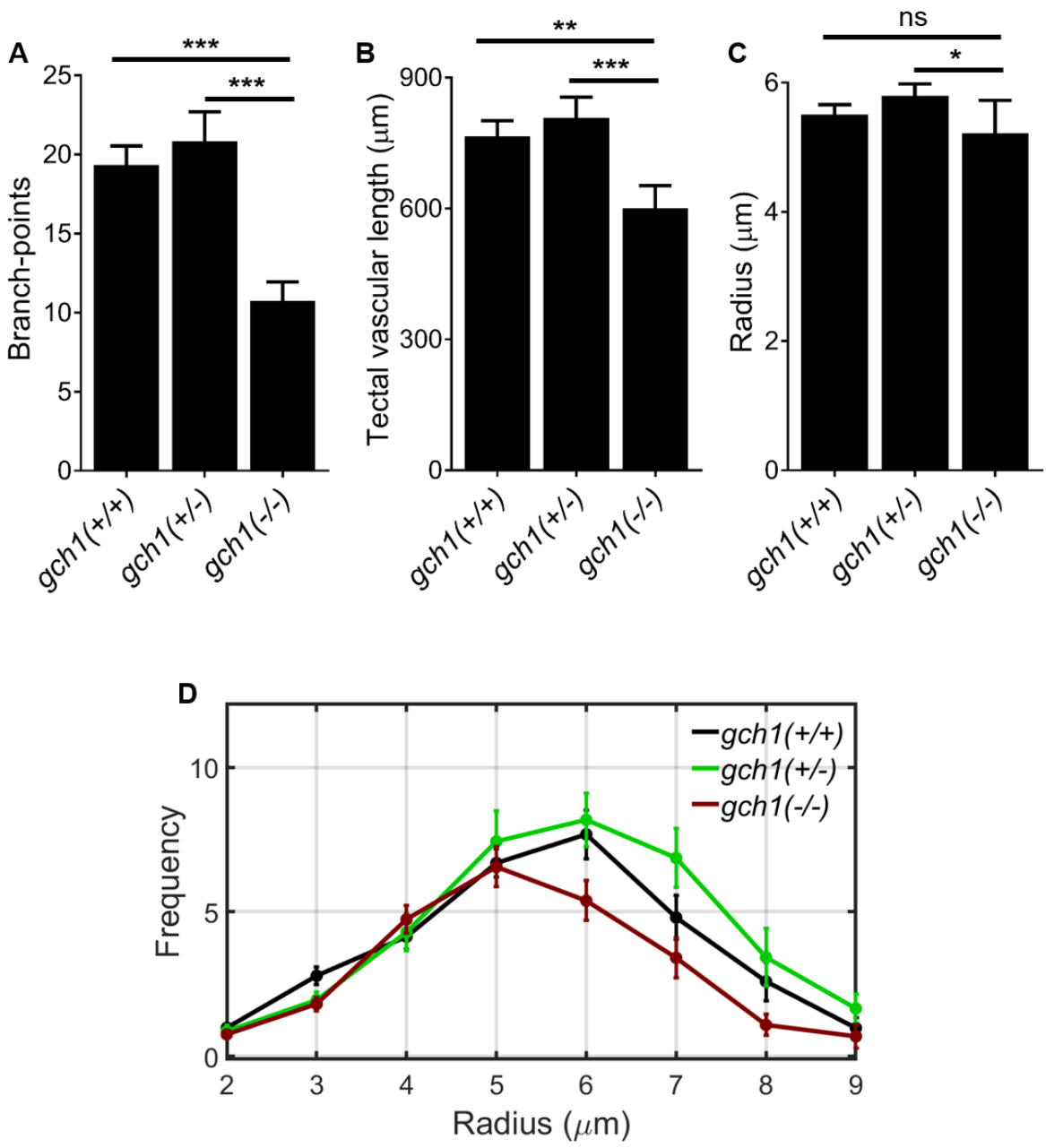

Figure 5-2: Effect of *gch1* mutation on cerebrovascular patterning. A: Number of tectal vessel branchpoints (n=18,17,17 for *gch1(+/+)*, *gch1(+/-)* and *gch1(-/-)*, respectively). **B:** Total tectal vessel length in same animals as **A. C:** Mean tectal vessel radius in same animals as in **B. D:** Histograms of tectal vessel radii of tectal vessels in same animals as in **A.** Data in **A-D** are mean ± s.e.m. *p<0.05, **p<0.01 and ***p<0.001 (one-way ANOVA).

5.3 Neurovascular coupling in impaired in homozygous mutants (*gch1(-/-)*)

Embryos were first genotyped at 3 dpf as wild types (*gch1*(+/+)), heterozygous (*gch1*(+/-)) or homozygous mutants (*gch1*(-/-)). NVC in response to 8 seconds light stimulation was then assessed as described in **section 2.2**. Representative time series for five larvae for change in neuronal calcium fluorescence in the teO and RBC speed in the tectal vessels for *gch1*(+/+), *gch1*(+/-) and *gch1*(-/-) are shown in **Figure 5-3A-B**. I found no significant differences in neuronal calcium peak frequency between the groups (*gch1*(+/+), *gch1*(+/-) and *gch1*(-/-)) (**Figure 5-4A**). However, I found *gch1*(-/-) to have reduced baseline blood flow and change in in RBC speed in response to visual stimulation compared to *gch1*(+/+) and *gch1*(+/-) larvae (**Figure 5-4B**). This suggested an impairment in NVC in homozygous *gch1* mutant larvae.

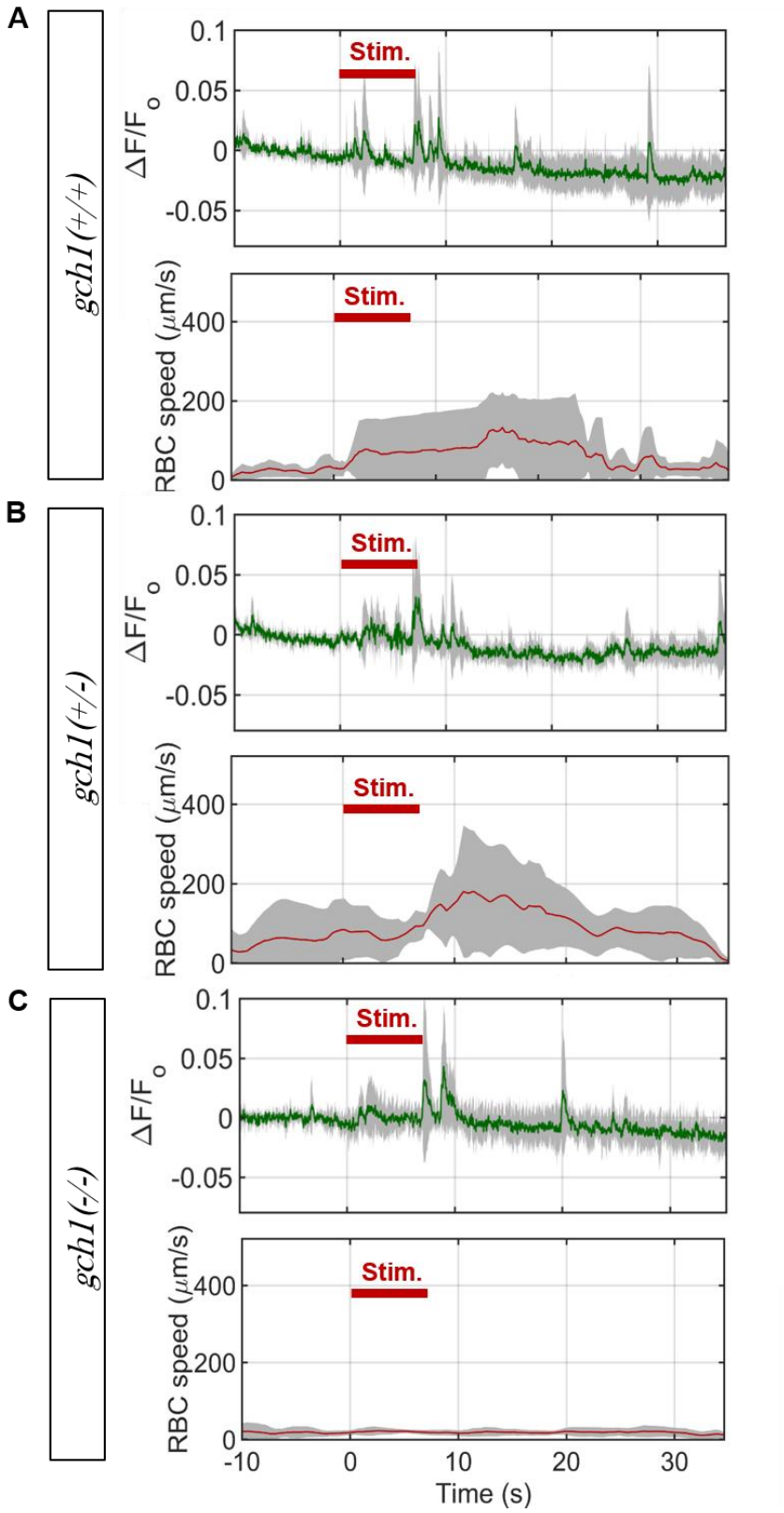

Figure 5-3: Time series of neuronal activation ($\Delta F/F_o$) and tectal vessel RBC speed in A: *gch1*(+/+), **B:** *gch1*(+/-) **and C:** *gch1*(-/-) (n=5 larvae/group). Visual stimulus is delivered for 0-8s shown by red bar on the graphs**.** Data in **A-C** are mean ± s.d.

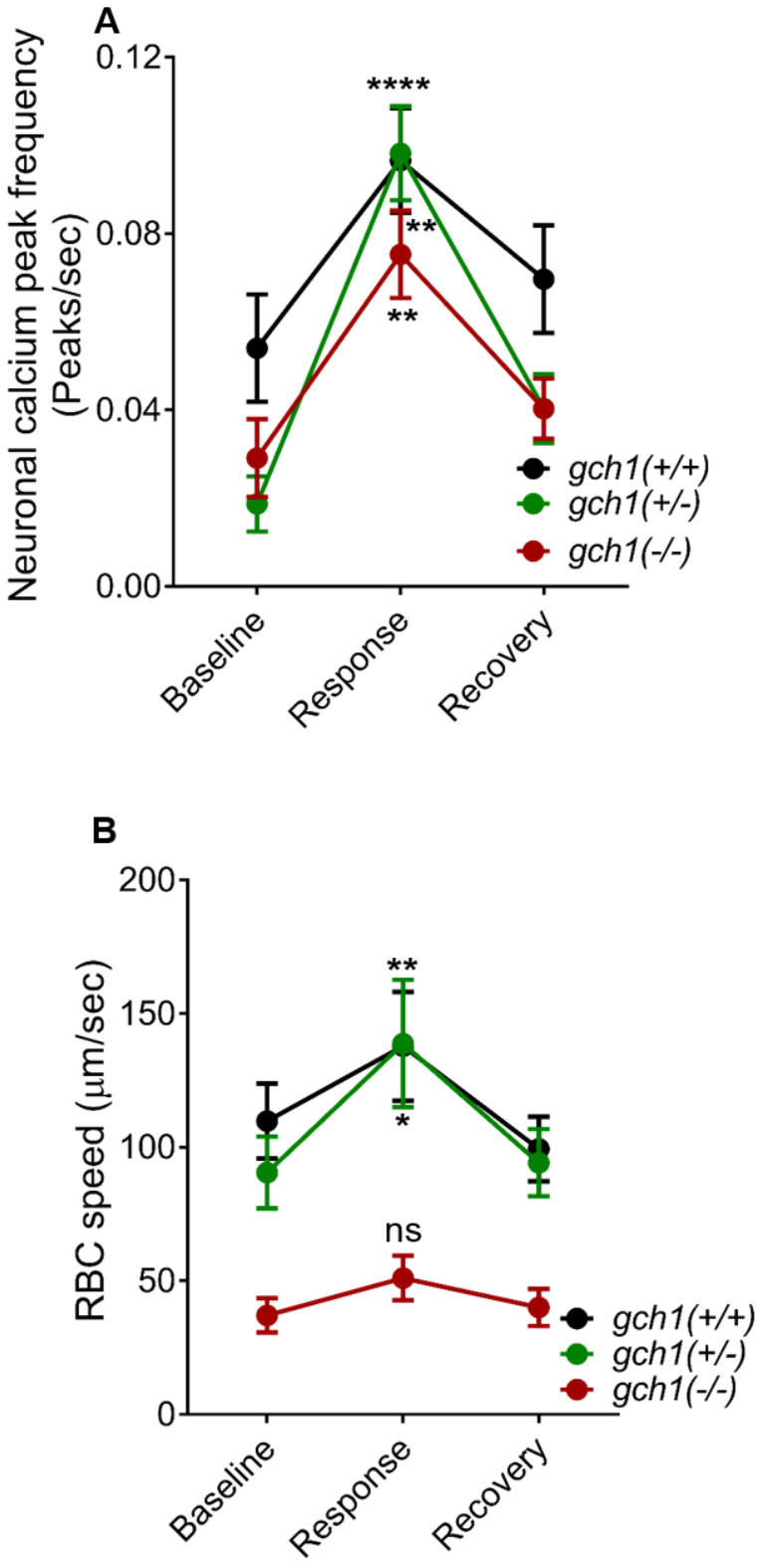

Figure 5-4: Effect of *gch1* mutation on neurovascular coupling. **A:** Frequency of peaks of neuronal activation during baseline, response and recovery time periods in *gch1*(+/+) (n=19 larvae), *gch1*(+/-) (n=19 larvae) and *gch1*(-/-) (n=23 larvae). **B:** RBC speed for baseline, response and recovery for same animals in **A.** Data in **A** and **B** are mean ± s.e.m. *p<0.05, **p<0.01 and ****p<0.0001 (two-way ANOVA).

5.4 Behavioural measurements of locomotion show reduction in total movement in homozygous *gch1(-/-)* mutants

Using Viewpoint zebrabox, the motion of all the three groups: *gch1*(+/+), *gch1*(+/-) and *gch1*(-/-) was assessed. Movement was tracked for 30 minutes with a sampling time of 1 minute.

Distance moved was analysed for high (speed>64 mm/s) and low (64 mm/s>speed>30 mm/s) speed locomotion (as described in **section 2.8**). Representative trajectories for *gch1*(+/+), *gch1*(+/-) and *gch1*(-/-) are shown in **Figure 5-5A** with low speed (3-6mm/s) trajectories marked in red and high speed (>64 mm/s) trajectories marked in green. I calculated the mean distance travelled at these two speed limits for each of the *gch1*(+/+), *gch1*(+/-) and *gch1*(-/-) and found that both slow and high speed movement in *gch1*(-/-) are significantly reduced compared to *gch1*(+/+) and *gch1*(+/-) siblings (**Figure 5-5B-C**)

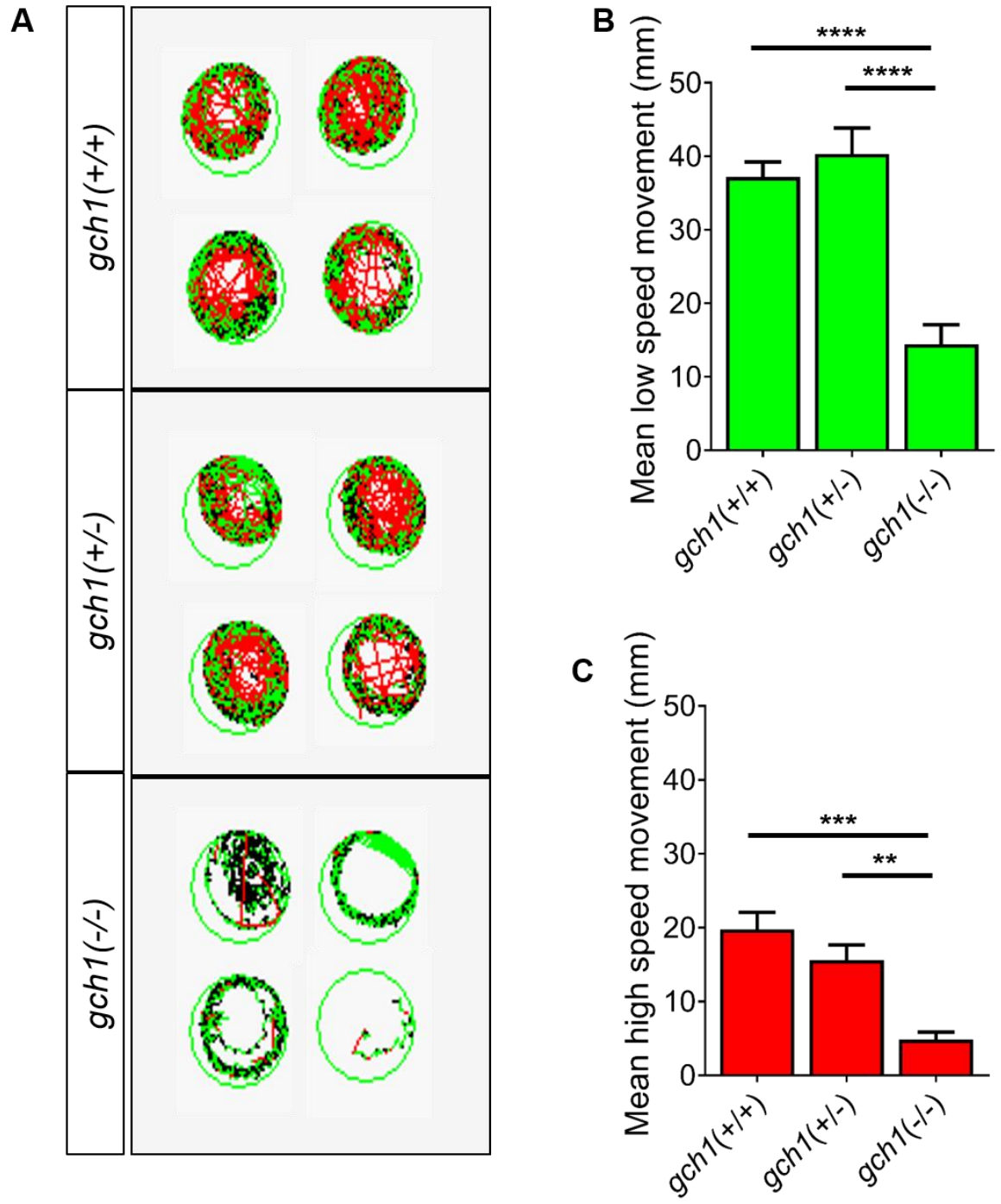

Figure 5-5: Effect of *gch1* mutation on locomotion in 8 dpf zebrafish. A: Representative trajectories of *gch1*(+/+), *gch1*(+/-) and *gch1*(-/-) siblings (n=4 larvae/group). **B:** Quantification of mean distance moved with low speed (30-60 mm/s) by *gch1(+/+)* (n=21 larvae), *gch1(+/-)* (n=16 larvae) and *gch1(-/-)* siblings (n=19 larvae). **C:** Quantification of mean distance covered with high speed by the same animals as in **B**. Data in **B** and **C** are mean ± s.e.m. **p<0.01, ***p<0.001 and ****p<0.0001 (one-way ANOVA).

5.5 Administration of SNP ameliorates cerebrovascular patterning defects in *gch1*(-/-) mutants

I next assessed the effect of SNP on the cerebrovascular patterning defects observed in *gch1*(-/-). Here, I have compared the cerebrovascular patterning in *gch1*(+/+) and *gch1*(-/-) with or without 0.1 mM SNP treatment (from 7-8 dpf for 24 h). Representative micrographs are shown in **Figure 5-6**. SNP treatment ameliorated the effect of *gch1* mutation on branch point and vascular length (**Figure 5-7A-B**). I did not observe statistically significant differences in vessel radius between different groups (**Figure 5-7C&D**)

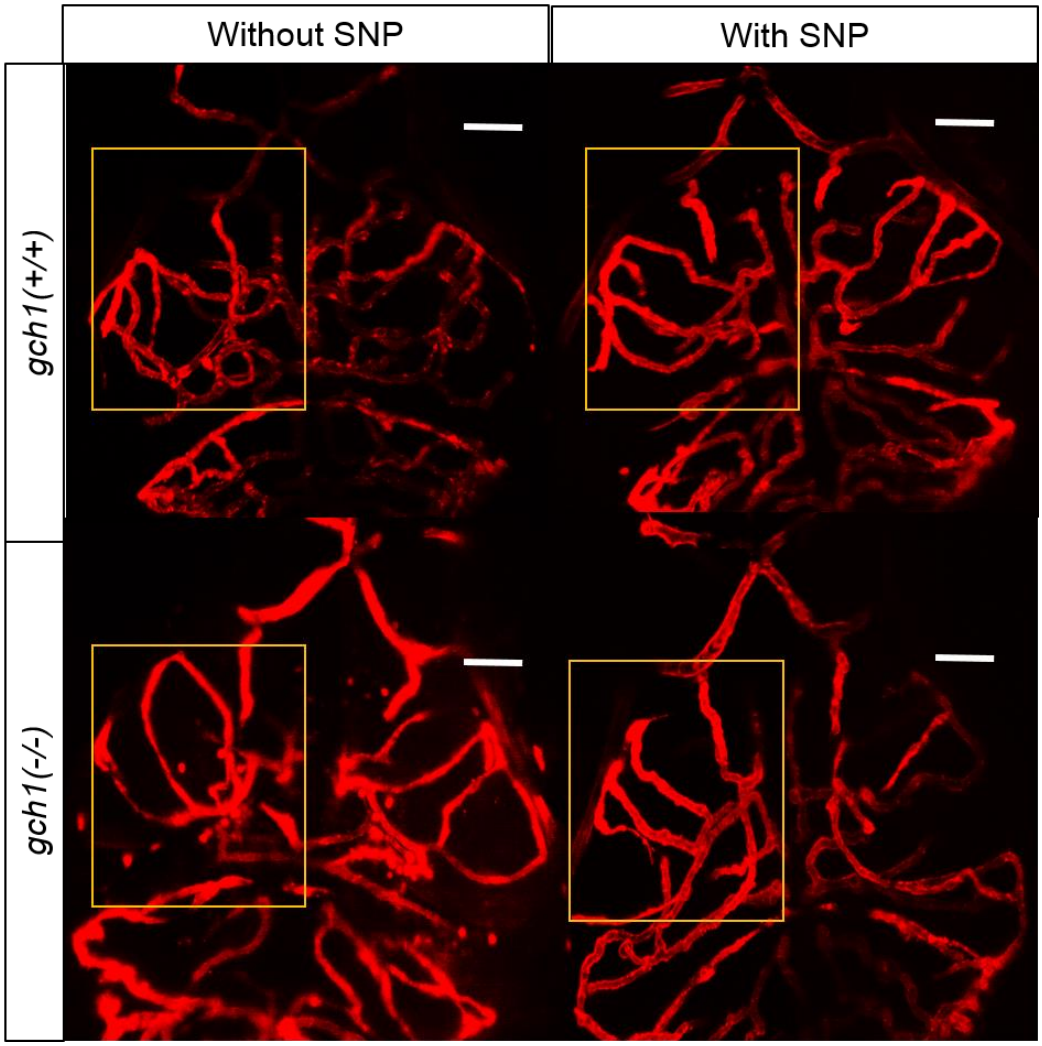

Figure 5-6: Representative micrographs of cerebral vessels of 8 dpf *gch1*(+/+), *gch1*(-/-) siblings with or without SNP treatment. Square indicates region of left optic tectum quantified for various vascular features (branch points, vascular length and vessel radius). Scale bar represents 20 µm.

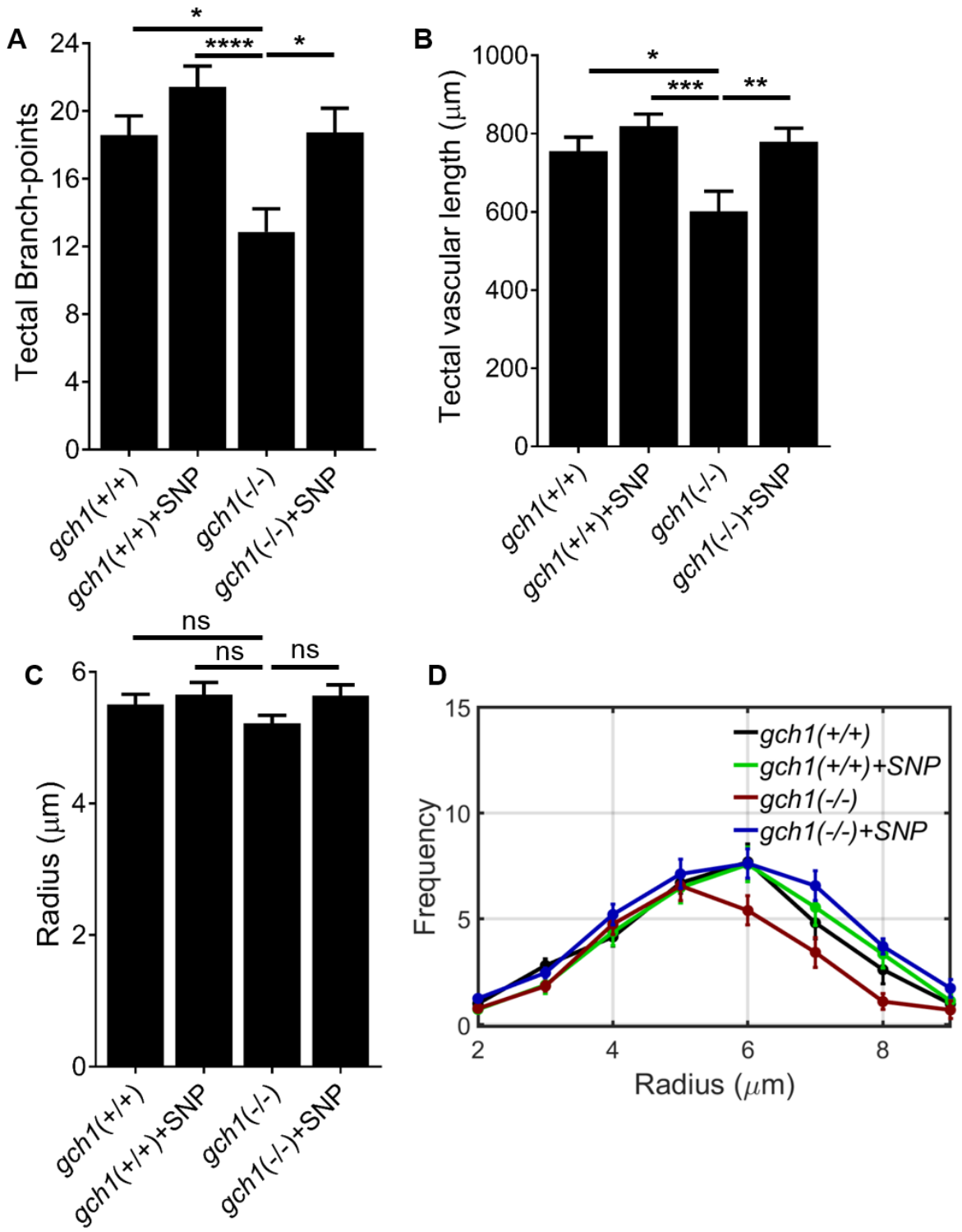

Figure 5-7: SNP rescues the deleterious effects of *gch1* mutation on the cerebrovascular patterning. A: Number of tectal vessel branch points for *gch1*(+/+) and *gch1*(-/-) siblings with or without SNP (n=16 larvae/group). **B:** Total tectal vessel length in same animals as **A. C:** Mean tectal vessel radius in same animals as in **A. D:** Histograms of tectal vessel radii of tectal vessels in same animals as in **A.** Data in **A**-**D** are mean ± s.e.m. *p<0.05, **p<0.01, ***p<0.001 and ****p<0.0001 (one-way ANOVA).

5.6 Administration of SNP rescues neurovascular coupling in *gch1*(-/-)

As described earlier, *gch1* is a key catalyst in the synthesis of BH4 which is also important for NO synthesis. Since SNP was shown to ameliorate all the glucose induced deficits on the NVC, I tested the effect on neurovascular dysfunction in *gch1*(-/-). Representative time series for five larvae for change in neuronal calcium fluorescence in the teO and RBC speed in the tectal vessels for *gch1*(-/-) and *gch1*(-/-) with or without SNP are shown in **Figure 5-8**. I found that overnight treatment with 0.1mM SNP did not affect the neuronal activation in response to red light stimulation (**Figure 5-9A**) however it rescued the increase in red blood cell speed, and thus NVC in response to light stimulation (**Figure 5-9B**).

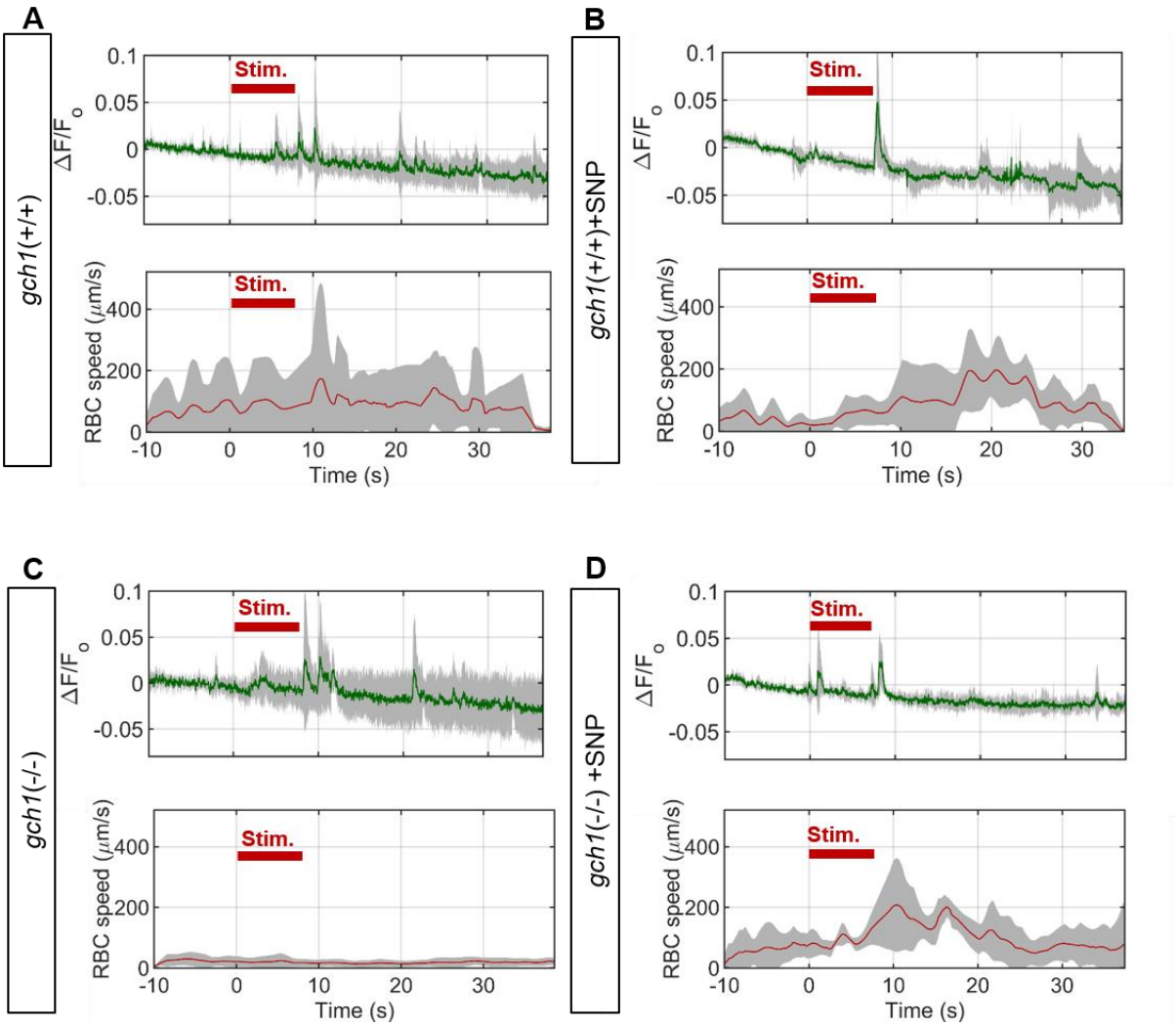

Figure 5-8: Time series of neuronal activation (*ΔF/F$_o$*) and tectal vessel RBC speed in A: *gch1*(+/+), **B:** *gch1*(-/-) **C:** *gch1*(+/+) + SNP **and D:** *gch1*(-/-) + SNP (n=5 larvae/group). Visual stimulus is delivered for 0-8s shown by red bar on the graphs**.** Data in **A-D** are mean ± s.d.

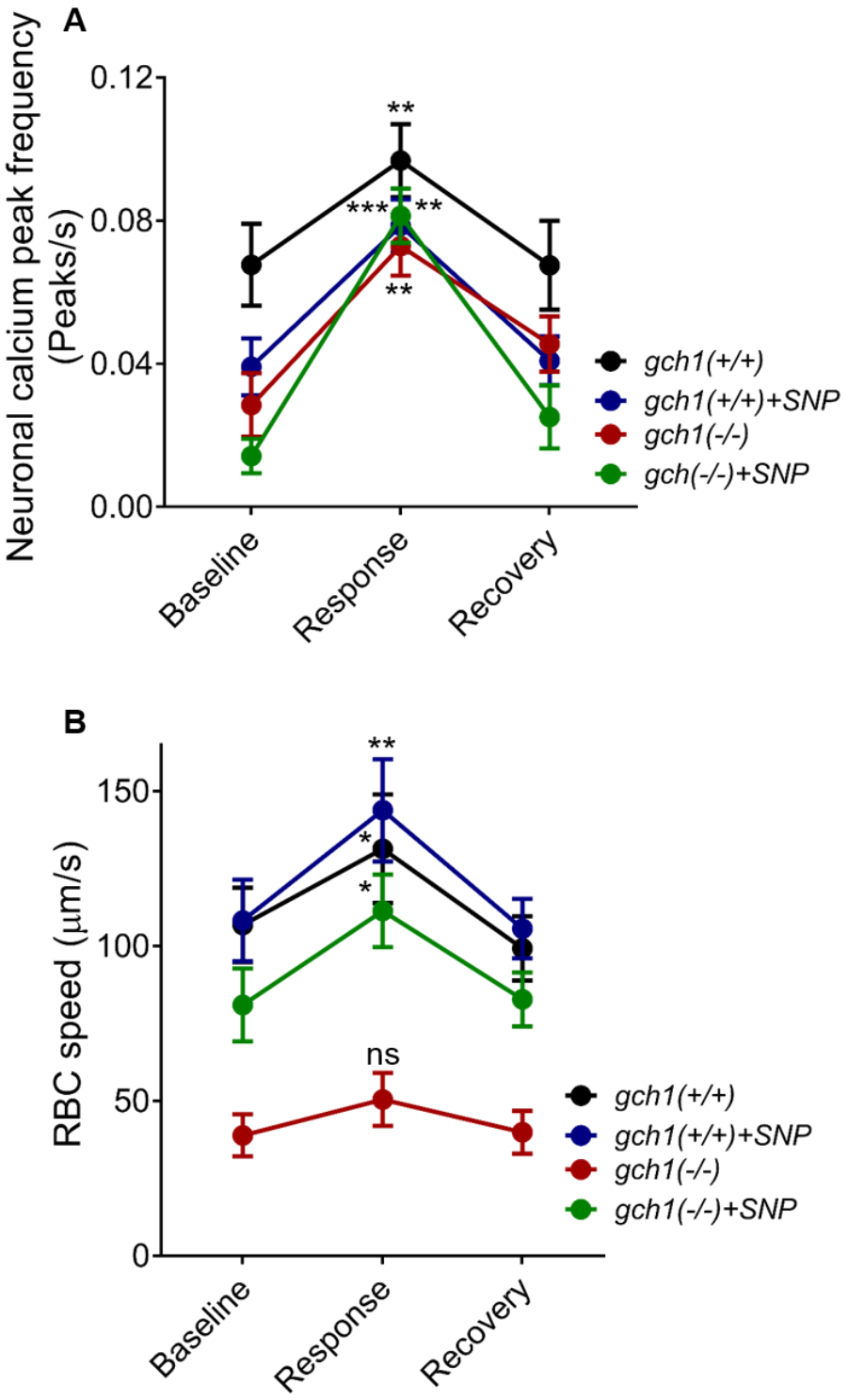

Figure 5-9: SNP rescues the neurovascular coupling defects in *gch1* mutants. **A:** Frequency of peaks of neuronal activation during baseline, response and recovery time periods in *gch1*(+/+) and *gch1*(-/-) with or without co-treatment with 0.1mM SNP (n=20 larvae/group). **B:** RBC speed for baseline, response and recovery for same animals in **A**. Data in **A** and **B** are mean ± s.e.m. *p<0.05, **p<0.01 and ***p<0.001 (two-way ANOVA).

5.7 Co-treatment of homozygous *gch1* mutants with SNP rescues the movement defects.

I then assessed the effect of SNP treatment on the locomotion of *gch1*(-/-) using Viewpoint-zebrabox with the protocol described earlier. Representative motion trajectories for *gch1*(+/+) and *gch1*(-/-) with or without SNP treatment are displayed in **Figure 5-10A**. I found that total distance moved by *gch1(-/-)* treated with SNP was significantly higher than *gch1*(-/-) only group of larvae (**Figure 5-10B-C**). This suggests NO donors could be a potential strategy to improve motor dysfunction linked to *gch1* mutations.

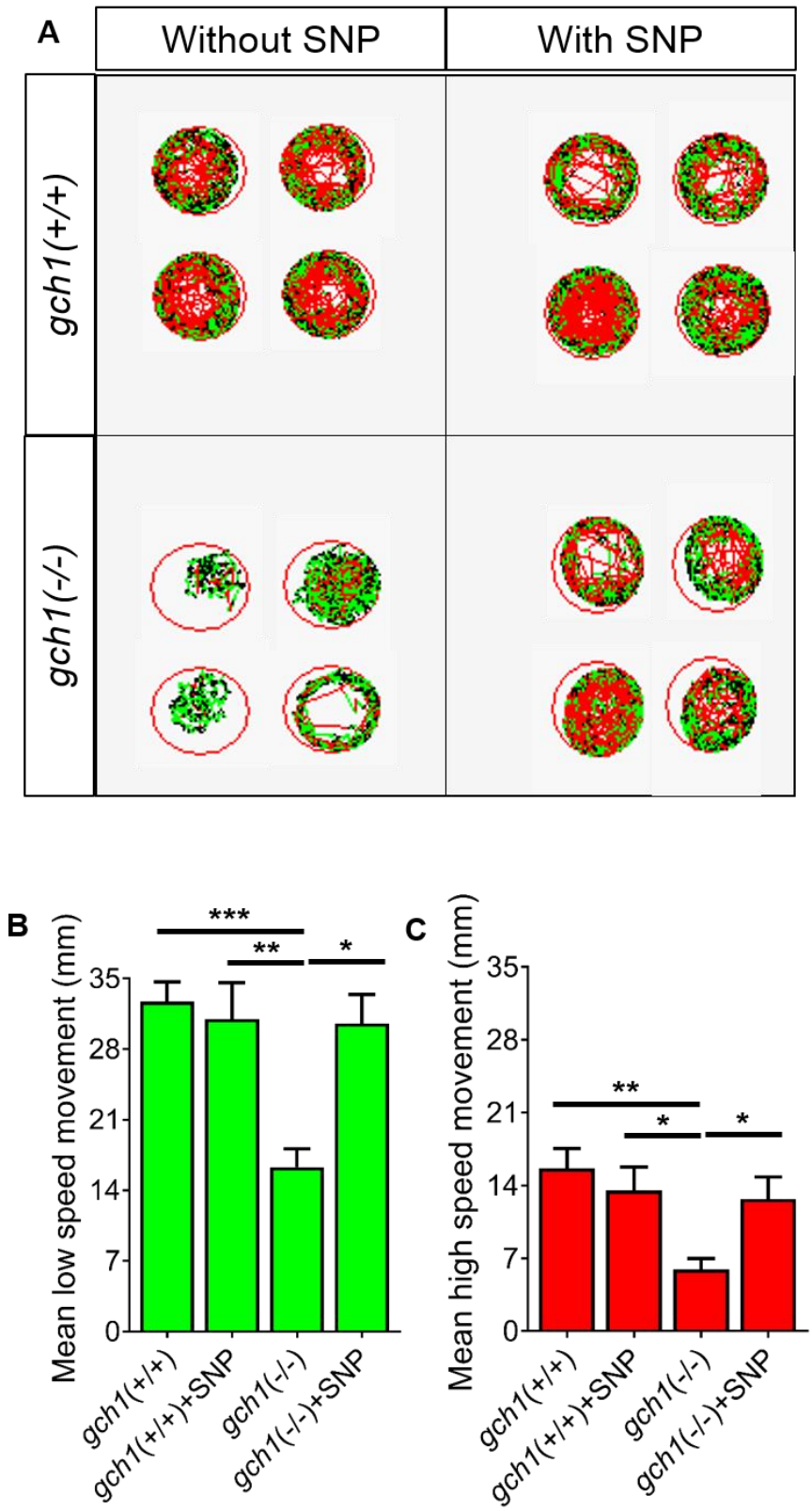

Figure 5-10: SNP rescues locomotion defects in *gch1* mutants. A: Representative trajectories of *gch1*(+/+) and *gch1*(-/-) siblings with or without SNP treatment (n=4 larvae/group). **B:** Quantification of mean distance moved with low speed (3-6 mm/s) by *gch1*(+/+), *gch1*(-/-) with or without SNP (n=36 larvae/ group). **C:** Quantification of mean distance covered with high speed by the same animals as in **B.** Data in **B** and **C** are mean ± s.e.m. *p<0.05, **p<0.01, ***p<0.001 (one-way ANOVA).

5.8 *gch1* mutants display increased NO reactivity which is reduced by co-treatment with SNP

NOS requires BH4 as an essential cofactor for NO synthesis (399), and production of BH4 is dependent on *gch1* (400). I used the DAF-FM staining protocol to test the NO reactivity in the homozygous *gch1* mutants with or without SNP treatment. Representative micrographs of the tectal vessels stained with DAF-FM in *gch1(+/+), gch1(-/-)* with or without SNP are shown in **Figure 5-11** . I found that homozygous *gch1* mutants showed significantly increased DAF-FM intensity compared to wild type siblings (**Figure 5-12**). Treatment of homozygous *gch1* mutants with SNP significantly decreased the intensity of the DAF-FM staining compared to untreated *gch1* mutant larvae (**Figure 5-12**). This is contrary to what was observed in the glucose exposed group co-treated with or without SNP in the **chapter 5**. Studies have shown that DAF-FM stain could possibly also stain reactive NO species (RNOS) other than NO only (401). While I have shown homozygous *gch1* mutants to have a similar neurovascular uncoupling phenotype to that of glucose exposed groups, homozygous mutants are lethal and do not survive past 10-15 days. In the light of these observations, it could be hypothesized that a moderate decrease in nNOS and/or eNOS could show a decrease in NO reactivity observed by DAF-FM staining (as shown in glucose exposed larvae in **chapter 5**). A complete loss of NO due to lack of essential enzyme for NO production (as seen in homozygous *gch1* mutants) could lead to a compensatory increase in iNOS (which is also associated to inflammatory phenotype and thus production of RNOS, (402)) causing non-specific DAF-FM staining. Furthermore, NO supplementation through SNP could provide a feedback signal and contribute to the decrease in reactive nitrite species non-specifically stained by DAF-FM in homozygous *gch1* mutants treated with SNP (**Figure 5-11** and **Figure 5-12**).

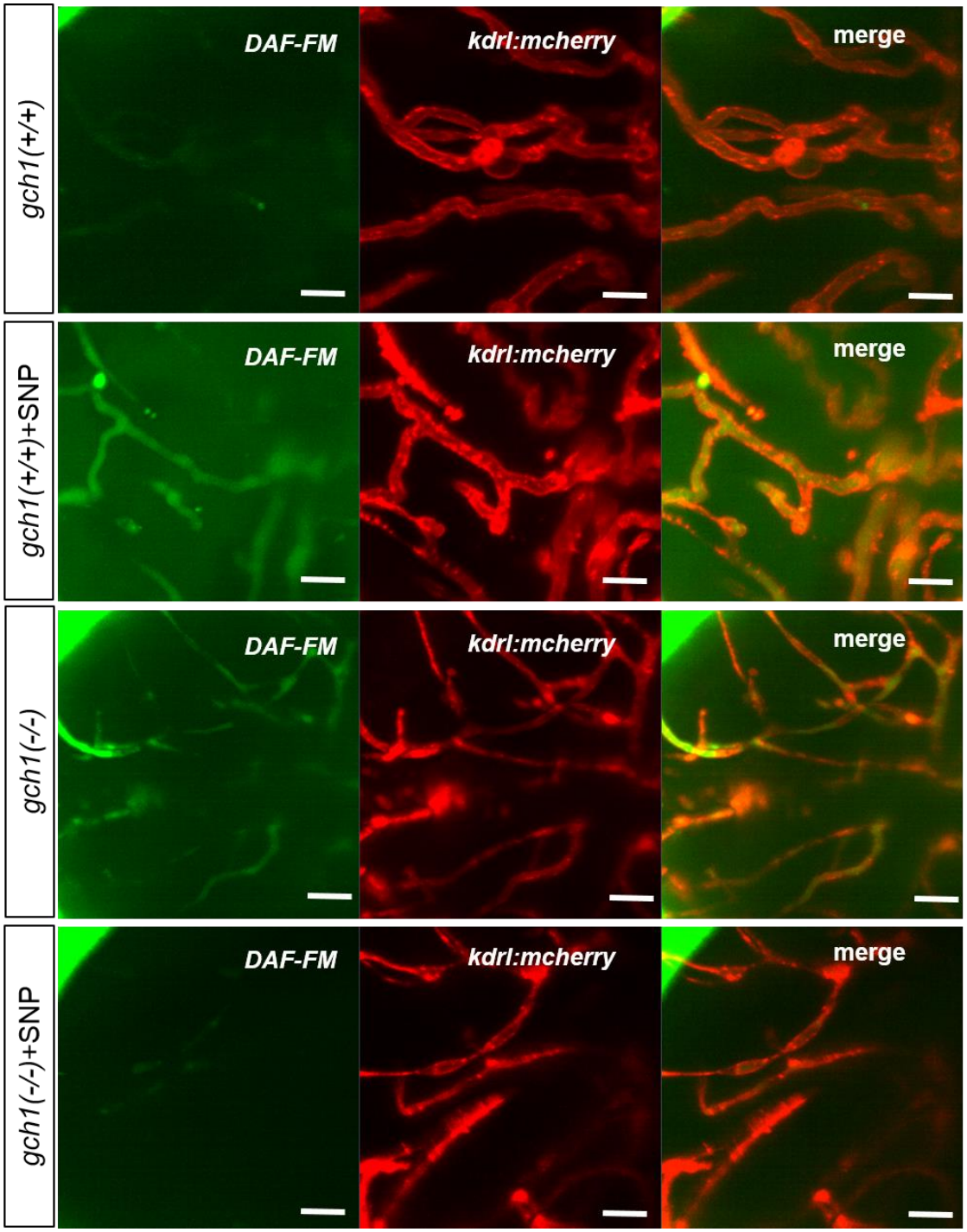

Figure 5-11: Representative micrographs of tectal vessels stained for NO reactivity with DAF-FM stain in *gch1*(+/) and *gch1*(-/-) siblings co-treated with or without SNP. Scale bar represents 20 µm.

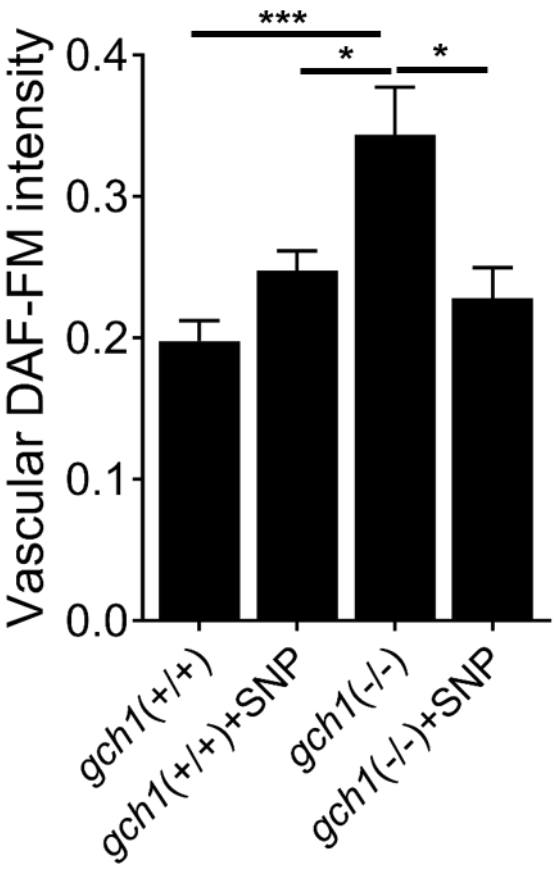

Figure 5-12: Quantification of DAF-FM staining in the tectal blood vessels in *gch1(*+/+) and *gch1(*-/-**) siblings co-treated with without SNP** (n =14, 13, 13 and 10 for *gch1(+/+)* and *gch1(-/-)* siblings co-treated with without SNP, respectively). Data is mean ± s.e.m. *p<0.05 and ***p<0.001 (one-way ANOVA).

5.9 Discussion

In this chapter I have shown the effect of a novel mutation in the enzyme (*gch1*) responsible for synthesis of an essential cofactor (BH_4) for the production of various neurotransmitters (such as dopamine and serotonin) and NO (396, 399). Recent studies have linked this gene with disorders associated with dopamine deficiency such as Parkinson's disease (397). Using the novel zebrafish model of NVC described in **chapter 3**, I have characterized neurovascular function (NVC and cerebrovascular patterning) in larvae with homozygous *gch1* mutation. I found that homozygous *gch1* mutants had impaired cerebrovascular patterning evidenced by reduced number of branch points and total vascular length. I further demonstrated that these anatomical defects found in the homozygous mutants are associated with neurovascular uncoupling and that despite having preserved neuronal responses to visual stimulation, the expected increase in RBC speed in response to the stimulus is not observed. The similarity between this observation and the effects of glucose exposure is interesting as it points to possible commonalities between neurological disorders such as Parkinson's disease and vascular disorders such as diabetes. I have also found that locomotion in the homozygous *gch1* mutants is reduced compared to wild type siblings and heterozygous *gch1* mutants.

Given the similarity in phenotype between the *gch1* mutants and larvae exposed to glucose, I tested the effect of SNP which had rescued the effect of glucose in the previous chapter. Excitingly, I found that treating homozygous *gch1* mutants with SNP rescued all the cerebrovascular patterning defects, recovered the NVC and improved the impairment in locomotion in homozygous mutants, suggesting NO is important to maintain brain function.

5.10 Conclusion and future work

From the observations of the effects of homozygous mutation on the cerebrovascular patterning and NVC, I have hereby shown the importance of NO and NVC in maintaining brain health. While here the *gch1* mutation is a global mutation, previous evidence points to a link between

endothelial specific mutation in *gch1* and development of Parkinson's disease (403, 404). In general, this and the previous chapter imply there are shared mechanisms between neurological disorders and vascular disorders such as diabetes. This calls for further research on the common factors between the two genres of the diseases. This is important to understand if diabetes and other cardiovascular abnormalities could be used as early prognostic markers for neurological diseases. Further work is needed to understand the effect of giving NO donors to *gch1* mutants and possible target effects of the drug on functionality of various cells in the NVC. The data on locomotion shown in this work suggest further investigation into the effects on cognitive function and memory in these mutants with or without drug treatments is warranted. This might support development of potential NO based drug therapies for treatment of cognitive disorders. Further work is also needed to test the specificity of SNP on the rescuing effect to see if this is solely mediated by SNP or is a general effect of any NO donor, such as isosorbide mononitrate. Studies with rodent endothelial specific *gch1* have shown various cardiovascular abnormalities in the animals further emphasizing the link between cardiovascular and neurological diseases.

All these evidences together provide a framework to be tested in higher model organisms in order to take it to the translational scale in future. In general, these data suggest the importance of NVC in the brain and that impaired NVC could lead to a plethora of diseases affecting the quality of human life.

6 Computational model of neurovascular unit simulating hyperglycemic neurovascular uncoupling

6.1 Aims

In this chapter, I aimed to develop a computational model of the NVU in order to simulate NVC in normal glucose conditions ($[glucose]_{blood}$ =5 mM) and describe the stimulus evoked increased in the neuronal activity, followed by vasodilation. Each compartment of the model (neuron, astrocyte and blood vessel) is modelled such that stimulating neurons leads to release of neuronal glutamate as an input to the astrocyte. The astrocyte is modelled to increase intracellular calcium in response to this neuronal glutamate to release vasodilator (338) EET onto a lumped blood vessel compartment. This blood vessel compartment comprises NO coupled to vessel diameter and modelled to represent both capillary/arteriolar dilation (depending on the parameters, δ and ω, see **section 2.10.3**). To simulate the effect of hyperglycemia ($[glucose]_{blood}$ >15 mM), I developed equations to simulate blood NO levels, governed by vasodilatory signals (EET) arising from NVC dependent on the modelled values of blood glucose (**section 2.10.3**).

Using the vascular feedback through TRPV4 on astrocytes computational model developed by Kenny et al. (338), I extended the vascular feedback to neurons via release of adenosine by astrocytes (160). Combining this with the model of hyperglycemia, I attempted to explain the observed effects of hyperglycemia on neuronal activity in my experimental work (**section 4.3**) and to predict the consequences on synaptic plasticity mechanisms such as spike time dependent plasticity (STDP) (described in **section 1.12.2**). I used a standard STDP kernel to

examine whether hyperglycemia might affect synaptic learning (a computational correlate of memory).

6.2 A minimal model of the neurovascular unit displays neurovascular coupling

The models used in this chapter are described in **section 2.10**. A schematic representation of the three compartments with the modelled parameters is shown in **Figure 6-1A.** I simulated the neuronal spiking in response to 8s stimulation as an input to the neuronal compartment. Random Gaussian noise was added to the stimulation pulse to make this more realistic (**Figure 6-1B**). Simulations produced using this model showed prominent spikes in response to stimulation and a corresponding increase in quantal release of glutamate from the neuron (**Figure 6-1C-D**). Furthermore, a prominent $[Ca^{2+}]_i$ response was observed in the astrocyte compartment (**Figure 6-2C**), followed by EET release (**Figure 6-2D**) and an increase in the positive current through TRPV4 (I_{TRPV4}) (**Figure 6-2E**). EET was modelled in the present study rather than prostaglandins to most of the computational modelling literature focussed on EET but will be a prospective direction (discussed in **chapter 7**).

Using the equations developed for vasodilator mediated release of NO by ECs (**section 2.10.3**), a prominent NO pulse (of 3 μM) was observed in the vessel compartment (as a result of activation of ECs) (**Figure 6-3C**), followed by an increase in vessel diameter (**Figure 6-3D**). All simulations of NVC were performed with glucose values set to 5mM (as found in normoglycemic humans and zebrafish (405, 406)). The peaks in neuronal membrane voltage and vessel dilation (as measured by changes in vessel diameter) were predicted to be 6-10 seconds apart (~10 s from first neuronal peak and ~6 s from the second neuronal peak), similar to those I observed experimentally in **section 3.6** (6.33±3.19 s, n=40).

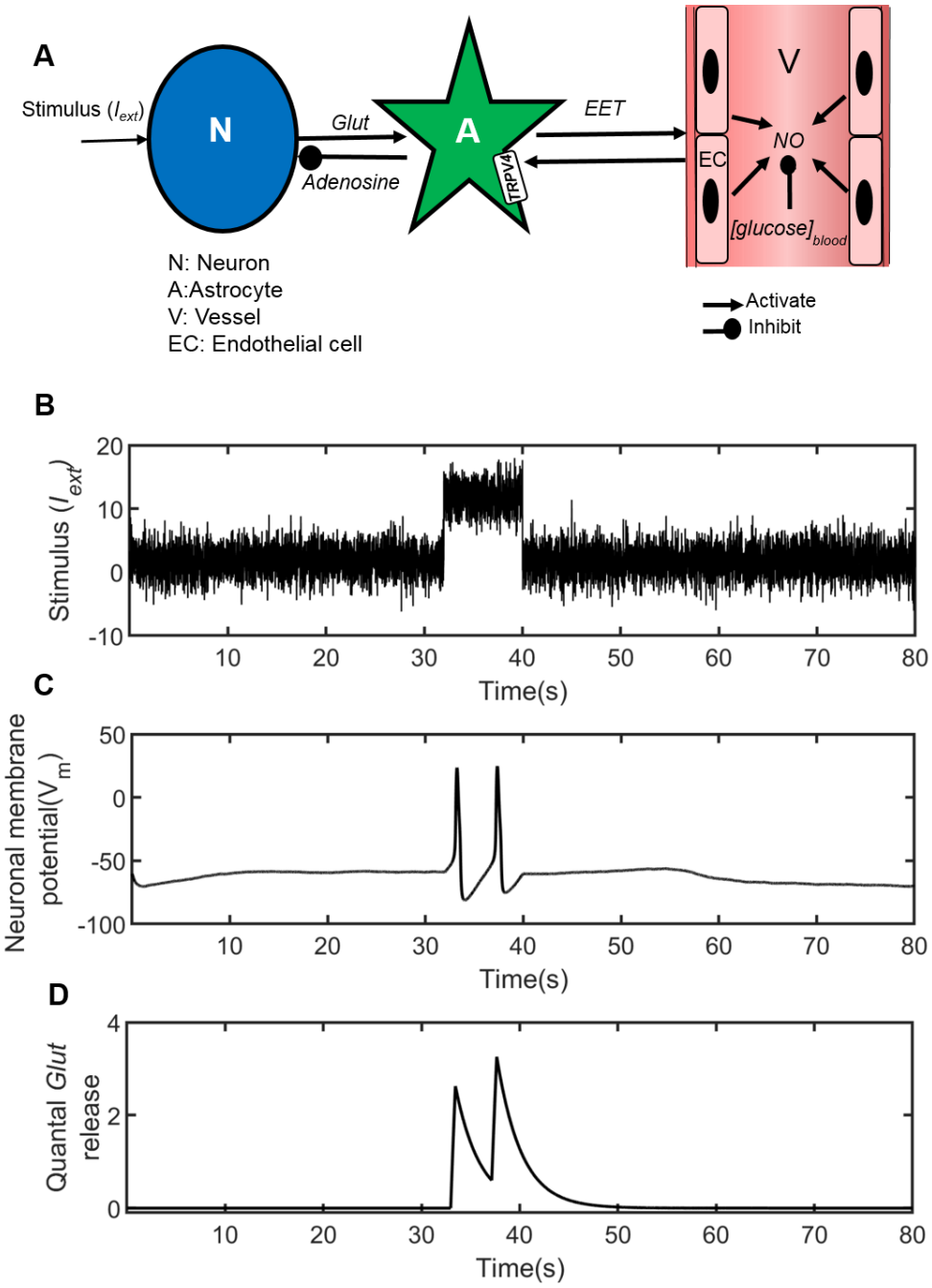

Figure 6-1: Neuronal compartment dynamics in response to an 8s stimulation with 5mM *[glucose]*$_{blood}$. A: Schematic representation of computational model of neurovascular unit showing the neuron (N), astrocyte (A) and blood vessel (V) compartment. Neuron upon stimulation with external current (I_{ext}) releases glutamate (*Glut*), activating the astrocyte which the releases EET, causing vasodilation and increases in endothelial cell (EC) derived NO. Vasodilation sends feedback to astrocyte through TRPV4 activation that causes inhibition of neuronal firing through astrocyte derived adenosine. **B:** Stimulation signal (I_{ext}) input to the neuron, modelling the experimental 8s stimulation protocol. Random Gaussian noise was added to make it experimentally realistic. **C:** Neuronal spiking output of the modified HH neuron model. **D:** Modelled glutamate (*Glut*) release in response to neuronal spiking as in **C.**

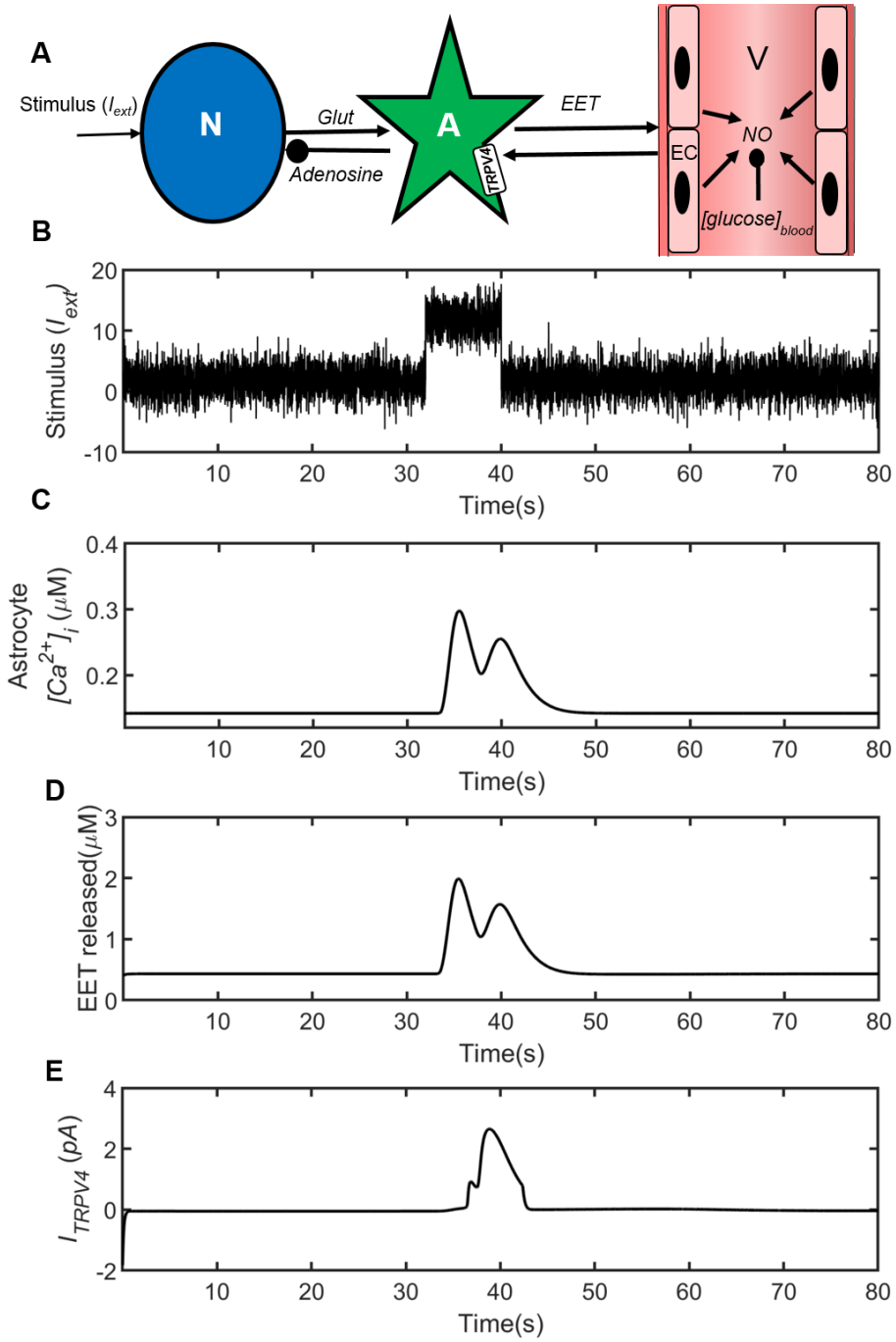

Figure 6-2:Astrocyte compartment dynamics in response to 8 s stimulation with 5mM *[glucose]*$_{blood}$. A: Schematic representation of computational model of neurovascular unit showing the neuron (N), astrocyte (A) and blood vessel (V) compartment. **B:** Stimulation signal (I_{ext}) input to the neuron to model the experimental 8s stimulation protocol. Random Gaussian noise was added to make it experimentally realistic. **C:** Astrocyte $[Ca^{2+}]_i$ dynamics in response to 8s stimulation. **D:** EET released by the astrocyte compartment in response to increase in $[Ca^{2+}]_i$. **E:** Astrocytic TRPV4 channel current (I_{TRPV4}) changes in response to 8s stimulation (produced by a combination of input from astrocyte $[Ca^{2+}]_i$ and vasodilatory feedback).

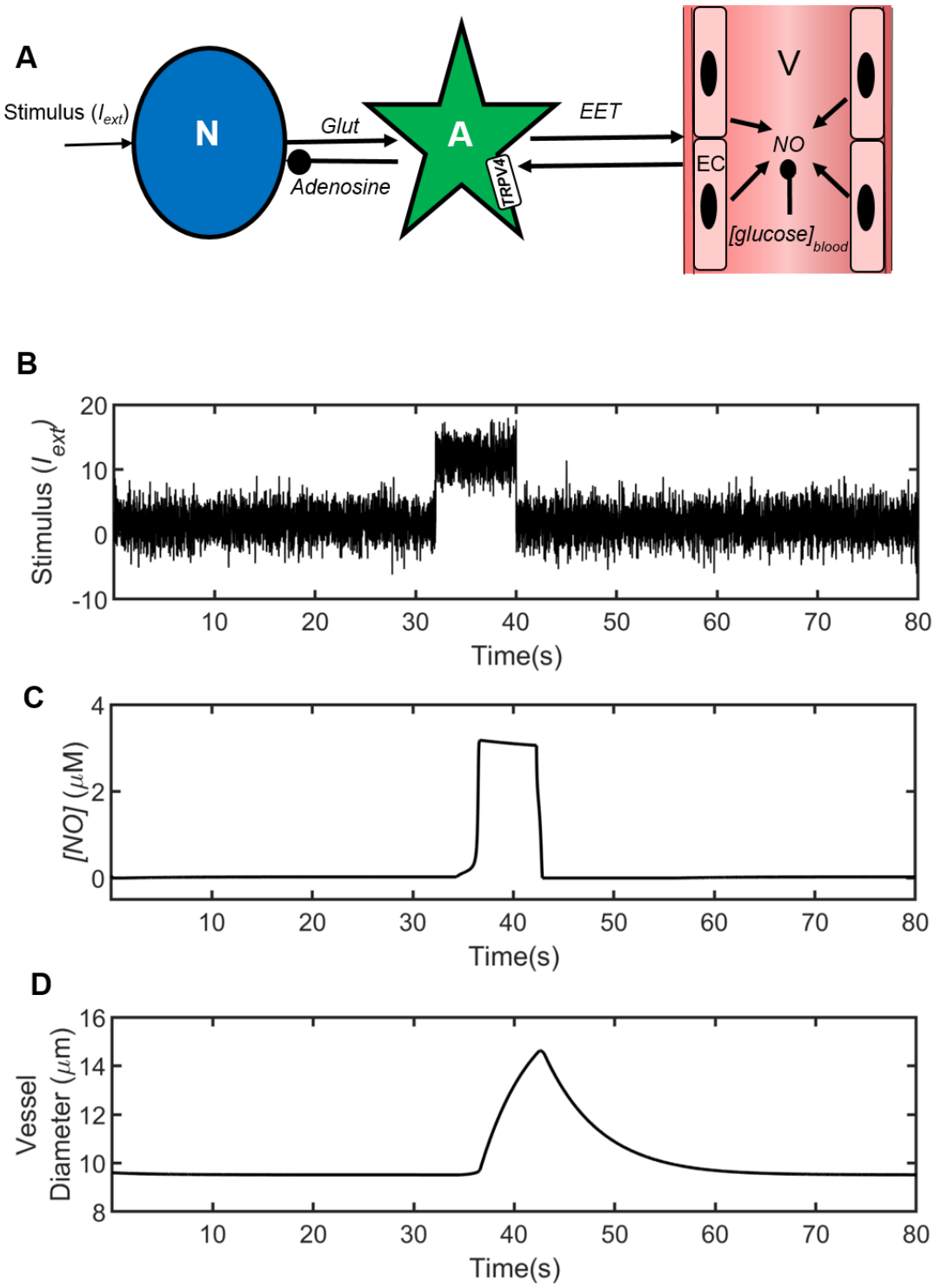

Figure 6-3: Blood vessel compartment dynamics in response to 8 s stimulation with 5mM *[glucose]*$_{blood}$. A: Schematic representation of computational model of neurovascular unit showing the neuron (N), astrocyte (A) and blood vessel (V) compartment. **B:** Stimulation signal (I_{ext}) input to the neuron to model the experimental 8 s stimulation protocol. Random Gaussian noise was added to make it experimentally realistic. **C:** Simulated NO release in the blood vessel compartment in response to astrocyte evoked EET release. **D:** Simulated increase in the vessel diameter (vasodilation) in response to increase in NO in response to 8 s stimulation.

6.3 The effect of high glucose on neurovascular coupling and neuronal firing: the role of TRPV4 feedback

Various studies have demonstrated cerebral blood flow deficits in diabetic patients and animal models of diabetes (407, 408). It is speculated that these result in impaired NVC, however the underlying mechanisms remain unclear. Using the minimal model of NVC described above, I examined whether changing glucose levels in the vessel compartment reproduced the effect of hyperglycemia on NVC. Patients with poorly controlled diabetes have blood glucose levels of 17-20 mM (409, 410). Thus, I applied an 8s stimulation to the model with glucose levels of 20mM in the vessel compartment. Compared to simulations with 5mM glucose, 20mM glucose abolished the evoked NO levels in the vessel compartment and thus abolished vasodilation in response to neuronal stimulus (**Figure 6-4B-C**). As a result of reduced vasodilation under hyperglycemia, the increase in I_{TRPV4} seen in the astrocyte compartment under conditions of 5mM glucose was also abolished by 20mM glucose (**Figure 6-4D**).

I next examined whether the reduction in the TRPV4 current by 20mM glucose affected neuronal activity through vascular feedback, as would be predicted by the hemoneural hypothesis (150, 339). Simulated neuronal responses to an 8s stimulation under 20mM glucose conditions are shown in **Figure 6-5B.**

To observe any changes in the neuronal peaks with sufficient statistical power, I simulated the model for 50 trials and quantified peaks observed during the baseline and recovery time periods defined for the simulations similar to the experimental quantification in **section 2.4.1**). I found neuronal peak frequency during the response time period compared to the baseline and recovery did not differ between 5 mM and 20 mM glucose (**Figure 6-5C**). I then quantified the number of non-stimulus specific (NSS) peaks, defined as number of peaks observed during baseline and recovery time periods for 5mM and 20mM glucose over 50 trials. This showed a significant increase in the spike count in the 20mM glucose trials (**Figure 6-5D**). Together,

these data suggest that although the neuronal responses to 8 s stimulation are conserved in 20mM glucose simulation, there is an increase in spontaneous neuronal firing following stimulation (similar to the increase in baseline neuronal Ca^{2+} peaks observed experimentally in 8 dpf zebrafish, (**section 4.14**).

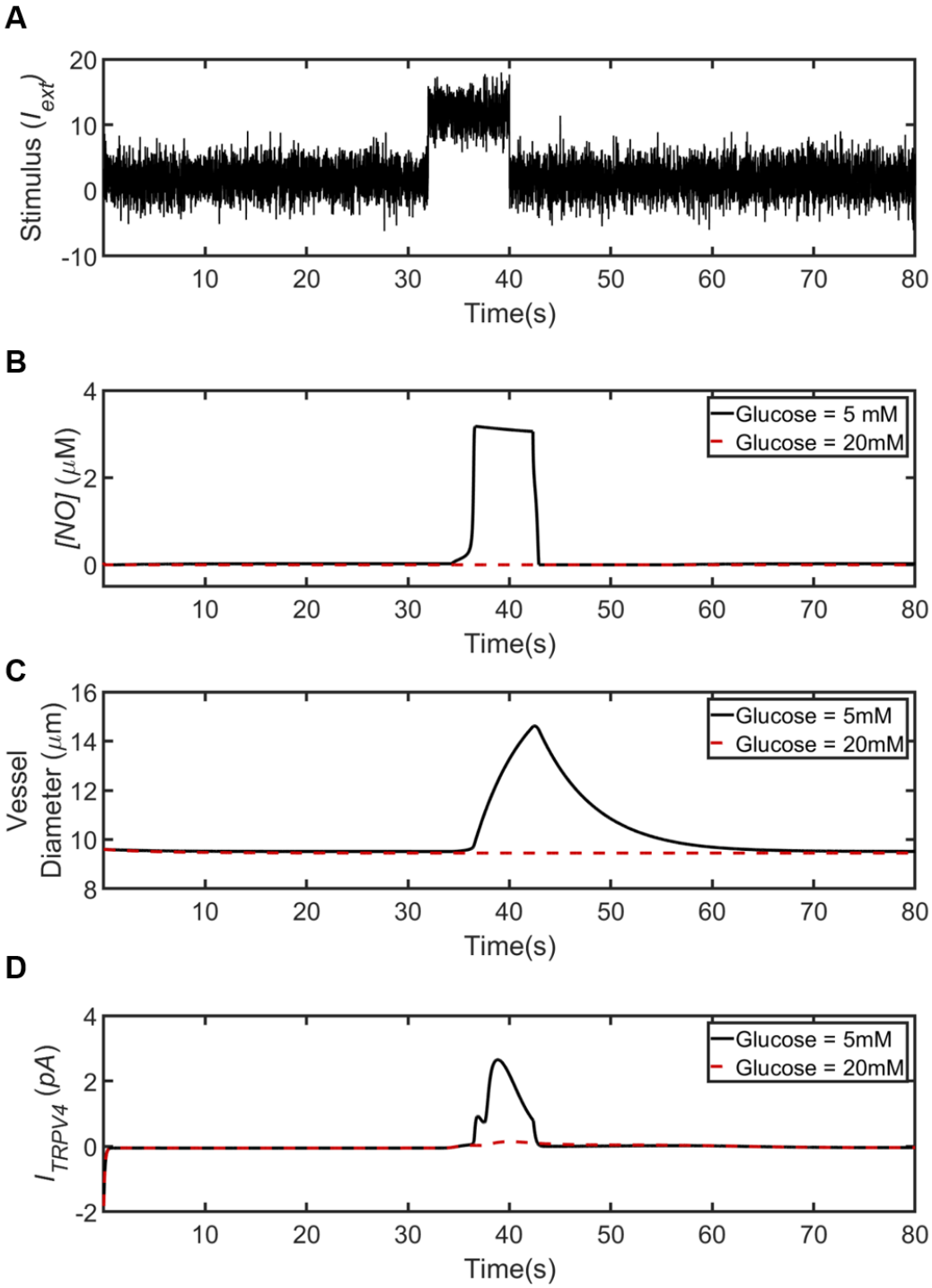

Figure 6-4: Blood vessel and astrocyte TRPV4 dynamics at 20mM *[glucose]*$_{blood}$. A: Stimulation signal (I_{ext}) input to the neuron to model the experimental 8 s stimulation protocol. Random Gaussian noise was added to make it experimentally realistic. **B:** I_{TRPV4} (TRPV4 channel current) in response to 8 s stimulation in the presence of 5 mM (black) and 20 mM (red) glucose. **C:** *[NO]* in the blood vessel compartment in response to 8 s stimulation in the presence of 5 mM (black) and 20 mM (red) glucose. **D:** Blood vessel diameter changes (vasodilation) in response to 8 s stimulation in the presence of 5 mM (black) and 20 mM (red) glucose.

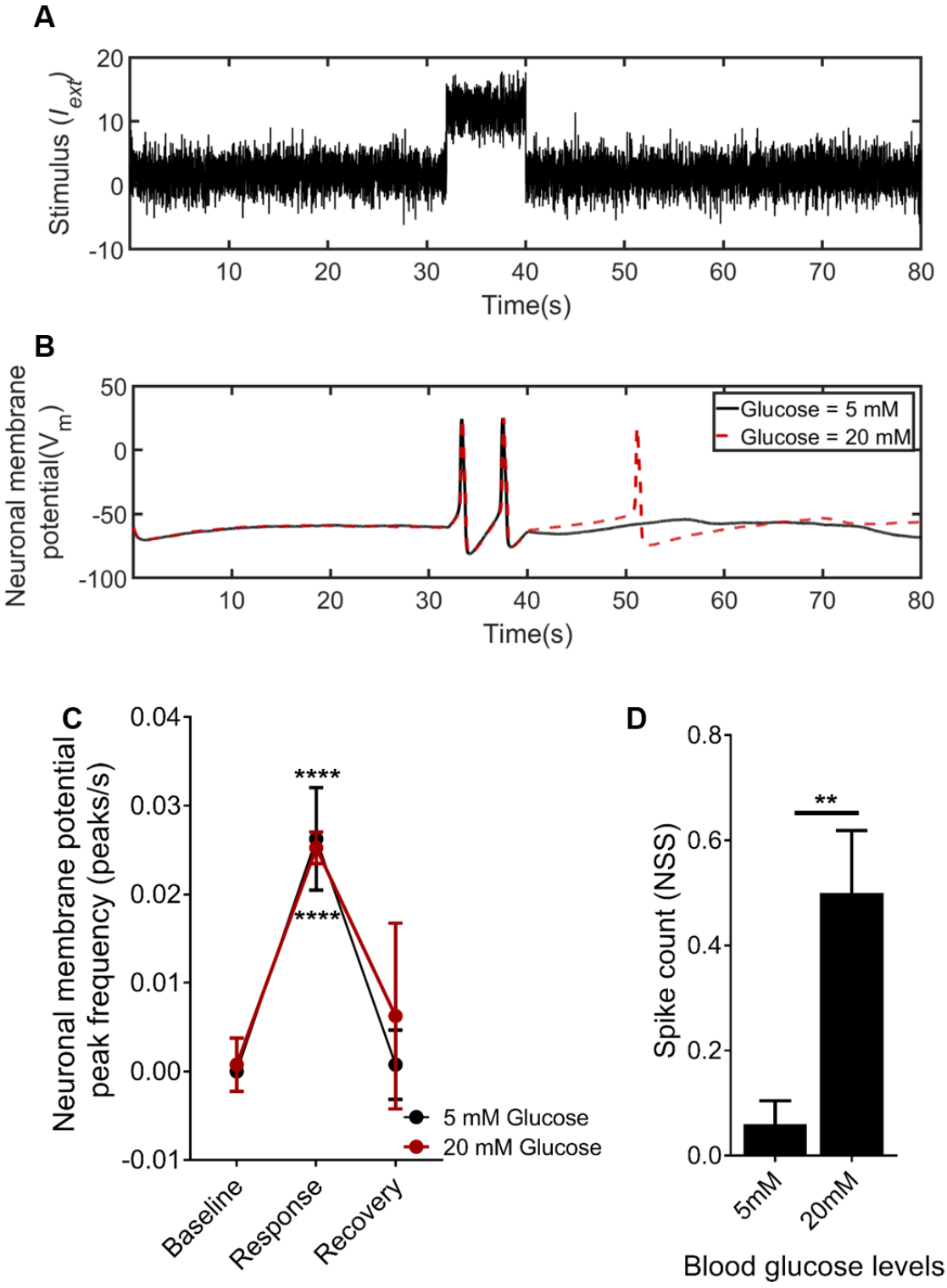

Figure 6-5: Neuronal compartment dynamics at 20mM *[glucose]*$_{blood}$. A: Stimulation signal (I_{ext}) input to the neuron to model the experimental 8 s stimulation protocol. Random Gaussian noise was added to make it experimentally realistic. **B:** Neuronal spikes in response to 8 s stimulation in the presence of 5 mM (black) and 20 mM (red) glucose. **C:** Quantification of neuronal membrane potential spike frequency (peaks/s) during baseline, response and recovery (n=50 simulation trials). **D:** Quantification of non-stimulus specific (NSS) spike count in the presence of 5 mM (black) and 20 mM (red) glucose (n=50 simulation trials) ((two-way ANOVA and unpaired t-test for **C** and **D**, respectively).

6.4 The effect of 20mM glucose exposure on modelled synaptic plasticity: an STDP basis

I next extended the model above to represent two neurons influenced by a single astrocyte and vessel (**Figure 6-6A**). This two neuron network model allows an examination and prediction of the effects of the neurovascular defects observed under hyperglycemic conditions, in particular the reduced vasodilation (from simulations, see **section 6.3**) or RBC speed (from experiments, see **section 4.3**) and increase in the NSS neuronal activity, on synaptic function. Using the standard STDP model for testing synaptic plasticity, I observed the change in the STDP weight throughout the course of 50 trials of training. On simulation, I found a decrease in synaptic weight during the course of training (50 trials) in the presence of 20mM glucose compared to 5mM glucose (**Figure 6-6B**). These data suggest a reduction in simulated STDP in the presence of 20mM glucose that can be tested with future experiments.

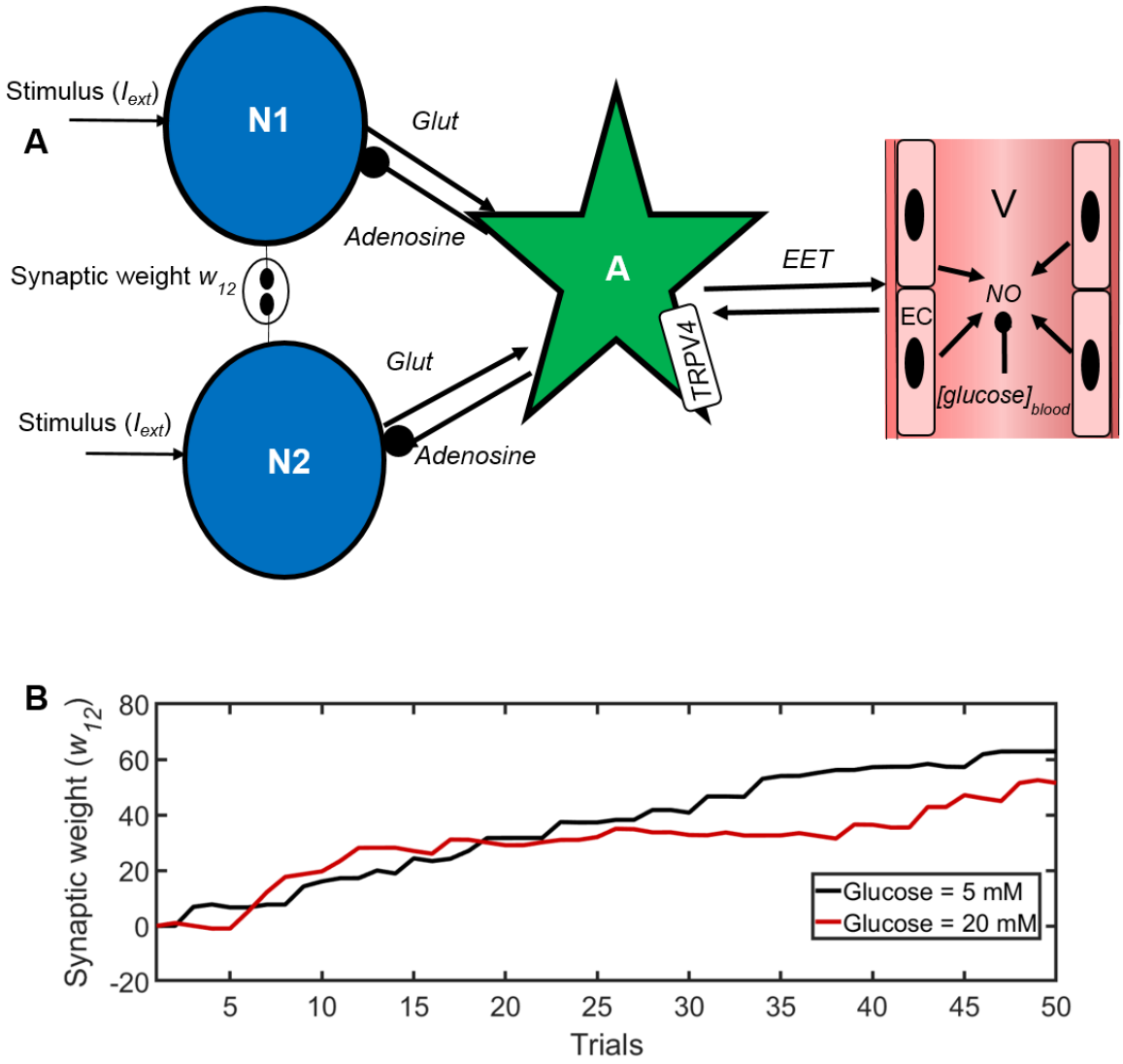

Figure 6-6: Effect of 20mM *[glucose]*$_{blood}$ on modelled synaptic plasticity (STDP). A: Schematic representation of the two neuron (N1 and N2) model coupled to a single astrocyte and vessel via glutamate release (*Glut*) in the feedforward direction through the astrocyte (via EET) and feedback (TRPV4 activation) release of adenosine to the neurons. Neurons N1 and N2 are connected by synapse with connection strength or weight, w_{12} **B:** which is updated over the course of training (n = 50 trials) in the presence of 5mM (black) and 20 mM (red) glucose.

6.5 Discussion

I have developed a computational model of the NVU that simulates neuronal dynamics as changes in the neuronal membrane potential, astrocyte $[Ca^{2+}]_i$ vessel NO and diameter to simulate NVC at normal (5mM) and high (20mM) glucose levels. The parameters of the model are tuned to represent the observed biological time scales for the neuronal, astrocyte and vessel compartment. Although there have been several computational models of NVC (as described in **section 1.12.1**), none have modelled the effect of disease such as diabetes, which are known to be associated with micro- and macrovascular impairment in humans and with impaired cognition (as discussed in **section 1.6**).

Using this model, I simulated responses in the neuron, astrocyte and vessel compartment which reliably reproduced the responses observed in the experimental zebrafish model of hyperglycemia in **chapter 4**. Using an 8 s stimulation paradigm (similar to that applied to my experimental zebrafish model), I have simulated NVC, characterized by an increase in neuronal spiking frequency and associated vasodilation. The simulation results are similar to those characterized in the zebrafish model of NVC, in which 8s visual stimulation evoked an increase in neuronal membrane potential spikes and increase in RBC speed. In addition, the computational model was able to predict variables that cannot currently be easily measured in the zebrafish such as astrocyte $[Ca^{2+}]_i$, TRPV4 current and NO levels. To further validate the model, these predictions should be measured in future experiments (discussed in **chapter 7**).

In **chapter 4**, I demonstrated the effect of hyperglycemia on NVC and suggested a possible role of NO in ameliorating the observed deficits. Although NO deficiency has been reported in both diabetes (411) and associated pathologies (412, 413), the mechanisms by which NO deficiency causes neurovascular deficits is unclear. Using the computational model, I predict

that high glucose levels (20 mM) leads to reduction in NO release in response to stimulation and a reduction in stimulus-evoked vasodilation in the 20mM glucose condition. This could explain the lack of RBC speed increase observed in the zebrafish (**section 4.3**). Using the computational model, I further show an effect of 20mM glucose on neuronal activity as a function of reduced TRPV4 current (339). This could be explained biologically by reduced expression of TRPV4 (**section 4.11**) or dysfunctional TRPV4 as an outcome of hyperglycemia. Further investigation is needed to investigate the mechanistic basis of these predictions of hyperglycemic TRPV4 reductions Finally, I have described the consequences of reduced vasodilation, reduced TRPV4 current and increased neuronal NSS activity on synaptic plasticity mechanisms. In the presence of 20mM glucose, the model predicts a reduction in the update of synaptic weight through a reduction in STDP, a marker of dysfunctional synaptic plasticity (see **section 4**). This effect of high glucose on synaptic plasticity mechanism, as predicted by the computational model in the present studies suggests future directions to design experiments testing effect of hyperglycemia on synaptic plasticity and learning. Dysfunctional synaptic plasticity is known to underlie cognitive defects such as learning, memory and choice preference (which I found to be altered by experimentally induced hyperglycemia in zebrafish, **section 4.13**).

6.6 Conclusions

Developing complementary computational models alongside experimental work can aid us in predicting the mechanisms underlying experimental observations. Furthermore, modelling complex disease pathologies can help predict possible interventions. This is important not only to increase our knowledge but to identify potential targets for drug discovery.

With the minimal computational model of the NVU presented, I have shown similar results to those obtained in my experimental model of NVC (**chapter 4**). Further, I have described the importance of NO in hyperglycemic dysfunction of NVC and, finally, proposed an influence of neurovascular function on synaptic plasticity. There are several advantages of developing simple computational models such as that in this thesis. Firstly, this helps to develop more biologically realistic single unit models to simulate and predict mechanisms of neurovascular and possibly hemoneural hypothesis. Secondly, simple minimal models are powerful tools to simulate neurovascular networks to show how single synaptic change could influence neuronal network activity (such as LFP, EEG) and also to simulate and predict the BOLD responses. Due to technical limitations, it is difficult to measure both deep brain capillary responses and surface arterioles alongside neuronal activity. Hence, complementing experimental data with computational modelling may help address such questions.

There have been several computational models of NVC that aim to understand the mechanisms of NVC but there are no models that attempt the explain the physiology of disrupted NVC in diseases such as diabetes. The minimal model shown here could be used as the foundation to add more vascular details such as modelling the endothelial calcium response and dynamics of glucose metabolism to describe further the disease pathology and its effect on the NVU.

The computational model presented here is simulated to show the effect of 20mM glucose on NVC but can be extended to simulate the effects of various factors such as *gch1* on NVC. In general, with the basic minimal computational model described in the present study, the effect of various interventions on the NVC could be studied to allow further prediction of the effect of various interventions.

7 General Discussions: On the importance of neurovascular coupling in brain function

7.1 Summary

NVC refers to increases in local cerebral blood flow to maintain energy supply to activated neurons. NVC in rodents is measured invasively through a window surgically created in the skull (414, 415). Furthermore, anaesthesia is required to perform the neurovascular measurements, making these less physiological and introducing confounding influences on neuronal activity and vascular tone. To circumvent these constraints, I developed a non-invasive zebrafish model of NVC that exploits their optical transparency and ease of genetic and pharmacological manipulation. Using lightsheet microscopy, I showed that NVC can be detected and quantified in unanesthetized transgenic zebrafish larvae at 8 dpf. Similar to the mammals, zebrafish larvae display spatiotemporal specificity of NVC which develops at a specific developmental stage (between 6-8 dpf). Studies have shown various underlying mechanisms of NVC in rodents including direct NO based modulation of cerebral blood blow by interneurons (26), neuronally evoked astrocytic release of vasoactive substance (through COX) (38) and more recently the involvement of pericytes in controlling capillary diameter (82). I have demonstrated the existence of both NO based modulation and COX based mechanism of NVC in zebrafish, suggesting the mechanisms of NVC are conserved between mammals and zebrafish and validating zebrafish as a tool for investigating the mechanisms of NVC. I have shown the utility of this model for investigating neurovascular dysfunction in vascular and neurodegenerative pathologies (diabetes and *gch1* loss-of-function specifically).

NVC is suggested to be affected in a plethora of neurological disorders and increasingly is associated with dementia (**section 1.5**). Studies investigating pathological mechanisms of AD and PD have shown reductions in cerebral blood flow (416-418). Recent studies have proposed various vascular diseases to be major risk factors for neurodegeneration (169, 203). Diabetes forms a major burden of vascular disease and diabetics are reported to be at increased risk of cognitive defects (419). Animal studies have shown reduction in stimulus associated vasodilation in the cerebral blood vessels with experimentally induced diabetes (244). Other studies have shown hyperglycemia associated NVU defects including activation of inflammatory markers in the brain and increased production of reactive species (199), pericyte drop-out (79) and increased blood brain barrier permeability (420). However, whether these deleterious changes cause defective NVC is unclear. Using my zebrafish model of NVC, I confirmed the negative consequences of 20mM glucose exposure (levels seen in poorly controlled diabetics) on both the anatomy and function of the NVU. The vascular phenotypes induced by glucose exposure included reduced RBC speed, impaired NVC, reduction in vascular anatomical features such as number of branchpoints, vascular length and vessel radius (see **chapter 4**). Glucose exposure affected various components of the NVU including increased expression of glial specific GFAP, GS, iGluSnFR and TRPV4, decrease in endothelial *claudin5a* and *klf2a,* reduction in number of *sm22ab* positive mural cells (including pericytes and smooth muscle cells) and reduced vascular NO. While all these glucose-induced defects have been detected in previous studies in other models, it has not been clear whether these defects are a resultant of NO bioavailability. In the present study, I also showed that co-treating glucose exposed zebrafish larvae with a NO donor SNP ameliorated all the deleterious effects of glucose suggesting an active role of NO in maintaining the function of NVC. All of these findings are summarised in **Figure 7-1**. SNP is commonly used for treating hypertension however its ability to treat diabetes related neurovascular dysfunction has not been tested. Thus,

my work suggests a possible NO based therapeutic treatment for diabetes which should be tested in preclinical mammalian models.

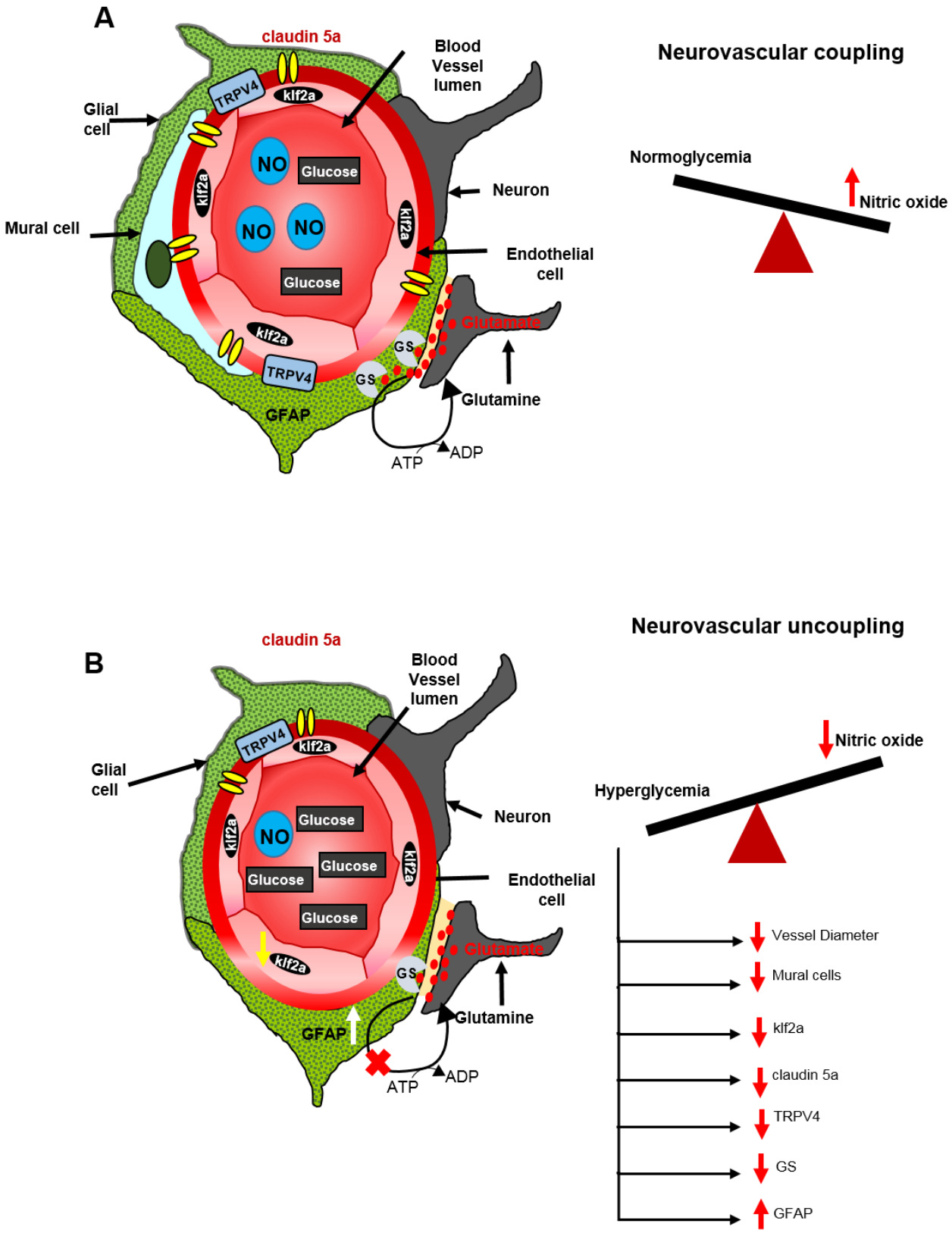

Figure 7-1: Schematic representation of the effect of hyperglycemia on neurovascular unit. A: Cross section of the neurovascular unit showing various markers tested in the zebrafish model under normoglycemia. **B:** Cross section of the neurovascular unit showing alterations of various markers assessed in zebrafish model under hyperglycemia

Gch1 plays an important role in producing an essential cofactor BH4 for NOS and also synthesis of monoaminergic neuromodulators such as serotonin and dopamine (396, 400) Various studies have shown *gch1* mutations are associated with PD (184, 185). Interestingly *gch1* knockout mice develop cardiovascular complications including pulmonary hypertension, diabetes, atherosclerosis and neuropathy (403). Using the novel zebrafish *gch1* mutants developed by Dr. Marcus Keating, I demonstrated these homozygous mutants display impaired NVC and cerebrovascular patterning. Supplementing NO (using SNP) ameliorated these defects. I speculate that SNP induced vasodilation and angiogenesis to maintain neurovascular function. The ability of a NO donor to rescue the effect of both hyperglycaemia and *gch1* mutation is fascinating and points to the central role of NO in neurovascular health. To date, there are no NO-based treatments for diseases associated with neurovascular dysfunction. This further emphasizes the potential for therapeutic strategies that target the cerebral vasculature and its function. Moore and Cao (150) in their seminal hemoneural hypothesis suggested vascular derived NO to be one possible way in which vasculature could modulate the neuronal activity.

To understand the cognitive and behavioural defects observed in various pathologies, it is essential to understand how these affect synaptic plasticity. Synaptic plasticity measurements involve measuring STDP in response to a stimulus. Using a minimal computational model of NVU, I demonstrated that NO can modulate vessel diameter, thereby influencing the activity of astrocytes through mechanical activation of TRPV4 (as established by (160, 338)). Further changes in astrocyte activity can modulate neuronal firing threshold through release of adenosine (160). This mechanism of vascular feedback could be disrupted in pathologies with NO deficiency such as diabetes and PD. Through the computational model proposed in the present study, I have proposed that disrupted vascular feedback under simulated hyperglycemic

conditions (20mM glucose), results in increases in non-stimulus specific neuronal activity which could disrupt the temporal relation between pre- and post-synaptic neurons in a two neuron model, thereby affecting synaptic plasticity. Disrupted synaptic plasticity is associated with learning and memory deficits and could thus underlie the cognitive defects associated with various disease pathologies.

7.2 Limitations and Future work

In the first part of my thesis, I developed a novel model of NVC in 8 dpf old zebrafish that can be used in future to investigate further unknown mechanisms. Future work using this model would involve investigating NVC in response to higher stimulus frequencies similar to that used in mammalian research. On similar lines to mammalian models, NVC could be investigated in different areas of the zebrafish brain and/or using different stimulus modalities. Within the constraint of a closed set up LSFM used in the present study, visual stimulus was the most practical and robust methodology to be used to investigate NVC. However, future research could combine open SPIM with auditory/ mechanical stimuli to investigate NVC in the forebrain/hindbrain. Amongst the various NVC mechanisms suggested, it is now known that NVC in the cerebellum is predominantly neuronal NO driven (26) and astrocyte derived prostaglandin driven in the cortex (38). Thus it would be interesting to see if such area specific mechanisms exist in zebrafish.

There is an ongoing debate about the contribution of various neuronal subtypes to NVC in the mammalian brain. Various studies have established that vasodilation in somatosensory cortex is mediated by excitation of glutamatergic neurons (375). Multiple reports have shown the existence of center-surround (dilation) and contra-ipsilateral (constriction) patterns of hemodynamics in the somatosensory cortex in response to sensory stimulation correlating the

strength of constriction in the surrounding region to the strength of inhibition (421-423). Various recent studies have established various different interneurons messengers to be involved in dilation or constriction of the cortical microvessels. Studies by Cauli et al. (424) have described the role of NO and vasoactive intestinal peptide release in vasodilation in the somatosensory cortex. On the contrary multiple reports have shown interneurons to release factors such as somatostation and neuropeptide-Y causing vasocontriction (424, 425). However, the specific contribution of any/each of these to cortical BOLD responses is yet to be resolved. The ease of genetic manipulation in zebrafish systems and the NVC model (described in the present thesis) provides an opportunity to investigate the contribution of specific neuronal subtypes (particularly the various types of interneurons) to NVC. Future research to develop neuronal subtype specific zebrafish optogenetic line and/or tamoxifen inducible tissue specific lines would help resolve the ongoing debate of the cell type specificity of NVC regulation.

I have shown non-specific NOS (nNOS, eNOS, iNOS) and COX (1 and 2) inhibition causes neurovascular uncoupling in zebrafish. However, the contribution of different NOS and COX isoforms to NVC is still unclear in mammals. Thus, future experiments with specific nNOS/eNOS/iNOS/COX1/COX2 inhibitors could establish the contribution of each. Furthermore, due to the constraint of most of the cellular calcium reporters existing as GCaMPs, it was difficult to visualize glial/endothelial calcium along with neuronal calcium changes. It would be interesting to use RCaMP2 (Red encoded calcium indicator) based transgenics to facilitate multicellular calcium imaging (426). Future studies with developing compound transgenic lines such as *GFAP:RCaMP* could help determine the role of radial glial cells in NVC (and thus their functional similarity to astrocytes).

Zebrafish are commonly used to study the contribution of various genes to vascular development (427). Combining gene editing technologies such as Crispr-Cas9 based gene

knock-out/knock-in (428) with the zebrafish model of NVC would allow examination of the genetic basis of NVC. This would also help understand the relation between genetic risk factors for human neurological disease (such as apoE, (429)) and also similarities/differences compared to NVC in mammalian models.

In the second part of my thesis, I used the zebrafish model of NVC to understand the importance of NO in hyperglycemia. A constraint of the present model of hyperglycemia was the inability to accurately measure blood glucose levels in larval zebrafish. To address this and also to completely investigate NVC in diabetes as a whole disease, future studies could be carried out with streptozotocin injection to induce diabetes (189). Due to the difficulty of injecting drugs at the larval form it was not used in this study. However, future research could examine NVC in adult zebrafish models where the streptozotocin injected method for inducing diabetes is established (430). This is also important to make zebrafish models more comparable to mammalian models wherein NVC is investigated in adult forms. Another method of studying NVC in diabetic models is to study NVC in *pdx-1* zebrafish mutants having reduced β-cells, decreased insulin and elevated glucose (431). This will also allow testing of novel NO based therapeutics in diabetes as a disease and not just glucose exposure. While I have shown the positive recovery effects of SNP, future investigations with other NO donors would establish the potential of NO based drugs for diabetes related treatments.

The behavioural improvements demonstrated with SNP treatment further provide exciting avenues for further research into the links between NO and behaviour/cognition. However, more detailed behavioural characterization should include other cognitive tests such as novel object recognition (NOR) (306) or spontaneous alteration burst (SAB) behaviour (432), which are common tests for hippocampal function (433). These would complement future studies investigating NVC in different brain areas under normal and disease states.

Presence of an eNOS orthologue in zebrafish is currently debated. While genetic studies have established that zebrafish do not possess eNOS, I have shown positive NO reactivity in the zebrafish vasculature using DAF-FM staining (**section 4.6**). I speculate that this NO reactivity could be a resultant of a zebrafish specific NOS whose existence, similarity/difference with respect to mammalian forms needs further investigation. Furthermore, it would be interesting to evaluate changes in NO during NVC (normal/hyperglycemic) and its relation to calcium signalling in vascular ECs and various other cells of the NVU. NO is also commonly known as a mediator of 0.1 Hz vessel oscillations called vasomotion (434) that are independent of heart rate and are affected in several diseases such as diabetes and AD (435, 436). Thus, investigating NO dynamics may help understand the relation of vasomotion to such diseases.

In the third part of my thesis, I extended the use of zebrafish model of NVC to study the effect of the PD related gene, *gch1* and excitingly show recovery of NVC with SNP treatment. Understanding the mechanisms of NVC disruption and positive effects of SNP in *gch1* mutants requires assessment of various NVU markers (such as blood brain barrier permeability markers, endothelial markers, mural cell coverage, glial cell reactivity) over the course of development from 4-9 dpf. This would help understand the factors that contribute to the onset of the pathology in the homozygous mutants.

I have also described the positive effects of SNP on the locomotion defects observed in the homozygous *gch1* mutants. This needs further investigation if the effects of SNP treatment can increase survival rates in the mutants. It would be interesting to investigate cognitive correlates such as light/dark preference, NOR and SAB in homozygous mutants with or without SNP treatment to correlate it to memory and/or hippocampal function. Furthermore, as mentioned earlier, to test if NO based drugs could be quintessential in improving effect of PD pathologies, future work is needed to test the effect of other NO donors.

In the last part of my thesis, I described a computational model simulating the effects of hyperglycemia and predicting related NVC defects (similar to that observed in experimental hyperglycemia). A future direction of this model would be to simulate the effects of SNP in ameliorating hyperglycemic effects of NVC.

The model described in the thesis has minimal parameters to describe the biological findings in the simplest possible framework but provides a foundation upon which to build a more complex model including other biological components as and when they are discovered. For example, the model can be developed further by adding equations representing pericyte and smooth muscle cell intracellular calcium changes. A limitation of the computational model is that the predicted vascular read out is diameter change and not RBC speed which limits its comparisons to the experimental data in this thesis. This is due to the uncertainty of zebrafish parameters such as blood pressure, resistance and viscosity. Future attempts to add various vascular parameters (such as intramural pressure, resistance), could help estimate RBC speed and also to simulate network of vessels connected in a similar way to VAN (328) and predict BOLD responses. Furthermore, scaling the whole NVU to the network would help predict changes in neuronal network parameters (such as EEG/LFP) under hyperglycemia. This could suggest possible EEG based biomarkers to aide prognosis of diabetes and related disorders. A neurovascular network model can also be used to simulate learning and cognitive defects associated with such disease. In general, a computational model of NVC with the scope to model disease can help understand the parametric difference that could underlie observations from animal models.

To conclude, I have first demonstrated a novel zebrafish model to investigate NVC followed by showing neurovascular uncoupling under various disease pathologies such as hyperglycemia and *gch1* mutation (related to cardiovascular complications and PD). To

understand the commonality of the mechanisms between these two pathologies, future research is needed to investigate genetic/functional/anatomic markers of the NVU.

8 References

1. Roy CS, Sherrington CS. On the regulation of the blood-supply of the brain. The Journal of physiology. 1890;11(1-2):85.
2. Nelson AR, Sweeney MD, Sagare AP, Zlokovic BV. Neurovascular dysfunction and neurodegeneration in dementia and Alzheimer's disease. Biochimica et biophysica acta. 2016 May;1862(5):887-900. PubMed PMID: 26705676. Pubmed Central PMCID: 4821735.
3. Lasta M, Pemp B, Schmidl D, Boltz A, Kaya S, Palkovits S, et al. Neurovascular dysfunction precedes neural dysfunction in the retina of patients with type 1 diabetes. Invest Ophthalmol Vis Sci. 2013 Jan 30;54(1):842-7. PubMed PMID: 23307962.
4. Arai K, Lok J, Guo S, Hayakawa K, Xing C, Lo EH. Cellular mechanisms of neurovascular damage and repair after stroke. Journal of child neurology. 2011 Sep;26(9):1193-8. PubMed PMID: 21628695. Pubmed Central PMCID: 3530192.
5. Iadecola C. The Neurovascular Unit Coming of Age: A Journey through Neurovascular Coupling in Health and Disease. Neuron. 2017 Sep 27;96(1):17-42. PubMed PMID: 28957666. Pubmed Central PMCID: 5657612.
6. Niedermeyer E. Alzheimer disease: caused by primary deficiency of the cerebral blood flow. Clinical EEG and neuroscience. 2006 Jul;37(3):175-7. PubMed PMID: 16929700.
7. Le Heron CJ, Wright SL, Melzer TR, Myall DJ, MacAskill MR, Livingston L, et al. Comparing cerebral perfusion in Alzheimer's disease and Parkinson's disease dementia: an ASL-MRI study. J Cerebr Blood F Met. 2014 Jun;34(6):964-70. PubMed PMID: WOS:000336831000006. English.
8. Huang CW, Hsu SW, Chang YT, Huang SH, Huang YC, Lee CC, et al. Cerebral Perfusion Insufficiency and Relationships with Cognitive Deficits in Alzheimer's Disease: A Multiparametric Neuroimaging Study. Sci Rep. 2018 Jan 24;8(1):1541. PubMed PMID: 29367598. Pubmed Central PMCID: 5784155.
9. Luchsinger JA, Reitz C, Patel B, Tang MX, Manly JJ, Mayeux R. Relation of diabetes to mild cognitive impairment. Arch Neurol. 2007 Apr;64(4):570-5. PubMed PMID: 17420320.
10. Whitmer RA, Gustafson DR, Barrett-Connor E, Haan MN, Gunderson EP, Yaffe K. Central obesity and increased risk of dementia more than three decades later. Neurology. 2008 Sep 30;71(14):1057-64. PubMed PMID: 18367704.
11. Ighodaro ET, Abner EL, Fardo DW, Lin AL, Katsumata Y, Schmitt FA, et al. Risk factors and global cognitive status related to brain arteriolosclerosis in elderly individuals. Journal of cerebral blood flow and metabolism : official journal of the International Society of Cerebral Blood Flow and Metabolism. 2017 Jan;37(1):201-16. PubMed PMID: 26738751. Pubmed Central PMCID: 5363738.
12. Rolfe D, Brown GC. Cellular energy utilization and molecular origin of standard metabolic rate in mammals. Physiological reviews. 1997;77(3):731-58.
13. Stamatovic SM, Keep RF, Andjelkovic AV. Brain endothelial cell-cell junctions: how to "open" the blood brain barrier. Curr Neuropharmacol. 2008 Sep;6(3):179-92. PubMed PMID: 19506719. Pubmed Central PMCID: 2687937.
14. Davis TL, Kwong KK, Weisskoff RM, Rosen BR. Calibrated functional MRI: mapping the dynamics of oxidative metabolism. Proceedings of the National Academy of Sciences of the United States of America. 1998 Feb 17;95(4):1834-9. PubMed PMID: 9465103. Pubmed Central PMCID: 19199.
15. Buxton RB, Frank LR. A model for the coupling between cerebral blood flow and oxygen metabolism during neural stimulation. Journal of Cerebral Blood Flow & Metabolism. 1997;17(1):64-72.

16. Zonta M, Angulo MC, Gobbo S, Rosengarten B, Hossmann K-A, Pozzan T, et al. Neuron-to-astrocyte signaling is central to the dynamic control of brain microcirculation. Nature neuroscience. 2003;6(1):43-50.
17. Kobayashi H, Magnoni M, Govoni S, Izumi F, Wada A, Trabucchi M. Neuronal control of brain microvessel function. Experientia. 1985;41(4):427-34.
18. Mosso A. Concerning the circulation of the blood in the human brain. Leipzig: Verlag von Viet & Company. 1881.
19. Sandrone S, Bacigaluppi M, Galloni MR, Cappa SF, Moro A, Catani M, et al. Weighing brain activity with the balance: Angelo Mosso's original manuscripts come to light. Brain. 2013:awt091.
20. Huo B-X, Smith JB, Drew PJ. Neurovascular coupling and decoupling in the cortex during voluntary locomotion. The Journal of Neuroscience. 2014;34(33):10975-81.
21. Hodgkin A, Huxley A. Resting and action potentials in single nerve fibres. The Journal of physiology. 1945;104(2):176.
22. Noble D. A modification of the Hodgkin—Huxley equations applicable to Purkinje fibre action and pacemaker potentials. The Journal of Physiology. 1962;160(2):317.
23. Carpenter DO, Alving BO. A contribution of an electrogenic Na+ pump to membrane potential in Aplysia neurons. The Journal of general physiology. 1968;52(1):1-21.
24. Attwell D, Laughlin SB. An energy budget for signaling in the grey matter of the brain. Journal of Cerebral Blood Flow & Metabolism. 2001;21(10):1133-45.
25. Attwell D, Buchan AM, Charpak S, Lauritzen M, MacVicar BA, Newman EA. Glial and neuronal control of brain blood flow. Nature. 2010;468(7321):232-43.
26. Cauli B, Tong X-K, Rancillac A, Serluca N, Lambolez B, Rossier J, et al. Cortical GABA interneurons in neurovascular coupling: relays for subcortical vasoactive pathways. The Journal of Neuroscience. 2004;24(41):8940-9.
27. Petzold GC, Murthy VN. Role of astrocytes in neurovascular coupling. Neuron. 2011 Sep 8;71(5):782-97. PubMed PMID: 21903073.
28. Perea G, Araque A. Properties of synaptically evoked astrocyte calcium signal reveal synaptic information processing by astrocytes. The Journal of neuroscience. 2005;25(9):2192-203.
29. Bezzi P, Volterra A. A neuron–glia signalling network in the active brain. Current opinion in neurobiology. 2001;11(3):387-94.
30. Fields RD. The other brain. Simon & Schuster: New York Rizzoli SO, Betz WJ (2005) Synaptic vesicle pools Nat Rev Neurosci. 2009;6(1):57-69.
31. . !!! INVALID CITATION !!!
32. Oberheim NA, Wang X, Goldman S, Nedergaard M. Astrocytic complexity distinguishes the human brain. Trends in neurosciences. 2006;29(10):547-53.
33. Mulligan SJ, MacVicar BA. Calcium transients in astrocyte endfeet cause cerebrovascular constrictions. Nature. 2004 Sep 9;431(7005):195-9. PubMed PMID: 15356633.
34. Paspalas CD, Papadopoulos GC. Ultrastructural relationships between noradrenergic nerve fibers and non-neuronal elements in the rat cerebral cortex. Glia. 1996;17(2):133-46.
35. Porter JT, McCarthy KD. Hippocampal astrocytes in situ respond to glutamate released from synaptic terminals. The Journal of Neuroscience. 1996;16(16):5073-81.
36. Araque A, Parpura V, Sanzgiri RP, Haydon PG. Tripartite synapses: glia, the unacknowledged partner. Trends in neurosciences. 1999;22(5):208-15.
37. Wang X, Lou N, Xu Q, Tian G-F, Peng WG, Han X, et al. Astrocytic Ca 2+ signaling evoked by sensory stimulation in vivo. Nature neuroscience. 2006;9(6):816.
38. Takano T, Tian G-F, Peng W, Lou N, Libionka W, Han X, et al. Astrocyte-mediated control of cerebral blood flow. Nature neuroscience. 2006;9(2):260-7.
39. Araque A, Sanzgiri RP, Parpura V, Haydon PG. Astrocyte-induced modulation of synaptic transmission. Canadian journal of physiology and pharmacology. 1999;77(9):699-706.
40. Brockhaus J, Deitmer JW. Long-lasting modulation of synaptic input to Purkinje neurons by Bergmann glia stimulation in rat brain slices. The Journal of physiology. 2002;545(2):581-93.

41. Araque A, Carmignoto G, Haydon PG, Oliet SH, Robitaille R, Volterra A. Gliotransmitters travel in time and space. Neuron. 2014;81(4):728-39.
42. Newman EA, Frambach DA, Odette LL. Control of Extracellular Potassium Levels by Retinal Glial-Cell K+ Siphoning. Science. 1984;225(4667):1174-5. PubMed PMID: WOS:A1984TG80300040. English.
43. Ishibashi T, Dakin KA, Stevens B, Lee PR, Kozlov SV, Stewart CL, et al. Astrocytes promote myelination in response to electrical impulses. Neuron. 2006;49(6):823-32.
44. Haydon PG, Carmignoto G. Astrocyte control of synaptic transmission and neurovascular coupling. Physiological reviews. 2006;86(3):1009-31.
45. Zonta M, Sebelin A, Gobbo S, Fellin T, Pozzan T, Carmignoto G. Glutamate-mediated cytosolic calcium oscillations regulate a pulsatile prostaglandin release from cultured rat astrocytes. J Physiol. 2003 Dec 1;553(Pt 2):407-14. PubMed PMID: 14500777. Pubmed Central PMCID: 2343582.
46. Sun W, McConnell E, Pare JF, Xu Q, Chen M, Peng W, et al. Glutamate-dependent neuroglial calcium signaling differs between young and adult brain. Science. 2013 Jan 11;339(6116):197-200. PubMed PMID: 23307741. Pubmed Central PMCID: 3569008.
47. Winship IR, Plaa N, Murphy TH. Rapid astrocyte calcium signals correlate with neuronal activity and onset of the hemodynamic response in vivo. The Journal of neuroscience : the official journal of the Society for Neuroscience. 2007 Jun 6;27(23):6268-72. PubMed PMID: 17554000.
48. Nizar K, Uhlirova H, Tian P, Saisan PA, Cheng Q, Reznichenko L, et al. In vivo stimulus-induced vasodilation occurs without IP3 receptor activation and may precede astrocytic calcium increase. The Journal of neuroscience : the official journal of the Society for Neuroscience. 2013 May 8;33(19):8411-22. PubMed PMID: 23658179. Pubmed Central PMCID: 3712855.
49. Mishra A, Reynolds JP, Chen Y, Gourine AV, Rusakov DA, Attwell D. Astrocytes mediate neurovascular signaling to capillary pericytes but not to arterioles. Nat Neurosci. 2016 Dec;19(12):1619-27. PubMed PMID: 27775719. Pubmed Central PMCID: 5131849.
50. Gebremedhin D, Ma Y, Falck JR, Roman RJ, VanRollins M, Harder DR. Mechanism of action of cerebral epoxyeicosatrienoic acids on cerebral arterial smooth muscle. American Journal of Physiology-Heart and Circulatory Physiology. 1992;263(2):H519-H25.
51. Hill RA, Tong L, Yuan P, Murikinati S, Gupta S, Grutzendler J. Regional blood flow in the normal and ischemic brain is controlled by arteriolar smooth muscle cell contractility and not by capillary pericytes. Neuron. 2015;87(1):95-110.
52. Michel J-B, Li Z, Lacolley P. Smooth muscle cells and vascular diseases. Cardiovascular research. 2012;95(2):135-7.
53. Nelson MT, Quayle JM. Physiological roles and properties of potassium channels in arterial smooth muscle. American Journal of Physiology-Cell Physiology. 1995;268(4):C799-C822.
54. Rossitti S, Frangos J, Girard PR, Bevan J. Regulation of vascular tone. Canadian journal of physiology and pharmacology. 1995;73(5):544-50.
55. Brayden JE. Membrane hyperpolarization is a mechanism of endothelium-dependent cerebral vasodilation. American Journal of Physiology-Heart and Circulatory Physiology. 1990;259(3):H668-H73.
56. Metea MR, Newman EA. Glial cells dilate and constrict blood vessels: a mechanism of neurovascular coupling. The Journal of neuroscience. 2006;26(11):2862-70.
57. Lindauer U, Megow D, Matsuda H, Dirnagl U. Nitric oxide: a modulator, but not a mediator, of neurovascular coupling in rat somatosensory cortex. American Journal of Physiology-Heart and Circulatory Physiology. 1999;277(2):H799-H811.
58. Girouard H, Bonev AD, Hannah RM, Meredith A, Aldrich RW, Nelson MT. Astrocytic endfoot Ca2+ and BK channels determine both arteriolar dilation and constriction. Proceedings of the National Academy of Sciences. 2010;107(8):3811-6.
59. Dunn KM, Nelson MT. Potassium channels and neurovascular coupling. Circulation journal: official journal of the Japanese Circulation Society. 2010;74(4):608.

60. Dabertrand F, Hannah RM, Pearson JM, Hill-Eubanks DC, Brayden JE, Nelson MT. Prostaglandin E2, a postulated astrocyte-derived neurovascular coupling agent, constricts rather than dilates parenchymal arterioles. Journal of Cerebral Blood Flow & Metabolism. 2013;33(4):479-82.
61. Coney AM, Marshall JM. Contribution of adenosine to the depression of sympathetically evoked vasoconstriction induced by systemic hypoxia in the rat. The Journal of physiology. 2003;549(2):613-23.
62. Rosenblum WI, Nelson GH. Tone regulates opposing endothelium-dependent and -independent forces: resistance brain vessels in vivo. The American journal of physiology. 1990 Jul;259(1 Pt 2):H243-7. PubMed PMID: 2375411.
63. Armstead WM, Mirro R, Busija DW, Leffler CW. Vascular responses to vasopressin are tone-dependent in the cerebral circulation of the newborn pig. Circ Res. 1989 Jan;64(1):136-44. PubMed PMID: 2909297.
64. Korn J, Christ B, Kurz H. Neuroectodermal origin of brain pericytes and vascular smooth muscle cells. Journal of Comparative Neurology. 2002;442(1):78-88.
65. Sims DE. The pericyte—a review. Tissue and Cell. 1986;18(2):153-74.
66. Gerhardt H, Betsholtz C. Endothelial-pericyte interactions in angiogenesis. Cell and tissue research. 2003;314(1):15-23.
67. Ozerdem U, Grako KA, Dahlin-Huppe K, Monosov E, Stallcup WB. NG2 proteoglycan is expressed exclusively by mural cells during vascular morphogenesis. Developmental Dynamics. 2001;222(2):218-27.
68. Alliot F, Rutin J, Leenen P, Pessac B. Pericytes and periendothelial cells of brain parenchyma vessels co-express aminopeptidase N, aminopeptidase A, and nestin. Journal of neuroscience research. 1999;58(3):367-78.
69. Armulik A, Abramsson A, Betsholtz C. Endothelial/pericyte interactions. Circulation research. 2005;97(6):512-23.
70. Armulik A, Genové G, Betsholtz C. Pericytes: developmental, physiological, and pathological perspectives, problems, and promises. Developmental cell. 2011;21(2):193-215.
71. Frank RN, Turczyn TJ, Das A. Pericyte coverage of retinal and cerebral capillaries. Investigative ophthalmology & visual science. 1990;31(6):999-1007.
72. Armulik A, Genové G, Mäe M, Nisancioglu MH, Wallgard E, Niaudet C, et al. Pericytes regulate the blood-brain barrier. Nature. 2010;468(7323):557-61.
73. Bell RD, Winkler EA, Sagare AP, Singh I, LaRue B, Deane R, et al. Pericytes control key neurovascular functions and neuronal phenotype in the adult brain and during brain aging. Neuron. 2010;68(3):409-27.
74. Chou J, Rollins S, Fawzi AA. Role of endothelial cell and pericyte dysfunction in diabetic retinopathy: review of techniques in rodent models. Advances in experimental medicine and biology. 2014;801:669-75. PubMed PMID: 24664757. Pubmed Central PMCID: 4324463.
75. Ferland-McCollough D, Slater S, Richard J, Reni C, Mangialardi G. Pericytes, an overlooked player in vascular pathobiology. Pharmacology & therapeutics. 2017 Mar;171:30-42. PubMed PMID: 27916653. Pubmed Central PMCID: 6008604.
76. Winkler EA, Bell RD, Zlokovic BV. Pericyte-specific expression of PDGF beta receptor in mouse models with normal and deficient PDGF beta receptor signaling. Molecular neurodegeneration. 2010;5(1):1.
77. Beltramo E, Porta M. Pericyte loss in diabetic retinopathy: mechanisms and consequences. Current medicinal chemistry. 2013;20(26):3218-25. PubMed PMID: 23745544.
78. Fu D, Yu JY, Yang S, Wu M, Hammad SM, Connell AR, et al. Survival or death: a dual role for autophagy in stress-induced pericyte loss in diabetic retinopathy. Diabetologia. 2016 Oct;59(10):2251-61. PubMed PMID: 27475954. Pubmed Central PMCID: 5016562.
79. Pfister F, Feng Y, vom Hagen F, Hoffmann S, Molema G, Hillebrands JL, et al. Pericyte migration: a novel mechanism of pericyte loss in experimental diabetic retinopathy. Diabetes. 2008 Sep;57(9):2495-502. PubMed PMID: 18559662. Pubmed Central PMCID: 2518502.

80. Harder DR, Alkayed NJ, Lange AR, Gebremedhin D, Roman RJ. Functional hyperemia in the brain hypothesis for astrocyte-derived vasodilator metabolites. Stroke. 1998;29(1):229-34.
81. Hall CN, Reynell C, Gesslein B, Hamilton NB, Mishra A, Sutherland BA, et al. Capillary pericytes regulate cerebral blood flow in health and disease. Nature. 2014;508(7494):55-60.
82. Peppiatt CM, Howarth C, Mobbs P, Attwell D. Bidirectional control of CNS capillary diameter by pericytes. Nature. 2006;443(7112):700-4.
83. Fernández-Klett F, Offenhauser N, Dirnagl U, Priller J, Lindauer U. Pericytes in capillaries are contractile in vivo, but arterioles mediate functional hyperemia in the mouse brain. Proceedings of the National Academy of Sciences. 2010;107(51):22290-5.
84. Attwell D, Mishra A, Hall CN, O'Farrell FM, Dalkara T. What is a pericyte? Journal of cerebral blood flow and metabolism : official journal of the International Society of Cerebral Blood Flow and Metabolism. 2016 Feb;36(2):451-5. PubMed PMID: 26661200. Pubmed Central PMCID: 4759679.
85. Hartmann DA, Underly RG, Grant RI, Watson AN, Lindner V, Shih AY. Pericyte structure and distribution in the cerebral cortex revealed by high-resolution imaging of transgenic mice. Neurophotonics. 2015 Oct;2(4):041402. PubMed PMID: 26158016. Pubmed Central PMCID: 4478963.
86. Ignarro LJ, Buga GM, Wood KS, Byrns RE, Chaudhuri G. Endothelium-derived relaxing factor produced and released from artery and vein is nitric oxide. Proceedings of the National Academy of Sciences. 1987;84(24):9265-9.
87. Palmer RM, Ferrige A, Moncada S. Nitric oxide release accounts for the biological activity of endothelium-derived relaxing factor. 1987.
88. Tang DG, Conti CJ, editors. Endothelial cell development, vasculogenesis, angiogenesis, and tumor neovascularization: an update. Seminars in thrombosis and hemostasis; 2004: Copyright© 2004 by Thieme Medical Publishers, Inc., 333 Seventh Avenue, New York, NY 10001, USA.
89. Andresen J, Shafi NI, Bryan RM. Endothelial influences on cerebrovascular tone. Journal of Applied Physiology. 2006;100(1):318-27.
90. Leventhal C, Rafii S, Rafii D, Shahar A, Goldman SA. Endothelial trophic support of neuronal production and recruitment from the adult mammalian subependyma. Molecular and Cellular Neuroscience. 1999;13(6):450-64.
91. Ge S, Song L, Pachter JS. Where is the blood–brain barrier… really? Journal of neuroscience research. 2005;79(4):421-7.
92. Bazzoni G, Dejana E. Endothelial cell-to-cell junctions: molecular organization and role in vascular homeostasis. Physiological reviews. 2004;84(3):869-901.
93. Rubin L, Staddon J. The cell biology of the blood-brain barrier. Annual review of neuroscience. 1999;22(1):11-28.
94. Gonzalez-Mariscal L, Betanzos A, Nava P, Jaramillo B. Tight junction proteins. Progress in biophysics and molecular biology. 2003;81(1):1-44.
95. Lampugnani MG, Corada M, Andriopoulou P, Esser S, Risau W, Dejana E. Cell confluence regulates tyrosine phosphorylation of adherens junction components in endothelial cells. Journal of cell science. 1997 Sep;110 (Pt 17):2065-77. PubMed PMID: 9378757.
96. Lee MJ, Thangada S, Claffey KP, Ancellin N, Liu CH, Kluk M, et al. Vascular endothelial cell adherens junction assembly and morphogenesis induced by sphingosine-1-phosphate. Cell. 1999 Oct 29;99(3):301-12. PubMed PMID: 10555146.
97. Ruffer C, Strey A, Janning A, Kim KS, Gerke V. Cell-cell junctions of dermal microvascular endothelial cells contain tight and adherens junction proteins in spatial proximity. Biochemistry. 2004 May 11;43(18):5360-9. PubMed PMID: 15122902.
98. Cai H, Harrison DG. Endothelial dysfunction in cardiovascular diseases: the role of oxidant stress. Circulation research. 2000;87(10):840-4.
99. Faraci FM, Lentz SR. Hyperhomocysteinemia, oxidative stress, and cerebral vascular dysfunction. Stroke. 2004;35(2):345-7.
100. Koizumi K, Wang G, Park L. Endothelial dysfunction and amyloid-β-induced neurovascular alterations. Cellular and molecular neurobiology. 2016;36(2):155-65.

101. Desai BS, Monahan AJ, Carvey PM, Hendey B. Blood–brain barrier pathology in Alzheimer's and Parkinson's disease: implications for drug therapy. Cell transplantation. 2007;16(3):285-99.
102. Alvarez JI, Teale JM. Breakdown of the blood brain barrier and blood–cerebrospinal fluid barrier is associated with differential leukocyte migration in distinct compartments of the CNS during the course of murine NCC. Journal of neuroimmunology. 2006;173(1):45-55.
103. Stamatovic SM, Keep RF, Andjelkovic AV. Brain endothelial cell-cell junctions: how to "open" the blood brain barrier. Current neuropharmacology. 2008;6(3):179-92.
104. Iadecola C. Neurovascular regulation in the normal brain and in Alzheimer's disease. Nature Reviews Neuroscience. 2004;5(5):347-60.
105. Dimitrijevic OB, Stamatovic SM, Keep RF, Andjelkovic AV. Effects of the chemokine CCL2 on blood–brain barrier permeability during ischemia–reperfusion injury. Journal of Cerebral Blood Flow & Metabolism. 2006;26(6):797-810.
106. Argaw AT, Zhang Y, Snyder BJ, Zhao M-L, Kopp N, Lee SC, et al. IL-1β regulates blood-brain barrier permeability via reactivation of the hypoxia-angiogenesis program. The Journal of Immunology. 2006;177(8):5574-84.
107. Zhang ZG, Zhang L, Jiang Q, Zhang R, Davies K, Powers C, et al. VEGF enhances angiogenesis and promotes blood-brain barrier leakage in the ischemic brain. The Journal of clinical investigation. 2000;106(7):829-38.
108. Abbott NJ. Inflammatory mediators and modulation of blood–brain barrier permeability. Cellular and molecular neurobiology. 2000;20(2):131-47.
109. Poole AW, Pula G, Hers I, Crosby D, Jones ML. PKC-interacting proteins: from function to pharmacology. Trends in pharmacological sciences. 2004;25(10):528-35.
110. Konstantoulaki M, Kouklis P, Malik AB. Protein kinase C modifications of VE-cadherin, p120, and β-catenin contribute to endothelial barrier dysregulation induced by thrombin. American Journal of Physiology-Lung Cellular and Molecular Physiology. 2003;285(2):L434-L42.
111. Spyridopoulos I, Luedemann C, Chen D, Kearney M, Chen D, Murohara T, et al. Divergence of angiogenic and vascular permeability signaling by VEGF inhibition of protein kinase C suppresses VEGF-induced angiogenesis, but promotes VEGF-induced, no-dependent vascular permeability. Arteriosclerosis, thrombosis, and vascular biology. 2002;22(6):901-6.
112. MacIntyre A, Abramov R, Hammond CJ, Hudson A, Arking E, Little CS, et al. Chlamydia pneumoniae infection promotes the transmigration of monocytes through human brain endothelial cells. Journal of neuroscience research. 2003;71(5):740-50.
113. Chen SH, Stins MF, Huang S-H, Chen YH, Kwon-Chung K, Chang Y, et al. Cryptococcus neoformans induces alterations in the cytoskeleton of human brain microvascular endothelial cells. Journal of medical microbiology. 2003;52(11):961-70.
114. Guo S, Kim WJ, Lok J, Lee S-R, Besancon E, Luo B-H, et al. Neuroprotection via matrix-trophic coupling between cerebral endothelial cells and neurons. Proceedings of the National Academy of Sciences. 2008;105(21):7582-7.
115. Haynes W, Webb D. Contribution of endogenous generation of endothelin-1 to basal vascular tone. The Lancet. 1994;344(8926):852-4.
116. Ali A, Barrett J, Eling T. Prostaglandin and thromboxane production by fibroblasts and vascular endothelial cells. Prostaglandins. 1980;20(4):667-88.
117. Chen BR, Kozberg MG, Bouchard MB, Shaik MA, Hillman EM. A critical role for the vascular endothelium in functional neurovascular coupling in the brain. Journal of the American Heart Association. 2014;3(3):e000787.
118. Segal SS, Duling BR. Conduction of vasomotor responses in arterioles: a role for cell-to-cell coupling? American Journal of Physiology-Heart and Circulatory Physiology. 1989;256(3):H838-H45.
119. Blinder P, Tsai PS, Kaufhold JP, Knutsen PM, Suhl H, Kleinfeld D. The cortical angiome: an interconnected vascular network with noncolumnar patterns of blood flow. Nature neuroscience. 2013;16(7):889.

120. Sunderland S. Blood supply of the nerves of the upper limb in man. Archives of Neurology & Psychiatry. 1945;53(2):91-115.
121. Mukouyama YS, Shin D, Britsch S, Taniguchi M, Anderson DJ. Sensory nerves determine the pattern of arterial differentiation and blood vessel branching in the skin. Cell. 2002 Jun 14;109(6):693-705. PubMed PMID: 12086669.
122. Gu XH, Terenghi G, Kangesu T, Navsaria HA, Springall DR, Leigh IM, et al. Regeneration pattern of blood vessels and nerves in cultured keratinocyte grafts assessed by confocal laser scanning microscopy. The British journal of dermatology. 1995 Mar;132(3):376-83. PubMed PMID: 7718453.
123. Oh WJ, Gu C. Establishment of neurovascular congruency in the mouse whisker system by an independent patterning mechanism. Neuron. 2013 Oct 16;80(2):458-69. PubMed PMID: 24139045. Pubmed Central PMCID: 3998758.
124. Bates D, Taylor GI, Minichiello J, Farlie P, Cichowitz A, Watson N, et al. Neurovascular congruence results from a shared patterning mechanism that utilizes Semaphorin3A and Neuropilin-1. Dev Biol. 2003 Mar 1;255(1):77-98. PubMed PMID: 12618135.
125. Carmeliet P. Blood vessels and nerves: common signals, pathways and diseases. Nature reviews Genetics. 2003 Sep;4(9):710-20. PubMed PMID: 12951572.
126. Stubbs D, DeProto J, Nie K, Englund C, Mahmud I, Hevner R, et al. Neurovascular congruence during cerebral cortical development. Cerebral cortex. 2009 Jul;19 Suppl 1:i32-41. PubMed PMID: 19386634. Pubmed Central PMCID: 2693536.
127. Sondell M, Lundborg G, Kanje M. Vascular endothelial growth factor has neurotrophic activity and stimulates axonal outgrowth, enhancing cell survival and Schwann cell proliferation in the peripheral nervous system. Journal of Neuroscience. 1999;19(14):5731-40.
128. Behar O, Golden JA, Mashimo H, Schoen FJ, Fishman MC. Semaphorin III is needed for normal patterning and growth of nerves, bones and heart. Nature. 1996;383(6600):525.
129. Takahashi Y, Imanaka T, Takano T. Spatial and temporal pattern of smooth muscle cell differentiation during development of the vascular system in the mouse embryo. Anatomy and embryology. 1996 Nov;194(5):515-26. PubMed PMID: 8905017.
130. Kawasaki T, Kitsukawa T, Bekku Y, Matsuda Y, Sanbo M, Yagi T, et al. A requirement for neuropilin-1 in embryonic vessel formation. Development. 1999 Nov;126(21):4895-902. PubMed PMID: 10518505.
131. Carmeliet P, Tessier-Lavigne M. Common mechanisms of nerve and blood vessel wiring. Nature. 2005;436(7048):193.
132. Quaegebeur A, Lange C, Carmeliet P. The neurovascular link in health and disease: molecular mechanisms and therapeutic implications. Neuron. 2011 Aug 11;71(3):406-24. PubMed PMID: 21835339.
133. Zlokovic BV. The blood-brain barrier in health and chronic neurodegenerative disorders. Neuron. 2008 Jan 24;57(2):178-201. PubMed PMID: 18215617.
134. Kozberg MG, Chen BR, DeLeo SE, Bouchard MB, Hillman EM. Resolving the transition from negative to positive blood oxygen level-dependent responses in the developing brain. Proceedings of the National Academy of Sciences of the United States of America. 2013 Mar 12;110(11):4380-5. PubMed PMID: 23426630. Pubmed Central PMCID: 3600493.
135. Anderson AW, Marois R, Colson ER, Peterson BS, Duncan CC, Ehrenkranz RA, et al. Neonatal auditory activation detected by functional magnetic resonance imaging. Magnetic resonance imaging. 2001 Jan;19(1):1-5. PubMed PMID: 11295339.
136. Born P, Rostrup E, Leth H, Peitersen B, Lou HC. Change of visually induced cortical activation patterns during development. Lancet. 1996 Feb 24;347(9000):543. PubMed PMID: 8596290.
137. Kozberg MG, Hillman EM. Neurovascular coupling develops alongside neural circuits in the postnatal brain. Neurogenesis. 2016;3(1):e1244439. PubMed PMID: 27900344. Pubmed Central PMCID: 5111578.

138. Zehendner CM, Tsohataridis S, Luhmann HJ, Yang JW. Developmental switch in neurovascular coupling in the immature rodent barrel cortex. PLoS One. 2013;8(11):e80749. PubMed PMID: 24224059. Pubmed Central PMCID: 3818260.
139. Binmöller FJ, Müller C. Postnatal development of dye-coupling among astrocytes in rat visual cortex. Glia. 1992;6(2):127-37.
140. Fujimoto K. Pericyte-endothelial gap junctions in developing rat cerebral capillaries: a fine structural study. The Anatomical record. 1995 Aug;242(4):562-5. PubMed PMID: 7486026.
141. Singer D. Neonatal tolerance to hypoxia: a comparative-physiological approach. Comparative biochemistry and physiology Part A, Molecular & integrative physiology. 1999 Jul;123(3):221-34. PubMed PMID: 10501017.
142. Harb R, Whiteus C, Freitas C, Grutzendler J. In vivo imaging of cerebral microvascular plasticity from birth to death. Journal of Cerebral Blood Flow & Metabolism. 2013;33(1):146-56.
143. Rowan RA, Maxwell DS. Patterns of vascular sprouting in the postnatal development of the cerebral cortex of the rat. The American journal of anatomy. 1981 Mar;160(3):247-55. PubMed PMID: 6164286.
144. Seregi A, Keller M, Hertting G. Are cerebral prostanoids of astroglial origin? Studies on the prostanoid forming system in developing rat brain and primary cultures of rat astrocytes. Brain Res. 1987 Feb 24;404(1-2):113-20. PubMed PMID: 3567558.
145. Stichel CC, Muller CM, Zilles K. Distribution of glial fibrillary acidic protein and vimentin immunoreactivity during rat visual cortex development. Journal of neurocytology. 1991 Feb;20(2):97-108. PubMed PMID: 2027041.
146. Cahalane DJ, Clancy B, Kingsbury MA, Graf E, Sporns O, Finlay BL. Network structure implied by initial axon outgrowth in rodent cortex: empirical measurement and models. PloS one. 2011;6(1):e16113.
147. Lewis TL, Jr., Courchet J, Polleux F. Cell biology in neuroscience: Cellular and molecular mechanisms underlying axon formation, growth, and branching. The Journal of cell biology. 2013 Sep 16;202(6):837-48. PubMed PMID: 24043699. Pubmed Central PMCID: 3776347.
148. Ben-Ari Y. Excitatory actions of gaba during development: the nature of the nurture. Nature reviews Neuroscience. 2002 Sep;3(9):728-39. PubMed PMID: 12209121.
149. Crook JM, Kisvarday ZF, Eysel UT. Evidence for a contribution of lateral inhibition to orientation tuning and direction selectivity in cat visual cortex: reversible inactivation of functionally characterized sites combined with neuroanatomical tracing techniques. The European journal of neuroscience. 1998 Jun;10(6):2056-75. PubMed PMID: 9753093.
150. Moore CI, Cao R. The hemo-neural hypothesis: on the role of blood flow in information processing. Journal of neurophysiology. 2008;99(5):2035-47.
151. Kitagami T, Yamada K, Miura H, Hashimoto R, Nabeshima T, Ohta T. Mechanism of systemically injected interferon-alpha impeding monoamine biosynthesis in rats: role of nitric oxide as a signal crossing the blood–brain barrier. Brain research. 2003;978(1):104-14.
152. Zhang JM, Wang HK, Ye CQ, Ge W, Chen Y, Jiang ZL, et al. ATP released by astrocytes mediates glutamatergic activity-dependent heterosynaptic suppression. Neuron. 2003 Dec 4;40(5):971-82. PubMed PMID: 14659095.
153. Araque A, Carmignoto G, Haydon PG. Dynamic signaling between astrocytes and neurons. Annual review of physiology. 2001;63(1):795-813.
154. Volterra A, Meldolesi J. Astrocytes, from brain glue to communication elements: the revolution continues. Nature reviews Neuroscience. 2005 Aug;6(8):626-40. PubMed PMID: 16025096.
155. Bal-Price A, Moneer Z, Brown GC. Nitric oxide induces rapid, calcium-dependent release of vesicular glutamate and ATP from cultured rat astrocytes. Glia. 2002 Dec;40(3):312-23. PubMed PMID: 12420311.
156. Maingret F, Fosset M, Lesage F, Lazdunski M, Honoré E. TRAAK is a mammalian neuronal mechano-gated K+ channel. Journal of Biological Chemistry. 1999;274(3):1381-7.

157. Dunn KM, Hill-Eubanks DC, Liedtke WB, Nelson MT. TRPV4 channels stimulate Ca2+-induced Ca2+ release in astrocytic endfeet and amplify neurovascular coupling responses. Proceedings of the National Academy of Sciences. 2013;110(15):6157-62.
158. Honoré E, Patel AJ, Chemin J, Suchyna T, Sachs F. Desensitization of mechano-gated K2P channels. Proceedings of the National Academy of Sciences. 2006;103(18):6859-64.
159. Nedergaard M, Ransom B, Goldman SA. New roles for astrocytes: redefining the functional architecture of the brain. Trends in neurosciences. 2003;26(10):523-30.
160. Kim KJ, Diaz JR, Iddings JA, Filosa JA. Vasculo-neuronal coupling: retrograde vascular communication to brain neurons. Journal of Neuroscience. 2016:1300-16.
161. Dunn KM, Hill-Eubanks DC, Liedtke WB, Nelson MT. TRPV4 channels stimulate Ca2+-induced Ca2+ release in astrocytic endfeet and amplify neurovascular coupling responses. Proceedings of the National Academy of Sciences of the United States of America. 2013 Apr 9;110(15):6157-62. PubMed PMID: 23530219. Pubmed Central PMCID: 3625327.
162. Shigaeff N, Jacinto A, Chiochetta G, Cendoroglo MS, Amaro E, Ikeda M, et al. Cognition and cerebral neurovascular coupling in the elderly with metabolic syndrome. Alzheimer's & Dementia. 2012;8(4):P492.
163. Logothetis NK. Neurovascular uncoupling: much ado about nothing. Front Neuroenergetics. 2010;2(2).
164. Ulmer JL, Krouwer HG, Mueller WM, Ugurel MS, Kocak M, Mark LP. Pseudo-reorganization of language cortical function at fMR imaging: a consequence of tumor-induced neurovascular uncoupling. American journal of neuroradiology. 2003;24(2):213-7.
165. Sumiyoshi A, Suzuki H, Shimokawa H, Kawashima R. Neurovascular uncoupling under mild hypoxic hypoxia: an EEG–fMRI study in rats. Journal of Cerebral Blood Flow & Metabolism. 2012;32(10):1853-8.
166. Postiglione A, Lassen N, Holman B. Cerebral blood flow in patients with dementia of Alzheimer's type. Aging Clinical and Experimental Research. 1993;5(1):19-26.
167. Mazza M, Marano G, Traversi G, Bria P, Mazza S. Primary cerebral blood flow deficiency and Alzheimer's disease: shadows and lights. Journal of Alzheimer's Disease. 2011;23(3):375-89.
168. Zlokovic BV. Neurovascular pathways to neurodegeneration in Alzheimer's disease and other disorders. Nature Reviews Neuroscience. 2011;12(12):723-38.
169. Kalaria RN. Vascular basis for brain degeneration: faltering controls and risk factors for dementia. Nutrition reviews. 2010;68(suppl 2):S74-S87.
170. Bell RD, Zlokovic BV. Neurovascular mechanisms and blood-brain barrier disorder in Alzheimer's disease. Acta neuropathologica. 2009 Jul;118(1):103-13. PubMed PMID: 19319544. Pubmed Central PMCID: 2853006.
171. Zlokovic BV. Neurovascular mechanisms of Alzheimer's neurodegeneration. Trends Neurosci. 2005 Apr;28(4):202-8. PubMed PMID: 15808355.
172. Tarantini S, Tucsek Z, Smith N, Valcarcel-Ares MN, Hodges E, Towner R, et al. Experimental Neurovascular Uncoupling Promotes Cognitive Impairment in Mice: Implications for Brain and Cerebromicrovascular Aging. The FASEB Journal. 2015;29(1 Supplement):789.10.
173. Hald ES, Timm CD, Alford PW. Amyloid Beta Influences Vascular Smooth Muscle Contractility and Mechanoadaptation. Journal of Biomechanical Engineering. 2016;138(11):111007.
174. Rodriguez J, Olabarria M, Chvatal A, Verkhratsky A. Astroglia in dementia and Alzheimer's disease. Cell Death & Differentiation. 2009;16(3):378-85.
175. Rosengarten B, Dannhardt V, Burr O, Pöhler M, Rosengarten S, Oechsner M, et al. Neurovascular coupling in Parkinson's disease patients: effects of dementia and acetylcholinesterase inhibitor treatment. Journal of Alzheimer's Disease. 2010;22(2):415-21.
176. Rosano C, Brach J, Longstreth WT, Jr., Newman AB. Quantitative measures of gait characteristics indicate prevalence of underlying subclinical structural brain abnormalities in high-functioning older adults. Neuroepidemiology. 2006;26(1):52-60. PubMed PMID: 16254454.

177. Louis ED, Brickman AM, DeCarli C, Small SA, Marder K, Schupf N, et al. Quantitative brain measurements in community-dwelling elderly persons with mild parkinsonian signs. Arch Neurol. 2008 Dec;65(12):1649-54. PubMed PMID: 19064753. Pubmed Central PMCID: 2676900.
178. Klein C, Grunewald A, Hedrich K. Early-onset parkinsonism associated with PINK1 mutations: frequency, genotypes, and phenotypes. Neurology. 2006 Apr 11;66(7):1129-30; author reply -30. PubMed PMID: 16606941.
179. Singleton AB, Farrer M, Johnson J, Singleton A, Hague S, Kachergus J, et al. alpha-Synuclein locus triplication causes Parkinson's disease. Science. 2003 Oct 31;302(5646):841. PubMed PMID: 14593171.
180. Li JQ, Tan L, Yu JT. The role of the LRRK2 gene in Parkinsonism. Mol Neurodegener. 2014 Nov 12;9:47. PubMed PMID: 25391693. Pubmed Central PMCID: 4246469.
181. Arkinson C, Walden H. Parkin function in Parkinson's disease. Science. 2018 Apr 20;360(6386):267-8. PubMed PMID: 29674580.
182. van Duijn CM, Dekker MC, Bonifati V, Galjaard RJ, Houwing-Duistermaat JJ, Snijders PJ, et al. Park7, a novel locus for autosomal recessive early-onset parkinsonism, on chromosome 1p36. American journal of human genetics. 2001 Sep;69(3):629-34. PubMed PMID: 11462174. Pubmed Central PMCID: 1235491.
183. Ramirez A, Heimbach A, Gruendemann J, Stiller B, Hampshire D, Cid LP, et al. Hereditary parkinsonism with dementia is caused by mutations in ATP13A2, encoding a lysosomal type 5 P-type ATPase. Nat Genet. 2006 Oct;38(10):1184-91. PubMed PMID: WOS:000241251100019. English.
184. Lewthwaite AJ, Lambert TD, Rolfe EB, Olgiati S, Quadri M, Simons EJ, et al. Novel GCH1 variant in Dopa-responsive dystonia and Parkinson's disease. Parkinsonism Relat Disord. 2015 Apr;21(4):394-7. PubMed PMID: 25634433. Pubmed Central PMCID: 4379065.
185. Momma K, Funayama M, Li YZ, Ichinose H, Motoyoshi K, Hattori N, et al. A new mutation in the GCH1 gene presents as early-onset Parkinsonism. Parkinsonism Relat D. 2009 Feb;15(2):160-1. PubMed PMID: WOS:000263401600016. English.
186. Rosengarten B, Dannhardt V, Burr O, Pohler M, Rosengarten S, Oechsner M, et al. Neurovascular coupling in Parkinson's disease patients: effects of dementia and acetylcholinesterase inhibitor treatment. Journal of Alzheimer's disease : JAD. 2010;22(2):415-21. PubMed PMID: 20847429.
187. Boltze J, Kleinschnitz C, Reymann KG, Reiser G, Wagner D-C, Kranz A, et al. Neurovascular pathophysiology in cerebral ischemia, dementia and the ageing brain–current trends in basic, translational and clinical research. Experimental & translational stroke medicine. 2012;4(1):1.
188. Soria B, Roche E, Berna G, Leon-Quinto T, Reig JA, Martin F. Insulin-secreting cells derived from embryonic stem cells normalize glycemia in streptozotocin-induced diabetic mice. Diabetes. 2000 Feb;49(2):157-62. PubMed PMID: 10868930.
189. Reed MJ, Meszaros K, Entes LJ, Claypool MD, Pinkett JG, Gadbois TM, et al. A new rat model of type 2 diabetes: the fat-fed, streptozotocin-treated rat. Metabolism: clinical and experimental. 2000 Nov;49(11):1390-4. PubMed PMID: 11092499.
190. Gleeson M, Connaughton V, Arneson L. Induction of hyperglycaemia in zebrafish (Danio rerio) leads to morphological changes in the retina. Acta Diabetologica. 2007;44(3):157-63.
191. Intine RV, Olsen AS, Sarras MP, Jr. A zebrafish model of diabetes mellitus and metabolic memory. Journal of visualized experiments : JoVE. 2013 Feb 28(72):e50232. PubMed PMID: 23485929. Pubmed Central PMCID: 3622110.
192. Obrosova IG, Drel VR, Kumagai AK, Szabo C, Pacher P, Stevens MJ. Early diabetes-induced biochemical changes in the retina: comparison of rat and mouse models. Diabetologia. 2006 Oct;49(10):2525-33. PubMed PMID: 16896942. Pubmed Central PMCID: 2228251.
193. Barber AJ, Antonetti DA, Kern TS, Reiter CE, Soans RS, Krady JK, et al. The Ins2Akita mouse as a model of early retinal complications in diabetes. Investigative Ophthalmology & Visual Science. 2005;46(6):2210-8.

194. Nacci C, Tarquinio M, Montagnani M. Molecular and clinical aspects of endothelial dysfunction in diabetes. Internal and emergency medicine. 2009 Apr;4(2):107-16. PubMed PMID: 19280353.
195. Dejana E, Hirschi KK, Simons M. The molecular basis of endothelial cell plasticity. Nat Commun. 2017 Feb 9;8:14361. PubMed PMID: 28181491. Pubmed Central PMCID: 5309780.
196. Popov D. Endothelial cell dysfunction in hyperglycemia: Phenotypic change, intracellular signaling modification, ultrastructural alteration, and potential clinical outcomes. International Journal of Diabetes Mellitus. 2010;2(3):189-95.
197. Tabit CE, Chung WB, Hamburg NM, Vita JA. Endothelial dysfunction in diabetes mellitus: molecular mechanisms and clinical implications. Reviews in endocrine & metabolic disorders. 2010 Mar;11(1):61-74. PubMed PMID: 20186491. Pubmed Central PMCID: 2882637.
198. Kemeny SF, Figueroa DS, Clyne AM. Hypo-and hyperglycemia impair endothelial cell actin alignment and nitric oxide synthase activation in response to shear stress. PLoS One. 2013;8(6):e66176.
199. Busik JV, Mohr S, Grant MB. Hyperglycemia-induced reactive oxygen species toxicity to endothelial cells is dependent on paracrine mediators. Diabetes. 2008.
200. Hayashi T, Matsui-Hirai H, Miyazaki-Akita A, Fukatsu A, Funami J, Ding Q-F, et al. Endothelial cellular senescence is inhibited by nitric oxide: implications in atherosclerosis associated with menopause and diabetes. Proceedings of the National Academy of Sciences. 2006;103(45):17018-23.
201. Behl Y, Krothapalli P, Desta T, Roy S, Graves DT. FOXO1 plays an important role in enhanced microvascular cell apoptosis and microvascular cell loss in type 1 and type 2 diabetic rats. Diabetes. 2009 Apr;58(4):917-25. PubMed PMID: 19168598. Pubmed Central PMCID: 2661587.
202. Zheng Z, Chen H, Zhao H, Liu K, Luo D, Chen Y, et al. Inhibition of JAK2/STAT3-mediated VEGF upregulation under high glucose conditions by PEDF through a mitochondrial ROS pathway in vitro. Invest Ophthalmol Vis Sci. 2010 Jan;51(1):64-71. PubMed PMID: 19696171.
203. Ciudin A, Espinosa A, Simo-Servat O, Ruiz A, Alegret M, Hernandez C, et al. Type 2 diabetes is an independent risk factor for dementia conversion in patients with mild cognitive impairment. Journal of diabetes and its complications. 2017 Aug;31(8):1272-4. PubMed PMID: 28545893.
204. Whitmer RA. Type 2 diabetes and risk of cognitive impairment and dementia. Current neurology and neuroscience reports. 2007 Sep;7(5):373-80. PubMed PMID: 17764626.
205. Rom S, Zuluaga-Ramirez V, Gajghate S, Seliga A, Winfield M, Heldt NA, et al. Hyperglycemia-Driven Neuroinflammation Compromises BBB Leading to Memory Loss in Both Diabetes Mellitus (DM) Type 1 and Type 2 Mouse Models. Molecular neurobiology. 2018:1-14.
206. Greenstein VC, Shapiro A, Zaidi Q, Hood DC. Psychophysical evidence for post-receptoral sensitivity loss in diabetics. Invest Ophthalmol Vis Sci. 1992 Sep;33(10):2781-90. PubMed PMID: 1526727.
207. Sharifi AM, Mousavi SH, Farhadi M, Larijani B. Study of high glucose-induced apoptosis in PC12 cells: role of bax protein. Journal of pharmacological sciences. 2007 Jul;104(3):258-62. PubMed PMID: 17652910.
208. Pulido JE, Pulido JS, Erie JC, Arroyo J, Bertram K, Lu MJ, et al. A role for excitatory amino acids in diabetic eye disease. Experimental diabetes research. 2007;2007:36150. PubMed PMID: 17713594. Pubmed Central PMCID: 1940058.
209. Figler RA, Wang G, Srinivasan S, Jung DY, Zhang Z, Pankow JS, et al. Links between insulin resistance, adenosine A2B receptors, and inflammatory markers in mice and humans. Diabetes. 2011;60(2):669-79.
210. Tomlinson DR, Moriarty RJ, Mayer JH. Prevention and reversal of defective axonal transport and motor nerve conduction velocity in rats with experimental diabetes by treatment with the aldose reductase inhibitor Sorbinil. Diabetes. 1984 May;33(5):470-6. PubMed PMID: 6202576.
211. Coleman E, Judd R, Hoe L, Dennis J, Posner P. Effects of diabetes mellitus on astrocyte GFAP and glutamate transporters in the CNS. Glia. 2004 Nov 1;48(2):166-78. PubMed PMID: 15378652.
212. Rungger-Brandle E, Dosso AA, Leuenberger PM. Glial reactivity, an early feature of diabetic retinopathy. Invest Ophthalmol Vis Sci. 2000 Jun;41(7):1971-80. PubMed PMID: 10845624.

213. Jing L, Mai L, Zhang JZ, Wang JG, Chang Y, Dong JD, et al. Diabetes inhibits cerebral ischemia-induced astrocyte activation - an observation in the cingulate cortex. International journal of biological sciences. 2013;9(9):980-8. PubMed PMID: 24163590. Pubmed Central PMCID: 3807018.
214. Lascola C, Kraig RP. Astroglial acid-base dynamics in hyperglycemic and normoglycemic global ischemia. Neuroscience & Biobehavioral Reviews. 1997;21(2):143-50.
215. Kraig RP, Chesler M. Astrocytic acidosis in hyperglycemic and complete ischemia. Journal of cerebral blood flow and metabolism : official journal of the International Society of Cerebral Blood Flow and Metabolism. 1990 Jan;10(1):104-14. PubMed PMID: 2298827. Pubmed Central PMCID: 3047406.
216. Higashi K, Fujita A, Inanobe A, Tanemoto M, Doi K, Kubo T, et al. An inwardly rectifying K(+) channel, Kir4.1, expressed in astrocytes surrounds synapses and blood vessels in brain. American journal of physiology Cell physiology. 2001 Sep;281(3):C922-31. PubMed PMID: 11502569.
217. Rivera-Aponte DE, Mendez-Gonzalez MP, Rivera-Pagan AF, Kucheryavykh YV, Kucheryavykh LY, Skatchkov SN, et al. Hyperglycemia reduces functional expression of astrocytic Kir4.1 channels and glial glutamate uptake. Neuroscience. 2015 Dec 3;310:216-23. PubMed PMID: 26404875. Pubmed Central PMCID: 4758357.
218. Rossi DJ, Brady JD, Mohr C. Astrocyte metabolism and signaling during brain ischemia. Nat Neurosci. 2007 Nov;10(11):1377-86. PubMed PMID: 17965658.
219. Ritter MR, Banin E, Moreno SK, Aguilar E, Dorrell MI, Friedlander M. Myeloid progenitors differentiate into microglia and promote vascular repair in a model of ischemic retinopathy. The Journal of clinical investigation. 2006;116(12):3266-76.
220. Saijo K, Glass CK. Microglial cell origin and phenotypes in health and disease. Nature reviews Immunology. 2011 Oct 25;11(11):775-87. PubMed PMID: 22025055.
221. Ling EA, Wong WC. The origin and nature of ramified and amoeboid microglia: a historical review and current concepts. Glia. 1993 Jan;7(1):9-18. PubMed PMID: 8423067.
222. Kirkley KS, Popichak KA, Afzali MF, Legare ME, Tjalkens RB. Microglia amplify inflammatory activation of astrocytes in manganese neurotoxicity. Journal of neuroinflammation. 2017 May 5;14(1):99. PubMed PMID: 28476157. Pubmed Central PMCID: 5418760.
223. Sorrentino FS, Allkabes M, Salsini G, Bonifazzi C, Perri P. The importance of glial cells in the homeostasis of the retinal microenvironment and their pivotal role in the course of diabetic retinopathy. Life sciences. 2016 Oct 1;162:54-9. PubMed PMID: 27497914.
224. Rangasamy S, McGuire PG, Nitta CF, Monickaraj F, Oruganti SR, Das A. Chemokine mediated monocyte trafficking into the retina: role of inflammation in alteration of the blood-retinal barrier in diabetic retinopathy. PloS one. 2014;9(10):e108508.
225. Glasgow BJ, Weisberger AK. A quantitative and cartographic study of retinal microvasculopathy in acquired immunodeficiency syndrome. American journal of ophthalmology. 1994 Jul 15;118(1):46-56. PubMed PMID: 8023875.
226. Bergers G, Song S. The role of pericytes in blood-vessel formation and maintenance. Neuro-oncology. 2005 Oct;7(4):452-64. PubMed PMID: 16212810. Pubmed Central PMCID: 1871727.
227. Sagare AP, Bell RD, Zhao Z, Ma Q, Winkler EA, Ramanathan A, et al. Pericyte loss influences Alzheimer-like neurodegeneration in mice. Nat Commun. 2013;4:2932. PubMed PMID: 24336108. Pubmed Central PMCID: 3945879.
228. Tilton RG, Faller AM, Burkhardt JK, Hoffmann PL, Kilo C, Williamson JR. Pericyte degeneration and acellular capillaries are increased in the feet of human diabetic patients. Diabetologia. 1985 Dec;28(12):895-900. PubMed PMID: 4092858.
229. Malik RA, Newrick PG, Sharma AK, Jennings A, Ah-See AK, Mayhew TM, et al. Microangiopathy in human diabetic neuropathy: relationship between capillary abnormalities and the severity of neuropathy. Diabetologia. 1989 Feb;32(2):92-102. PubMed PMID: 2721843.
230. Miller AG, Smith DG, Bhat M, Nagaraj RH. Glyoxalase I is critical for human retinal capillary pericyte survival under hyperglycemic conditions. Journal of Biological Chemistry. 2006;281(17):11864-71.

231. Geraldes P, Hiraoka-Yamamoto J, Matsumoto M, Clermont A, Leitges M, Marette A, et al. Activation of PKC-δ and SHP-1 by hyperglycemia causes vascular cell apoptosis and diabetic retinopathy. Nature Medicine. 2009;15(11):1298.
232. Van Hall G, Strømstad M, Rasmussen P, Jans Ø, Zaar M, Gam C, et al. Blood lactate is an important energy source for the human brain. Journal of Cerebral Blood Flow & Metabolism. 2009;29(6):1121-9.
233. Wyss MT, Jolivet R, Buck A, Magistretti PJ, Weber B. In vivo evidence for lactate as a neuronal energy source. Journal of Neuroscience. 2011;31(20):7477-85.
234. Silver IA, Erecinska M. Extracellular glucose concentration in mammalian brain: continuous monitoring of changes during increased neuronal activity and upon limitation in oxygen supply in normo-, hypo-, and hyperglycemic animals. The Journal of neuroscience : the official journal of the Society for Neuroscience. 1994 Aug;14(8):5068-76. PubMed PMID: 8046468.
235. Abbott NJ, Rönnbäck L, Hansson E. Astrocyte–endothelial interactions at the blood–brain barrier. Nature Reviews Neuroscience. 2006;7(1):41.
236. Pardridge WM, Boado RJ, Farrell CR. Brain-type glucose transporter (GLUT-1) is selectively localized to the blood-brain barrier. Studies with quantitative western blotting and in situ hybridization. The Journal of biological chemistry. 1990 Oct 15;265(29):18035-40. PubMed PMID: 2211679.
237. Shah K, Desilva S, Abbruscato T. The role of glucose transporters in brain disease: diabetes and Alzheimer's Disease. International journal of molecular sciences. 2012 Oct 3;13(10):12629-55. PubMed PMID: 23202918. Pubmed Central PMCID: 3497292.
238. Garvey WT, Huecksteadt TP, Matthaei S, Olefsky JM. Role of glucose transporters in the cellular insulin resistance of type II non-insulin-dependent diabetes mellitus. J Clin Invest. 1988 May;81(5):1528-36. PubMed PMID: 3366906. Pubmed Central PMCID: 442586.
239. Vanhanen M, Koivisto K, Kuusisto J, Mykkänen L, Helkala E-L, Hänninen T, et al. Cognitive function in an elderly population with persistent impaired glucose tolerance. Diabetes care. 1998;21(3):398-402.
240. Pasquier F, Boulogne A, Leys D, Fontaine P. Diabetes mellitus and dementia. Diabetes & metabolism. 2006;32(5):403-14.
241. Mogi M, Horiuchi M. Neurovascular coupling in cognitive impairment associated with diabetes mellitus. Circulation Journal. 2011;75(5):1042-8.
242. Duarte JV, Pereira JM, Quendera B, Raimundo M, Moreno C, Gomes L, et al. Early disrupted neurovascular coupling and changed event level hemodynamic response function in type 2 diabetes: an fMRI study. Journal of Cerebral Blood Flow & Metabolism. 2015;35(10):1671-80.
243. Pelligrino D, Miletich D, Albrecht R. Diminished muscarinic receptor-mediated cerebral blood flow response in streptozotocin-treated rats. American Journal of Physiology-Endocrinology And Metabolism. 1992;262(4):E447-E54.
244. Vetri F, Xu H, Paisansathan C, Pelligrino DA. Impairment of neurovascular coupling in type 1 diabetes mellitus in rats is linked to PKC modulation of BKCa and Kir channels. American Journal of Physiology-Heart and Circulatory Physiology. 2012;302(6):H1274-H84.
245. Kjos SL, Buchanan TA. Gestational diabetes mellitus. New England journal of medicine. 1999;341(23):1749-56.
246. Carr DB, Utzschneider KM, Hull RL, Tong J, Wallace TM, Kodama K, et al. Gestational diabetes mellitus increases the risk of cardiovascular disease in women with a family history of type 2 diabetes. Diabetes care. 2006;29(9):2078-83.
247. Shah BR, Retnakaran R, Booth GL. Increased risk of cardiovascular disease in young women following gestational diabetes mellitus. Diabetes care. 2008;31(8):1668-9.
248. Clausen TD, Mathiesen ER, Hansen T, Pedersen O, Jensen DM, Lauenborg J, et al. High prevalence of type 2 diabetes and pre-diabetes in adult offspring of women with gestational diabetes mellitus or type 1 diabetes: the role of intrauterine hyperglycemia. Diabetes care. 2008;31(2):340-6.
249. Clapham DE. TRP channels as cellular sensors. Nature. 2003;426(6966):517.

250. Pedersen SF, Nilius B. Transient receptor potential channels in mechanosensing and cell volume regulation. Methods Enzymol. 2007;428:183-207. PubMed PMID: 17875418.
251. Lin SY, Corey DP. TRP channels in mechanosensation. Curr Opin Neurobiol. 2005 Jun;15(3):350-7. PubMed PMID: 15922584.
252. Nakagawa H, Hiura A. Capsaicin, transient receptor potential (TRP) protein subfamilies and the particular relationship between capsaicin receptors and small primary sensory neurons. Anatomical science international. 2006 Sep;81(3):135-55. PubMed PMID: 16955665.
253. Hardie RC, Raghu P, Moore S, Juusola M, Baines RA, Sweeney ST. Calcium influx via TRP channels is required to maintain PIP2 levels in Drosophila photoreceptors. Neuron. 2001;30(1):149-59.
254. Shibasaki K, Ikenaka K, Tamalu F, Tominaga M, Ishizaki Y. A novel subtype of astrocytes expressing TRPV4 (transient receptor potential vanilloid 4) regulates neuronal excitability via release of gliotransmitters. The Journal of biological chemistry. 2014 May 23;289(21):14470-80. PubMed PMID: 24737318. Pubmed Central PMCID: 4031503.
255. Watanabe H, Vriens J, Janssens A, Wondergem R, Droogmans G, Nilius B. Modulation of TRPV4 gating by intra- and extracellular Ca2+. Cell calcium. 2003 May-Jun;33(5-6):489-95. PubMed PMID: 12765694.
256. Sukumaran SV, Singh TU, Parida S, Narasimha Reddy Ch E, Thangamalai R, Kandasamy K, et al. TRPV4 channel activation leads to endothelium-dependent relaxation mediated by nitric oxide and endothelium-derived hyperpolarizing factor in rat pulmonary artery. Pharmacological research. 2013 Dec;78:18-27. PubMed PMID: 24075884.
257. Yin J, Hoffmann J, Kaestle SM, Neye N, Wang L, Baeurle J, et al. Negative-feedback loop attenuates hydrostatic lung edema via a cGMP-dependent regulation of transient receptor potential vanilloid 4. Circ Res. 2008 Apr 25;102(8):966-74. PubMed PMID: 18323527.
258. Filosa JA, Yao X, Rath G. TRPV4 and the regulation of vascular tone. Journal of cardiovascular pharmacology. 2013 Feb;61(2):113-9. PubMed PMID: 23107877. Pubmed Central PMCID: 3564998.
259. Monaghan K, McNaughten J, McGahon MK, Kelly C, Kyle D, Yong PH, et al. Hyperglycemia and Diabetes Downregulate the Functional Expression of TRPV4 Channels in Retinal Microvascular Endothelium. PLoS One. 2015;10(6):e0128359. PubMed PMID: 26047504. Pubmed Central PMCID: 4457535.
260. Echaniz-Laguna A, Dubourg O, Carlier P, Carlier RY, Sabouraud P, Pereon Y, et al. Phenotypic spectrum and incidence of TRPV4 mutations in patients with inherited axonal neuropathy. Neurology. 2014 May 27;82(21):1919-26. PubMed PMID: 24789864.
261. McEntagart M. TRPV4 axonal neuropathy spectrum disorder. Journal of clinical neuroscience : official journal of the Neurosurgical Society of Australasia. 2012 Jul;19(7):927-33. PubMed PMID: 22617546.
262. Ryskamp DA, Iuso A, Krizaj D. TRPV4 links inflammatory signaling and neuroglial swelling. Channels. 2015;9(2):70-2. PubMed PMID: 25891181. Pubmed Central PMCID: 4594509.
263. Zhang X, Toronov VY, Fabiani M, Gratton G, Webb AG. The study of cerebral hemodynamic and neuronal response to visual stimulation using simultaneous NIR optical tomography and BOLD fMRI in humans. Proceedings of SPIE--the International Society for Optical Engineering. 2005;5686(115):566-72. PubMed PMID: 21776185. Pubmed Central PMCID: 3138137.
264. Miao P, Rege A, Li N, Thakor NV, Tong S. High resolution cerebral blood flow imaging by registered laser speckle contrast analysis. IEEE transactions on bio-medical engineering. 2010 May;57(5):1152-7. PubMed PMID: 20142159.
265. Mesquita RC, Franceschini MA, Boas DA. Resting state functional connectivity of the whole head with near-infrared spectroscopy. Biomedical optics express. 2010 Jul 28;1(1):324-36. PubMed PMID: 21258470. Pubmed Central PMCID: 3005169.
266. Tsytsarev V, Premachandra K, Takeshita D, Bahar S. Imaging cortical electrical stimulation in vivo: fast intrinsic optical signal versus voltage-sensitive dyes. Optics letters. 2008 May 1;33(9):1032-4. PubMed PMID: 18451977.

267. Stosiek C, Garaschuk O, Holthoff K, Konnerth A. In vivo two-photon calcium imaging of neuronal networks. Proceedings of the National Academy of Sciences of the United States of America. 2003 Jun 10;100(12):7319-24. PubMed PMID: 12777621. Pubmed Central PMCID: 165873.
268. Liao L-D, Tsytsarev V, Delgado-Martínez I, Li M-L, Erzurumlu R, Vipin A, et al. Neurovascular coupling: in vivo optical techniques for functional brain imaging. Biomedical engineering online. 2013;12(1):1.
269. Mayerich D, Abbott L, McCormick B. Knife-edge scanning microscopy for imaging and reconstruction of three-dimensional anatomical structures of the mouse brain. Journal of microscopy. 2008 Jul;231(Pt 1):134-43. PubMed PMID: 18638197.
270. Huisken J, Stainier DY. Selective plane illumination microscopy techniques in developmental biology. Development. 2009 Jun;136(12):1963-75. PubMed PMID: 19465594. Pubmed Central PMCID: 2685720.
271. Swoger J, Pampaloni F, Stelzer EH. Light-sheet-based fluorescence microscopy for three-dimensional imaging of biological samples. Cold Spring Harbor protocols. 2014 Jan 1;2014(1):1-8. PubMed PMID: 24371323.
272. Bilotta J, Saszik S. The zebrafish as a model visual system. International Journal of Developmental Neuroscience. 2001;19(7):621-9.
273. Bovenkerk B, Kaldewaij F. The Use of Animal Models in Behavioural Neuroscience Research. Ethical Issues in Behavioral Neuroscience: Springer; 2014. p. 17-46.
274. Lieschke GJ, Currie PD. Animal models of human disease: zebrafish swim into view. Nature Reviews Genetics. 2007;8(5):353-67.
275. Rubinstein AL. Zebrafish: from disease modeling to drug discovery. Current opinion in drug discovery & development. 2003 Mar;6(2):218-23. PubMed PMID: 12669457.
276. Karlovich CA, John RM, Ramirez L, Stainier DY, Myers RM. Characterization of the Huntington's disease (HD) gene homologue in the zebrafish Danio rerio. Gene. 1998 Sep 14;217(1-2):117-25. PubMed PMID: 9795179.
277. Groth C, Nornes S, McCarty R, Tamme R, Lardelli M. Identification of a second presenilin gene in zebrafish with similarity to the human Alzheimer's disease gene presenilin2. Development genes and evolution. 2002 Nov;212(10):486-90. PubMed PMID: 12424519.
278. Patton EE, Zon LI. The art and design of genetic screens: zebrafish. Nature reviews Genetics. 2001 Dec;2(12):956-66. PubMed PMID: 11733748.
279. Sumbre G, de Polavieja GG. The world according to zebrafish: how neural circuits generate behavior. Front Neural Circuits. 2014;8:91. PubMed PMID: 25126059. Pubmed Central PMCID: 4115616.
280. Stewart AM, Braubach O, Spitsbergen J, Gerlai R, Kalueff AV. Zebrafish models for translational neuroscience research: from tank to bedside. Trends Neurosci. 2014 May;37(5):264-78. PubMed PMID: 24726051. Pubmed Central PMCID: 4039217.
281. Bernardos RL, Raymond PA. GFAP transgenic zebrafish. Gene expression patterns : GEP. 2006 Oct;6(8):1007-13. PubMed PMID: 16765104.
282. Goldman D, Hankin M, Li Z, Dai X, Ding J. Transgenic zebrafish for studying nervous system development and regeneration. Transgenic research. 2001;10(1):21-33. PubMed PMID: 11252380.
283. Muto A, Ohkura M, Kotani T, Higashijima S, Nakai J, Kawakami K. Genetic visualization with an improved GCaMP calcium indicator reveals spatiotemporal activation of the spinal motor neurons in zebrafish. Proceedings of the National Academy of Sciences of the United States of America. 2011 Mar 29;108(13):5425-30. PubMed PMID: 21383146. Pubmed Central PMCID: 3069178.
284. Lau BY, Mathur P, Gould GG, Guo S. Identification of a brain center whose activity discriminates a choice behavior in zebrafish. Proceedings of the National Academy of Sciences of the United States of America. 2011 Feb 8;108(6):2581-6. PubMed PMID: 21262817. Pubmed Central PMCID: 3038752.

285. Wullimann MF, Mueller T. Teleostean and mammalian forebrains contrasted: Evidence from genes to behavior. The Journal of comparative neurology. 2004 Jul 19;475(2):143-62. PubMed PMID: 15211457.
286. von Trotha JW, Vernier P, Bally-Cuif L. Emotions and motivated behavior converge on an amygdala-like structure in the zebrafish. The European journal of neuroscience. 2014 Nov;40(9):3302-15. PubMed PMID: 25145867. Pubmed Central PMCID: 4278443.
287. Li L, Dowling J. Zebrafish visual sensitivity is regulated by a circadian clock. Visual neuroscience. 1997;15(5):851-7.
288. Friedrich RW, Jacobson GA, Zhu P. Circuit neuroscience in zebrafish. Current Biology. 2010;20(8):R371-R81.
289. Burrill JD, Easter SS. Development of the retinofugal projections in the embryonic and larval zebrafish (Brachydanio rerio). Journal of Comparative Neurology. 1994;346(4):583-600.
290. Nevin LM, Robles E, Baier H, Scott EK. Focusing on optic tectum circuitry through the lens of genetics. BMC biology. 2010;8(1):1.
291. Scott EK, Baier H. The cellular architecture of the larval zebrafish tectum, as revealed by gal4 enhancer trap lines. Frontiers in neural circuits. 2009;3:13.
292. Roeser T, Baier H. Visuomotor behaviors in larval zebrafish after GFP-guided laser ablation of the optic tectum. The Journal of Neuroscience. 2003;23(9):3726-34.
293. Sajovic P, Levinthal C. Visual response properties of zebrafish tectal cells. Neuroscience. 1982;7(10):2427-40.
294. Sajovic P, Levinthal C. Visual cells of zebrafish optic tectum: mapping with small spots. Neuroscience. 1982;7(10):2407-26.
295. Grama A, Engert F. Direction selectivity in the larval zebrafish tectum is mediated by asymmetric inhibition. Frontiers in neural circuits. 2012;6:59.
296. Ramdya P, Engert F. Emergence of binocular functional properties in a monocular neural circuit. Nature neuroscience. 2008;11(9):1083-90.
297. Kysil EV, Meshalkina DA, Frick EE, Echevarria DJ, Rosemberg DB, Maximino C, et al. Comparative Analyses of Zebrafish Anxiety-Like Behavior Using Conflict-Based Novelty Tests. Zebrafish. 2017 Jun;14(3):197-208. PubMed PMID: WOS:000402566000001. English.
298. Serra EL, Medalha CC, Mattioli R. Natural preference of zebrafish (Danio rerio) for a dark environment. Brazilian journal of medical and biological research = Revista brasileira de pesquisas medicas e biologicas. 1999 Dec;32(12):1551-3. PubMed PMID: 10585639.
299. Blaser RE, Penalosa YM. Stimuli affecting zebrafish (Danio rerio) behavior in the light/dark preference test. Physiology & behavior. 2011 Oct 24;104(5):831-7. PubMed PMID: 21839758.
300. Colwill RM, Creton R. Locomotor behaviors in zebrafish (Danio rerio) larvae. Behavioural processes. 2011 Feb;86(2):222-9. PubMed PMID: 21147203. Pubmed Central PMCID: 3063417.
301. Haug MF, Biehlmaier O, Mueller KP, Neuhauss SC. Visual acuity in larval zebrafish: behavior and histology. Frontiers in zoology. 2010 Mar 1;7:8. PubMed PMID: 20193078. Pubmed Central PMCID: 2848032.
302. Bianco IH, Kampff AR, Engert F. Prey capture behavior evoked by simple visual stimuli in larval zebrafish. Frontiers in systems neuroscience. 2011;5:101. PubMed PMID: 22203793. Pubmed Central PMCID: 3240898.
303. Brockerhoff SE. Measuring the optokinetic response of zebrafish larvae. Nature protocols. 2006;1(5):2448-51. PubMed PMID: 17406490.
304. Masino MA, Fetcho JR. Fictive swimming motor patterns in wild type and mutant larval zebrafish. J Neurophysiol. 2005 Jun;93(6):3177-88. PubMed PMID: 15673549.
305. Hill SA, Liu X-P, Borla MA, José JV, O'Malley DM. Neurokinematic modeling of complex swimming patterns of the larval zebrafish. Neurocomputing. 2005;65:61-8.
306. May Z, Morrill A, Holcombe A, Johnston T, Gallup J, Fouad K, et al. Object recognition memory in zebrafish. Behavioural brain research. 2016 Jan 1;296:199-210. PubMed PMID: 26376244.

307. Guo S. Linking genes to brain, behavior and neurological diseases: what can we learn from zebrafish? Genes, Brain and Behavior. 2004;3(2):63-74.
308. Aston-Jones G, Rajkowski J, Cohen J. Locus coeruleus and regulation of behavioral flexibility and attention. Progress in brain research. 2000;126:165-82.
309. Ahrens MB, Orger MB, Robson DN, Li JM, Keller PJ. Whole-brain functional imaging at cellular resolution using light-sheet microscopy. Nature methods. 2013;10(5):413-20.
310. Tomizawa K, Inoue Y, Nakayasu H. A monoclonal antibody stains radial glia in the adult zebrafish (Danio rerio) CNS. Journal of neurocytology. 2000 Feb;29(2):119-28. PubMed PMID: 11068340.
311. Pellegrini E, Mouriec K, Anglade I, Menuet A, Le Page Y, Gueguen MM, et al. Identification of aromatase-positive radial glial cells as progenitor cells in the ventricular layer of the forebrain in zebrafish. The Journal of comparative neurology. 2007 Mar 1;501(1):150-67. PubMed PMID: 17206614.
312. Kirby BB, Takada N, Latimer AJ, Shin J, Carney TJ, Kelsh RN, et al. In vivo time-lapse imaging shows dynamic oligodendrocyte progenitor behavior during zebrafish development. Nature neuroscience. 2006;9(12):1506.
313. Kawai H, Arata N, Nakayasu H. Three-dimensional distribution of astrocytes in zebrafish spinal cord. Glia. 2001 Dec;36(3):406-13. PubMed PMID: 11746776.
314. Grupp L, Wolburg H, Mack AF. Astroglial structures in the zebrafish brain. The Journal of comparative neurology. 2010 Nov 1;518(21):4277-87. PubMed PMID: 20853506.
315. Lyons DA, Talbot WS. Glial cell development and function in zebrafish. Cold Spring Harbor perspectives in biology. 2014 Nov 13;7(2):a020586. PubMed PMID: 25395296. Pubmed Central PMCID: 4315925.
316. Ito Y, Tanaka H, Okamoto H, Ohshima T. Characterization of neural stem cells and their progeny in the adult zebrafish optic tectum. Dev Biol. 2010 Jun 1;342(1):26-38. PubMed PMID: 20346355.
317. Fleming A, Diekmann H, Goldsmith P. Functional characterisation of the maturation of the blood-brain barrier in larval zebrafish. PLoS One. 2013;8(10):e77548. PubMed PMID: 24147021. Pubmed Central PMCID: 3797749.
318. Eliceiri BP, Gonzalez AM, Baird A. Zebrafish model of the blood-brain barrier: morphological and permeability studies. Methods in molecular biology. 2011;686:371-8. PubMed PMID: 21082382. Pubmed Central PMCID: 4222041.
319. Matsuoka RL, Marass M, Avdesh A, Helker CS, Maischein HM, Grosse AS, et al. Radial glia regulate vascular patterning around the developing spinal cord. Elife. 2016 Nov 17;5. PubMed PMID: 27852438. Pubmed Central PMCID: 5123865.
320. Than-Trong E, Bally-Cuif L. Radial glia and neural progenitors in the adult zebrafish central nervous system. Glia. 2015 Aug;63(8):1406-28. PubMed PMID: 25976648.
321. Isogai S, Horiguchi M, Weinstein BM. The vascular anatomy of the developing zebrafish: an atlas of embryonic and early larval development. Developmental biology. 2001;230(2):278-301.
322. Gore AV, Monzo K, Cha YR, Pan W, Weinstein BM. Vascular development in the zebrafish. Cold Spring Harbor perspectives in medicine. 2012;2(5):a006684.
323. Childs S, Chen JN, Garrity DM, Fishman MC. Patterning of angiogenesis in the zebrafish embryo. Development. 2002 Feb;129(4):973-82. PubMed PMID: 11861480.
324. Chen Q, Jiang L, Li C, Hu D, Bu JW, Cai D, et al. Haemodynamics-driven developmental pruning of brain vasculature in zebrafish. PLoS biology. 2012;10(8):e1001374. PubMed PMID: 22904685. Pubmed Central PMCID: 3419171.
325. Xie J, Farage E, Sugimoto M, Anand-Apte B. A novel transgenic zebrafish model for blood-brain and blood-retinal barrier development. BMC developmental biology. 2010;10(1):1.
326. van Leeuwen LM, Evans RJ, Jim KK, Verboom T, Fang X, Bojarczuk A, et al. A transgenic zebrafish model for the in vivo study of the blood and choroid plexus brain barriers using claudin 5. Biology open. 2018 Feb 2;7(2). PubMed PMID: 29437557. Pubmed Central PMCID: 5861362.

327. Aubert A, Costalat R. Interaction between astrocytes and neurons studied using a mathematical model of compartmentalized energy metabolism. J Cerebr Blood F Met. 2005 Nov;25(11):1476-90. PubMed PMID: WOS:000232815000008. English.
328. Boas DA, Jones SR, Devor A, Huppert TJ, Dale AM. A vascular anatomical network model of the spatio-temporal response to brain activation. Neuroimage. 2008 Apr 15;40(3):1116-29. PubMed PMID: 18289880. Pubmed Central PMCID: 2577617.
329. Nadkarni S, Jung P. Dressed neurons: modeling neural-glial interactions. Physical biology. 2004 Jun;1(1-2):35-41. PubMed PMID: 16204820.
330. Somjen GG, Kager H, Wadman WJ. Computer simulations of neuron-glia interactions mediated by ion flux. Journal of computational neuroscience. 2008 Oct;25(2):349-65. PubMed PMID: 18297383.
331. Chander BS, Chakravarthy VS. A computational model of neuro-glio-vascular loop interactions. PLoS One. 2012;7(11):e48802. PubMed PMID: 23185276. Pubmed Central PMCID: 3502400.
332. Blanchard S, Saillet S, Ivanov A, Benquet P, Benar CG, Pelegrini-Issac M, et al. A New Computational Model for Neuro-Glio-Vascular Coupling: Astrocyte Activation Can Explain Cerebral Blood Flow Nonlinear Response to Interictal Events. PLoS One. 2016;11(2):e0147292. PubMed PMID: 26849643. Pubmed Central PMCID: 4743967.
333. Chhabria K, Chakravarthy VS. Low-Dimensional Models of "Neuro-Glio-Vascular Unit" for Describing Neural Dynamics under Normal and Energy-Starved Conditions. Frontiers in neurology. 2016;7:24. PubMed PMID: 27014179. Pubmed Central PMCID: 4783418.
334. Witthoft A, Em Karniadakis G. A bidirectional model for communication in the neurovascular unit. Journal of theoretical biology. 2012 Oct 21;311:80-93. PubMed PMID: 22828568.
335. Kager H, Wadman WJ, Somjen GG. Simulated seizures and spreading depression in a neuron model incorporating interstitial space and ion concentrations. J Neurophysiol. 2000 Jul;84(1):495-512. PubMed PMID: 10899222.
336. Hodgkin AL, Huxley AF. A quantitative description of membrane current and its application to conduction and excitation in nerve. J Physiol. 1952 Aug;117(4):500-44. PubMed PMID: 12991237. Pubmed Central PMCID: 1392413.
337. Gafaniz R, Sanches J. ATP consumption and neural electrical activity: a physiological model for brain imaging. Conference proceedings : Annual International Conference of the IEEE Engineering in Medicine and Biology Society IEEE Engineering in Medicine and Biology Society Annual Conference. 2010;2010:5480-3. PubMed PMID: 21096289.
338. Kenny A, Plank MJ, David T. The role of astrocytic calcium and TRPV4 channels in neurovascular coupling. Journal of computational neuroscience. 2018 Feb;44(1):97-114. PubMed PMID: 29152668.
339. Kim KJ, Ramiro Diaz J, Iddings JA, Filosa JA. Vasculo-Neuronal Coupling: Retrograde Vascular Communication to Brain Neurons. The Journal of neuroscience : the official journal of the Society for Neuroscience. 2016 Dec 14;36(50):12624-39. PubMed PMID: 27821575. Pubmed Central PMCID: 5157107.
340. Frost WN, Castellucci VF, Hawkins RD, Kandel ER. Mono-Synaptic Connections Made by the Sensory Neurons of the Gill-Withdrawal and Siphon-Withdrawal Reflex in Aplysia Participate in the Storage of Long-Term-Memory for Sensitization. Proceedings of the National Academy of Sciences of the United States of America. 1985;82(23):8266-9. PubMed PMID: WOS:A1985AVT4000096. English.
341. Citri A, Malenka RC. Synaptic plasticity: multiple forms, functions, and mechanisms. Neuropsychopharmacology : official publication of the American College of Neuropsychopharmacology. 2008 Jan;33(1):18-41. PubMed PMID: 17728696.
342. Manabe T, Wyllie DJ, Perkel DJ, Nicoll RA. Modulation of synaptic transmission and long-term potentiation: effects on paired pulse facilitation and EPSC variance in the CA1 region of the hippocampus. J Neurophysiol. 1993 Oct;70(4):1451-9. PubMed PMID: 7904300.
343. MacDermott AB, Role LW, Siegelbaum SA. Presynaptic ionotropic receptors and the control of transmitter release. Annu Rev Neurosci. 1999;22:443-85. PubMed PMID: 10202545.

344. Bergles DE, Diamond JS, Jahr CE. Clearance of glutamate inside the synapse and beyond. Curr Opin Neurobiol. 1999 Jun;9(3):293-8. PubMed PMID: 10395570.
345. Toni N, Buchs PA, Nikonenko I, Bron CR, Muller D. LTP promotes formation of multiple spine synapses between a single axon terminal and a dendrite. Nature. 1999 Nov 25;402(6760):421-5. PubMed PMID: 10586883.
346. Hebb DO. Studies of the organization of behavior I. Behavior of the rat in a field orientation. J Comp Psychol. 1938 Apr;25(2):333-53. PubMed PMID: WOS:000200111900006. English.
347. Kato H, Saito HA, Aihara T, Tsukada M. Hippocampal LTP Depends on Spatial and Temporal Correlation of Inputs. Neural networks : the official journal of the International Neural Network Society. 1996 Nov;9(8):1357-65. PubMed PMID: 12662539.
348. Zhang LI, Tao HW, Holt CE, Harris WA, Poo M. A critical window for cooperation and competition among developing retinotectal synapses. Nature. 1998 Sep 3;395(6697):37-44. PubMed PMID: 9738497.
349. Izhikevich EM, Desai NS. Relating STDP to BCM. Neural computation. 2003 Jul;15(7):1511-23. PubMed PMID: 12816564.
350. Masquelier T. Relative spike time coding and STDP-based orientation selectivity in the early visual system in natural continuous and saccadic vision: a computational model. Journal of computational neuroscience. 2012 Jun;32(3):425-41. PubMed PMID: 21938439.
351. Kilkenny C, Browne W, Cuthill IC, Emerson M, Altman DG, Group NCRRGW. Animal research: reporting in vivo experiments: the ARRIVE guidelines. British journal of pharmacology. 2010 Aug;160(7):1577-9. PubMed PMID: 20649561. Pubmed Central PMCID: 2936830.
352. Tian L, Hires SA, Mao T, Huber D, Chiappe ME, Chalasani SH, et al. Imaging neural activity in worms, flies and mice with improved GCaMP calcium indicators. Nature methods. 2009;6(12):875-81.
353. Meza Santoscoy PL. Analysis of the transcriptional and behavioural responses to seizure onset in a zebrafish model of epilepsy: University of Sheffield; 2014.
354. Nakai J, Ohkura M, Imoto K. A high signal-to-noise Ca2+ probe composed of a single green fluorescent protein. Nature biotechnology. 2001;19(2):137-41.
355. Bergmann K, Meza Santoscoy P, Lygdas K, Nikolaeva Y, MacDonald RB, Cunliffe VT, et al. Imaging Neuronal Activity in the Optic Tectum of Late Stage Larval Zebrafish. Journal of developmental biology. 2018 Mar 9;6(1). PubMed PMID: 29615555. Pubmed Central PMCID: 5875565.
356. Hogan BM, Herpers R, Witte M, Heloterä H, Alitalo K, Duckers HJ, et al. Vegfc/Flt4 signalling is suppressed by Dll4 in developing zebrafish intersegmental arteries. Development. 2009;136(23):4001-9.
357. Traver D, Paw BH, Poss KD, Penberthy WT, Lin S, Zon LI. Transplantation and in vivo imaging of multilineage engraftment in zebrafish bloodless mutants. Nature immunology. 2003;4(12):1238-46.
358. MacDonald RB, Kashikar ND, Lagnado L, Harris WA. A Novel Tool to Measure Extracellular Glutamate in the Zebrafish Nervous System In Vivo. Zebrafish. 2017 Jun;14(3):284-6. PubMed PMID: 28027028. Pubmed Central PMCID: 5466054.
359. Antoniadis A, Oppenheim G. Wavelets and statistics. New York: Springer-Verlag; 1995. 410 p. p.
360. Yilmaz A, Javed O, Shah M. Object tracking: A survey. Acm Computing Surveys (CSUR). 2006;38(4):13.
361. Wolf W, editor Key frame selection by motion analysis. Acoustics, Speech, and Signal Processing, 1996 ICASSP-96 Conference Proceedings, 1996 IEEE International Conference on; 1996: IEEE.
362. Hoyer K, Holzner M, Lüthi B, Guala M, Liberzon A, Kinzelbach W. 3D scanning particle tracking velocimetry. Experiments in Fluids. 2005;39(5):923.
363. Elsinga GE, Scarano F, Wieneke B, van Oudheusden BW. Tomographic particle image velocimetry. Experiments in fluids. 2006;41(6):933-47.

364. McAndrew A. An introduction to digital image processing with matlab notes for scm2511 image processing. School of Computer Science and Mathematics, Victoria University of Technology. 2004;264(1).
365. Gupta G. Algorithm for image processing using improved median filter and comparison of mean, median and improved median filter. International Journal of Soft Computing and Engineering (IJSCE). 2011;1(5):304-11.
366. Anoraganingrum D, editor Cell segmentation with median filter and mathematical morphology operation. Image Analysis and Processing, 1999 Proceedings International Conference on; 1999: IEEE.
367. Wilkinson RN, Elworthy S, Ingham PW, van Eeden FJ. A method for high-throughput PCR-based genotyping of larval zebrafish tail biopsies. BioTechniques. 2013 Dec;55(6):314-6. PubMed PMID: 24344681.
368. Inoue D, Wittbrodt J. One for all—a highly efficient and versatile method for fluorescent immunostaining in fish embryos. PloS One. 2011;6(5):e19713.
369. Burkitt AN, Clark GM. Analysis of integrate-and-fire neurons: synchronization of synaptic input and spike output. Neural computation. 1999 May 15;11(4):871-901. PubMed PMID: 10226187.
370. Farr H, David T. Models of neurovascular coupling via potassium and EET signalling. Journal of theoretical biology. 2011 Oct 7;286(1):13-23. PubMed PMID: 21781976.
371. Ogawa S, Lee TM, Stepnoski R, Chen W, Zhuo XH, Ugurbil K. An approach to probe some neural systems interaction by functional MRI at neural time scale down to milliseconds. Proceedings of the National Academy of Sciences of the United States of America. 2000 Sep 26;97(20):11026-31. PubMed PMID: WOS:000089566100065. English.
372. Hillman EM. Coupling mechanism and significance of the BOLD signal: a status report. Annu Rev Neurosci. 2014;37:161-81. PubMed PMID: 25032494. Pubmed Central PMCID: 4147398.
373. Stuermer CA. Retinotopic organization of the developing retinotectal projection in the zebrafish embryo. The Journal of neuroscience : the official journal of the Society for Neuroscience. 1988 Dec;8(12):4513-30. PubMed PMID: 2848935.
374. Attwell D, Iadecola C. The neural basis of functional brain imaging signals. Trends Neurosci. 2002 Dec;25(12):621-5. PubMed PMID: 12446129.
375. Lacroix A, Toussay X, Anenberg E, Lecrux C, Ferreiros N, Karagiannis A, et al. COX-2-Derived Prostaglandin E2 Produced by Pyramidal Neurons Contributes to Neurovascular Coupling in the Rodent Cerebral Cortex. The Journal of neuroscience : the official journal of the Society for Neuroscience. 2015 Aug 26;35(34):11791-810. PubMed PMID: 26311764.
376. Mapelli L, Gagliano G, Soda T, Laforenza U, Moccia F, D'Angelo EU. Granular Layer Neurons Control Cerebellar Neurovascular Coupling Through an NMDA Receptor/NO-Dependent System. The Journal of neuroscience : the official journal of the Society for Neuroscience. 2017 Feb 1;37(5):1340-51. PubMed PMID: 28039371.
377. Endemann DH, Schiffrin EL. Nitric oxide, oxidative excess, and vascular complications of diabetes mellitus. Current hypertension reports. 2004 Apr;6(2):85-9. PubMed PMID: 15010009.
378. Kojima H, Urano Y, Kikuchi K, Higuchi T, Hirata Y, Nagano T. Fluorescent Indicators for Imaging Nitric Oxide Production. Angewandte Chemie. 1999 Nov 2;38(21):3209-12. PubMed PMID: 10556905.
379. Dekker RJ, van Thienen JV, Rohlena J, de Jager SC, Elderkamp YW, Seppen J, et al. Endothelial KLF2 links local arterial shear stress levels to the expression of vascular tone-regulating genes. The American journal of pathology. 2005 Aug;167(2):609-18. PubMed PMID: 16049344. Pubmed Central PMCID: 1603569.
380. Gimbrone MA, Jr., Garcia-Cardena G. Vascular endothelium, hemodynamics, and the pathobiology of atherosclerosis. Cardiovascular pathology : the official journal of the Society for Cardiovascular Pathology. 2013 Jan-Feb;22(1):9-15. PubMed PMID: 22818581. Pubmed Central PMCID: 4564111.
381. Mooradian AD. Effect of aging on the blood-brain barrier. Neurobiology of aging. 1988 Jan-Feb;9(1):31-9. PubMed PMID: 3288893.

382. Popescu BO, Toescu EC, Popescu LM, Bajenaru O, Muresanu DF, Schultzberg M, et al. Blood-brain barrier alterations in ageing and dementia. J Neurol Sci. 2009 Aug 15;283(1-2):99-106. PubMed PMID: 19264328.
383. Starr JM, Wardlaw J, Ferguson K, MacLullich A, Deary IJ, Marshall I. Increased blood-brain barrier permeability in type II diabetes demonstrated by gadolinium magnetic resonance imaging. Journal of neurology, neurosurgery, and psychiatry. 2003 Jan;74(1):70-6. PubMed PMID: 12486269. Pubmed Central PMCID: 1738177.
384. Duband JL, Gimona M, Scatena M, Sartore S, Small JV. Calponin and Sm22 as Differentiation Markers of Smooth-Muscle - Spatiotemporal Distribution during Avian Embryonic-Development. Differentiation. 1993 Dec;55(1):1-11. PubMed PMID: WOS:A1993MM58100001. English.
385. Kurz H, Fehr J, Nitschke R, Burkhardt H. Pericytes in the mature chorioallantoic membrane capillary plexus contain desmin and alpha-smooth muscle actin: relevance for non-sprouting angiogenesis. Histochem Cell Biol. 2008 Nov;130(5):1027-40. PubMed PMID: WOS:000259997900018. English.
386. Kroehne V, Freudenreich D, Hans S, Kaslin J, Brand M. Regeneration of the adult zebrafish brain from neurogenic radial glia-type progenitors. Development. 2011 Nov;138(22):4831-41. PubMed PMID: 22007133.
387. Derouiche A, Frotscher M. Astroglial processes around identified glutamatergic synapses contain glutamine synthetase: evidence for transmitter degradation. Brain Res. 1991 Jun 28;552(2):346-50. PubMed PMID: 1680531.
388. Saravia FE, Revsin Y, Gonzalez Deniselle MC, Gonzalez SL, Roig P, Lima A, et al. Increased astrocyte reactivity in the hippocampus of murine models of type 1 diabetes: the nonobese diabetic (NOD) and streptozotocin-treated mice. Brain Res. 2002 Dec 13;957(2):345-53. PubMed PMID: 12445977.
389. Baviera M, Roncaglioni MC, Tettamanti M, Vannini T, Fortino I, Bortolotti A, et al. Diabetes mellitus: a risk factor for seizures in the elderly-a population-based study. Acta Diabetol. 2017 Sep;54(9):863-70. PubMed PMID: 28631057.
390. Bourin M, Hascoet M. The mouse light/dark box test. European journal of pharmacology. 2003 Feb 28;463(1-3):55-65. PubMed PMID: 12600702.
391. Steenbergen PJ, Richardson MK, Champagne DL. Patterns of avoidance behaviours in the light/dark preference test in young juvenile zebrafish: a pharmacological study. Behavioural brain research. 2011 Sep 12;222(1):15-25. PubMed PMID: 21421013.
392. Grillon C. Startle reactivity and anxiety disorders: aversive conditioning, context, and neurobiology. Biological psychiatry. 2002 Nov 15;52(10):958-75. PubMed PMID: 12437937.
393. Kulesskaya N, Voikar V. Assessment of mouse anxiety-like behavior in the light-dark box and open-field arena: role of equipment and procedure. Physiology & behavior. 2014 Jun 22;133:30-8. PubMed PMID: 24832050.
394. Bringmann A, Grosche A, Pannicke T, Reichenbach A. GABA and Glutamate Uptake and Metabolism in Retinal Glial (Muller) Cells. Frontiers in endocrinology. 2013;4:48. PubMed PMID: 23616782. Pubmed Central PMCID: 3627989.
395. Pelster B, Burggren WW. Disruption of hemoglobin oxygen transport does not impact oxygen-dependent physiological processes in developing embryos of zebra fish (Danio rerio). Circulation research. 1996;79(2):358-62.
396. Mataga N, Imamura K, Watanabe Y. 6R-tetrahydrobiopterin perfusion enhances dopamine, serotonin, and glutamate outputs in dialysate from rat striatum and frontal cortex. Brain Res. 1991 Jun 14;551(1-2):64-71. PubMed PMID: 1680529.
397. Grimes DA, Barclay CL, Duff J, Furukawa Y, Lang AE. Phenocopies in a large GCH1 mutation positive family with dopa responsive dystonia: confusing the picture? Journal of neurology, neurosurgery, and psychiatry. 2002 Jun;72(6):801-4. PubMed PMID: 12023430. Pubmed Central PMCID: 1737930.

398. Camargos S, Scholz S, Simon-Sanchez J, Paisan-Ruiz C, Lewis P, Hernandez D, et al. DYT16, a novel young-onset dystonia-parkinsonism disorder: identification of a segregating mutation in the stress-response protein PRKRA. The Lancet Neurology. 2008 Mar;7(3):207-15. PubMed PMID: 18243799.
399. Xia Y, Tsai AL, Berka V, Zweier JL. Superoxide generation from endothelial nitric-oxide synthase. A Ca2+/calmodulin-dependent and tetrahydrobiopterin regulatory process. The Journal of biological chemistry. 1998 Oct 2;273(40):25804-8. PubMed PMID: 9748253.
400. Tatham AL, Crabtree MJ, Warrick N, Cai S, Alp NJ, Channon KM. GTP cyclohydrolase I expression, protein, and activity determine intracellular tetrahydrobiopterin levels, independent of GTP cyclohydrolase feedback regulatory protein expression. The Journal of biological chemistry. 2009 May 15;284(20):13660-8. PubMed PMID: 19286659. Pubmed Central PMCID: 2679467.
401. Zhang X, Kim WS, Hatcher N, Potgieter K, Moroz LL, Gillette R, et al. Interfering with nitric oxide measurements. 4,5-diaminofluorescein reacts with dehydroascorbic acid and ascorbic acid. The Journal of biological chemistry. 2002 Dec 13;277(50):48472-8. PubMed PMID: 12370177.
402. Dijkstra G, Moshage H, van Dullemen HM, de Jager-Krikken A, Tiebosch AT, Kleibeuker JH, et al. Expression of nitric oxide synthases and formation of nitrotyrosine and reactive oxygen species in inflammatory bowel disease. The Journal of pathology. 1998 Dec;186(4):416-21. PubMed PMID: 10209492.
403. Doehring A, Antoniades C, Channon KM, Tegeder I, Lotsch J. Clinical genetics of functionally mild non-coding GTP cyclohydrolase 1 (GCH1) polymorphisms modulating pain and cardiovascular risk. Mutation research. 2008 Sep-Oct;659(3):195-201. PubMed PMID: 18515178.
404. Bailey J, Shaw A, Fischer R, Ryan BJ, Kessler BM, McCullagh J, et al. A novel role for endothelial tetrahydrobiopterin in mitochondrial redox balance. Free radical biology & medicine. 2017 Mar;104:214-25. PubMed PMID: 28104455. Pubmed Central PMCID: 5338462.
405. Eames SC, Philipson LH, Prince VE, Kinkel MD. Blood Sugar Measurement in Zebrafish Reveals Dynamics of Glucose Homeostasis. Zebrafish. 2010 Jun;7(2):205-13. PubMed PMID: WOS:000278544100010. English.
406. Emerging Risk Factors C, Sarwar N, Gao P, Seshasai SR, Gobin R, Kaptoge S, et al. Diabetes mellitus, fasting blood glucose concentration, and risk of vascular disease: a collaborative meta-analysis of 102 prospective studies. Lancet. 2010 Jun 26;375(9733):2215-22. PubMed PMID: 20609967. Pubmed Central PMCID: 2904878.
407. Dandona P, James IM, Newbury PA, Woollard ML, Beckett AG. Cerebral blood flow in diabetes mellitus: evidence of abnormal cerebrovascular reactivity. British medical journal. 1978 Jul 29;2(6133):325-6. PubMed PMID: 687900. Pubmed Central PMCID: 1606446.
408. Dandona P, James IM, Woollard ML, Newbury P, Beckett AG. Instability of cerebral blood-flow in insulin-dependent diabetics. Lancet. 1979 Dec 8;2(8154):1203-5. PubMed PMID: 92619.
409. American Diabetes A. Diagnosis and classification of diabetes mellitus. Diabetes Care. 2013 Jan;36 Suppl 1:S67-74. PubMed PMID: 23264425. Pubmed Central PMCID: 3537273.
410. Classification and diagnosis of diabetes mellitus and other categories of glucose intolerance. National Diabetes Data Group. Diabetes. 1979 Dec;28(12):1039-57. PubMed PMID: 510803.
411. Williams SB, Cusco JA, Roddy MA, Johnstone MT, Creager MA. Impaired nitric oxide-mediated vasodilation in patients with non-insulin-dependent diabetes mellitus. Journal of the American College of Cardiology. 1996 Mar 1;27(3):567-74. PubMed PMID: 8606266.
412. Mather KJ, Lteif A, Steinberg HO, Baron AD. Interactions between endothelin and nitric oxide in the regulation of vascular tone in obesity and diabetes. Diabetes. 2004 Aug;53(8):2060-6. PubMed PMID: WOS:000223027000018. English.
413. Clapp BR, Hingorani AD, Kharbanda RK, Mohamed-Ali V, Stephens JW, Vallance P, et al. Inflammation-induced endothelial dysfunction involves reduced nitric oxide bioavailability and increased oxidant stress. Cardiovasc Res. 2004 Oct 1;64(1):172-8. PubMed PMID: 15364625.

414. Shih AY, Driscoll JD, Drew PJ, Nishimura N, Schaffer CB, Kleinfeld D. Two-photon microscopy as a tool to study blood flow and neurovascular coupling in the rodent brain (vol 32, pg 1277, 2013). J Cerebr Blood F Met. 2013 Feb;33(2):319-. PubMed PMID: WOS:000314739600021. English.
415. Horton NG, Wang K, Kobat D, Clark CG, Wise FW, Schaffer CB, et al. In vivo three-photon microscopy of subcortical structures within an intact mouse brain. Nat Photonics. 2013 Mar;7(3):205-9. PubMed PMID: WOS:000316154700013. English.
416. Girouard H, Iadecola C. Neurovascular coupling in the normal brain and in hypertension, stroke, and Alzheimer disease. Journal of applied physiology. 2006;100(1):328-35.
417. Hsu JL, Jung TP, Hsu CY, Hsu WC, Chen YK, Duann JR, et al. Regional CBF changes in Parkinson's disease: a correlation with motor dysfunction. European journal of nuclear medicine and molecular imaging. 2007 Sep;34(9):1458-66. PubMed PMID: 17437108.
418. Bes A, Guell A, Fabre N, Dupui P, Victor G, Geraud G. Cerebral blood flow studied by Xenon-133 inhalation technique in parkinsonism: loss of hyperfrontal pattern. Journal of cerebral blood flow and metabolism : official journal of the International Society of Cerebral Blood Flow and Metabolism. 1983 Mar;3(1):33-7. PubMed PMID: 6822615.
419. Cukierman T, Gerstein HC, Williamson JD. Cognitive decline and dementia in diabetes - systematic overview of prospective observational studies. Diabetologia. 2005 Dec;48(12):2460-9. PubMed PMID: WOS:000233721600004. English.
420. Hawkins BT, Lundeen TF, Norwood KM, Brooks HL, Egleton RD. Increased blood-brain barrier permeability and altered tight junctions in experimental diabetes in the rat: contribution of hyperglycaemia and matrix metalloproteinases. Diabetologia. 2007 Jan;50(1):202-11. PubMed PMID: 17143608.
421. Devor A, Ulbert I, Dunn AK, Narayanan SN, Jones SR, Andermann ML, et al. Coupling of the cortical hemodynamic response to cortical and thalamic neuronal activity. Proceedings of the National Academy of Sciences of the United States of America. 2005 Mar 8;102(10):3822-7. PubMed PMID: 15734797. Pubmed Central PMCID: 550644.
422. Devor A, Tian P, Nishimura N, Teng IC, Hillman EM, Narayanan SN, et al. Suppressed neuronal activity and concurrent arteriolar vasoconstriction may explain negative blood oxygenation level-dependent signal. The Journal of neuroscience : the official journal of the Society for Neuroscience. 2007 Apr 18;27(16):4452-9. PubMed PMID: 17442830. Pubmed Central PMCID: 2680207.
423. Devor A, Hillman EM, Tian P, Waeber C, Teng IC, Ruvinskaya L, et al. Stimulus-induced changes in blood flow and 2-deoxyglucose uptake dissociate in ipsilateral somatosensory cortex. The Journal of neuroscience : the official journal of the Society for Neuroscience. 2008 Dec 31;28(53):14347-57. PubMed PMID: 19118167. Pubmed Central PMCID: 2655308.
424. Cauli B, Tong X, Rancillac A, Serluca N, Lambolez B, Rossier J, et al. Cortical GABA interneurons in neurovascular coupling: relays for subcortical vasoactive pathways. The Journal of neuroscience: the official journal of the Society for Neuroscience. 2004;24(41):8940-9.
425. Uhlirova H, Kilic K, Tian P, Thunemann M, Desjardins M, Saisan PA, et al. Cell type specificity of neurovascular coupling in cerebral cortex. Elife. 2016 May 31;5. PubMed PMID: 27244241. Pubmed Central PMCID: 4933561.
426. Inoue M, Takeuchi A, Horigane S, Ohkura M, Gengyo-Ando K, Fujii H, et al. Rational design of a high-affinity, fast, red calcium indicator R-CaMP2. Nat Methods. 2015 Jan;12(1):64-70. PubMed PMID: 25419959.
427. Stainier DYR, Fishman MC. The Zebrafish as a Model System to Study Cardiovascular Development. Trends in Cardiovascular Medicine. 1994 Sep-Oct;4(5):207-12. PubMed PMID: WOS:A1994PK64000002. English.
428. Ran FA, Hsu PD, Wright J, Agarwala V, Scott DA, Zhang F. Genome engineering using the CRISPR-Cas9 system. Nature protocols. 2013 Nov;8(11):2281-308. PubMed PMID: WOS:000326164100014. English.

429. Tang MX, Stern Y, Marder K, Bell K, Gurland B, Lantigua R, et al. The APOE-epsilon 4 allele and the risk of Alzheimer disease among African Americans, Whites, and Hispanics. Jama-J Am Med Assoc. 1998 Mar 11;279(10):751-5. PubMed PMID: WOS:000072366900031. English.
430. Jorgens K, Hillebrands JL, Hammes HP, Kroll J. Zebrafish: a model for understanding diabetic complications. Experimental and clinical endocrinology & diabetes : official journal, German Society of Endocrinology [and] German Diabetes Association. 2012 Apr;120(4):186-7. PubMed PMID: 22402952.
431. Kimmel RA, Dobler S, Schmitner N, Walsen T, Freudenblum J, Meyer D. Diabetic pdx1-mutant zebrafish show conserved responses to nutrient overload and anti-glycemic treatment. Scientific Reports. 2015 Sep 18;5. PubMed PMID: WOS:000361370800003. English.
432. Bogli SY, Huang MY. Spontaneous alternation behavior in larval zebrafish. The Journal of experimental biology. 2017 Jan 15;220(Pt 2):171-3. PubMed PMID: 27811295.
433. Kimble DP. Effects of combined entorhinal cortex-hippocampal lesions on locomotor behavior, spontaneous alternation and spatial maze learning in the rat. Physiology & behavior. 1978 Aug;21(2):177-87. PubMed PMID: 693644.
434. Harrison DG, Cai H. Endothelial control of vasomotion and nitric oxide production. Cardiology clinics. 2003 Aug;21(3):289-302. PubMed PMID: 14621446.
435. Di Marco LY, Farkas E, Martin C, Venneri A, Frangi AF. Is Vasomotion in Cerebral Arteries Impaired in Alzheimer's Disease? Journal of Alzheimers Disease. 2015;46(1):35-53. PubMed PMID: WOS:000354786000005. English.
436. Meyer MF, Rose CJ, Hulsmann JO, Schatz H, Pfohl M. Impaired 0.1-Hz vasomotion assessed by laser Doppler anemometry as an early index of peripheral sympathetic neuropathy in diabetes. Microvasc Res. 2003 Mar;65(2):88-95. PubMed PMID: WOS:000182447300003. English.